NASA CONTRACTOR REPORT

NASA CR-1733

OPTICAL PROPAGATION MEASUREMENTS AT EMERSON LAKE – 1968

by Gus E. Mevers, Melvin P. Keister, Jr., and David L. Fried

Prepared by
AUTONETICS DIVISION
NORTH AMERICAN ROCKWELL CORPORATION
Anaheim, Calif. 92803
for Langley Research Center

NATIONAL AERONAUTICS AND SPACE ADMINISTRATION • WASHINGTON, D. C. • SEPTEMBER 1971

1. Report No.	2. Government Accession No.	3. Recipient's Catalog No.
NASA CR-1733		

4. Title and Subtitle	5. Report Date
OPTICAL PROPAGATION MEASUREMENTS AT EMERSON LAKE - 1968	6. Performing Organization Code September 1971

7. Author(s)	8. Performing Organization Report No.
G. E. Mevers, M. P. Keister, and David L. Fried	C8-3042/401

9. Performing Organization Name and Address	10. Work Unit No.
Autonetics Division North American Rockwell 3370 Miraloma Avenue Anaheim, California 92803	115-00-00-00
	11. Contract or Grant No. NAS1-7705
	13. Type of Report and Period Covered Contractor Report
12. Sponsoring Agency Name and Address National Aeronautics and Space Administration Washington, D.C. 20546	14. Sponsoring Agency Code

15. Supplementary Notes

16. Abstract

A series of carefully controlled measurements concerned with optical propagation in an inhomogenous atmosphere were conducted at Emerson Lake (dry), Twenty-Nine Palms, California, to test the validity or range of validity of present optical propagation theory. Measurements were made of atmospheric-produced scintillation and wavefront distortion for wavelengths of 0.5 to 10.6 microns and over ranges of 0.5 to 5.0 km. The tests were made in strict accordance with the dictates of present theory, so that direct comparisons could be made between measurement results and theoretical predictions. The results of these measurements substantiate the predictions of theory for 0.5 to 1.15 micron wavelengths over short range transmission, but give a positive indication, in the form of a saturation of scintillation, of its failure at long ranges. The measurement results also indicate that the saturation level of scintillation is wavelength dependent and that a functional relationship exists between predicted and measured scintillation for a condition of saturation. In addition, both optical and temperature measurements of the optical strength of turbulence were made for comparison of the two techniques in making scintillation predictions. The results indicate that the optical method presently provides more useable results, but that it may be possible, with modifications in the data reduction procedure, to obtain equivalent results from the temperature measurements. Recommendations are given for additional measurements to more carefully cover those aspects of optical propagation outside the bounds of present theory which have been observed during this program and to broaden the scope of experimental checks on theory.

17. Key Words (Suggested by Author(s))	18. Distribution Statement
Atmospheric effects on laser beams Laser communications Atmospheric physics	Unclassified - Unlimited

19. Security Classif. (of this report)	20. Security Classif. (of this page)	21. No. of Pages	22. Price*
Unclassified	Unclassified	229	$3.00

*For sale by the National Technical Information Service, Springfield, Virginia 22151

FOREWORD

This final report, submitted in accordance with Contract NAS 1-7705, relates the procedures followed and the results obtained for a one-year experimental measurements program to determine the effect of an inhomogeneous atmosphere on optical propagation. It is submitted by North American Rockwell Corp., through its Autonetics Division, Electro Sensor Systems Division, Electro-Optical Laboratory, to the National Aeronautics and Space Administration, Langley Research Center, Hampton, Virginia. The NASA Project Engineer for this work was Duncan E. McIver.

ACKNOWLEDGEMENTS

We wish to express our gratitude to the United States Marine Corps, Twenty-Nine Palms, California, for allowing us to use Emerson Lake as a measurement site and especially to Lt. Colonel J. P. Kelly, USMC, for his assistance in implementing the range. We also wish to thank Messrs. R. S. Lawrence and G. R. Ochs for the Environmental Science Services Administration, Boulder, Colorado, for not only the use of their high-speed temperature probe, but also their assistance in the field with collecting data.

CONTENTS

ILLUSTRATIONS

TABLES

OPTICAL PROPAGATION MEASUREMENTS AT EMERSON LAKE - 1968

By Gus E. Mevers, Melvin P. Keister, Jr., and David L. Fried
Autonetics Division of North American Rockwell Corp.

I. INTRODUCTION AND SUMMARY

The present body of optical propagation theory, which is based on the Rytov approximation, has by virtue of concentrated activities in recent years been refined to the point that very unambiguous quantitative predictions can be made for optical system performance in the atmosphere. In general, present theory can predict both the atmospheric-produced scintillation and wavefront distortion experienced by an optical system for such parameters as transmission range, wavelength, optical strength of turbulence, system receiver area, and transmitter diameter. Present theory, in addition, can accommodate the convolution of scintillation and wavefront distortion to predict the effect of the atmosphere on the performance of an optical imaging system. In fact, a survey of present theory would demonstrate that the codification of fundamental design guidelines for atmospheric-optical systems is possible.

With this in-depth knowledge of what is usually the limiting factor to performance of optical systems in the atmosphere, it should be possible to meet the requirements of the optical designer for quantitative predictive design data for long-range optical systems. This might be the case if it were not for the problem that there has existed such a paucity of experimental data to properly test the validity or range of validity of present theory. At the time this program was planned, even some of the most fundamental predictions of theory had not been exposed to careful scrutiny of experimentation. Of the data that has been available (some of which has raised serious questions concerning the validity of the Rytov approximation), much of it is questionable because of experimental approach or because of the large spread in measurement results. (Concerning the matter of experimental approach, the reader is referred to Appendix A.) In addition, measurement data for wavelengths outside the visible range have been non-existent. Partly as a result of this situation, a one-year experimental program was initiated by the Langley Research Center of the National Aeronautics and Space Administration and performed by the Electro-Optical Laboratory, Electro Sensor Systems Division of North American Rockwell Corp.,

through its Autonetics Division, under Contract NAS 1-7705. The NASA Project Engineer for this program was D. E. McIver. This experimental program consisted of seven different measurements divided into three basic classes: scintillation, wavefront deformation, and temperature probe measurements.

A. PROGRAM OBJECTIVE

The broad objective of this program was to conduct, in strict adherence with the dictates of present propagation theory, a series of carefully controlled measurements of the effect of an inhomogenous atmosphere on horizontal optical propagation, and to compare the results of these measurements to the predictions of theory. Then from these comparisons, attempt to ascertain the range of validity of present theory. To meet these objectives, measurements were made with optical wavelengths that ranged from 0. 5 to 10. 6 microns, over transmission ranges of 1 to 5 km, with both coherent and incoherent sources, and with several types of optical receivers.

This program also had as an objective, the collection of data to determine the relative merits between temperature and optical measurements of the strength of turbulence.

B. SUMMARY

Highlights of the program results can be summarized as follows:

1. For the ranges of 1. 0 km or less, good agreement between measurements and theoretical predictions of scintillation was obtained for 0. 50 (incoherent source), 0. 514 and 1. 15 microns. Careful control of the measurement techniques resulted in a comparatively small spread between theory and experimental results.
2. It appears that scintillation log-amplitude variance, σ_ℓ^2, predictions made using spherical wave theory are a better fit to our measurements than σ_ℓ^2 predictions made using present theory concerned with finite laser sources.
3. Positive observations were made of saturation of scintillation at 0. 514 and 1. 15 microns for transmission ranges of 1. 5 km and beyond.

4. The level at which saturation of scintillation occurs appears to be wavelength dependent.

5. At 0.514 microns, the measured log-amplitude variance of scintillation, for conditions of saturation, is functionally related to the predicted value in the following manner:

$$\sigma_\ell^2(\text{meas}) = 0.55 \left[\sigma_\ell^2(\text{pred})\right]^{-0.17}$$

(Note the decrease in the measured scintillation with increasing predicted strength of turbulence.)

6. The log-normal distribution of 10.6 micron scintillation, unlike all other wavelengths measured, could not be confirmed. For all other wavelengths measured the log-normal distribution was verified both for unsaturated and saturated scintillation.

7. Measurements of the strength of turbulence made with high-speed temperature bridge were not in good agreement with those made optically. It appears possible, however, to obtain good agreement by deviating from the standard technique of temperature data reduction.

II. MEASUREMENT RANGE AND RANGE FACILITIES

A. MEASUREMENT SITE

The measurement site used for this program was Emerson Lake (dry) located on the western edge of the Marine Corps Training Center Reservation, Twenty-nine Palms, California. In selecting a site that would produce the most meaningful data for this program, we sought a location with features that would insure uniform turbulence conditions over as great a range as possible. Emerson Lake has several unique characteristics to provide these conditions. First, the lake bed is flat so that a transmitted beam would be a constant height above the ground. Measurements indicated that the average lake bed elevation change along the selected line-of-site could be accounted for in terms of the curvature of the earth. Second, the area is open and consequently does not suffer from abrupt changes in the wind direction. The lake bed itself is about 3 km wide and 5 km long and in the direction of the predominant wind there are no sharp changes in ground elevation for a distance of about 15 km. Third, the surface texture of the lake bed is quite uniform. This produces a heat transfer between ground and air that is uniform over the optical path. It also insures a uniform ground turbulence generation mechanism, i. e., a constant Obukhov length over the path length. Figure 1 is an aerial photograph taken during our early survey of sites that illustrates some of these characteristics discussed.

B. RANGE FACILITIES

The main facilities used to support this measurement program comprise a North American Rockwell Corp., facility referred to as the Laser System Testing and Applied Research Facility (L* Facility). This facility consists of two vehicles, designated the Main Instrumentation Van (MIV) and Satellite Vehicle, and a transportable laser mount. The Main Instrumentation Van, shown in Figure 2 is a fully-instrumented 8 x 35 foot trailer equipped with air conditioning, stabilization jacks, and life support equipment. The MIV also has on board a sufficient supply of tools and a built-in work area so that most field repairs can be performed. Power for the MIV is furnished by a 40 kilowatt diesel-powered generator. The Satellite Vehicle is a 3. 5-ton self-powered vehicle equipped with a 60 kilowatt diesel-powered generator, a 3-ton refrigeration capacity closed-cycle water chilling unit to supply cooling water to the laser, electronic rack space, and a built-in work area. (This vehicle housed

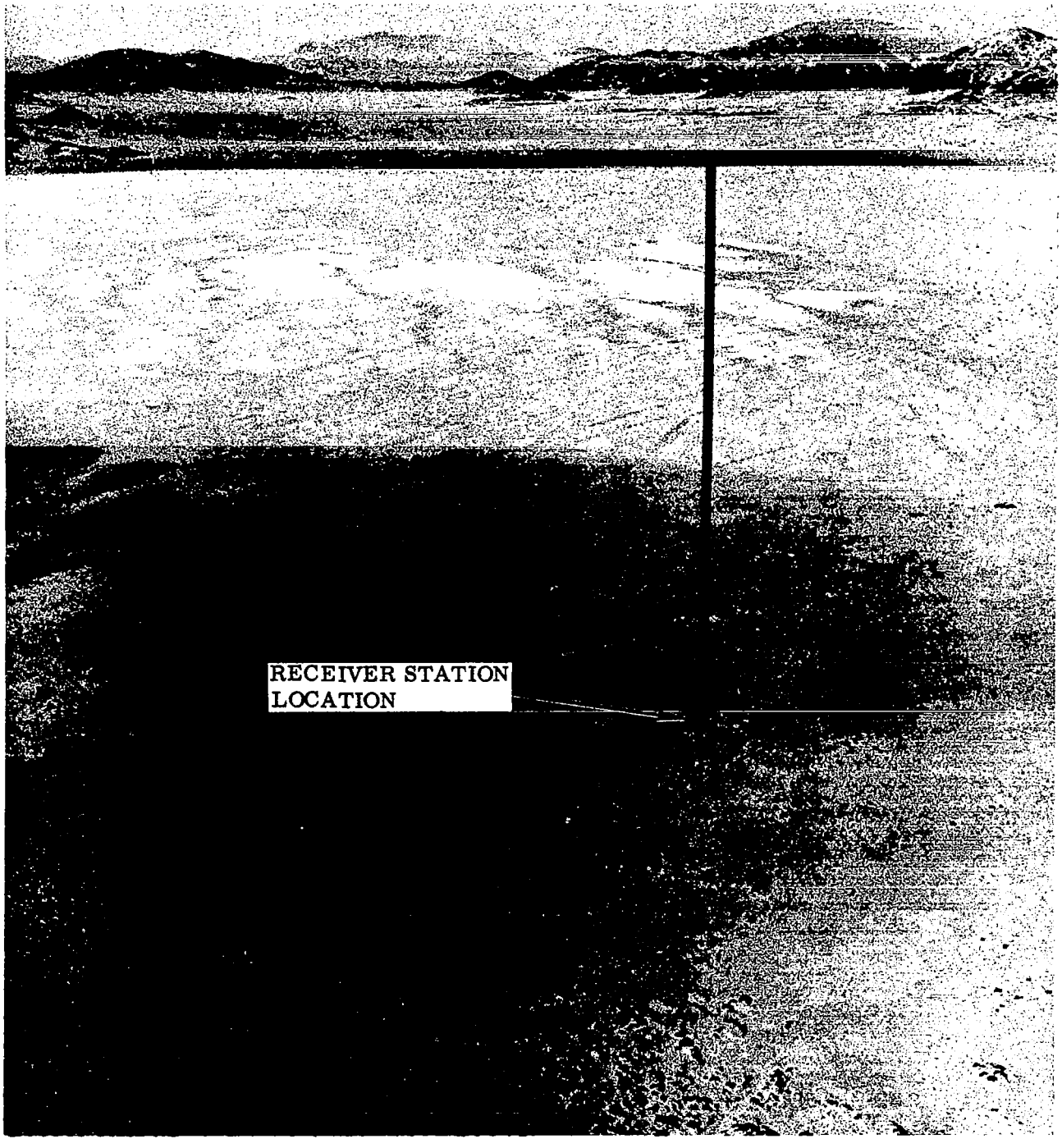

FIGURE 1. Aerial Photograph of Emerson Lake. The black line represents the approximate position of the optical path used for the measurements program. The "X" marks the location of the receiver station and main base of operation.

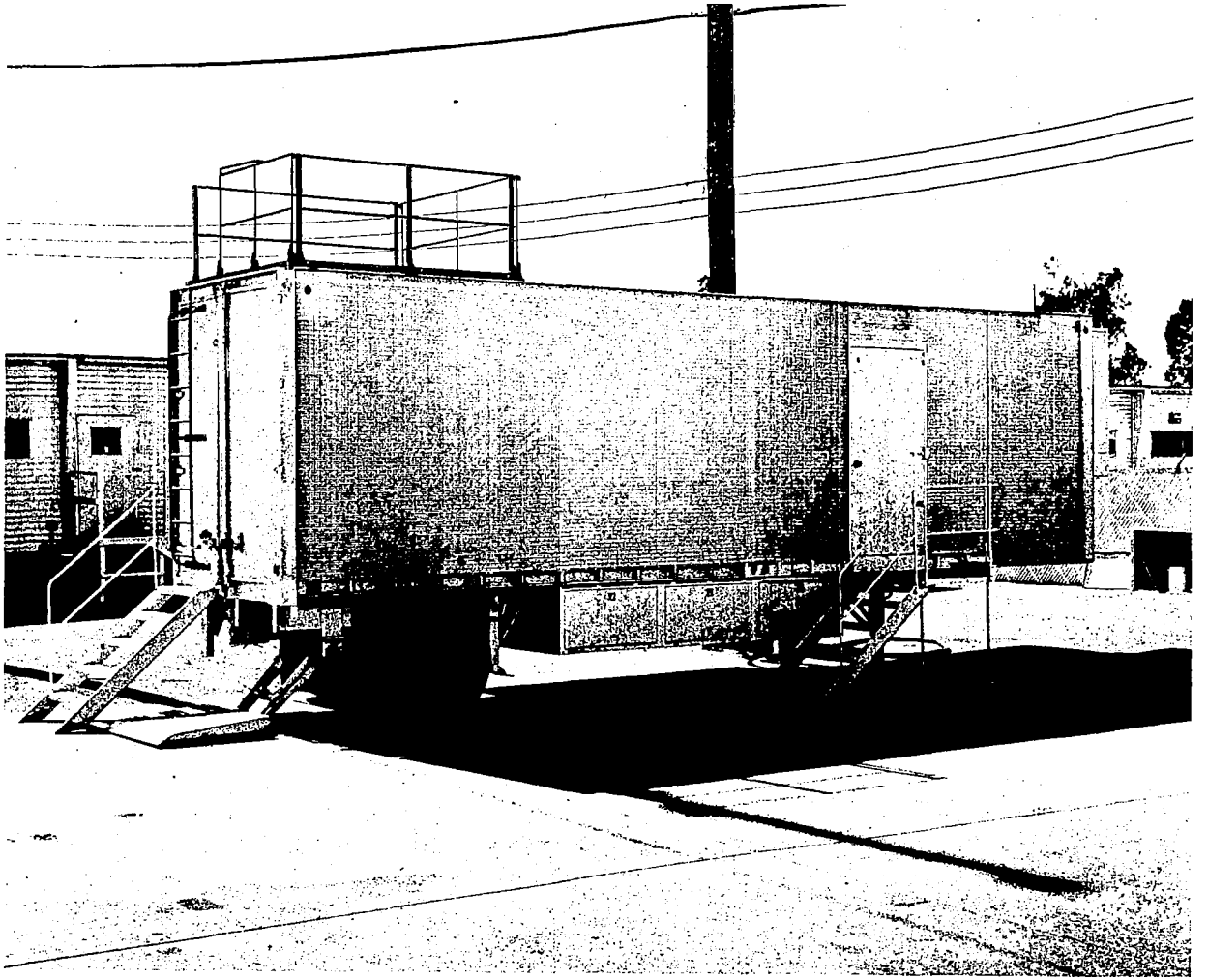

FIGURE 2. Main Instrumentation Van (MIV). This 8 x 35 foot instrumented van was used to accumulate and record the data collected at the optical receivers. Not shown in the photograph is a 40 kilowatt transportable diesel-powered generator that supplied power to the MIV and other operations at the receiver station.

all laser power supplies used during the measurement program.) The transportable laser mount, shown in Figure 3, is a converted military search light mount which has a 7 x 5 foot aluminum platform suspended on the search light yoke for mounting laser sources. This entire platform can be adjusted through small azimuth-elevation angles with a pointing accuracy of about one arc minute. A set of electrically-driven leveling jacks are mounted on three steel outriggers, 120° apart, that have been welded to the main frame of the mount. For this program, a mounting assembly was also constructed on the aluminum platform so that small adjustable periscopes could be mounted. These periscopes were used for fine pointing the laser sources. In addition to these facilities, four laser sources and a Xenon arc lamp source were provided for this program. The laser sources were: Spectra-Physics Model 140 Argon Laser, Model 125 He-Ne Laser, Model 115 He-He Laser, and a Coherent Radiation Model 40 CO_2 Laser. The Xenon source was a PEK, 75 watt unit.

C. RANGE PREPARATION

The first step in range preparation was to establish a straight line 5 km long on the lake bed for the measurement range. This task was accomplished with a T-3 theodolite set up at mid-range. At the same time, the range was chained off using a standard surveyor's steel tape and markers were placed every 250 meters along the measurement path. After the range had been surveyed, construction of the main base of operations was started at the south-end of the range. The first step was to construct at the range termination point a 5 x 6 x 5 foot solid concrete block that was used to mount the various optical receivers that were used during the measurement program. A 30 x 50 foot fenced compound was built around the concrete platform, a 1000 gallon diesel fuel storage tank was located in the compound, and a building was constructed to cover the concrete platform. This building, in addition to providing a shelter for the optical receivers, also was used for storage of field support materials such as water, dry ice, cryogents, motor oil, etc. When this construction was completed, the L* Facility was moved to the field site and the MIV and its power generator were located inside the compound as shown in Figure 4. Since the MIV housed all data recording equipment, it was located as close as possible to the receiver platform to keep cable lengths short. Installation of an annemometer to record wind speed, routing all power and signal cables, and installing a radio telephone in the MIV for outside communication completed preparation of the main base of operations.

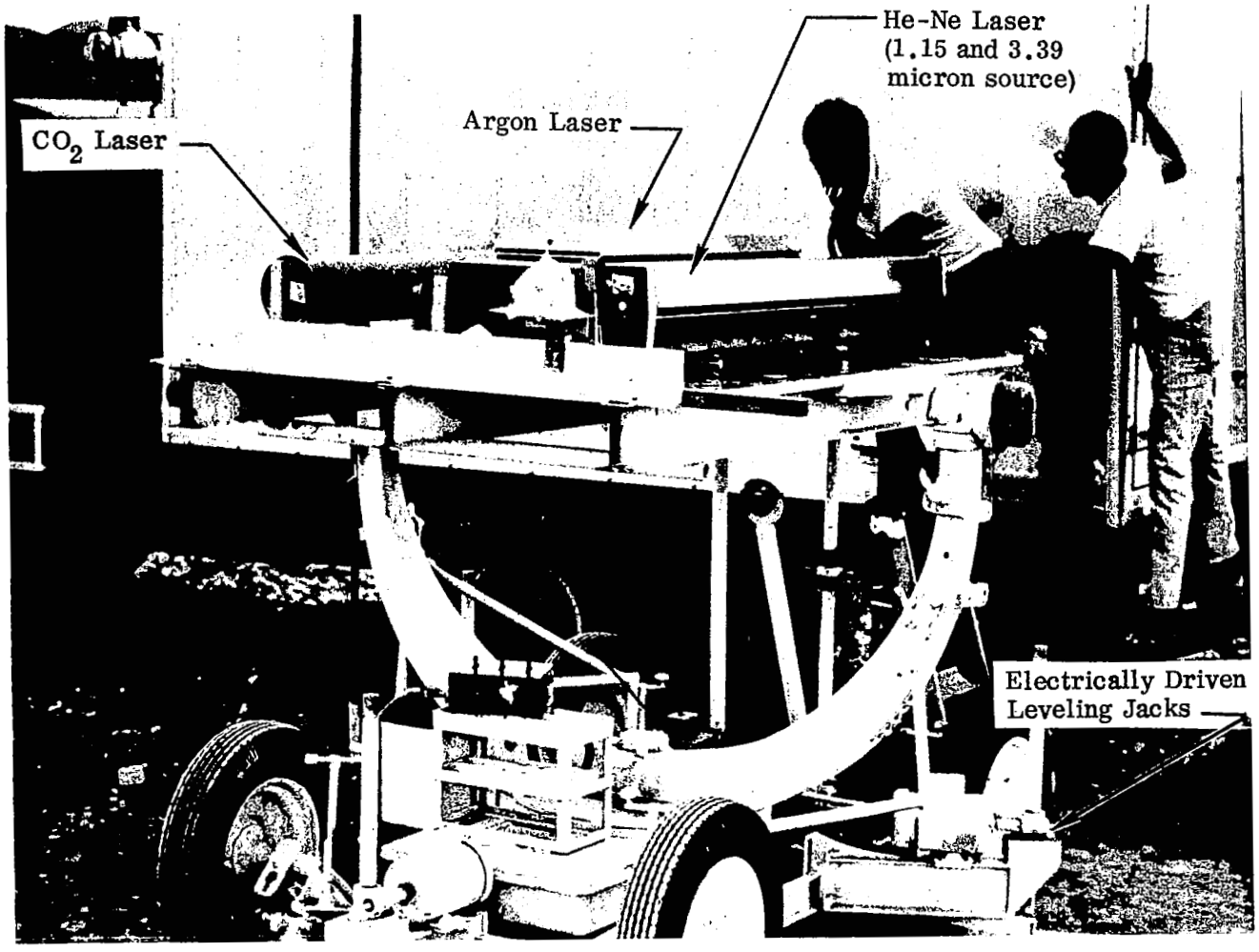

FIGURE 3. Transportable Laser Mount

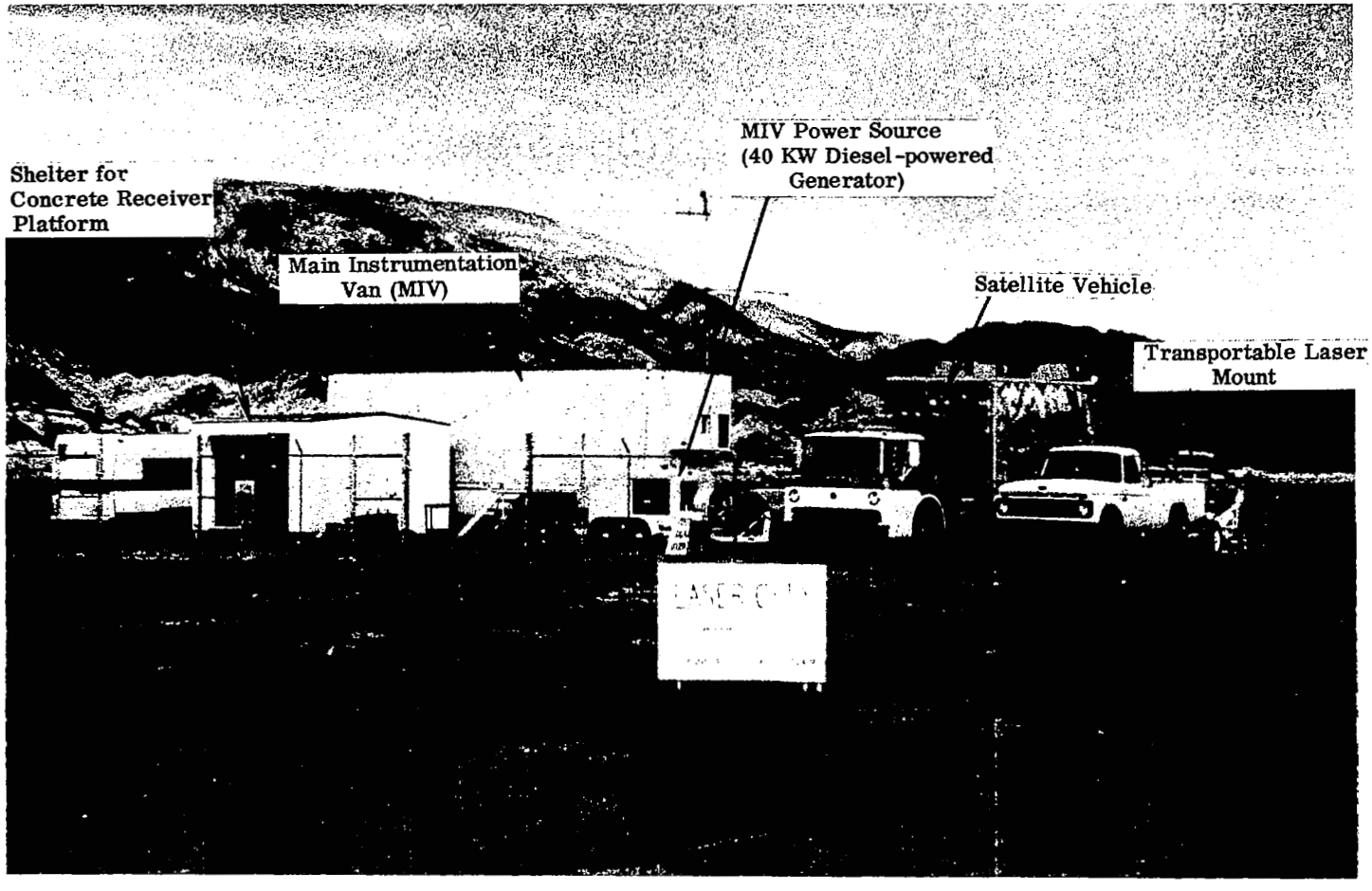

FIGURE 4. Main Base of Operations at Emerson Lake for Field Measurements Program

The argon and He-Ne laser sources were then mounted on the laser platform, as shown in Figure 5, and bore sighted to each other. In later measurements, the Xenon arc lamp, shown in Figure 5, was replaced with the CO_2 laser as shown in Figure 3.

The Model 115 He-Ne Laser, which was used for strength of turbulence measurements during the program and which remained at a fixed distance of 200 meters from the receiver platform, was mounted on a steel pier sunk several feet in the ground. To eliminate beam pointing problems caused by wind and solar heating, a wooden shelter, as shown in Figure 6, was constructed over the laser mount. Routing of power lines and installation of signal cables to operate a beam blocker that was used for certain portions of the measurements marked the completion of measurement range preparations.

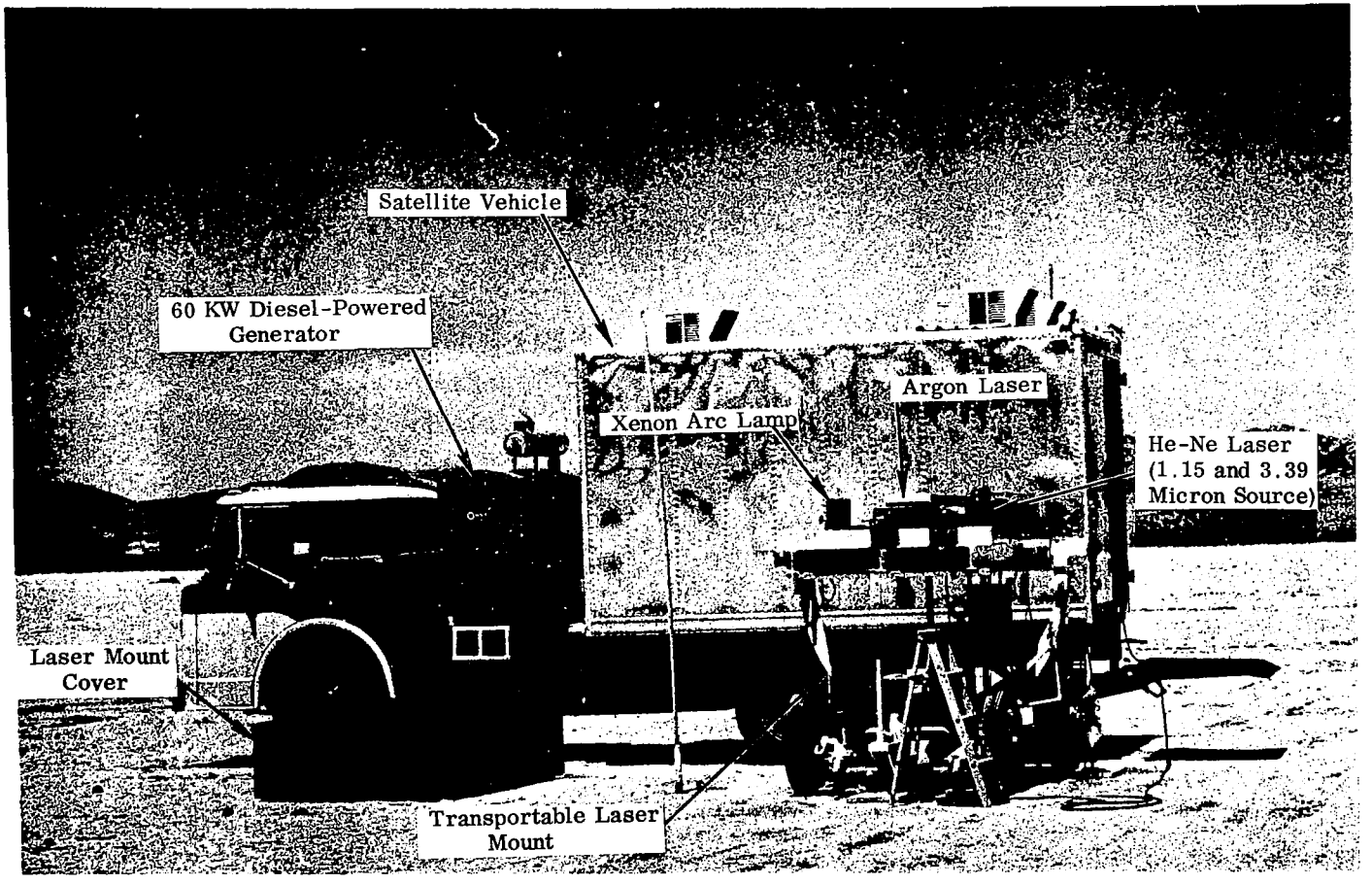

FIGURE 5. Down-range Transmitter Station. This is the self-contained transportable transmitter station used for the field measurements program. The transportable laser mount is shown located on the leeward side of the Satellite Vehicle. This technique was used to eliminate beam pointing problems caused by wind. The laser power supplies are located inside the Satellite Vehicle, and the refrigeration unit for laser water cooling is attached to the truck frame.

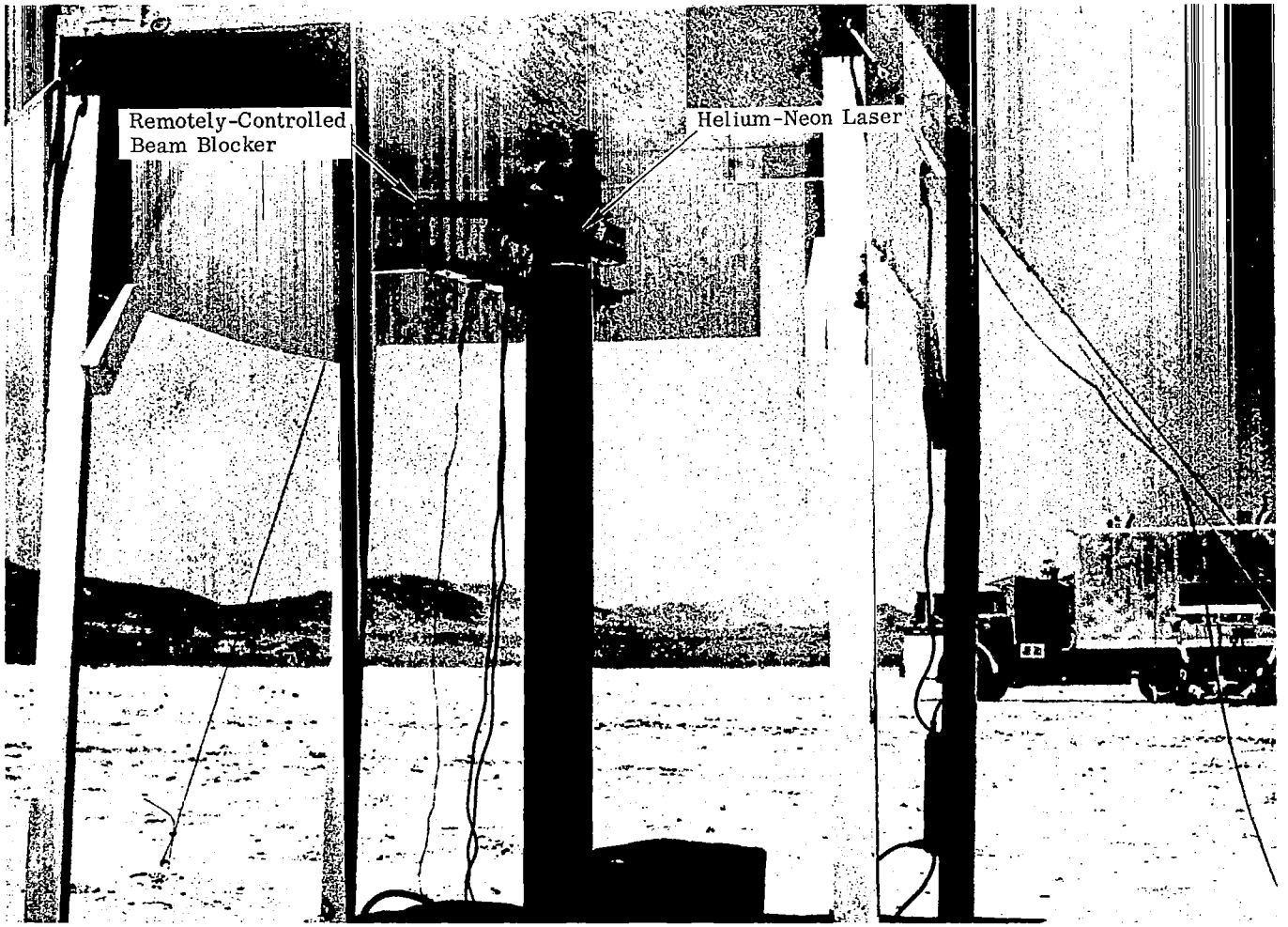

FIGURE 6. Laser Station for Refractive Index Structure Constant (C_N^2) Measurement. This station, located 200 meters down range, was essentially unmanned during the measurement program. Therefore, for background measurements, the laser output was blocked remotely from the MIV with the equipment shown. The shelter seen was constructed to eliminate beam pointing problems caused by wind and solar heating.

III. MEASUREMENTS PROGRAM

The field measurements program conducted for this contract consisted of some 500 separate measurements concerned with the effect of an inhomogeneous atmosphere on optical propagation. Table I presents the time order of these measurements and gives some details and comments of their execution. To assist the reader in following the data given in Table I, the following interpolation of two data runs are given:

The information for data run #309 indicates the measurement was made on 5/30/68 at 0233 hours and that data was collected over a transmission range of 1.0 km with 0.514 and 1.15 micron "point" collectors and with the aperture averaging receiver with the aperture diameter set at 2 cm.

The information for data run #907 indicates the measurement was made on 7/03/68 at 0104 hours and that data was collected over a transmission range of 0.5 km with the 0.500 micron (incoherent source detector) "point" collector. However, the data was discarded because it was determined unfit for use as a result of problems in performing the change from analog to digital format.

The measurements performed consisted of three types: Scintillation, Wavefront Distortion, and Temperature Probe Measurements.

The scintillation measurements consisted of:

1. Near simultaneous measurements with 0.50 micron (incoherent source detector) and 0.514 micron "point" collector for a transmission range of 0.5 km. These data were collected to check the effect of chromatic averaging of scintillation.
2. Simultaneous measurements with 0.514 and 1.15 micron "point" collector for transmission ranges of 1.0 and 1.5 km.
3. Simultaneous measurements with 1.15 and 10.6 micron "point" collector for a transmission range of 1.5 km.

4. Simultaneous measurements with a variable aperture receiver (0.514 micron detector) and a 0.514 micron "point" collector for transmission ranges of 1.0, 3.0, and 5.0 km. At each transmission range, data were collected with the variable aperture receiver over a range of collector diameters from 1 to 15 cm. These tests were made to determine the effect of aperture averaging of scintillation.

5. Simultaneous measurements with two identical 0.514 micron "point" collectors. These measurements were made to check the overall accuracy of the data collection and reduction procedures.

For the wavefront distortion measurements, data was collected simultaneously with a wavefront distortion measurements receiver (0.514 micron detector) and a 0.514 micron "point" collector for transmission ranges of 1.5 and 3.0 km.

The temperature probe measurements consisted of about 30 measurements of temperature fluctuations with a high speed temperature bridge. These data were collected to evaluate the ability of this technique to provide useable values for the optical strength of turbulence.

At the same time each of the above measurements were made, "point" collector data at 0.633 microns for transmission over a fixed 0.2 km path were collected. These data were used to determine the optical strength of turbulence which provided a means of making predictions for comparison with the other data.

For all of the measurements conducted, every effort was made to collect data within the dictates of present optical propagation theory so that meaningful checks of predictions could be made. In addition, to insure the quality of the program results, we have discarded those data, as some of the comments in Table I indicate, for which we felt the data taken was subject to some question.

The sections to follow will discuss these different measurements, the experimental and data reduction techniques, and the results obtained.

TABLE I

MEASUREMENT PROGRAM CHRONICLE

RUN #	DATE	TIME (PDST)	RANGE (km)	DATA* (cm)								COMMENTS
				+ 0.500	+ 0.514	+ 0.514	LARGE APER.	+ 1.15	+ 10.6	SEEING MONITOR	TEMP. PROBE	
101	5/24/68	2048	1.0		X							
102	5/24/68	2051	1.0		X							
103	5/24/68	2053	1.0		X							
104	5/24/68	2118	1.0		X							
105	5/24/68	2125	1.0		X							
106	5/24/68	2128	1.0		X							
107	5/24/68	2131	1.0		X							
108	5/24/68	2134	1.0		X							
110	5/24/68	2140	1.0		X							
111	5/24/68	2144	1.0		X							

*Each data run made included a "Point" collector measurement with a 0.633 micron laser at a 0.2 km range.

+"Point" collector measurement

TABLE I - Continued

RUN #	DATE	TIME (PDST)	RANGE (km)	DATA* (cm)								COMMENTS
				+ 0.500	+ 0.514	+ 0.514	LARGE APER.	+ 1.15	+ 10.6	SEEING MONITOR	TEMP. PROBE	
112	5/24/68	2147	1.0		X							
113	5/24/68	2150	1.0		X							
114	5/24/68	2153	1.0		X							
115	5/24/68	2156	1.0		X							
201	5/29/68	0435	1.0		X							These data not used because ultra calm wind conditions resulted in anomalous turbulence conditions
202	5/29/68	0438	1.0		X							These data not used because ultra calm wind conditions resulted in anomolous turbulence conditions
203	5/29/68	0443	1.0		X							These data not used because ultra calm wind conditions resulted in anomalous turbulence conditions

TABLE I - Continued

RUN #	DATE	TIME (PDST)	RANGE (km)	DATA* (cm)								COMMENTS
				+ 0.500	+ 0.514	+ 0.514	LARGE APPER.	+ 1.15	+ 10.6	SEEING MONITOR	TEMP. PROBE	
204	5/29/68	0447	1.0					X				These data not used because ultra calm wind conditions resulted in anomalous turbulence conditions
205	5/29/68	0449	1.0					X				These data not used because ultra calm wind conditions resulted in anomalous turbulence conditions
206	5/29/68	0452	1.0					X				These data not used because ultra calm wind conditions resulted in anomalous turbulence conditions
207	5/29/68	0454	1.0					X				These data not used because ultra calm wind conditions resulted in anomalous turbulence conditions
208	5/29/68	0457	1.0					X				These data not used because ultra calm wind conditions resulted in anomalous turbulence conditions

TABLE I - Continued

RUN #	DATE	TIME (PDST)	RANGE (km)	DATA* (cm)								COMMENTS
				+ 0.500	+ 0.514	+ 0.514	LARGE APPER.	+ 1.15	+ 10.6	SEEING MONITOR	TEMP. PROBE	
209	5/29/68	0501	1.0		X							These data not used because ultra calm wind conditions resulted in anomalous turbulence conditions
210	5/29/68	0505	1.0		X							These data not used because ultra calm wind conditions resulted in anomalous turbulence conditions
211	5/29/68	0508	1.0		X							These data not used because ultra calm wind conditions resulted in anomalous turbulence conditions
212	5/29/68	0512	1.0					X				These data not used because ultra calm wind conditions resulted in anomalous turbulence conditions
213	5/29/68	0515	1.0					X				These data not used because ultra calm wind conditions resulted in anomalous turbulence conditions

TABLE I - Continued

RUN #	DATE	TIME (PDST)	RANGE (km)	DATA* (cm)								COMMENTS
				+ 0.500	+ 0.514	+ 0.514	LARGE APPER.	+ 1.15	+ 10.6	SEEING MONITOR	TEMP. PROBE	
214	5/29/68	0523	1.0		X			X				These data not used because ultra calm wind conditions resulted in anomalous turbulence conditions
215	5/29/68	0525	1.0		X			X				These data not used because ultra calm wind conditions resulted in anomalous turbulence conditions
216	5/29/68	0528	1.0		X			X				These data not used because ultra calm wind conditions resulted in anomalous turbulence conditions
217	5/29/68	0530	1.0		X			X				These data not used because ultra calm wind conditions resulted in anomalous turbulence conditions
301	5/29/68	0542	1.0		X			X				These data not used because ultra calm wind conditions resulted in anomalous turbulence conditions

TABLE I - Continued

RUN #	DATE	TIME (PDST)	RANGE (km)	DATA* (cm) + 0.500	+ 0.514	+ 0.514	LARGE APPER.	+ 1.15	+ 10.6	SEEING MONITOR	TEMP. PROBE	COMMENTS
302	5/29/68	0545	1.0		X			X				These data not used because ultra calm wind conditions resulted in anomalous turbulence conditions
303	5/29/68	0547	1.0		X			X				These data not used because ultra calm wind conditions resulted in anomalous turbulence conditions
304	5/29/68	0554	1.0		X			X				These data not used because ultra calm wind conditions resulted in anomalous turbulence conditions
305	5/29/68	0556	1.0		X			X				These data not used because ultra calm wind conditions resulted in anomalous turbulence conditions
306	5/29/68	0559	1.0		X			X				These data not used because ultra calm wind conditions resulted in anomalous turbulence conditions

TABLE I - Continued

RUN #	DATE	TIME (PDST)	RANGE (km)	DATA* (cm)								COMMENTS
				+ 0.500	+ 0.514	+ 0.514	LARGE APPER.	+ 1.15	+ 10.6	SEEING MONITOR	TEMP. PROBE	
307	5/29/68	0602	1.0		X			X				These data not used because ultra calm wind conditions resulted in anomalous turbulence conditions
308	5/30/68	0230	1.0		X		1	X				
309	5/30/68	0233	1.0		X		2	X				
310	5/30/68	0237	1.0		X		3	X				
311	5/30/68	0240	1.0		X		4	X				
312	5/30/68	0242	1.0		X		5	X				
313	5/30/68	0245	1.0		X		6	X				
314	5/30/68	0248	1.0		X		7	X				
315	5/30/68	0250	1.0		X		8	X				
316	5/30/68	0253	1.0		X		9	X				
317	5/30/68	0255	1.0		X		10	X				
401	5/30/68	0305	1.0		X		11	X				

TABLE I - Continued

RUN #	DATE	TIME (PDST)	RANGE (km)	DATA* (cm) + 0.500	+ 0.514	+ 0.514	LARGE APPER.	+ 1.15	+ 10.6	SEEING MONITOR	TEMP. PROBE	COMMENTS
402	5/30/68	0307	1.0		X		12	X				
403	5/30/68	0310	1.0		X		13	X				
404	5/30/68	0313	1.0		X		14	X				
405	5/30/68	0315	1.0		X		15	X				
406	5/30/68	2331	3.0		X		1					
407	5/30/68	2334			X		2					
408	5/31/68	0021	3.0		X		3					
409	5/31/68	0024	3.0		X		4					
410	5/31/68	0027	3.0		X		5					
411	5/31/68	0029	3.0		X		6					
412	5/31/68	0032	3.0		X		7					
413	5/31/68	0034	3.0		X		8					
414	5/31/68	0037	3.0		X		9					

TABLE I - Continued

RUN #	DATE	TIME (PDST)	RANGE (km)	DATA* (cm)								COMMENTS
				+ 0.500	+ 0.514	+ 0.514	LARGE APPER.	+ 1.15	+ 10.6	SEEING MONITOR	TEMP. PROBE	
415	5/31/68	0039	3.0		X		10					
501	5/31/68	0053	3.0		X		11					
502	5/31/68	0055	3.0		X		12					
503	5/31/68	0058	3.0		X		13					
504	5/31/68	0100	3.0		X		14					
505	5/31/68	0102	3.0		X		15					
506	5/31/68	0205	5.0		X		1					
507	5/31/68	0207	5.0		X		3					
508	5/31/68	0210	5.0		X		5					
509	5/31/68	0213	5.0		X		7					
510	5/31/68	0215	5.0		X		9					
511	5/31/68	0217	5.0		X		11					
512	5/31/68	0220	5.0		X		13					These data not used because of equipment problem in field

TABLE I - Continued

RUN #	DATE	TIME (PDST)	RANGE (km)	DATA* (cm)								COMMENTS
				+ 0.500	+ 0.514	+ 0.514	LARGE APPER.	+ 1.15	+ 10.6	SEEING MONITOR	TEMP. PROBE	
513	5/31/68	0230	5.0		X		13					
514	5/31/68	0234	5.0		X		15					
601	5/31/68	0434	0.5	X								These data not used because extraordinary wind conditions produced instability of the source mount.
602	5/31/68	0436	0.5	X								These data not used because extraordinary wind conditions produced instability of the source mount.
603	5/31/68	0438	0.5	X								These data not used because extraordinary wind conditions produced instability of the source mount.
701	6/28/68	0104									X	Platinum temperature detectors separated by 10 cm during measurements

TABLE I - Continued

RUN #	DATA	TIME (PDST)	RANGE (km)	DATA* (cm) + 0.500	+ 0.514	+ 0.514	LARGE APPER.	+ 1.15	+ 10.6	SEEING MONITOR	TEMP. PROBE	COMMENTS
702	6/28/68	0106									X	Platinum temperature detectors separated by 10 cm during measurements
703	6/28/68	0109									X	Platinum temperature detectors separated by 10 cm during measurements
704	6/28/68	0111									X	Platinum temperature detectors separated by 10 cm during measurements.
705	6/28/68	0113									X	Platinum temperature detectors separated by 10 cm during measurements.
706	6/28/68	0116									X	Platinum temperature detectors separated by 10 cm during measurements.
707	6/28/68	0118									X	Platinum temperature detectors separated by 10 cm during measurements.
708	6/28/68	0120									X	Platinum temperature detectors separated by 10 cm measurements.

TABLE I - Continued

RUN #	DATE	TIME (PDST)	RANGE (km)	DATA* (cm)								COMMENTS
				+ 0.500	+ 0.514	+ 0.514	LARGER APPER.	+ 1.15	+ 10.6	SEEING MONITOR	TEMP. PROBE	
709	6/28/68	0122									X	Platinum temperature detectors separated by 10 cm during measurements.
710	6/28/68	0124									X	Platinum temperature detectors separated by 10 cm during measurements.
711	6/28/68	0126									X	Platinum temperature detectors separated by 10 cm during measurements.
801	6/28/68	0142									X	Platinum temperature detectors separated by 10 cm during measurements.
802	6/28/68	0145									X	Platinum temperature detectors separated by 10 cm during measurements.
803	6/28/68	0147									X	Platinum temperature detectors separated by 10 cm during measurements.
804	6/28/68	0149									X	Platinum temperature detectors separated by 10 cm during measurements.

TABLE I - Continued

RUN #	DATE	TIME (PDST)	RANGE (km)	DATA* (cm)								COMMENTS
				+ 0.500	+ 0.514	+ 0.514	LARGER APPER.	+ 1.15	+ 10.6	SEEING MONITOR	TEMP. PROBE	
805	6/28/68	0151									X	These data not used because of equipment problem in field.
806	6/28/68	0153									X	Platinum temperature detectors separated by 10 cm during measurements.
807	6/28/68	9155									X	Platinum temperature detectors separated by 10 cm during measurements.
808	6/28/68	0157									X	Platinum temperature detectors separated by 10 cm during measurements.
809	6/28/68	0159									X	Platinum temperature detectors separated by 10 cm during measurements.
810	6/28/68	0219									X	Platinum temperature detectors separated by 10 cm during measurements.
811	6/28/68	0221									X	Platinum temperature detectors separated by 10 cm during measurements.

TABLE I - Continued

RUN #	DATE	TIME (PDST)	RANGE (km)	DATA* (cm) + 0.500	+ 0.514	+ 0.514	LARGER APPER.	+ 1.15	+ 10.6	SEEING MONITOR	TEMP. PROBE	COMMENTS
812	6/28/68	0223									X	Platinum temperature detectors separated by 10 cm during measurements.
813	6/28/68	0224									X	Platinum temperature detectors separated by 10 cm during measurements.
814	6/28/68	0226									X	Platinum temperature detectors separated by 10 cm during measurements.
815	6/28/68	0228									X	Platinum temperature detectors separated by 10 cm during measurements.
816	6/28/68	0230									X	Platinum temperature detectors separated by 10 cm during measurements.
817	6/28/68	0232									X	Platinum temperature detectors separated by 10 cm during measurements.
818	6/28/68	0234									X	Platinum temperature detectors separated by 10 cm during measurements.

TABLE I - Continued

RUN #	DATE	TIME (PDST)	RANGE (km)	DATA* (cm)								COMMENTS
				+ 0.500	+ 0.514	+ 0.514	LARGER APPER.	+ 1.15	+ 10.6	SEEING MONITOR	TEMP. PROBE	
819	6/28/68	0236									X	Platinum temperature detectors separated by 10 cm during measurements.
820	6/28/68	0238									X	Platinum temperature detectors separated by 10 cm during measurements.
821	6/28/68	0240									X	Platinum temperature detectors separated by 10 cm during measurements.
901	7/03/68	0049	0.5	X								These data not used because of improper blocking of argon laser caused pickup of 0.514 micron light in 0.500 micron detector.
902	7/03/68	0051	0.5	X								These data not used because of improper blocking of argon laser caused pickup of 0.514 micron light in 0.500 micron detector.
903	7/03/68	0054	0.5		X							

TABLE I - Continued

RUN #	DATE	TIME (PDST)	RANGE (km)	DATA* (cm)								COMMENTS
				+ 0.500	+ 0.514	+ 0.514	LARGER APPER.	+ 1.15	+ 10.6	SEEING MONITOR	TEMP. PROBE	
904	7/03/68	0056	0.5	X								
905	7/03/68	0059	0.5	X								
906	7/03/68	0101	0.5		X							
907	7/03/68	0104	0.5	X								These data not used because of problem in analog-to-digital conversion
908	7/03/68	0107	0.5	X								These data not used because of problem in analog-to-digital conversion
909	7/03/68	0110	0.5		X							
910	7/03/68	0114	0.5	X								
911	7/03/68	0116	0.5	X								
912	7/03/68	0120	0.5		X							
913	7/03/68	0123	0.5	X								These data not used because of problem in analog-to-digital conversion.

TABLE I - Continued

RUN #	DATE	TIME (PDST)	RANGE (km)	DATA* (cm)								COMMENTS
				+ 0.500	+ 0.514	+ 0.514	LARGER APPER.	+ 1.15	+ 10.6	SEEING MONITOR	TEMP. PROBE	
914	7/03/68	0126	0.5	X								
915	7/03/68	0128	0.5		X							
1001	7/03/68	0133	0.5	X								
1002	7/03/68	0140	0.5	X								
1003	7/03/68	0143	0.5		X							
1004	7/03/68	0146	0.5	X								
1005	7/03/68	0149	0.5	X								
1006	7/03/68	0151	0.5		X							
1007	7/03/68	0154	0.5	X								
1008	7/03/68	0156	0.5	X								
1009	7/03/68	0159	0.5		X							
1101	7/10/68	0129	1.0					X	X			
1102	7/10/68	0132	1.0					X	X			

TABLE I - Continued

RUN #	DATE	TIME (PDST)	RANGE (km)	DATA* (cm) + 0.500	+ 0.514	+ 0.514	LARGER APPER.	+ 1.15	+ 10.6	SEEING MONITOR	TEMP. PROBE	COMMENTS
1103	7/10/68	0134	1.0					X	X			
1104	7/10/68	0208	1.0					X	X			
1105	7/10/68	0211	1.0					X	X			These data not used because of equipment problem in field.
1106	7/10/68	0214	1.0					X	X			
1107	7/10/68	0217	1.0					X	X			
1108	7/10/68	0220	1.0					X	X			
1109	7/10/68	0222	1.0					X	X			
1110	7/10/68	0225	1.0					X	X			
1111	7/10/68	0227	1.0					X	X			
1112	7/10/68	0230	1.0					X	X			These data not used because of problem in analog-to-digital conversion
1113	7/10/68	0232	1.0					X	X			
1114	7/10/68	0235	1.0					X	X			

TABLE I - Continued

RUN #	DATE	TIME (PDST)	RANGE (km)	DATA* (cm)								COMMENTS
				+ 0.500	+ 0.514	+ 0.514	LARGER APPER.	+ 1.15	+ 10.6	SEEING MONITOR	TEMP. PROBE	
1115	7/10/68	0237	1.0					X	X			
1116	7/10/68	0240	1.0					X	X			
1117	7/10/68	0243	1.0					X	X			
1118	7/10/68	0246	1.0					X	X			
1201	7/11/68	0222	1.5		X	X		X				Aperture centers of 0.514 micron detectors separated by 20 cm during measurement.
1202	7/11/68	0225	1.5		X	X		X				Aperture centers of 0.514 micron detectors separated by 20 cm during measurement
1203	7/11/68	0227	1.5		X	X		X				Aperture centers of 0.514 micron detectors separated by 20 cm during measurement
1204	7/11/68	0230	1.5		X	X		X				Aperture center of 0.514 micron detectors separated by 20 cm during measurement

TABLE I - Continued

RUN #	DATE	TIME (PDST)	RANGE (km)	DATA* (cm)								COMMENTS
				+ 0.500	+ 0.514	+ 0.514	LARGER APPER.	+ 1.15	+ 10.6	SEEING MONITOR	TEMP. PROBE	
1205	7/11/68	0232	1.5		X	X		X				Aperture centers of 0.514 micron detectors separated by 20 cm during measurement
1206	7/11/68	0234	1.5		X	X		X				Aperture centers of 0.514 micron detectors separated by 20 cm during measurement
1207	7/11/68	0236	1.5		X	X		X				Aperture centers of 0.514 micron detectors separated by 20 cm during measurement
1208	7/11/68	0238	1.5		X	X		X				Aperture centers of 0.514 micron detectors separated by 20 cm during measurement
1209	7/11/68	0240	1.5		X	X		X				Aperture centers of 0.514 micron detectors separated by 20 cm during measurement

TABLE I- Continued

RUN #	DATE	TIME (PDST)	RANGE (km)	DATA* (cm)								COMMENTS
				+ 0.500	+ 0.514	+ 0.514	LARGER APPER.	+ 1.15	+ 10.6	SEEING MONITOR	TEMP. PROBE	
1210	7/11/68	0242	1.5		X	X		X				Aperture centers of 0.514 micron detectors separated by 20 cm during measurement
1211	7/11/68	0244	1.5		X	X		X				Aperture centers of 0.514 micron detectors separated by 20 cm during measurement
1212	7/11/68	0246	1.5		X	X		X				Aperture centers of 0.514 micron detectors separated by 20 cm during measurement
1213	7/11/68	0248	1.5		X	X		X				Aperture centers of 0.514 micron detectors separated by 20 cm during measurement
1214	7/11/68	0250	1.5		X	X		X				Aperture centers of 0.514 micron detectors separated by 20 cm during measurement

TABLE I - Continued

RUN #	DATE	TIME (PDST)	RANGE (km)	DATA* (cm)								COMMENTS
				+ 0.500	+ 0.514	+ 0.514	LARGER APPER.	+ 1.15	+ 10.6	SEEING MONITOR	TEMP. PROBE	
1215	7/11/68	0252	1.5		X	X		X				Aperture centers of 0.514 micron detectors separated by 20 cm during measurement
1216	7/11/68	0254	1.5		X	X		X				Aperture centers of 0.514 micron detectors separated by 20 cm during measurement
1217	7/11/68	0256	1.5		X	X		X				Aperture center of 0.514 micron detectors separated by 20 cm during measurement
1218	7/11/68	0258	1.5		X	X		X				Aperture centers of 0.514 micron detectors separated by 20 cm during measurement
1219	7/11/68	0300	1.5		X	X		X				Aperture center of 0.514 micron detectors separated by 20 cm during measurement

TABLE I - Continued

RUN #	DATE	TIME (PDST)	RANGE (km)	DATA* (cm)								COMMENTS
				+ 0.500	+ 0.514	+ 0.514	LARGER APPER.	+ 1.15	+ 10.6	SEEING MONITOR	TEMP. PROBE	
1220	7/11/68	0302	1.5		X	X		X				Aperture center of 0.514 micron detectors separated by 20 cm during measurement
1301	7/13/68	0343	1.5		X							
1302	7/13/68	0349	1.5		X					X		"Seeing" monitor measurement made between Run #1301 and 1302
1303	7/13/68	0357	1.5		X							
1304	7/13/68	0402	1.5		X					X		"Seeing" monitor measurement made between Run #1303 and 1304
1305	7/13/68	0410	1.5		X					X		"Seeing" monitor measurement made between Run #1305 and 1306
1306	7/13/68	0415	1.5		X					X		"Seeing" monitor measurement made before Run #1307
1307	7/13/68	0435	1.5		X							
1308	7/13/68	0557	3.0		X					X		"Seeing" monitor measurement made between Run #1308 and 1309
1309	7/13/68	0604	3.0		X							

TABLE I - Concluded

RUN #	DATE	TIME (PDST)	RANGE (km)	DATA* (cm)								COMMENTS
				+ 0.500	+ 0.514	+ 0.514	LARGER APPER.	1.15	10.6	SEEING MONITOR	TEMP. PROBE	
1310	7/13/68	0608	3.0		X						X	"Seeing" monitor measurement made between Run #1310 and 1311
1311	7/13/68	0622	3.0		X							

IV. SCINTILLATION MEASUREMENTS

Present optical propagation theory (spherical wave)[1,2], based on the Rytov approximation, predicts the functional relationship between optical wavelength, transmission range, strength of optical turbulence, and the scintillation observed with a "point" collector* by means of the following equation.

$$C_\ell(o) = \sigma_\ell^2 = 0.124\,(2\pi/\lambda)^{7/6} Z^{11/6} C_N^2, \qquad (1)$$

Here, $C_\ell(o)$ (or σ_ℓ^2)† is the log-amplitude variance of the measured scintillation.

λ is the optical wavelength, Z is the transmission range and C_N^2 is the refractive index structure constant -- a measure of the optical strength or turbulence.

It is the validity or range of validity of these predictions that the major body of this experimental program was concerned with. In addition to these basic scintillation measurements, "point" collector data was also taken to test theoretical predictions on chromatic averaging× and data was obtained for large aperture averaging of scintillation to check predictions of the log-amplitude covariance.

A. SCINTILLATION RECEIVERS

To make these scintillation measurements six different optical receivers were designed and constructed.‡ Five of the optical receivers were used for "point" collector measurements and one was used for data collection on aperture averaging. Table II provides a list of characteristics for the "point" collector receivers.

---

*A "point" collector is an aperture small enough so that the intensity distribution across the aperture is well correlated.

†In this report we shall use the notation $C_\ell(o)$ and σ_ℓ^2 interchangeably to denote the log-amplitude variance.

×Theory predicts that within an optical bandwidth of about 0.1 microns there should be no appreciable chromatic averaging of scintillation.

‡A seventh optical receiver was also constructed for 3.39 micron "point" collector measurements, but its liquid nitrogen dewar developed a leak and measurements could not be made.

TABLE II

CHARACTERISTICS OF "POINT" COLLECTOR RECEIVERS

OPTICAL WAVELENGTH (MICRONS)	OPTICAL BANDWIDTH (MICRONS)	TYPE DETECTOR	COLLECTOR DIAMETER (mm)	ELECTRICAL BANDWIDTH (Hz)	OBSERVED SOURCE
0.5145	0.005	S-20 Photomultiplier	2.3	3×10^3	Spectra-Physics Model 140, Argon Laser
0.5	0.08	S-20 Photomultiplier	2.3	3×10^3	PEK 75 Watt High Pressure Xenon Arc Lamp
0.6328	0.005	S-20 Photomultiplier	1.2	3×10^3	Spectra-Physics Model 115, He-Ne Laser
1.15	0.01	Dry Ice-Cooled S-1 Photomultiplier	3.4	3×10^3	Spectra-Physics Model 125, He-Ne Laser
10.6	0.3	Liquid-Neon-Cooled Mercury-Doped Germanium	10.3	1×10^3	Coherent Radiation Model 40, CO_2 Laser

Figure 7 shows the mechanical assembly of the type receiver package that was used for the 0.5, 0.514, 0.633, and 1.15 micron measurements. Each of these receivers, as shown, was equipped with a retractable eyepiece and AZ-EL mount for pointing at its observed source. Each of these receivers used a photomultiplier detector. The dynode chain circuits of the various detectors are shown in Figure 8, and the line driver circuit used in conjunction with the detectors is shown in Figure 9. The 10.6 micron "point" collector receiver, shown in Figure 10, was a liquid-neon cooled, mercury-doped germanium detector approximately 2 millimeters in diameter. An irtran objective lens plus a cold aperture stop was used to limit the field-of-view to a few degrees to insure an acceptably small level of background noise. The line driver used with this detector is shown in Figure 11. The line driver was designed so that the bias voltage of the detector could be "bucked-out", thus making it possible to utilize a greater portion of the dynamic range of the magnetic tape when data was recorded. During the design of the electronics for these various detectors extreme care was given to obtain the maximum dynamic range. Subsequent tests made in the laboratory after the receiver packages were constructed indicated that linear outputs could be obtained over a dynamic range equal to or greater than 60 db. The aperture averaging receiver, shown in Figure 12, was a 15 centimeter aperture f/10, refractive telescope that used a folding mirror to conserve size (see Figure 13). An adjustable aperture stop was used to vary the collector diameter from 1 to 15 centimeters. The retractable eyepiece shown was used for pointing at the source and the adjustable neutral density filter was used to keep the average value of the received signal approximately constant at the detector as the collector aperture was varied. The detector and electronics used with this receiver were identical to those used for the 0.514 micron "point" collector receiver.

B. DATA COLLECTION

To collect the scintillation data the optical receivers used for a particular measurement were mounted on a pair of aluminum "H" beams, as shown in Figure 14, that were attached to the concrete receiver platform.

The various receivers were then roughly pointed toward the sources located down range with an eyepiece that allowed viewing directly through the field stop and objective lens of the receivers. The 10.6 micron receiver was the exception to this procedure, but because of its relatively large field-of-view it could be rough aligned with just a

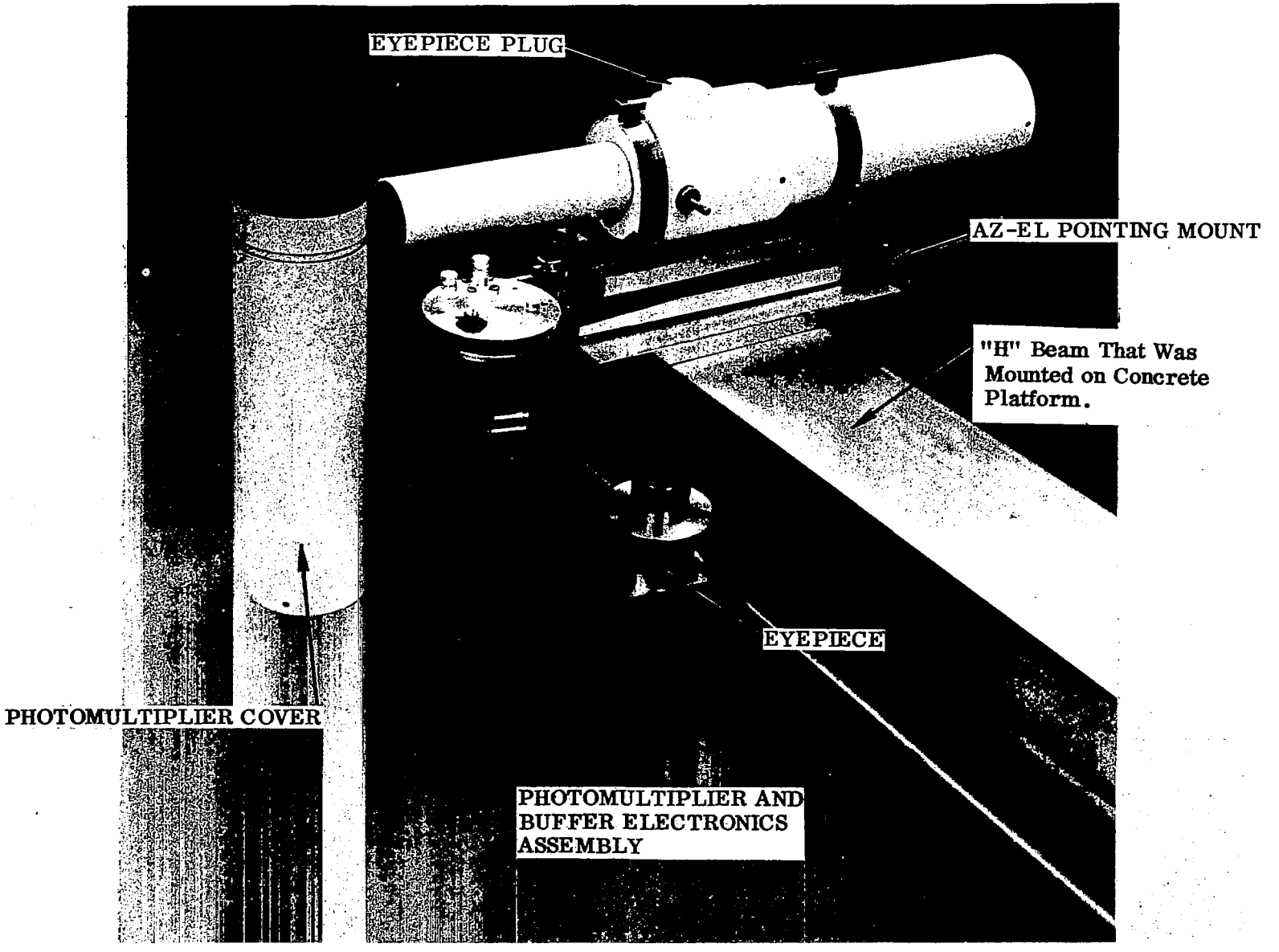

FIGURE 7. "Point" Collector Optical Receiver. Four assemblies such as this were constructed for the 0.63, 0.51, 0.50 (incoherent source detector) and 1.15 micron "point" collector measurements. For 1.15 micron measurements, the photomultiplier cover shown was replaced with a dry ice-cooled container.

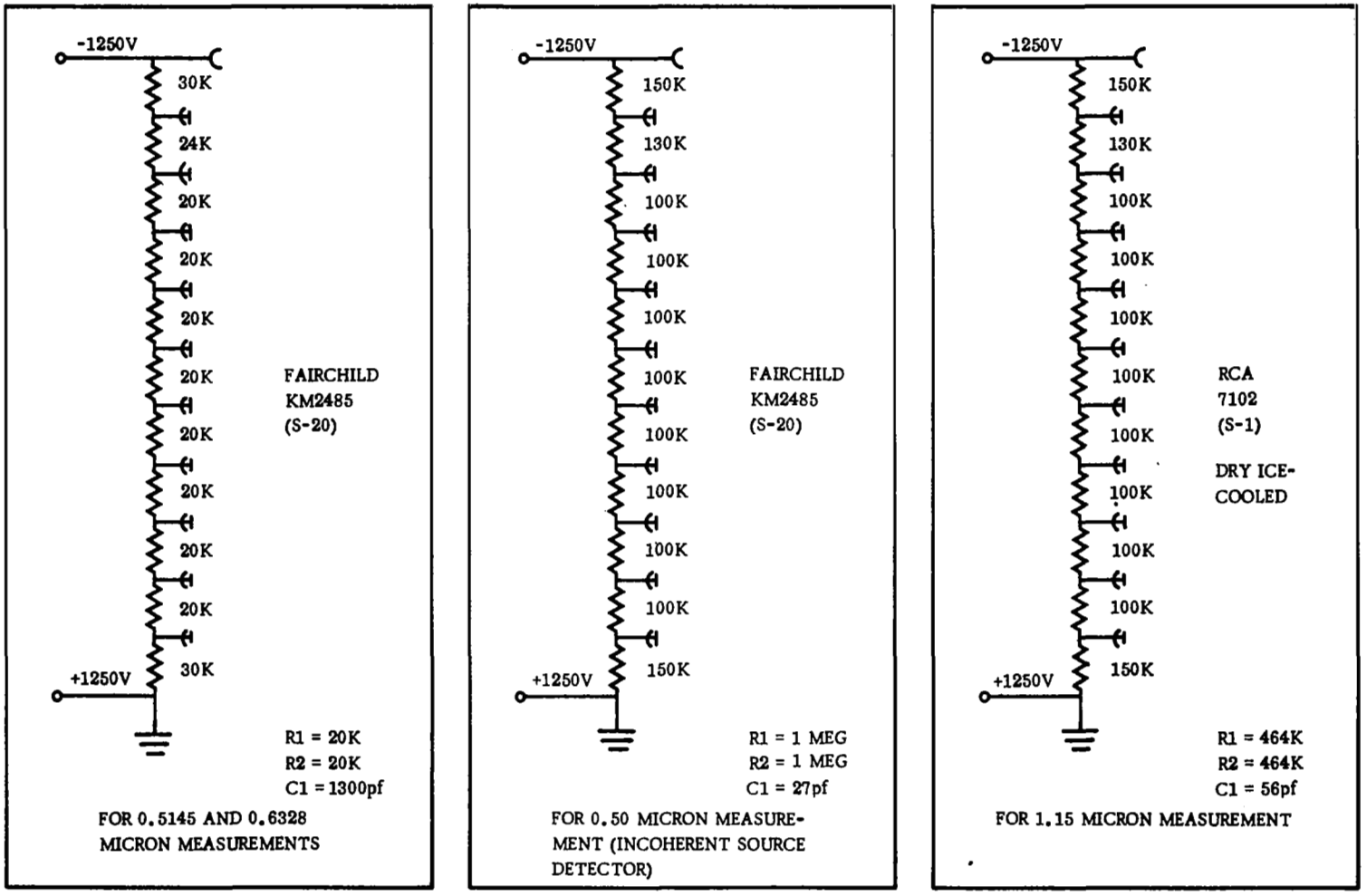

FIGURE 8. Dynode Circuits for Photomultiplier "Point" Collector Receivers

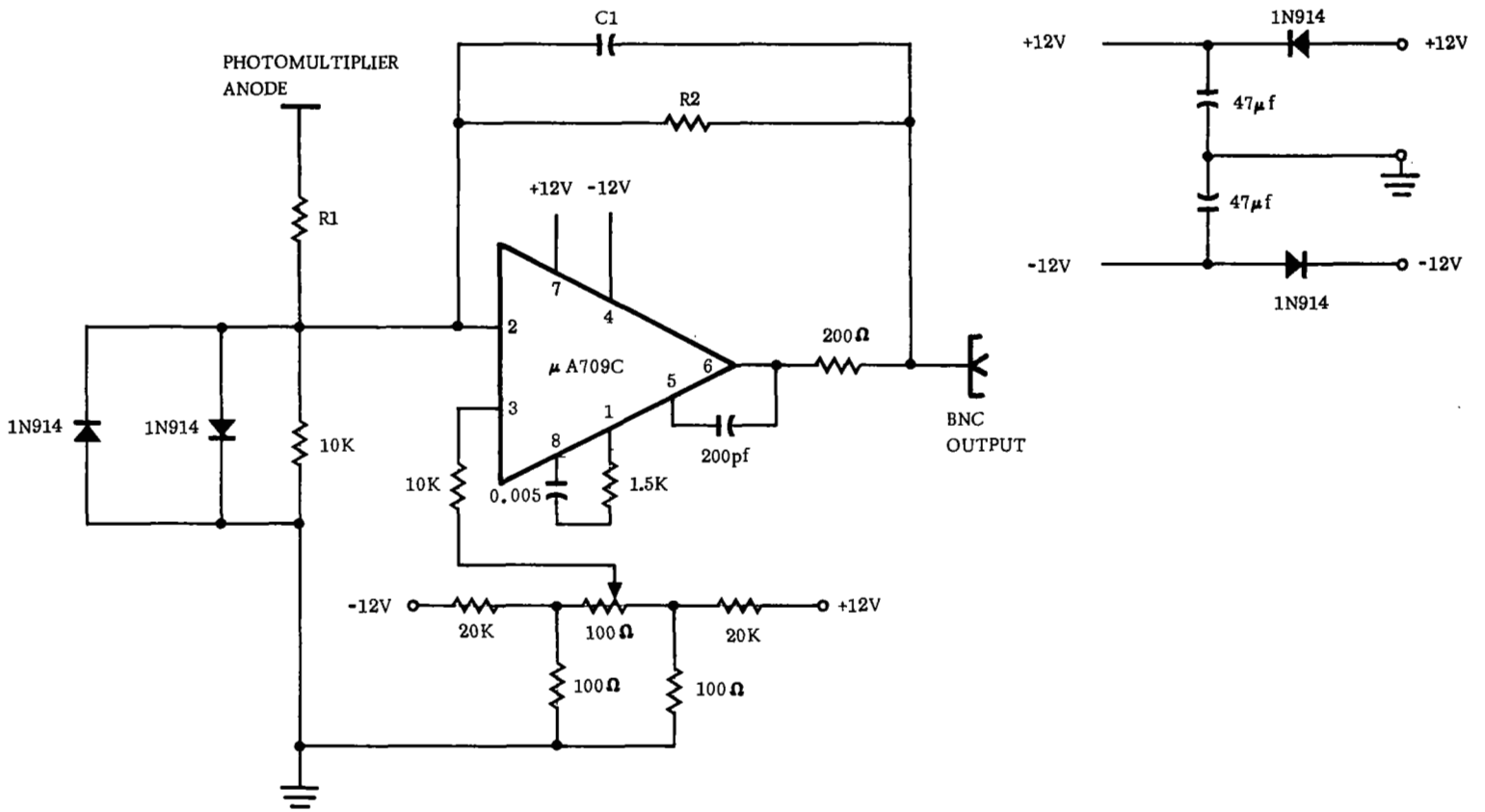

FIGURE 9. Photomultiplier Line Driver Circuit

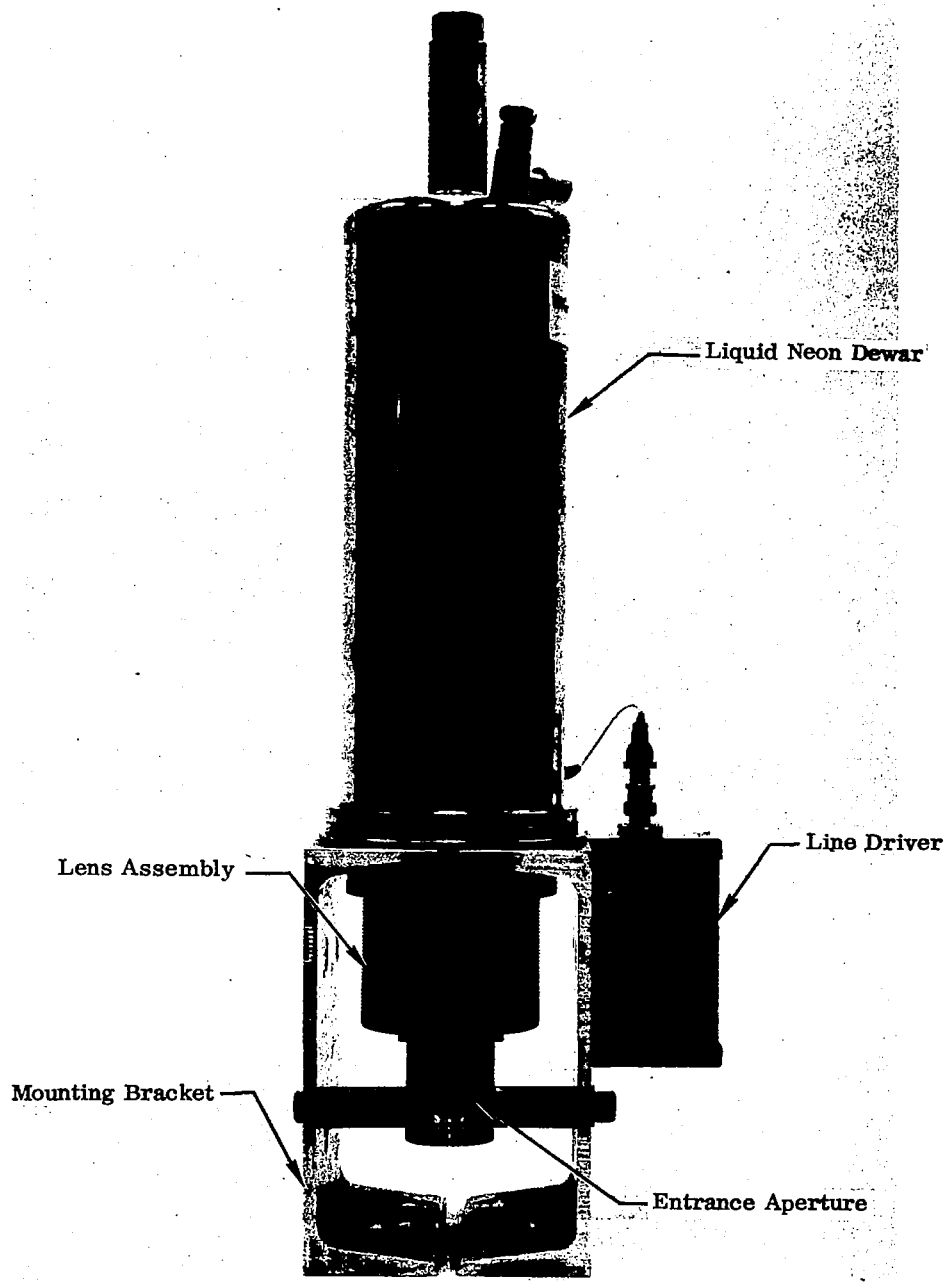

FIGURE 10. 10.6 Micron "Point" Collector. This photograph shows the 10.6 micron "point" collector with line driver. Radiation entering the aperture shown was reflected upward by means of a diagonal mirror and focused on the detector with an Irtran lens. A liquid neon-cooled Hg:Ge detector was used.

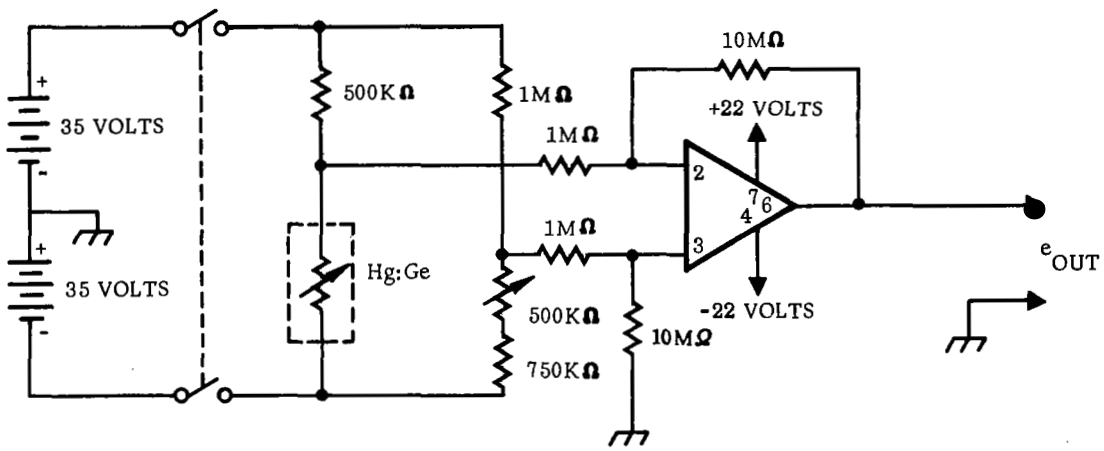

FIGURE 11. Line Driver Circuit Used with 10.6 Micron "Point" Collector

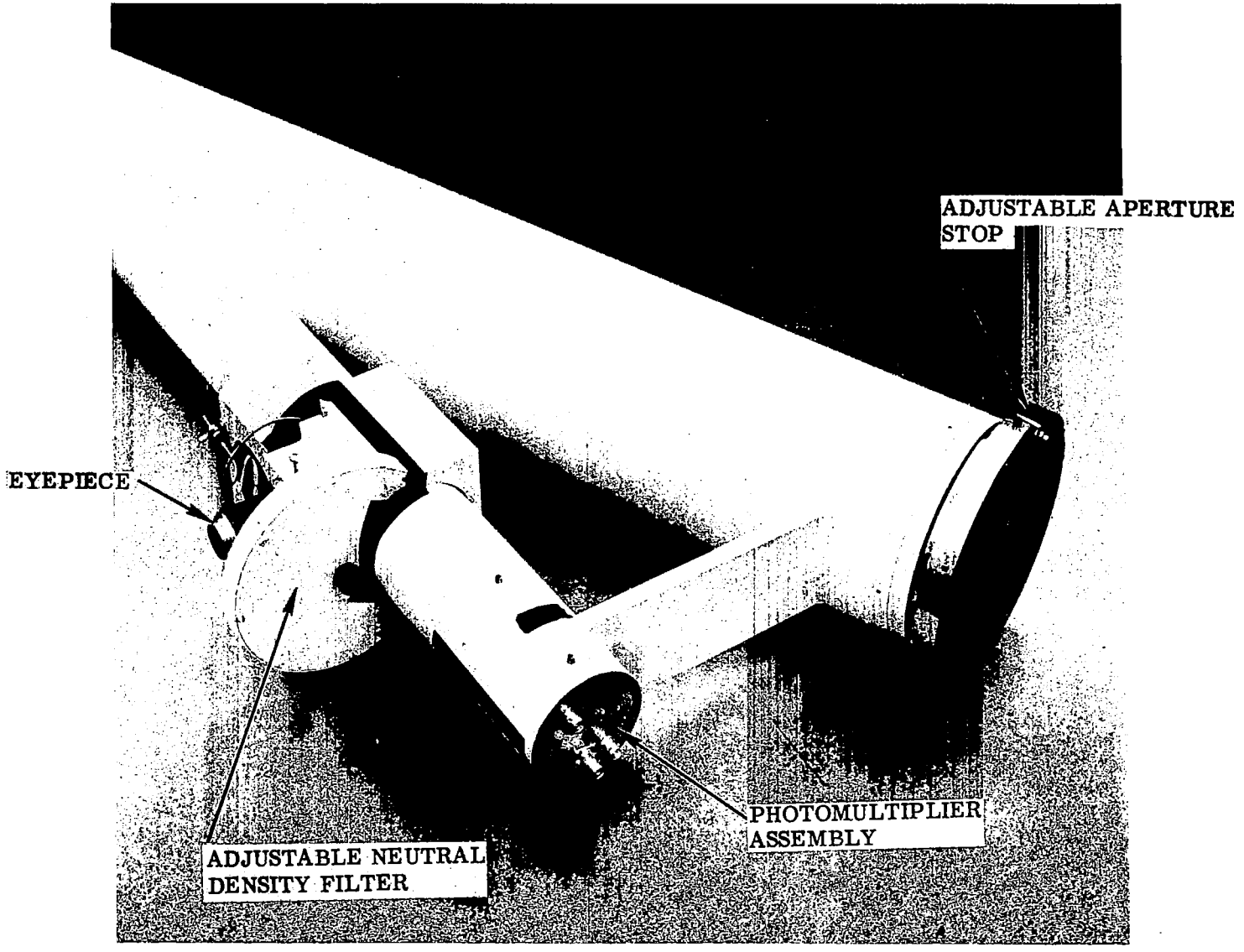

FIGURE 12. Optical Receiver Used for Aperture Averaging Measurements

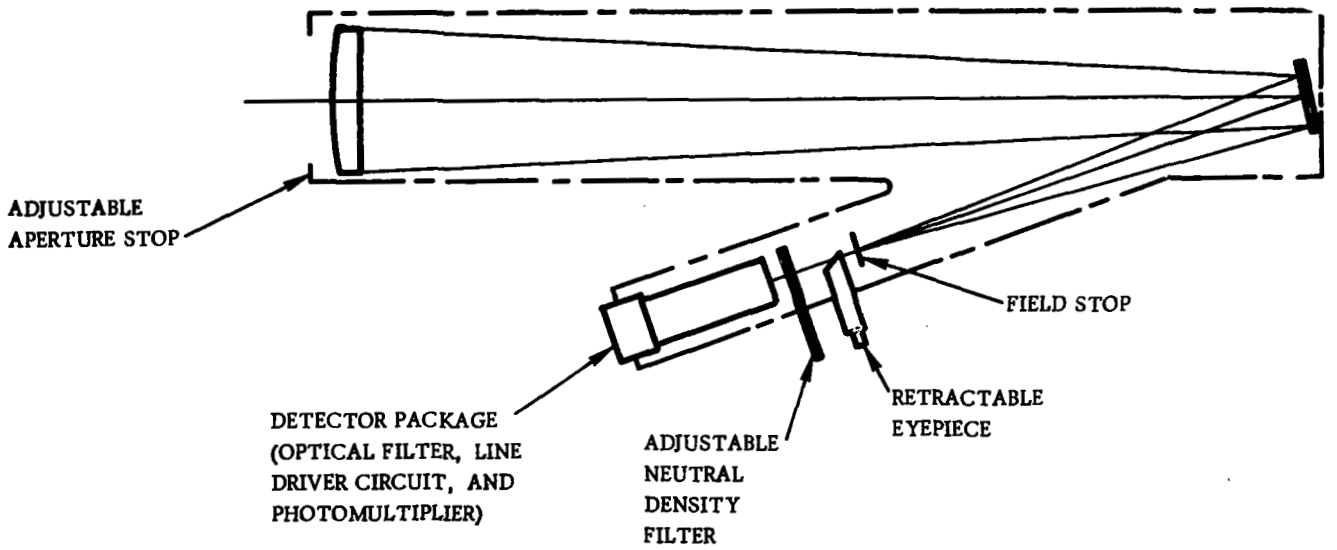

FIGURE 13. Optical Schematic of Aperture Averaging Receiver

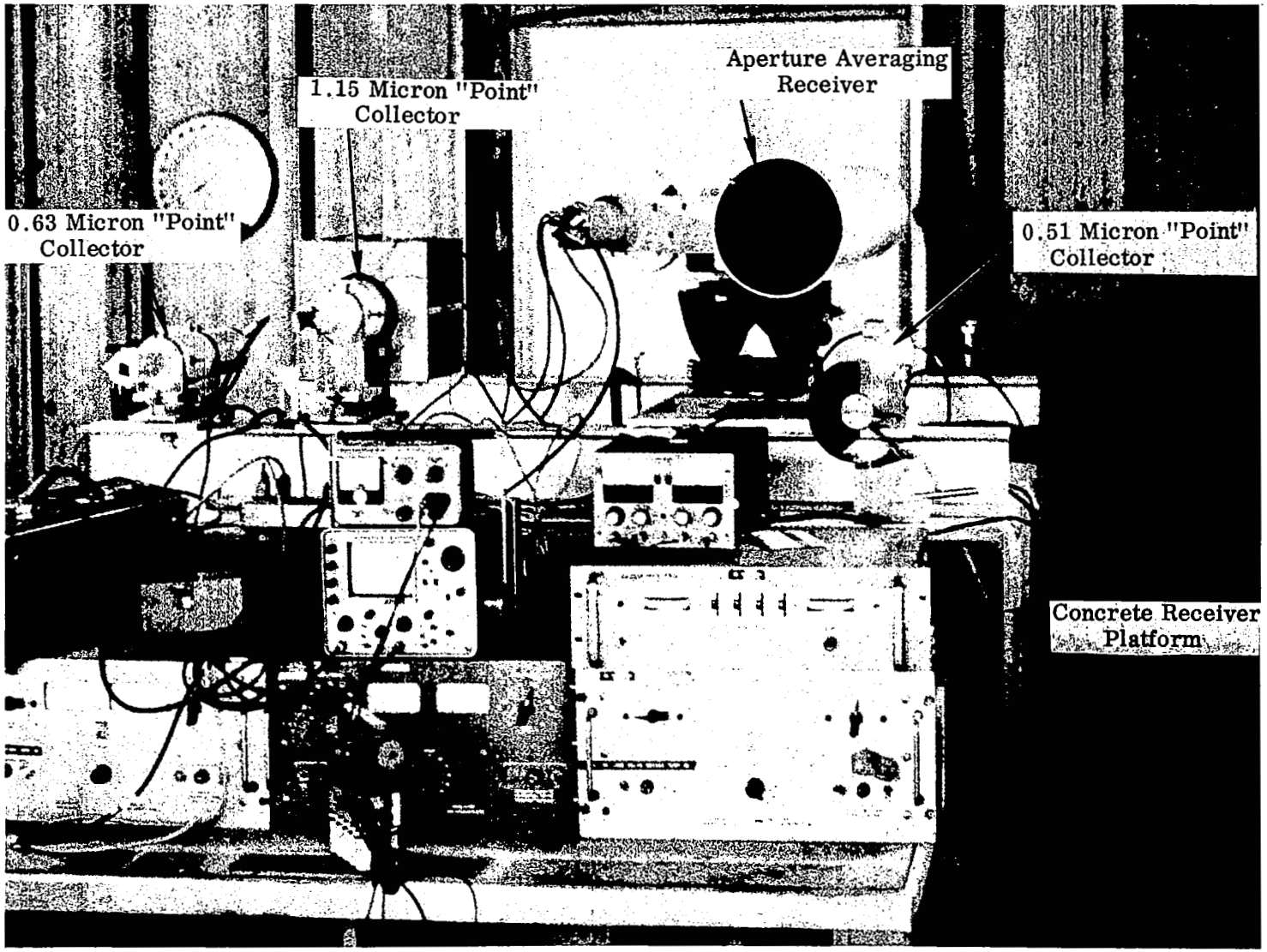

FIGURE 14. Optical Receivers for Scintillation Measurements. These receivers were mounted at approximately the same level above the lake bed as the laser sources: 1.75 meters.

"rifle barrel" technique. Each laser source was then peaked-up and aligned for peak power at its respective receiver (laser beam centered). Performing this procedure posed little problem with the argon laser and the 0.633 micron laser because the output was visible and with the xenon arc lamp and 10.6 micron laser because of the beam spread, but the 1.15 micron laser source proved quite difficult. The early attempts to rough align this source using a S-1 image converter tube proved unsatisfactory. Consequently, a technique was used of operating the laser at 0.633 microns, performing the rough alignment, substituting end-mirrors for 1.15 micron operating and then making final alignment. When the source alignment procedure was completed, final alignment of the various receivers was made and output signal level adjustments were made with optical attenuators to prevent excessive saturation of the detectors. This was especially important with the 0.514 micron receivers because of the brightness of the argon laser. The 0.633 micron receiver which we used for the strength of turbulence measurement and always observed a laser source 0.2 km down range required little adjustment after the initial corrections were made. With this procedure completed, the output signals from the various receivers were fed into a magnetic tape recorder. The recorder was instrumented to record 4 FM data channels with a bandwidth of dc to 2.5 KHz, a voice channel for a measurement log, and a logic channel. The signal level recorded on the logic channel (in FM form) was later used to control data processing in the digital computer. For each scintillation measurement made, a basic data block 90 seconds in duration was recorded. This data block was divided into two segments of 60 and 30 seconds. The first 60 seconds was laser signal plus background. The laser sources were then blocked and a 30 second record was made of the background viewed by each receiver. To provide a degree of uniformity to the data collection timing and to provide the necessary logic signals the circuit shown in Figure 15 was used in the following manner. When the 60 second timer was started a signal was produced and recorded on the logic channel which indicated a logic change from false to true. At the end of 60 seconds the logic level was automatically changed from true back to false. After the laser sources were blocked, the 30 second timer was started and a similar logic level change procedure took place in 30 seconds. During later data processing the true logic level was used to ear-mark those data to be processed.

Following these procedures scintillation data were accumulated for different wavelengths from 0.5 to 10 microns, for different aperture sizes from 1 to 15 cm and

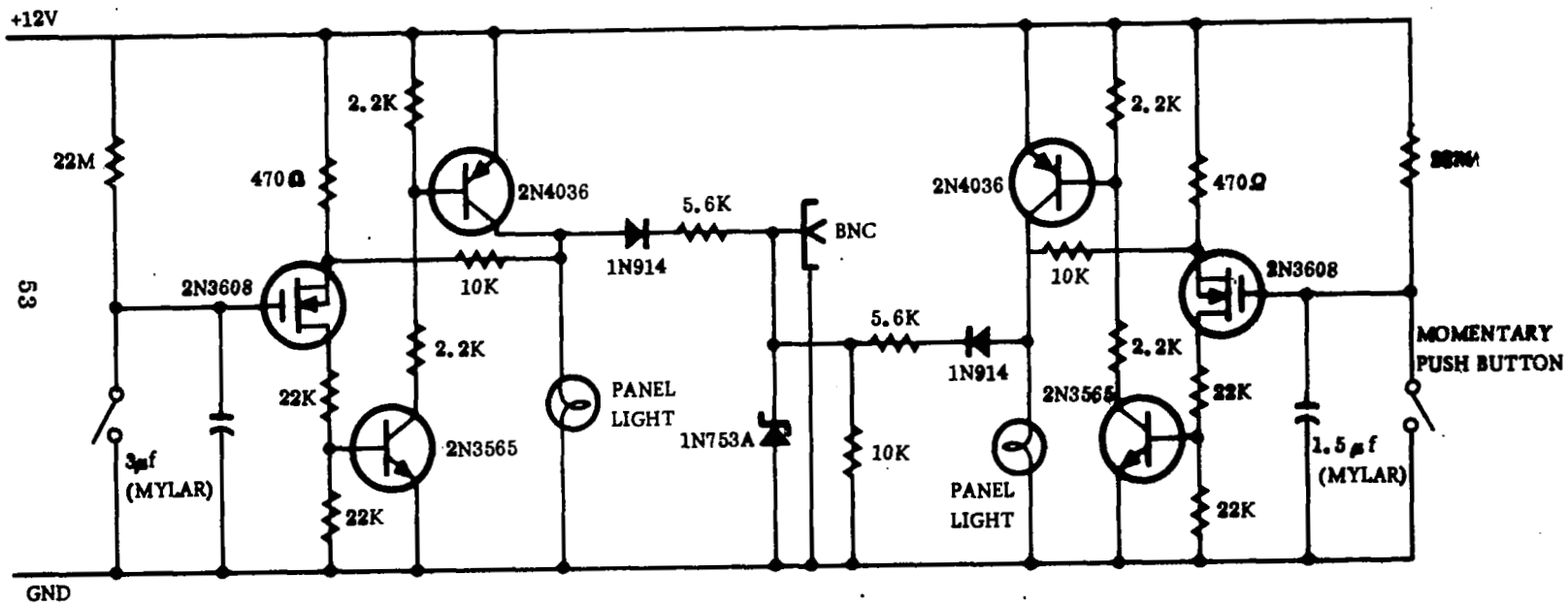

FIGURE 15. Timer and Logic Level Generator Circuit. This circuit provided the 60 and 30 second time base that was used in collection of scintillation data. It also provided the logic level control that was used to tag recorded data for later processing.

for different ranges from 1 to 5 km. For every scintillation measurement, data from the 0.633 "point" collector, which observed a source at the relatively short range of 200 meters, were recorded as a reference optical strength of atmospheric turbulence measurement.

C. ANALOG TO DIGITAL DATA CONVERSION

Before the collected scintillation data could be computer reduced the four recorded data channels and one logic channel were converted from analog to digital format. These five signals, before being operated on by the converter, were fed into conditioning amplifiers so that the signal amplitudes could be adjusted and summed with the proper off-set voltage needed to scale the A-to-D converter. When each reel of analog tape was played into the converter the amplitude, off-set, and system noise was checked to insure proper conversion. The A-to-D converter used, sampled each of the five channels in sequence starting with the logic channel, at a rate of 1000 times a second per channel, with a digital equivalent of the analog voltage sampled, scaled from 0 to 1000. The output was recorded on digital tape in a format compatible with the magnetic tape readers of the I. B. M. Systems 360 Computer.

D. DATA REDUCTION

The data reduction sequence as initially programmed into the high-speed computer is shown in Figure 16. The first step in the input routine, as shown, was a logic level test. Since the logic level placed on the tape during data recording was our only tag on data to be processed, any spurious noise or tape drop-outs could have resulted in processing the incorrect data. Hence, the computer was programmed to test any indication of logic level change over 2000 samples before it made a decision to act on the logic level information. The data, which was read in serially, was then separated into the four data channels and the probability distribution of the signal plus background and background alone was computed. From the background probability distribution, the average value was computed. This was then used to extract the background contribution from the signal plus background data. After this process, a log-intensity vs. probability distribution was computed from the signal data of each channel. These computed data were then put into a CRT display format, tagged for

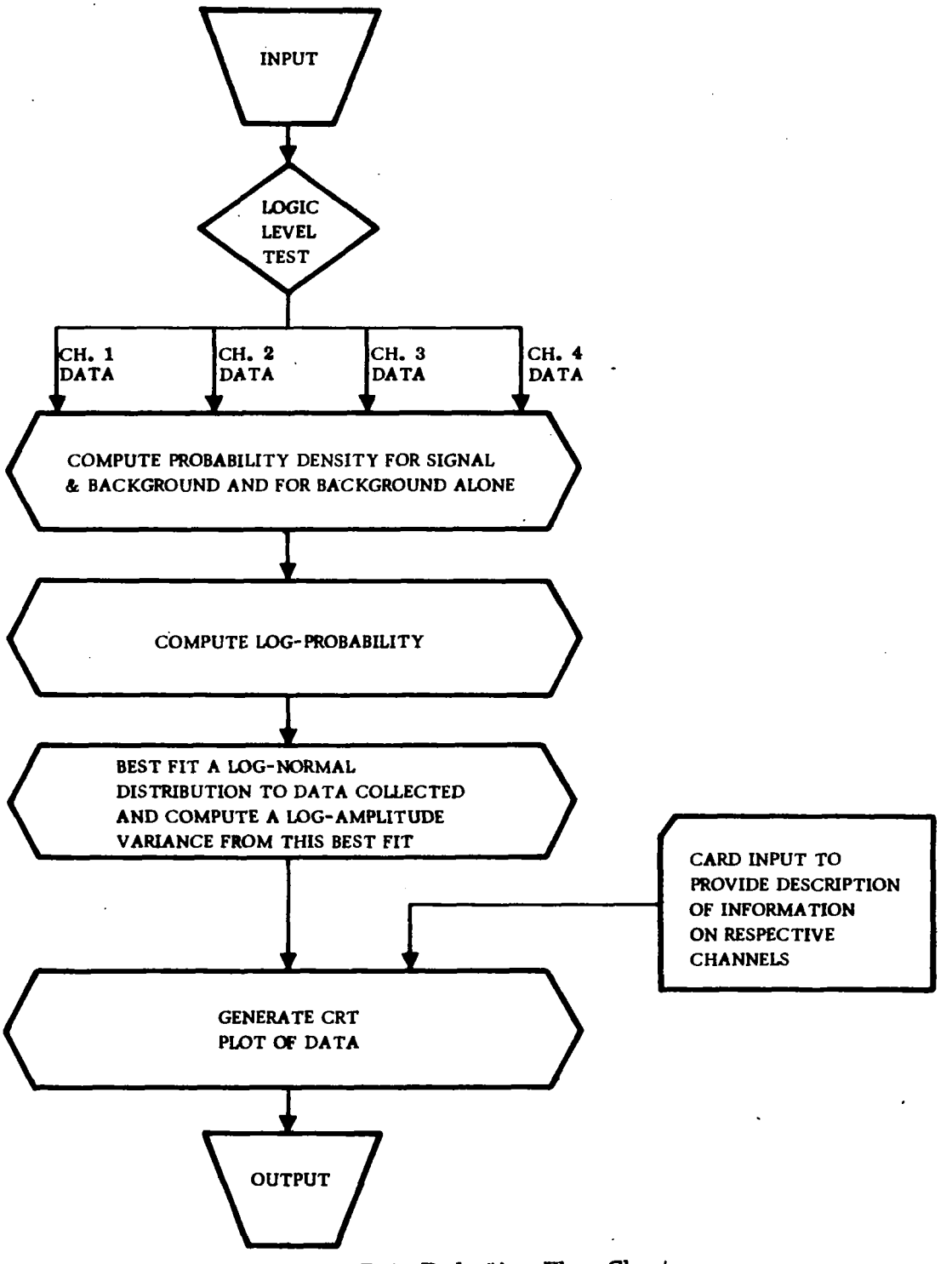

FIGURE 16. Data Reduction Flow Chart

identification, and output. Figure 17* is a fair typical example of the computer outputs obtained. With each of these CRT outputs a best fit (log) normal distribution was performed by hand** to the computed distribution data. This best fit routine was used to compute σ_ℓ^2, rather than from the actual data recorded because saturation effects in the optical detectors could have resulted in poor results in some cases. (In this regard the reader is referred to Appendix A.)

From a best fit straight line, such as shown in Figure 17, the log-amplitude variance can be determined with the following equation

$$\sigma_\ell^2 = \left[1/2\left(\frac{\ell n I_1 - \ell n I_2}{\sigma_1 - \sigma_2}\right)\right]^2 , \qquad (2)$$

where

I_1 and I_2 are two (arbitrarily chosen) intensities and σ_1 and σ_2 are the corresponding number of standard deviations, plus or minus relative to the 50% position. Since the abscissa of the plot in Figure 17 is 8 and the ordinate ranges from $\ell nI = 0$ to $\ell nI = 7$, σ_ℓ^2 was obtained with the following equation

*The abcissa for Figure 17 and subsequent computer generated CRT outputs shown in this report has a scale of "standard deviations" which correspond to cumulative probabilities for a Gaussian distribution. In our data reduction routine the computer was programmed to compute the cumulative probability and then approximate the corresponding sigma value (from C. Hastings, Jr., "Approximations for Digital Computer", Princeton University Press, P. 192). The following table gives the sigma values shown on the CRT output and the equivalent cumulative probability.

-4σ	= 0.00003	$+\sigma$	= 0.8413
-3σ	= 0.0013	$+2\sigma$	= 0.9772
-2σ	= 0.0228	$+3\sigma$	= 0.9987
$-\sigma$	= 0.1587	$+4\sigma$	= 0.99997
0	= 0.5000		

**Originally the computer had been programmed to compute this best fit, and although this program was fully checked-out by means of scintillation data collected on a previous program, we found that the computer best fit routine did not have the versatility to handle all of the different types of data collected during this program. Therefore, it was dropped from the computer program and the best fit was done by hand for all the data collected.

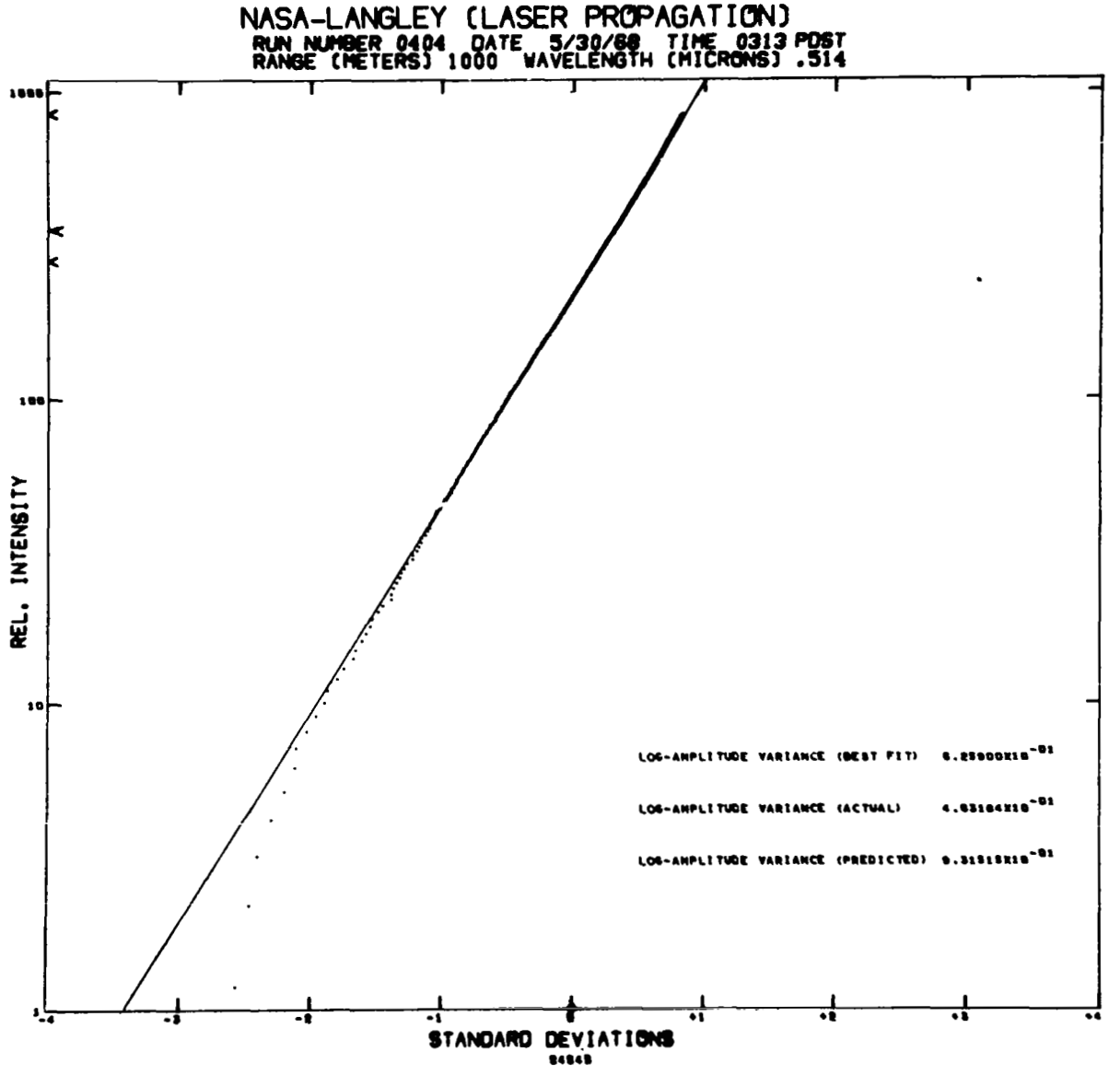

FIGURE 17. Typical Computer CRT Output of Scintillation Probability Distribution

$$\sigma_\ell^2 = \left(1/2 \frac{7\ Y\ a}{8\ X\ b}\right)^2 \tag{3}$$

where

a is the linear dimension of the abscissa, b is the linear dimension of the ordinate, and Y/X is the slope of the best fit line.

Using the proper values of a and b for the CRT output,

$$\sigma_\ell^2 = 0.227\ (Y/X)^2. \tag{4}$$

Table III gives a tabulation of the log-amplitude variance values computed for all the scintillation measurements using this technique. In order to test the predictions of equation 1, predicted values of σ_ℓ^2 (also denoted as $C_\ell(o)$) were computed from measured values using the constants listed in Table IV$^\infty$, which were obtained from equation 1.

E. MEASUREMENT RESULTS AND ANALYSIS

In the paragraphs to follow, the results of the scintillation measurements will be presented starting with those data which appear to agree with theory, then those data which clearly do not agree, and finally those data which appear anomalous or inclusive.

1. $\sigma_\ell^2(0.514, 1000)$ vs. $\sigma_\ell^2(0.633, 200)$

The first set of data which we wish to report compares simultaneous measurement of $\sigma_\ell^2(0.633, 200)$ with $\sigma_\ell^2(0.514, 1000)$ made during Runs #101 - 115. (The notation $\sigma_\ell^2(\lambda, R)$ denotes the log-amplitude variance for a wavelength λ, in microns, and a path length R, in meters.) These data, like all the rest we shall use in this section, were obtained from the slope of the probability distribution of intensity scintillation, in the manner described just previously. Utilizing the factor of 24.34 obtained from Table IV, predicted values for $\sigma_\ell^2(0.514, 1000)$ were obtained from the

$^\infty$The constants presented in Table IV are given in terms of the notation $\sigma_\ell^2(\lambda, R)$. This notation refers to values (measured or predicted) of Log-amplitude variance for wavelength λ (in microns) and range R (in meters).

TABLE III

MEASURED VALUED OF LOG-AMPLITUDE VARIANCE (σ_ℓ^2) OF SCINTILLATION

RUN #	MEASUREMENT						
	0.633μ	0.500μ	0.514μ	0.514μ	LARGE APERTURE	1.15μ	10.6μ
101	0.0169		0.3023				
102	0.0143		0.2845				
103	0.0136		0.2807				
104	0.0102		0.2217				
105	0.0105		0.2135				
106	0.0097		0.1969				
107	0.0092		0.1960				
108	0.0085		0.2098				
110	0.0101		0.2096				
111	0.0104		0.2256				
112	0.0104		0.2310				
113	0.0105		0.2381				
114	0.0095		0.2429				
115	0.0090		0.2442				

TABLE III - Continued

RUN #	MEASUREMENT						
	0.633μ	0.500μ	0.514μ	0.514μ	LARGE APERTURE	1.15μ	10.6μ
308	0.0189		0.4475		0.2864	0.1683	
309	0.0227		0.4789		0.2300	0.1912	
310	0.0152		0.5002		0.1346	0.1447	
311	0.0175		0.4264		0.1023	0.1665	
312	0.0189		0.5183		0.0872	0.1800	
313	0.0187		0.4294		0.0535	0.1311	
314	0.0159		0.4789		0.0622	0.1846	
315	0.0156		0.4365		0.0502	0.1547	
316	0.0188		0.5374		0.0597	0.1914	
317	0.0227		0.4329		0.0346	0.1547	
401	0.0255		0.6444		0.0517	0.2283	
402	0.0289		0.6509		0.0483	0.2533	
403	0.0263		0.5789		0.0421	0.2216	
404	0.0259		0.6380		0.0382	0.2256	
405	0.0243		0.7293		0.0377	0.1747	

TABLE III - Continued

RUN #	MEASUREMENT						
	0.633μ	0.500μ	0.514μ	0.514μ	LARGE APERTURE	1.15μ	10.6μ
406	0.0111		0.5230		0.3963		
407	0.0208		0.5183		0.3173		
408	0.0101		0.5230		0.2560		
409	0.0182		0.4958		0.2074		
410	0.0143		0.5183		0.2128		
411	0.0103		0.5002		0.2072		
412	0.0162		0.5137		0.2124		
413	0.0181		0.5046		0.1827		
414	0.0155		0.4915		0.1657		
415	0.0175		0.4789		0.1373		
501	0.0095		0.5137		0.1604		
502	0.0149		0.5091		0.1560		
503	0.0147		0.4707		0.1365		
504	0.0108		0.4628		0.1363		
505	0.0146		0.4915		0.1478		

TABLE III - Continued

RUN #	MEASUREMENT						
	0.633μ	0.500μ	0.514μ	0.514μ	LARGE APERTURE	1.15μ	10.6μ
506	0.0243		0.3726		0.2332		
507	0.0215		0.3724		0.1665		
508	0.0189		0.3509		0.1421		
509	0.0139		0.3755		0.1203		
510	0.0146		0.3726		0.1191		
511	0.0175		0.3842		0.1044		
513	0.0113		0.3840		0.1148		
514	0.0092		0.4059		0.1143		
701	0.0144						
702	0.0108						
703	0.0099						
704	0.0094						
705	0.0075						
706	0.0107						
707	0.0093						

TABLE III - Continued

RUN #	MEASUREMENT						
	0.633μ	0.500μ	0.514μ	0.514μ	LARGE APERTURE	1.15μ	10.6μ
708	0.0097						
709	0.0125						
710	0.0087						
711	0.0068						
801	0.0071						
802	0.0064						
803	0.0062						
804	0.0037						
806	0.0073						
807	0.0083						
808	0.0065						
809	0.0046						
810	0.0144						
811	0.0259						
812	0.0198						

TABLE III - Continued

RUN #	MEASUREMENT						
	0.633μ	0.500μ	0.514μ	0.514μ	LARGE APERTURE	1.15μ	10.6μ
813	0.0196						
814	0.0187						
815	0.0261						
816	0.0231						
817	0.0235						
818	0.0263						
819	0.0281						
820	0.0146						
821	0.0226						
903	0.0099		0.1145				
904	0.0156	0.1111					
905	0.0132	0.1274					
906	0.0228						
909	0.0180		0.1483				
910	0.0198	0.1504					

TABLE III - Continued

RUN #	MEASUREMENT						
	0.633μ	0.500μ	0.514μ	0.514μ	LARGE APERTURE	1.15μ	10.6μ
911	0.0132	0.0850					
912	0.0190		0.1477				
914	0.0193	0.1136					
915	0.0202		0.1525				
1001	0.0192	0.1287					
1002	0.0206	0.1325					
1003	0.0197		0.1479				
1004	0.0185	0.1386					
1005	0.0246	0.1433					
1006	0.0179		0.1305				
1007	0.0178	0.1451					
1008	0.0247	0.1531					
1009	0.0221		0.1734				
1101	0.0270					0.2804	0.0285
1102	0.0219					0.2408	0.0232

TABLE III - Continued

RUN #	MEASUREMENT						
	0.633μ	0.500μ	0.514μ	0.514μ	LARGE APERTURE	1.15μ	10.6μ
1103	0.0203					0.1904	0.0157
1104	0.0121					0.1038	0.0156
1106	0.0263					0.1311	0.0211
1107	0.0236					0.1754	0.0235
1108	0.0430					0.2926	0.0360
1109	0.0182					0.2302	0.0325
1110	0.0287					0.4059	0.0571
1111	0.0211					0.3448	0.0516
1113	0.0314					0.4337	0.0541
1114	0.0202					0.3749	0.0501
1115	0.0193					0.3227	0.0422
1116	0.0160					0.3801	0.0389
1117	0.0214					0.3044	0.0378
1118	0.0192					0.3138	0.0337
1201	0.0119		0.6367	0.6004		0.3026	

TABLE III - Continued

RUN #	MEASUREMENT						
	0.633 μ	0.500 μ	0.514 μ	0.514 μ	LARGE APERTURE	1.15 μ	10.6 μ
1202	0.0177		0.5889	0.5992		0.3492	
1203	0.0093		0.5639	0.5800		0.2766	
1204	0.0166		0.5713	0.5958		0.2823	
1205	0.0159		0.6062	0.5576		0.3061	
1206	0.0164		0.5639	0.5639		0.2630	
1207	0.0307		0.5484	0.5277		0.2748	
1208	0.0233		0.5454	0.5494		0.2930	
1209	0.0190		0.5823	0.5618		0.2732	
1210	0.0148		0.5384	0.5364		0.2963	
1211	0.0194		0.5545	0.5211		0.2735	
1212	0.0154		0.5713	0.5649		0.2927	
1213	0.0193		0.5746	0.5757		0.2941	
1214	0.0180		0.5525	0.5464		0.2975	
1215	0.0203		0.5221	0.5494		0.2809	
1216	0.0214		0.5424	0.5671		0.3027	

TABLE III - Concluded

RUN #	MEASUREMENT						
	0.633μ	0.500μ	0.514μ	0.514μ	LARGE APERTURE	1.15μ	10.6μ
1217	0.0171		0.5394	0.5493		0.2629	
1218	0.0202		0.5414	0.5434		0.2832	
1219	0.0207		0.5639	0.5545		0.2849	
1220	0.0159		0.5535	0.5404		0.2562	
1301	0.0226		0.5394				
1302	0.0150		0.4993				
1303	0.0163		0.5202				
1304	0.0200		0.5221				
1305	0.0182		0.5746				
1306	0.0179		0.6004				
1307	0.0281		0.5073				
1308	0.0041		0.5628				
1309	0.0082		0.6292				
1310	0.0045		0.6779				
1311	0.0023		0.7229				

TABLE IV

DATA CONVERSION EQUATIONS*

1.	σ_ℓ^2pred(0.50, 500)	=	(7.06)	σ_ℓ^2meas(0.633, 200)
2.	σ_ℓ^2pred(0.514, 500)	=	(6.83)	σ_ℓ^2meas(0.633, 200)
3.	σ_ℓ^2pred(0.514, 1000)	=	(24.34)	σ_ℓ^2meas(0.633, 200)
4.	σ_ℓ^2pred(0.514, 1000)	=	(2.56)	σ_ℓ^2meas(1.15, 1000)
5.	σ_ℓ^2pred(0.514, 1500)	=	(51.18)	σ_ℓ^2meas(0.633, 200)
6.	σ_ℓ^2pred(0.514, 1500)	=	(2.56)	σ_ℓ^2meas(1.15, 1500)
7.	σ_ℓ^2pred(0.514, 3000)	=	(182.52)	σ_ℓ^2meas(0.633, 200)
8.	σ_ℓ^2pred(0.514, 5000)	=	(465.55)	σ_ℓ^2meas(0.633, 200)
9.	σ_ℓ^2pred(1.15, 1000)	=	(9.52)	σ_ℓ^2meas(0.633, 200)
10.	σ_ℓ^2pred(1.15, 1500)	=	(20.03)	σ_ℓ^2meas(0.633, 200)
11.	σ_ℓ^2pred(10.6, 1000)	=	(0.71)	σ_ℓ^2meas(0.633, 200)
12.	C_N^2	=	(3.34×10^{-12})	σ_ℓ^2meas(0.633, 200)

*The notation $\sigma_\ell^2(\lambda, R)$ refers to values (measured or predicted) of log-amplitude variance for wavelength λ (in microns) and range R (in meters).

measured values of $\sigma_\ell^2(0.633, 200)$, for comparison with the measured values of $\sigma_\ell^2(0.514, 1000)$. The scatter plot of measured versus predicted values is shown in Figure 18. As can be seen, the points are clustered near the ideal 10:10 ratio line. To determine exactly how well measured and predicted values compared, the ratio, R, of measured to predicted value,

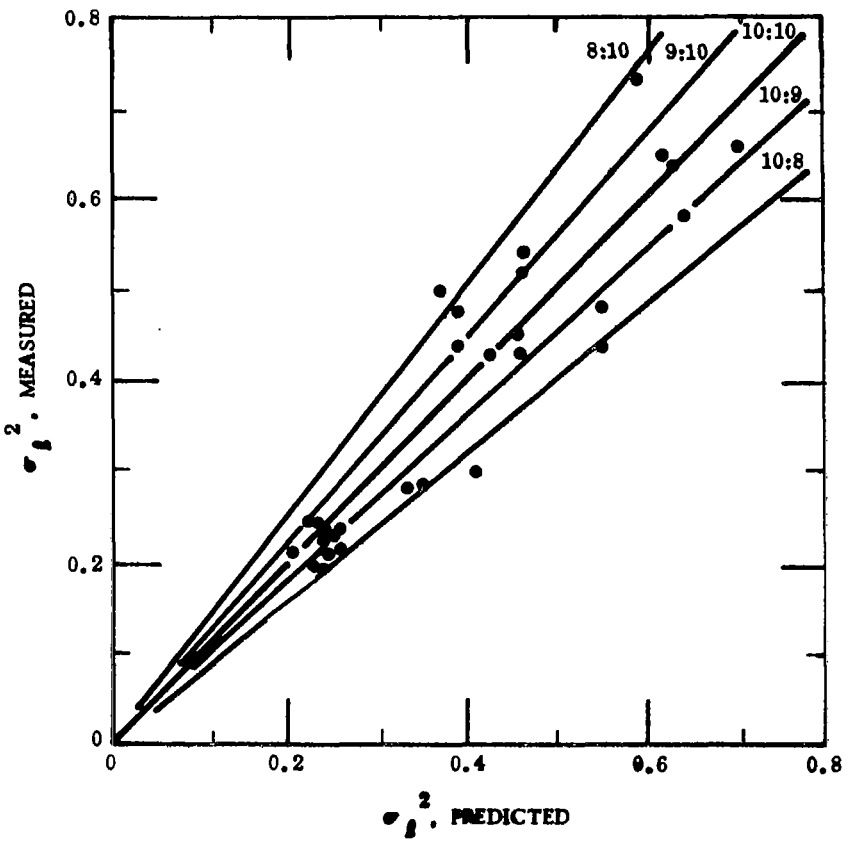

FIGURE 18. Measured vs. Predicted $\sigma\ell^2$ for 0.514μ at 1.0 km. Data Runs #101 - 115 (5/24/68) and #308 - 405 (5/30/68). Predictions based on 0.633μ $\sigma\ell^2$ measured for 0.2 km.

$$R = \sigma_\ell^2, \text{meas}/\sigma_\ell^2 \text{pred}, \quad (5)$$

was obtained for each of the data runs and the probability distribution of R was obtained. This distribution is plotted in Figure 19. As can be seen, the distribution appears reasonably close to Gaussian. The mean, μ, is 0.936, which is quite close to the ideal ratio of unity. The normalized variance of the distribution, σ/μ, indicates about a 15% rms spread in our combined measurement accuracy of $\sigma_\ell^2(0.514, 1000)$ and $\sigma_\ell^2(0.633, 200)$, or in the ability of the turbulence in the 200 meter path to correctly indicate the turbulence over the full 1000 meter path. The fact that μ is so close to unity must be taken as a very positive confirmation of the Rytov Approximation, at least in some limited range.

2. $\sigma_\ell^2(1.15, 1000)$ vs. $\sigma_\ell^2(0.633, 200)$

We now wish to consider two sets of data relating to σ_ℓ^2 measured for 1.15μ over 1000 meters and for 0.633μ over 200 meters. The data sets are taken from Runs #308 - 405 and Runs #1101 - 1118. The predicted values for $\sigma_\ell^2(1.15, 1000)$ are obtained from $\sigma_\ell^2(0.633, 200)$ using the factor 9.52 obtained from Table IV. The scatter plots of $\sigma_\ell^2(1.15, 1000)$ measured versus predicted for the two sets of data are shown in Figures 20 and 21. For the first set, the points are satisfactorily clustered about the ideal 10:10 ratio line. For the second data set, the scatter of points is much wider. For each of the data sets, the probability distribution of the ratio of measured to predicted value of $\sigma_\ell^2(1.15, 1000)$ was plotted. The results are shown in Figures 22 and 23. Again it is seen that the distributions are reasonably close to normal. In the two cases, the ratio has mean values of $\mu = 0.898$ and $\mu = 1.16$, both of which are acceptably close to the ideal value of unity. This lends farther credence to the validity of the theoretical predictions, at least within some limited range. We must, however, face the matter that while the first set of data shows a reasonable ratio of rms spread to mean σ/μ, namely 14 percent, for the second set of data σ/μ has the rather large value of 44 percent. The most likely explanation for this is that during the period of data taken for Runs #1101 - 1118, the wind was sufficiently non-uniform over that 1000 meter path, that the turbulence observed in the 200 meter path was not well correlated

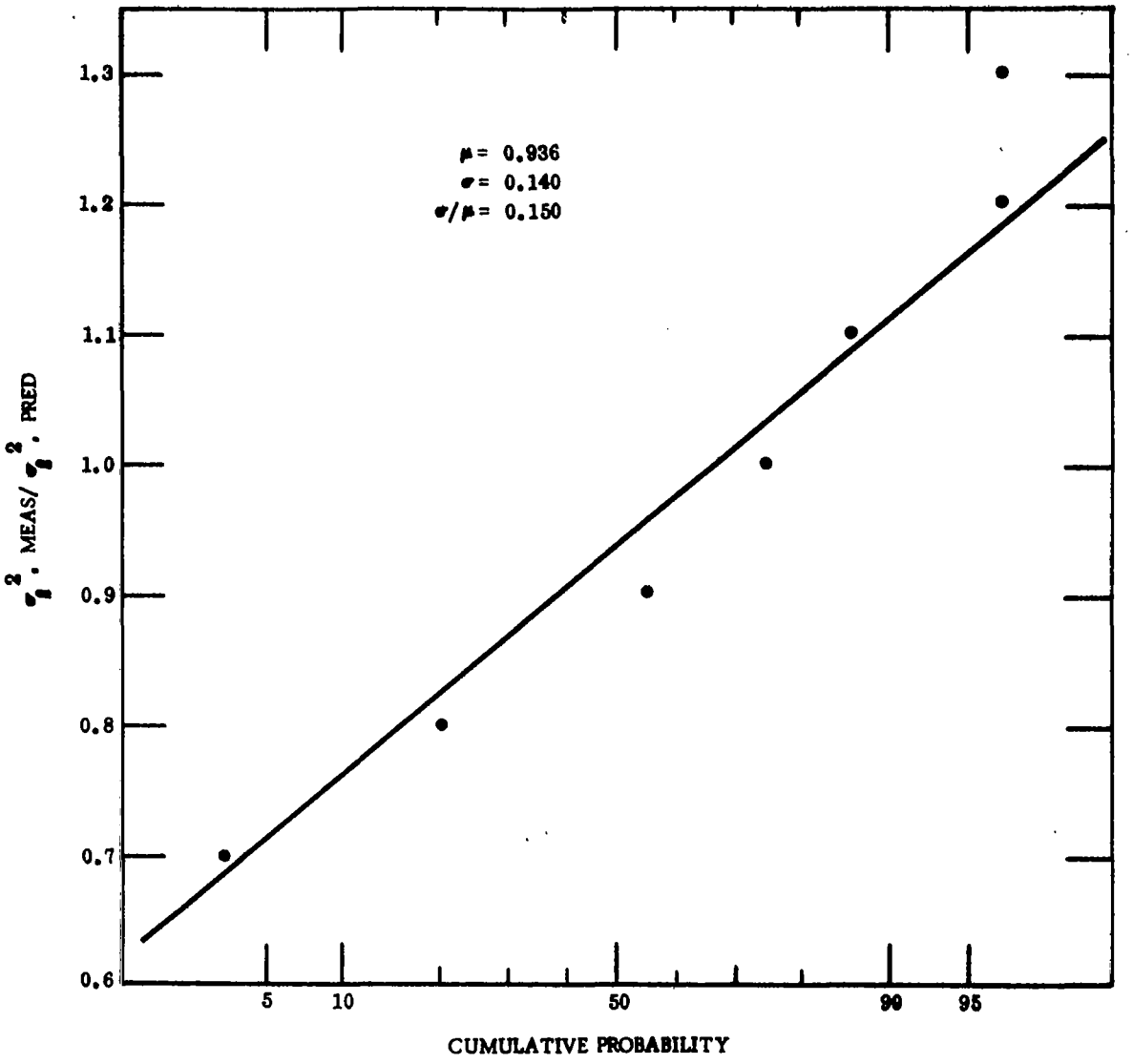

FIGURE 19. Probability Distribution of Ratio, $\sigma\ell^2$, meas/$\sigma\ell^2$, pred for 0.514μ Measurement at 1.0 km. Predictions based on 0.633μ measurements at 0.2 km. Data taken from Runs #101 - 115 (5/24/68) and #308 - 405 (5/30/68).

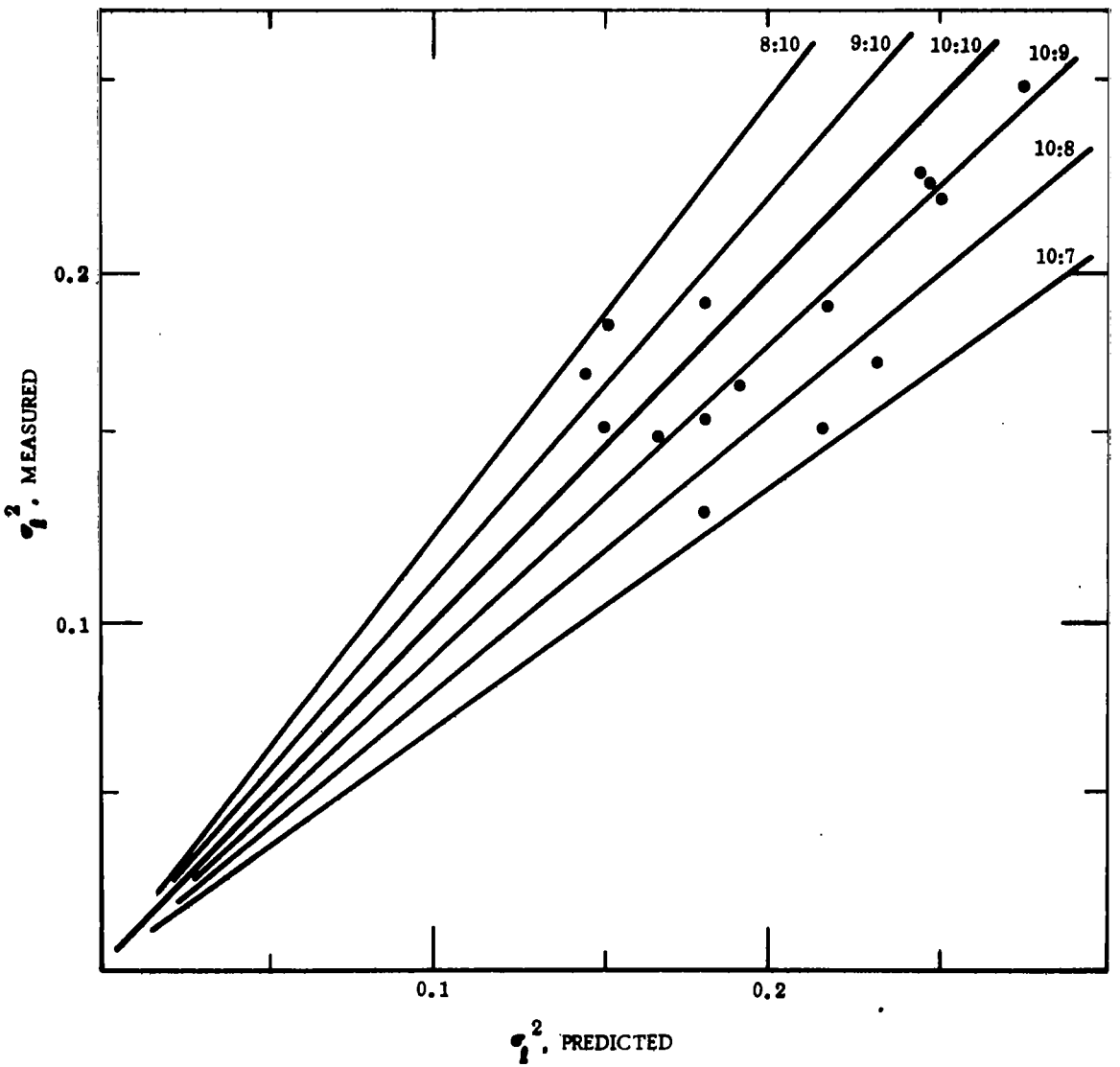

FIGURE 20. Measured vs. Predicted $\sigma\ell^2$ for 1.15μ at 1.0 km. Data Runs #308 - 405 (5/30/68). Predictions based on 0.633μ $\sigma\ell^2$ measured for 0.2 km.

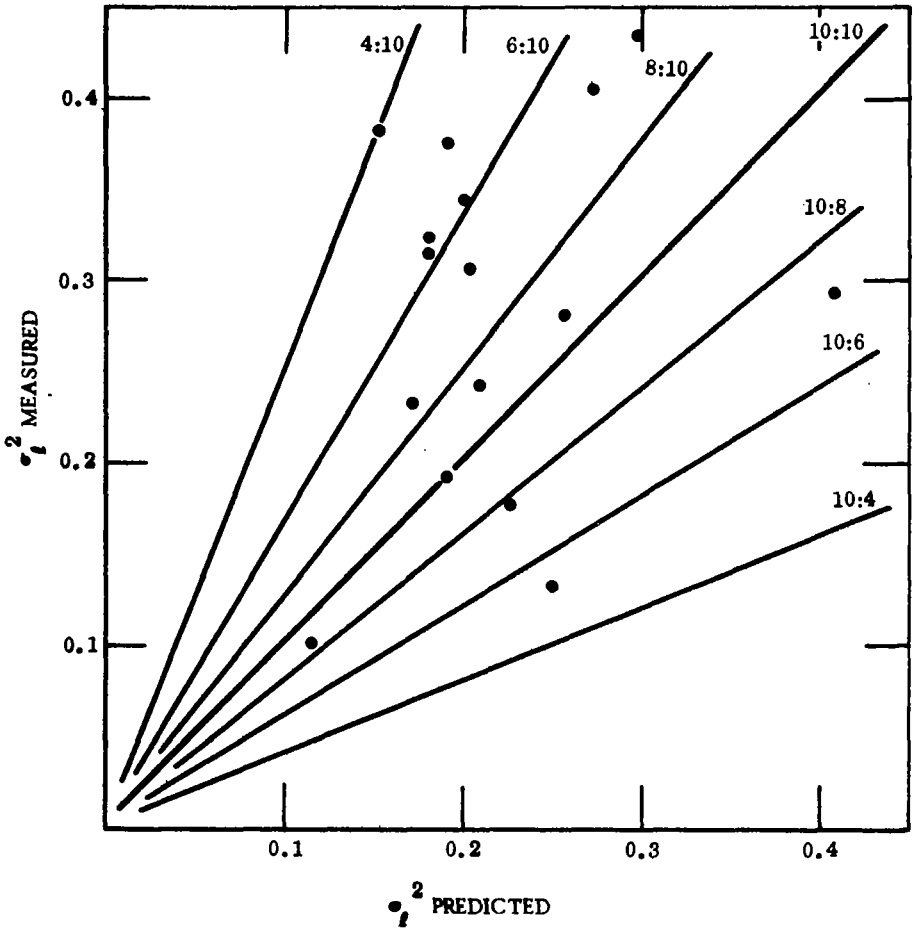

FIGURE 21. Measured vs. Predicted $\sigma\ell^2$ for 1.15μ at 1.0 km. Data Runs #1101 - 1118 (7/10/68). Predictions based on 0.633μ $\sigma\ell^2$ measured for 0.2 km.

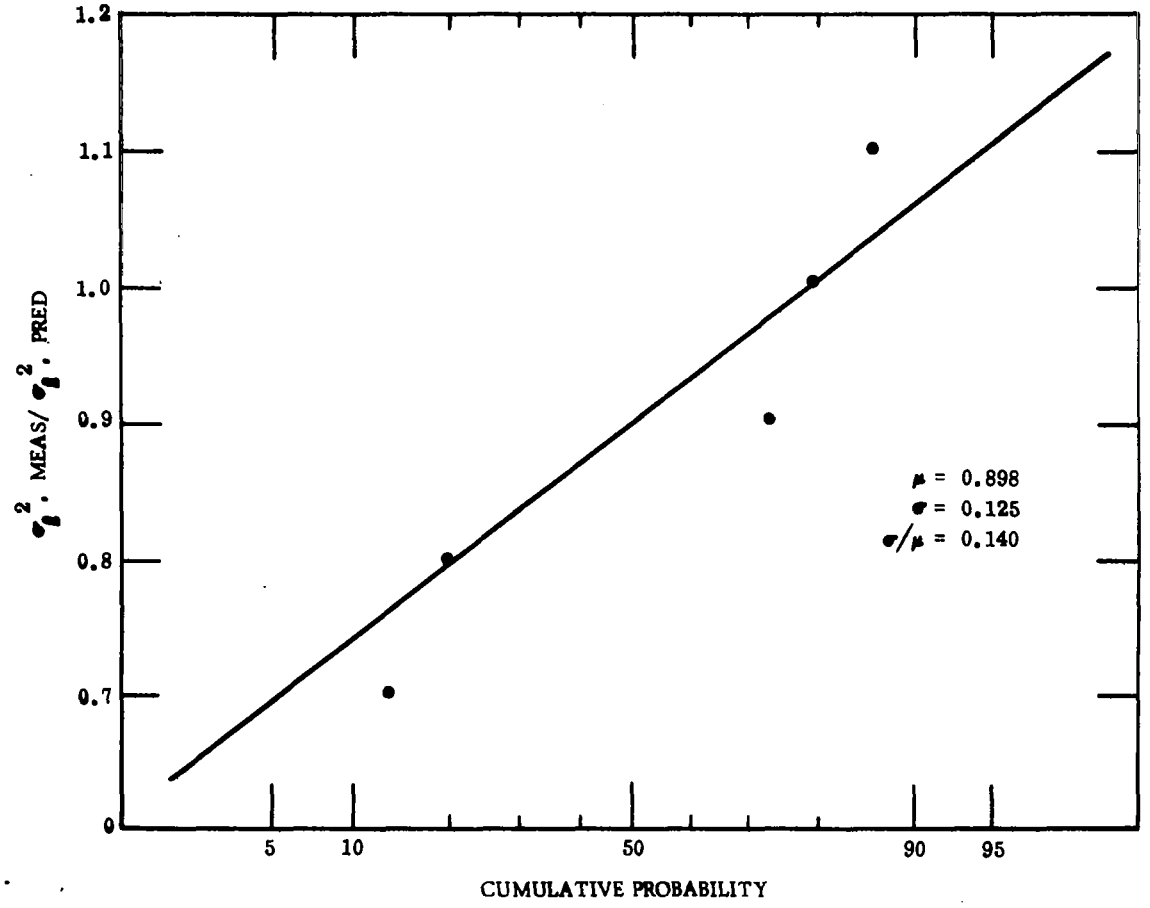

FIGURE 22. Probability Distribution of Ratio, σ_ℓ^2, meas/σ_ℓ^2, pred for 1.15μ Measurements at 1.0 km. Predictions based on 0.633μ measurements at 0.2 km. Data taken from Runs #308 - 405 (5/30/68).

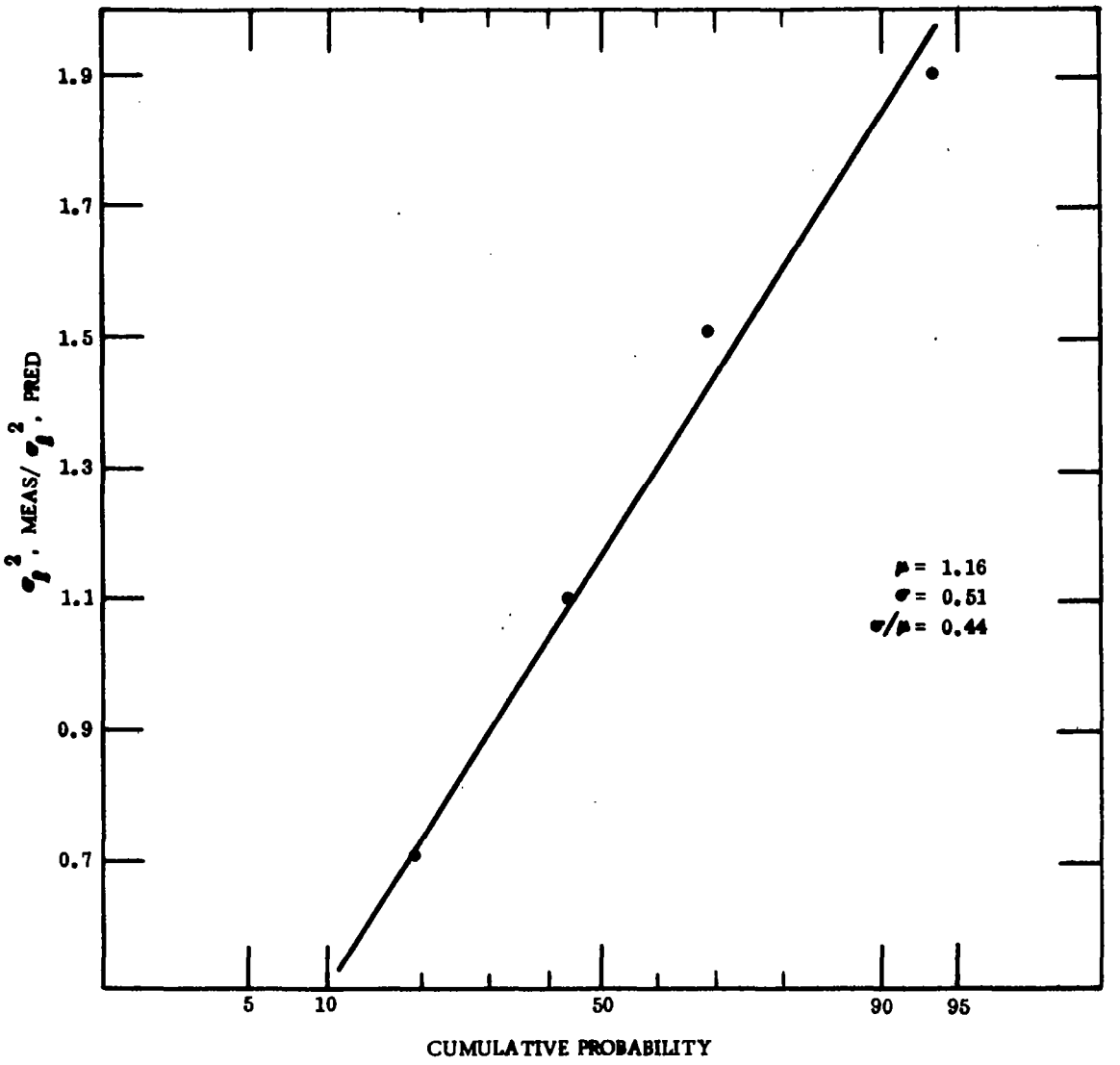

FIGURE 23. Probability Distribution of Ratio, σ_ℓ^2, meas/σ_ℓ^2, pred for 1.15μ Measurements at 1.0 km. Predictions based on 0.633μ measurements at 0.2 km. Data taken from Runs #1101 - 1118 (7/10/68).

with the turbulence for the entire 1000 meters. There is, of course, no assurance of this, but it is difficult to see what other aspect of measurements could have changed between the first and second data set. It is hard to imagine any way in which the accuracy of the measurement of σ_ℓ^2 could have changed between the sets and thus produced the different values of σ/μ. Further evidence for this is developed later in discussing Runs #1101 - 1118 in terms of the 10.6μ scintillation.

3. $\sigma_\ell^2(0.514, 1500)$ vs. $\sigma_\ell^2(0.514, 1500)$

In order to check the accuracy with which σ_ℓ^2 could be measured, a series of measurements during Data Runs #1201 - 1220 were performed with the Argon Laser (0.514μ emission) at 1500 meter range and with a pair of "point" collectors separated by approximately 20 cm. (Reasonable care was taken to insure that the two collectors were symmetrically placed about the center of the beam, though it was not possible to do this with great accuracy because of the large diameter of the laser beam -- in excess of 1.5 meters apparent size.) Referring to the collectors as "C" and "D", we computed $\sigma_\ell^2(0.514, 1500;C)$ and $\sigma_\ell^2(0.514, 1500;D)$ for each test. The ratio of the two values of log-amplitude variance should be unity. The deviation from unity and the spread in the distribution of the ratio values is a direct measure of the accuracy with which log-amplitude variance was measured. The probability distribution of the ratio $\sigma_\ell^2(0.514, 1500;C)$ and $\sigma_\ell^2(0.514, 1500;D)$, obtained from the data, is shown in Figure 24. The mean value ($\mu = 0.981$), as expected, was very close to unity. The distribution of values is Gaussian with an rms spread of 3.8 percent, implying that each of the individual log-amplitude variance measurements, having a nominal mean value of 0.55, had an uncertainty of $\pm 0.55\ (0.038/\sqrt{2}) = \pm 0.015$. This same accuracy, of course, can not be attributed to measurements made at 0.633μ or 1.15μ since the signal-to-noise ratio is never as good as for 0.514μ, and this will tend to produce poorer precision in determination of σ_ℓ^2. In the case of 0.633 measurements, the matter is farther complicated by the very small values of σ_ℓ^2 expected, so that the accuracy, though not as good percentage wise, is probably better in an absolute sense.

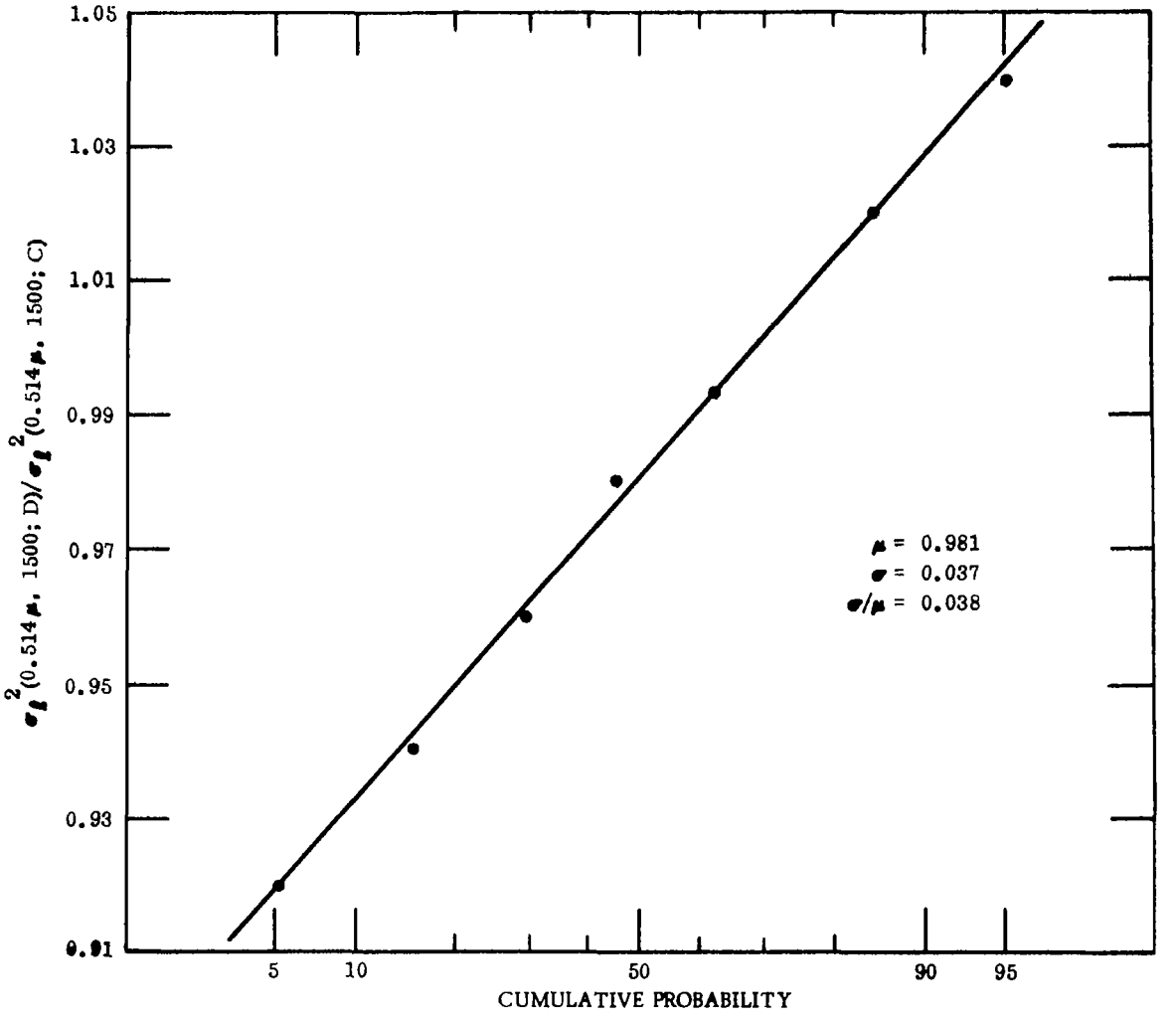

FIGURE 24. Probability Distribution of Ratio, σ_ℓ^2, meas/σ_ℓ^2, meas for 0.514μ Measurements at 1.5 km. Data Runs #1201 - 1220 (7/11/68). Data taken with two identical 0.514μ "point" collectors. Separation between collector aperture centers approximately 20 cm.

4. $\sigma_\ell^2(0.514, 1000)$ vs. $\sigma_\ell^2(1.15, 1000)$

During Data Runs No. 308 - 405, scintillation data were taken with both the Argon laser, producing 0.514 μ illumination and the He-Ne laser producing 1.15 μ radiation, with both of these sources operating over nearly the same 1000 meter path (exit apertures of the lasers separated by less than 0.5 meters and collector apertures by slightly greater than 1.0 meter). The scintillation data from each of these sources was separately compared with the 0.63 μ, 200 meter reference data, with the results shown in Figures 19 and 22. To explore the possibility that some of the spread between predicted and measured values of σ_ℓ^2 was due to the fact that the turbulence over the 200 meter path was not strictly representative of the turbulence over the entire 1000 meter path, i.e., that the statistics of the turbulence were not strictly homogeneous over the path, at least for the one-minute measurements periods we used, we utilized the relationship that $\sigma_\ell^2(0.514, 1000) = 2.56\ \sigma_\ell^2(1.15, 1000)$ as obtained from Table IV to compare the 0.514 μ and 1.15 μ scintillation. This permitted us to make our measurements using only wavelength scaling, without considering path length differences, and obtain a data spread when there was, unlike the data of Figure 24, at least one measurement that posed some minor problem of signal strength. The scatter plot of this comparison, with all the data put into the form of measured and predicted values for $\sigma_\ell^2(0.514, 1000)$ is shown in Figure 25. The probability distribution for the ratio of measured to predicted values for $\sigma_\ell^2(0.514, 1000)$ is shown in Figure 26. As can be seen, the data presents a reasonable fit to a Gaussian distribution with a mean value $\mu = 1.067$ and an rms spread of 13 percent. This spread is quite consistent with our earlier results, where measurements over a long and a short path length were compared, and suggests that, at least most of the time, the 200-meter path, with a one-minute measurement period manifests turbulence effects that are statistically representative of the effects observed over the longer paths.

5. $\sigma_\ell^2(0.500, 500)$ and $\sigma_\ell^2(0.514, 500)$ vs. $\sigma_\ell^2(0.633, 200)$

In order to determine the applicability of propagation theory, developed for a coherent, truly monochromatic source, to an incoherent narrow band but definitely not monochromatic source, Data Runs No. 903 - 1009 were taken with a filtered

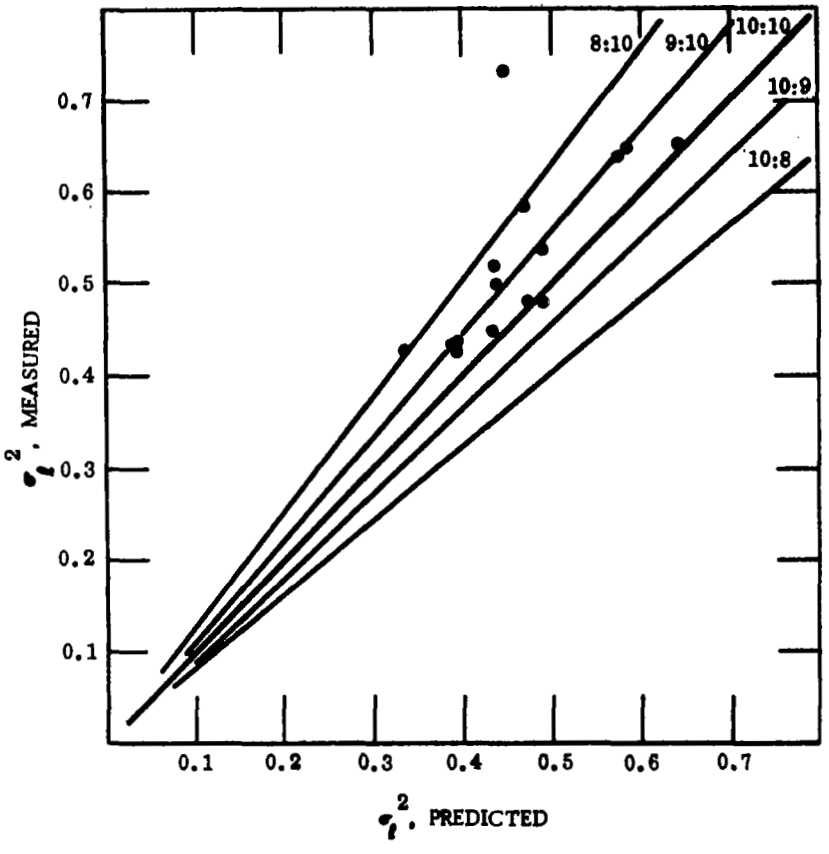

FIGURE 25. Measured vs. Predicted σ_ℓ^2 for 0.514 μ at 1.0 km. Data Runs No. 308-405 (5/30/68). Predictions based on 1.15 μ σ_ℓ^2 measured for 1.0 km.

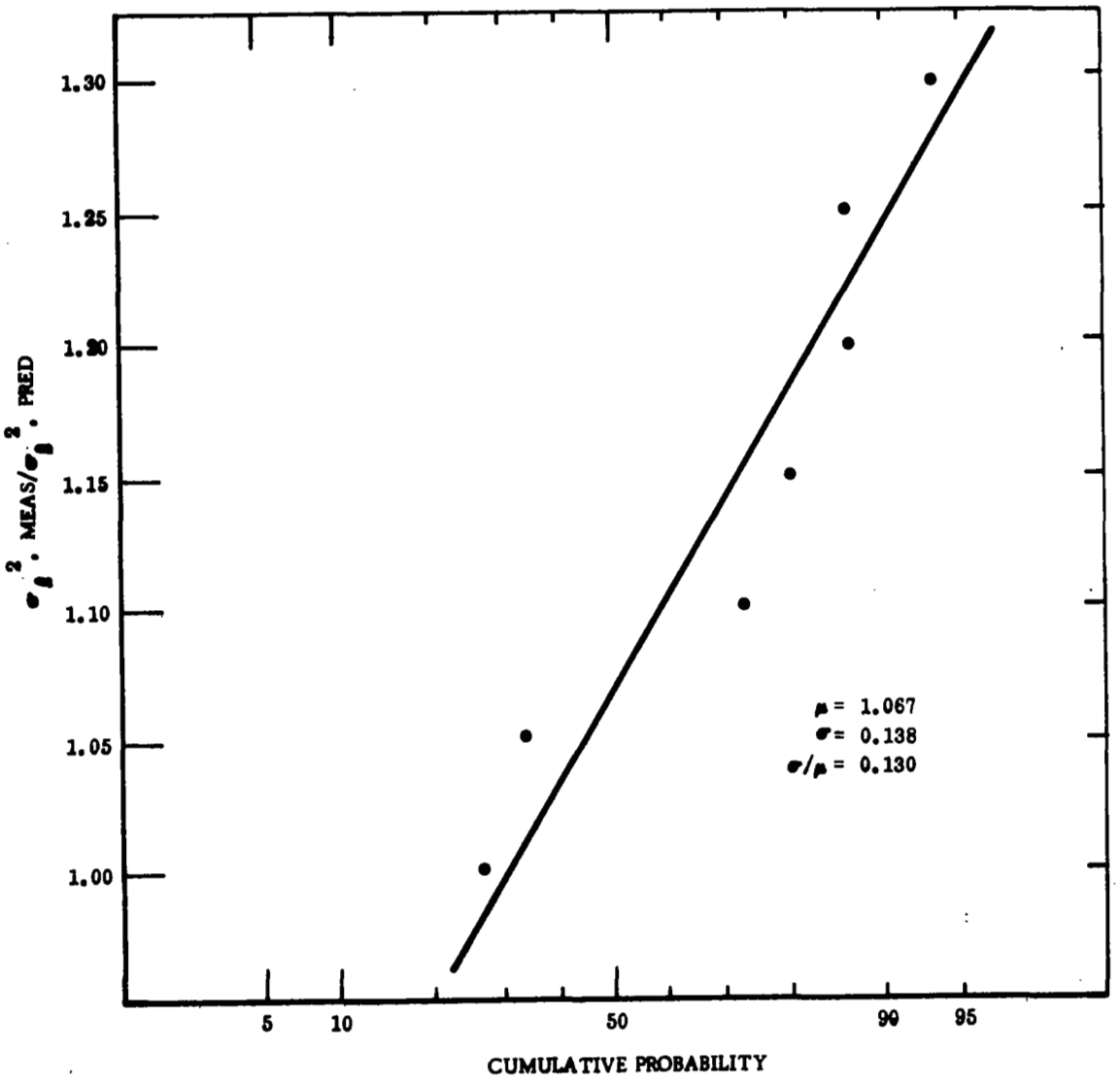

FIGURE 26. Probability Distribution of Ratio, σ^2, meas/σ^2, pred for 0.514 μ Measurements at 1.0 km. Predictions based on 1.15 μ measurements at 1.0 km. Data taken from Runs No. 308 - 405 (5/30/68).

Xenon arc lamp (lamp output filtered at optical receiver) and the Argon laser, at 0.514 μ, both at 500 meters range, and with the standard reference source 0.633 μ at 200 meters. The filtered arc lamp output was at 0.500 ± 0.040 μ. Because it was not possible to keep the two blue lights separate as far as the receivers were concerned, it was necessary to alternately run the argon laser and the Xenon arc lamp. In each case, the measured log-amplitude variance was compared to a value predicted from the measured value of $\sigma_\ell^2(0.633, 200)$. The coefficients relating this value to $\sigma_\ell^2(0.500, 500)$, and $\sigma_\ell^2(0.514, 500)$, as obtained from Table IV, were 7.06 and 6.83, respectively. The scatter plots for the measured and predicted values are shown in Figures 27a and 27b. In Figures 28 and 29, we show the probability distributions for the ratio of measured to predicted values for each of the two sources. The distributions are at least consistent with the assumption of a Gaussian spread. The mean values of $\mu = 0.953$ and $\mu = 1.137$ for the incoherent and coherent sources, respectively, are in reasonable agreement with the expected value of unity, though it must be commented that the 1.137 value is about two standard deviations away from unity.

It is interesting to note how much larger the rms spread of the incoherent source data is (16.4 percent) than the spread of coherent source data (6.1 percent). We attribute this to the much lower signal-to-noise ratio associated with the incoherent source, due to the much lower intensity (watts per steradian) of the Xenon arc lamp.

6. Effect of Laser Beam Diameter on σ_ℓ^2

With the scintillation data that we have presented to this point, which appears to be in reasonable agreement with the predictions of the Rytov Approximation as developed for spherical wave propagation theory,[1,2] it is reasonable to ask what the effect of using a laser source rather than a true point source is predicted to be[3], and how this compares with the experimental data.

According to the results of reference 3, the ratio $\mathcal{R}$, of the scintillation σ_ℓ^2 predicted for a laser source to the scintillation σ_ℓ^2 predicted for a point source will depend on

$$\Omega = \frac{k a_o^2}{Z} \quad , \tag{6}$$

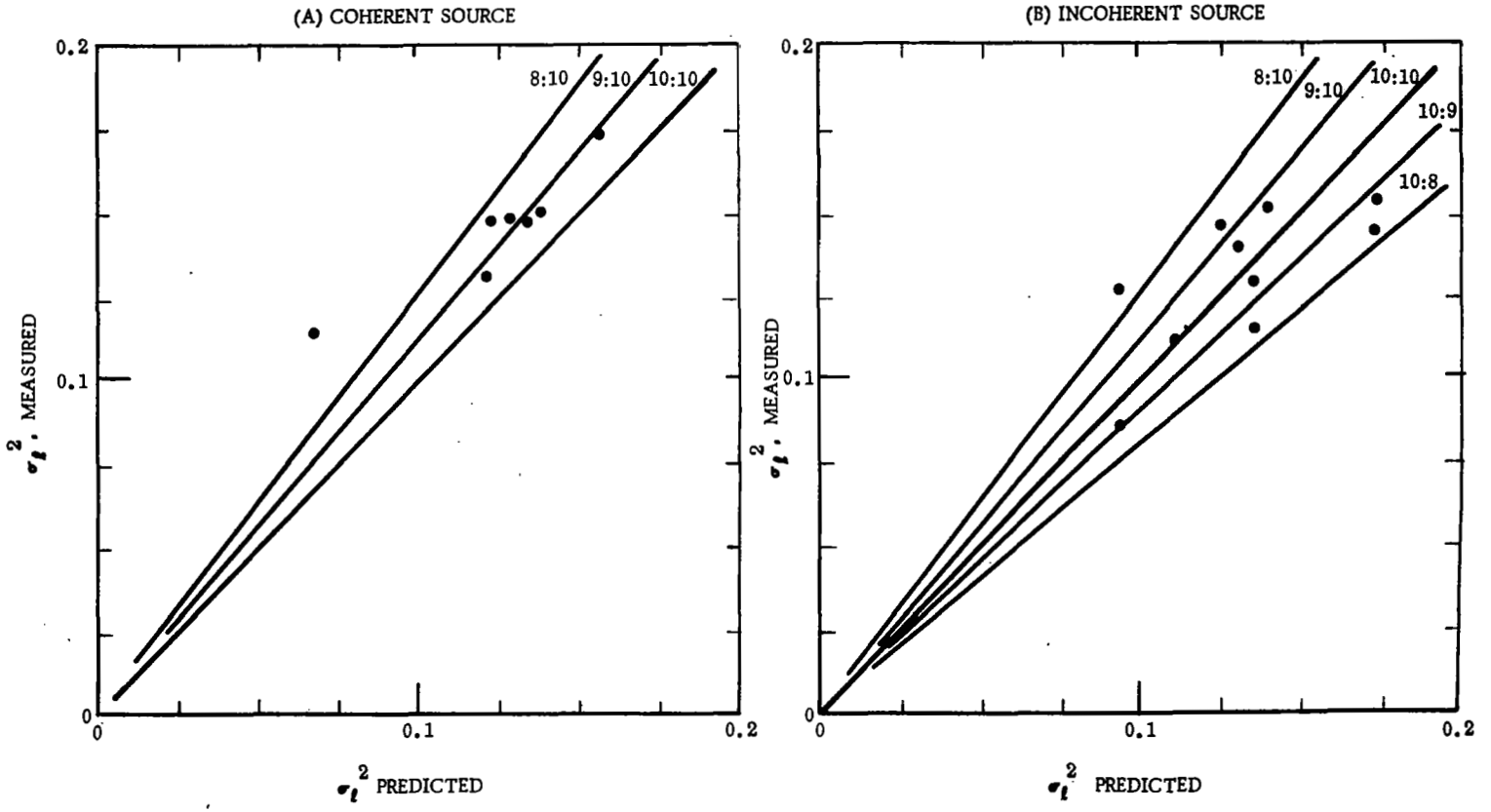

FIGURE 27. Measured vs. Predicted for 0.514 μ Laser and Xenon Arc Lamp (λ = 5000 Å, $\Delta\lambda$ = 800Å) at 0.5 km. Data Runs No. 903 - 1009 (7/3/68). Predictions based on 0.633 μ σ_l^2 measured for 0.2 km.

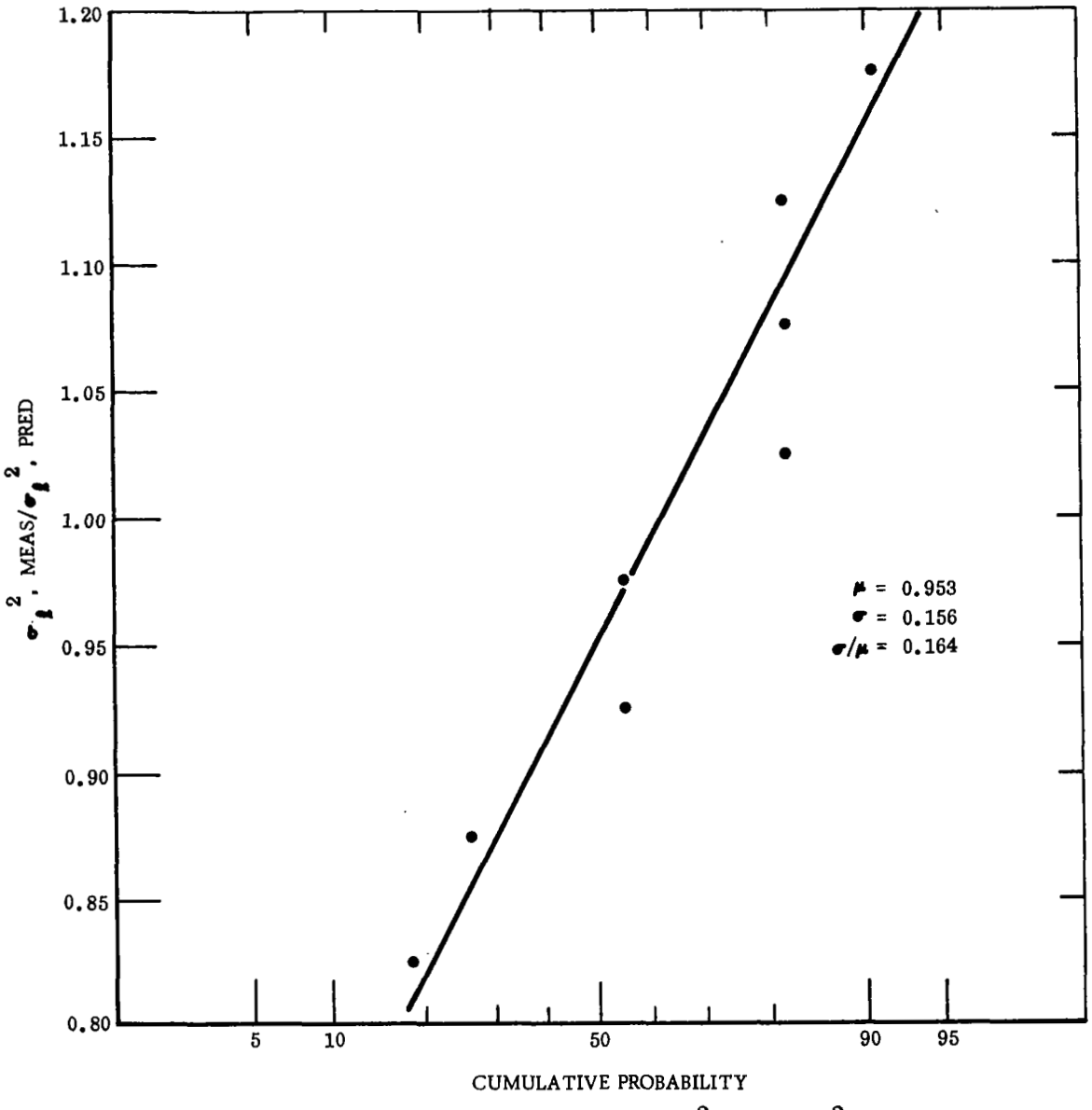

FIGURE 28. Probability Distribution of Ratio, σ_ℓ^2, meas/σ_ℓ^2, pred for 0.50 μ Measurements at 0.5 km. Predictions based on 0.633 μ measurements at 0.2 km. Data taken from Runs No. 903 - 1009 (7/3/68).

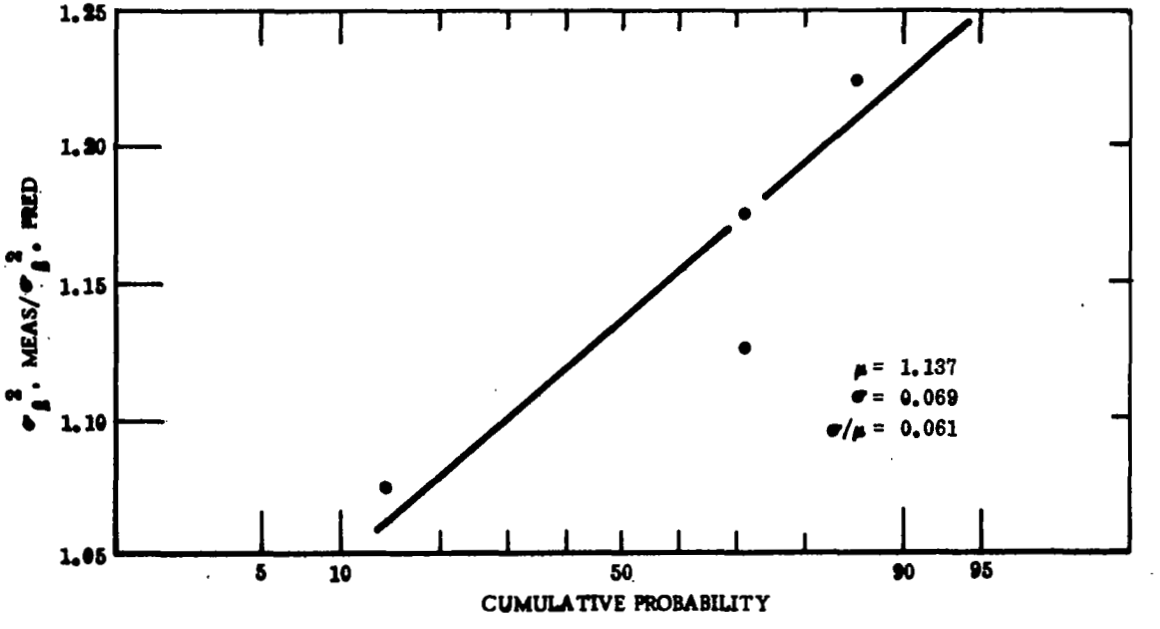

FIGURE 29. Probability Distribution of Ratio, σ_ℓ^2, meas/σ_ℓ^2, pred for 0.514 μ Measurements at 0.5 km. Predictions based on 0.633 μ measurements at 0.2 km. Data taken from runs No. 903 - 1009 (7/3/68).

where $k = 2\pi/\lambda$ is the wave number, and α_o is defined by the Gaussian amplitude taper of the laser amplitude at the source. Thus the laser amplitude is defined by the taper, $\exp(-\rho^2/2\alpha_o^2)$, where ρ is a radial distance from the center line of the laser. The manufacturers generally specify the laser "diameter", D, in terms of the distance between the points at which the output intensity is down to e^{-2} of its peak value. Hence

$$\alpha_o = D/2\sqrt{2} \quad , \tag{7}$$

and

$$\Omega = \frac{\pi D^2}{4\lambda Z} \quad . \tag{8}$$

Utilizing the data in reference 3 for a collimated laser beam and fitting this data with the interpolation formula

$$\mathscr{R} = 0.642\Omega^{-0.75}, \quad (5 \times 10^{-3} < \Omega > 1 \times 10^{-1}) \tag{9}$$

where $\mathscr{R}$ is defined by the relationship

$$\mathscr{R} = \frac{\sigma_\ell^2(\text{predicted for a laser source})}{\sigma_\ell^2(\text{predicted for a point source})} \quad . \tag{10}$$

We can now make correction for the laser beam size. The correction factor itself is the ratio of $\mathscr{R}$ for the laser in terms of which the measured and predicted values were presented (such as 0.514 μ laser), to the value of $\mathscr{R}$ for the laser with which the data was was taken to obtain the predicted value, (generally the 0.633 μ laser).

In Table V, we show the various values of $\mathscr{R}$. Table VI shows the values of μ, the ratio of measured to predicted values of σ_ℓ^2 for various measurements presented previously* and makes the corrections between μ_{sph}, value of μ obtained using

*The data on σ_ℓ^2 that will be presented in what follows this discussion will show clear deviations for the Rytov Approximation based results. The deviations were of such a magnitude that the question of testing the relatively minor correction between laser and spherical wave results will be entirely inapplicable for these results. Hence the data we treat in Table VI will be the only data for which we shall consider applying a correction factor for the difference between spherical wave and laser propagation theory.

TABLE V

CORRECTION OF THEORY FOR FINITE SIZE OF LASER BEAM

SOURCE	λ (MICRONS)	Z(METERS)	D(METERS)	$\mathscr{R}$
Spectra Physics Model 115 Laser	0.633	200	3.5×30^{-3}	0.781
Spectra Physics Model 125 Laser	1.15	1000	4.8×10^{-3}	0.877
Spectra Physics Model 140 Laser	0.514	$\frac{500}{1000}$	2×10^{-3}	$\frac{0.893}{0.944}$
Xenon Arc Lamp	0.500	500	Zero	1.000

spherical wave theory[1,2] and μ_{laser}, the value of μ obtained using laser theory.[3] The conclusion that we are forced to draw from the data of Table VI is that the correction from spherical wave to laser source theory does not improve the closeness of μ to the ideal value of unity and in fact appears to hurt it. To the extent that the accuracy of the measurements permit any firm conclusion, it must be that we do not fully understand, even in the range in which Rytov Approximation is accurate, the consequences to σ_ℓ^2 of using a laser source rather than a point source. We shall not consider a correction factor for the difference in any of our subsequent data analysis.

7. $\sigma_\ell^2(0.514, 1500)$ vs. $\sigma_\ell^2(0.633, 200)$

In Data Runs No. 1201 - 1220 and No. 1301 - 1307, measurements were made of the log-amplitude variance, σ_ℓ^2 for the 0.514 μ source at 1500 meters. Reference measurements based on the 0.633 μ laser source at 200 meters were used to obtain predicted values for $(0.514\mu, 1500)$. Scatter plots of the measured and predicted values of $\sigma_\ell^2(0.514, 1500)$ are shown in Figures 30 and 31. It is quite clear from these data that the measured values are, for all intents and purposes, independent of the predicted values! For each of the data sets, there is about a 2:1 spread in predicted values, with less than a 20 percent spread in the measured values and with the latter at a significantly lower mean value than the former. We take this to be a clear

TABLE VI

CORRECTIONS TO μ TO CONVERT FROM SPHERICAL WAVE TO LASER THEORY

MEASUREMENT	CORRECTION FACTOR	$\mu_{SPHERICAL}$	μ_{LASER}
$\sigma_\ell^2(0.514, 1000)$ vs. $\sigma_\ell^2(0.633, 200)$	$\frac{0.944}{0.781} = 1.210$	0.936	1.135
$\sigma_\ell^2(1.15, 1000)$ vs. $\sigma_\ell^2(0.633, 200)$	$\frac{0.877}{0.781} = 1.123$	0.898 (1.16)*	1.010 (1.307)
$\sigma_\ell^2(0.514, 1000)$ vs. $\sigma_\ell^2(1.15, 1000)$	$\frac{0.944}{0.877} = 1.076$	1.067	1.148
$\sigma_\ell^2(0.500, 500)$ vs. $\sigma_\ell^2(0.633, 200$	$\frac{1.000}{0.781} = 1.280$	0.953	1.221
$\sigma_\ell^2(0.514, 500)$ vs. $\sigma_\ell^2(0.633, 200)$	$\frac{0.893}{0.781} = 1.142$	1.137	1.300

*The rms spread in this data is so large as to make the accuracy of this value quite questionable.

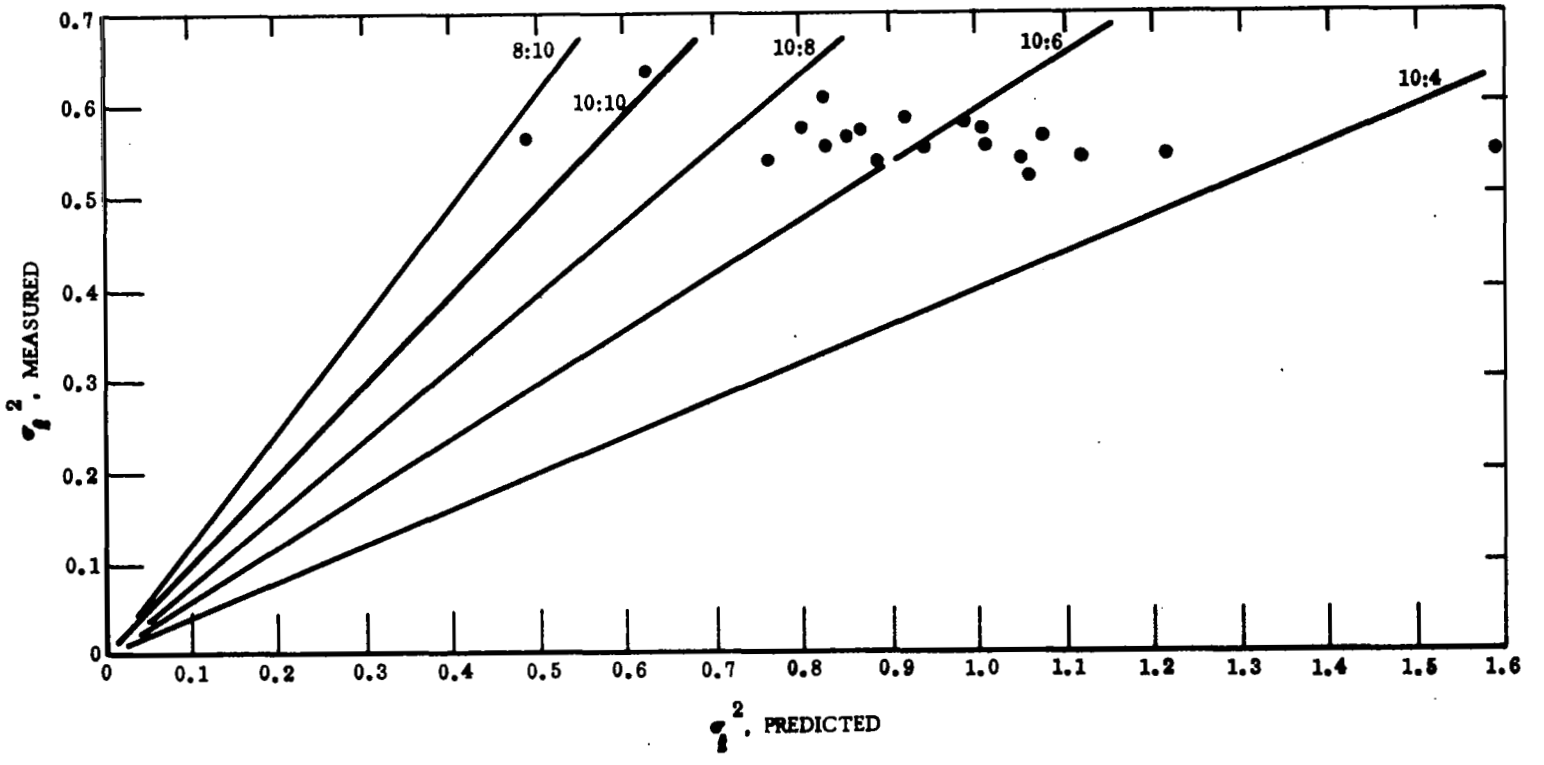

FIGURE 30. Measured vs. Predicted σ_l^2 for 0.514 μ at 1.5 km. Data Runs No. 1201 - 1220 (7/11/68). Predictions based on 0.633 μ σ_l^2 measured for 0.2 km.

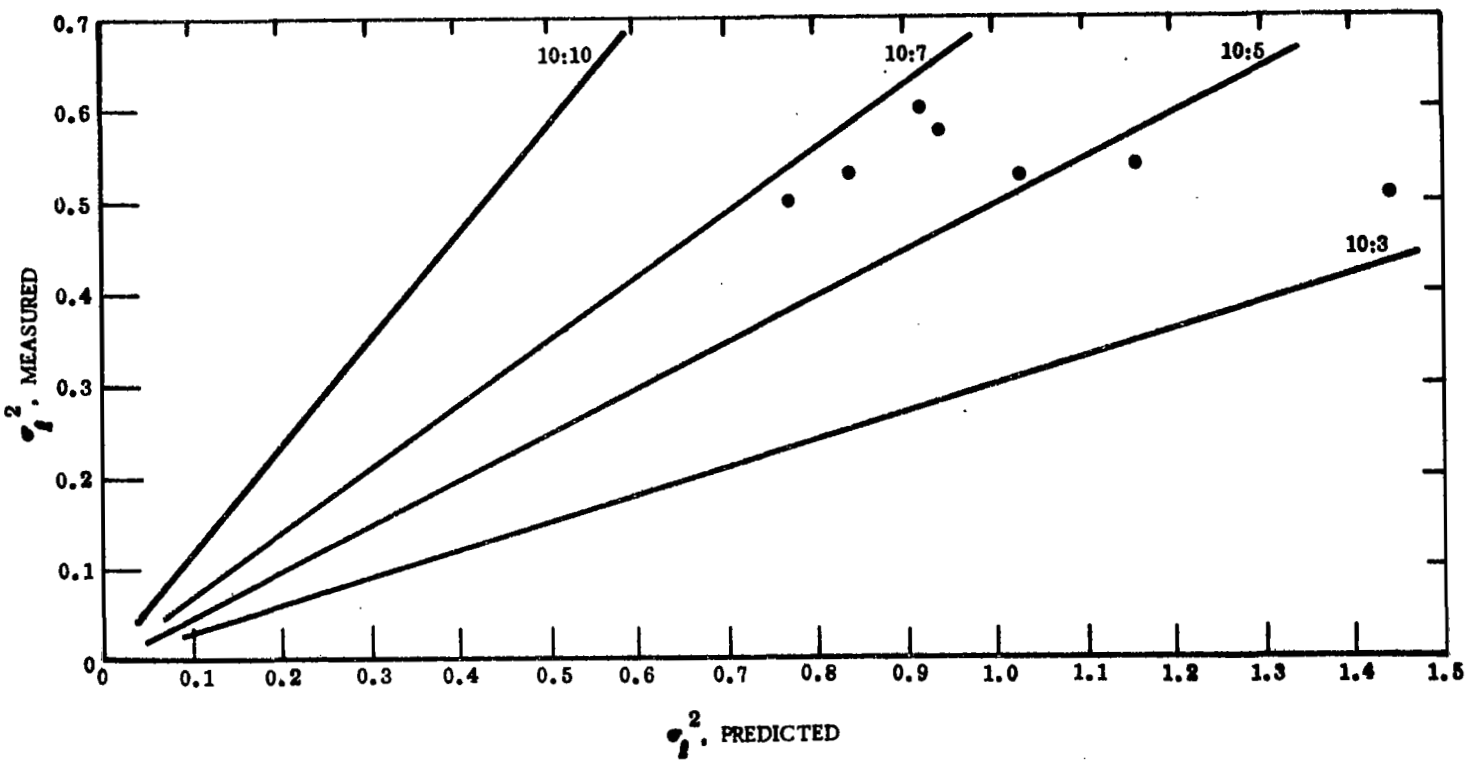

FIGURE 31. Measured vs. Predicted σ_ℓ^2 for 0.514 μ at 1.5 km. Data Runs No. 1301 - 1307 (7/13/68). Predictions based on 0.633 μ σ_ℓ^2 measured for 0.2 km.

indication of the existence of a saturation of scintilation such as reported elsewhere.[4,5] because we use a probability distribution measurement technique for determination of σ_ℓ^2, we believe these results are subject to less question than the results of references 4 and 5 - relative to the matter analysed in Appendix A.

To examine the measured values of $\sigma_\ell^2(0.514, 1500)$ more closely, in Figures 32 and 33, we plotted the probability distribution of the measured values of $\sigma_\ell^2(0.514, 1500)$, (Note that this is unlike our previous data treatment where we considered probability distribution for the ratio of measured to predicted values.) The distribution are both apparently Gaussian with mean values of 0.5527 and 0.5215. The measure ments show percentage spread of 4.4 percent for the first data set and 8.3 percent for the second. Such spread are entirely compatible with the assumption that the expected value of σ_ℓ^2 for these measurement conditions should be practically constant, i.e., almost entirely independent of the strength of turbulence. We base this conclusion on the measurement accuracy manifested by the data in Figure 24.

8. $\sigma_\ell^2(0.514, 3000)$ vs. $\sigma_\ell^2(0.633, 200)$

Additional log-amplitude variance data manifesting saturation of scintillation was taken with the 0.514 μ source at 3000 meters range during Data Runs No. 406 - 505 and No. 1308 - 1311. The predicted values were obtained from the 0.633 μ source at 200 meters range. Scatter plots of measured versus predicted values are shown in Figures 34 and 35. It is again apparent that there is no noticeable correlation between predicted and measured values of $\sigma(0.514, 300)$. It is interesting to note that although there are only a few data points in Figure 35, they are clustered around a significantly higher measured value of σ_ℓ^2 than are the data for Figure 34. To more fully examine the data, we have plotted the probability distribution of the measured values of σ_ℓ^2, for each of the data sets. The results are shown in Figures 36 and 37.[+] The mean values are 0.497 when the predicted values are larger, and 0.655 when the predicted values are smaller. The rms spread of 4.6 percent for the Data Set No. 406 - 505 is

+Because of the very few data points in Data Set No. 1308 - 1311, it was necessary in plotting Figure 37 to prepare distribution plots starting both from the high values and from the low values, resulting in the two distributions represented by the dotted lines, and take the average of the two. This precaution, which is not necessary with larger data sets, is required here to avoid biasing the results.

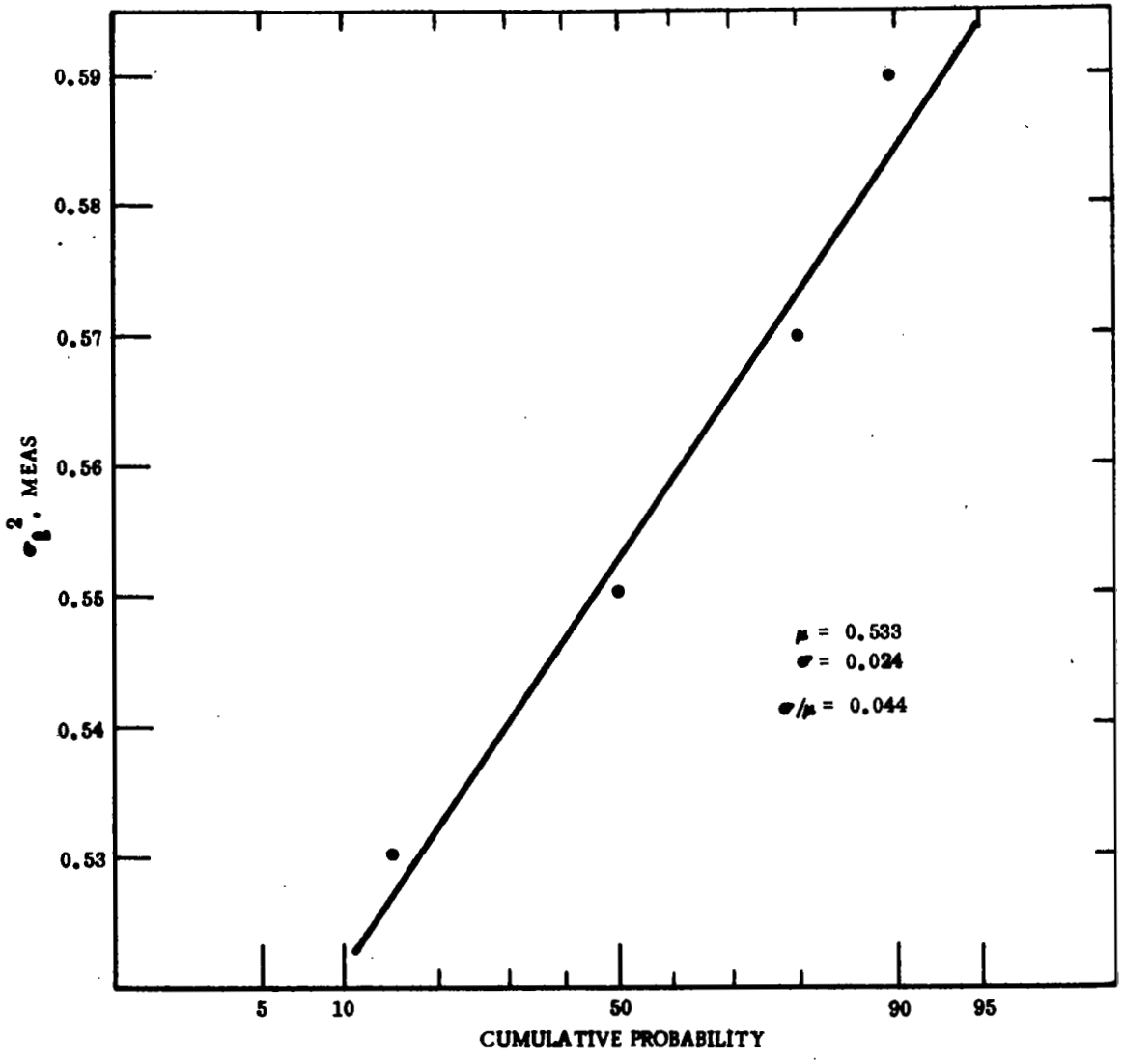

FIGURE 32. Probability Distribution of σ_ℓ^2, meas for 0.514 μ Measurements at 1.5 km. Data taken from Runs No. 1201 - 1220 (7/11/68)

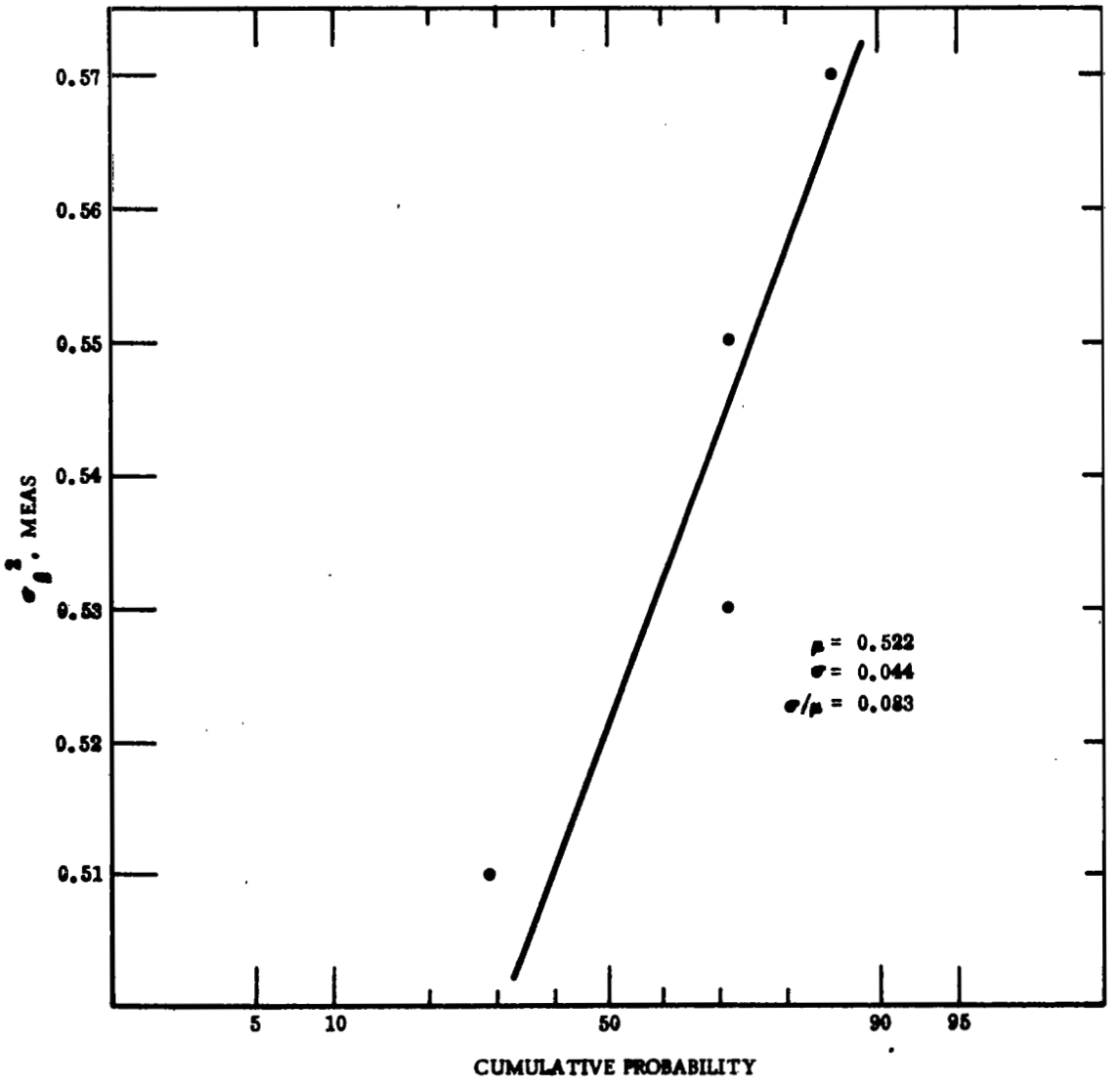

FIGURE 33. Probability Distribution of σ_{ℓ}^2, meas for 0.514 μ Measurements at 1.5 km. Data taken from Runs No. 1301 - 1307 (7/13/68).

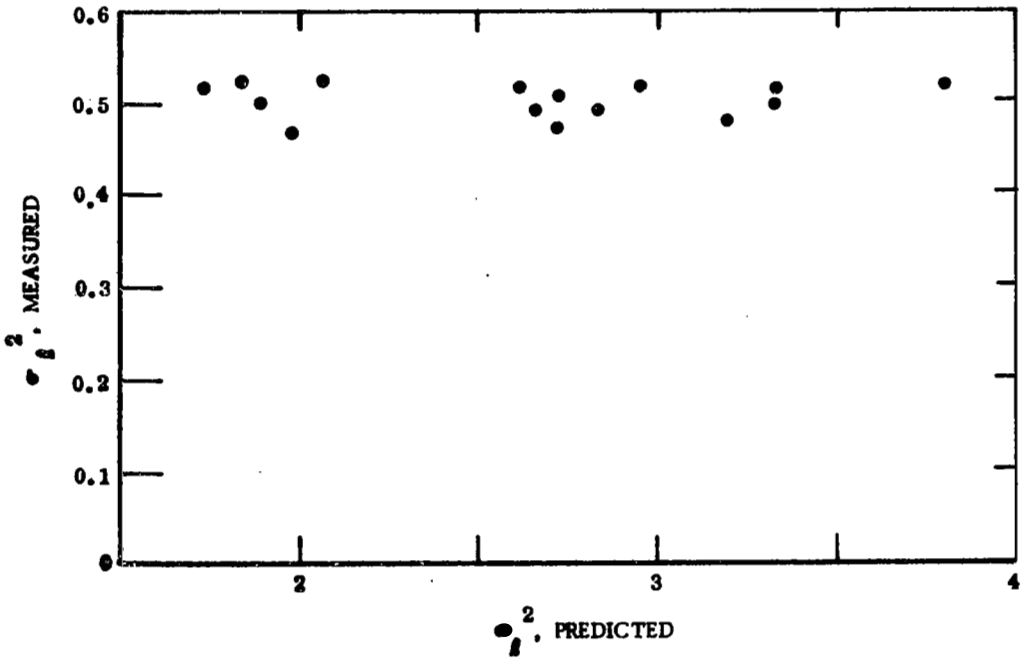

FIGURE 34. Measured vs. Predicted σ_ℓ^2 for 0.514 μ at 3.0 km. Data Runs No. 406 - 505 (5/31/68). Prediction based on 0.633 $\mu\,\sigma_\ell^2$ measured for 0.2 km.

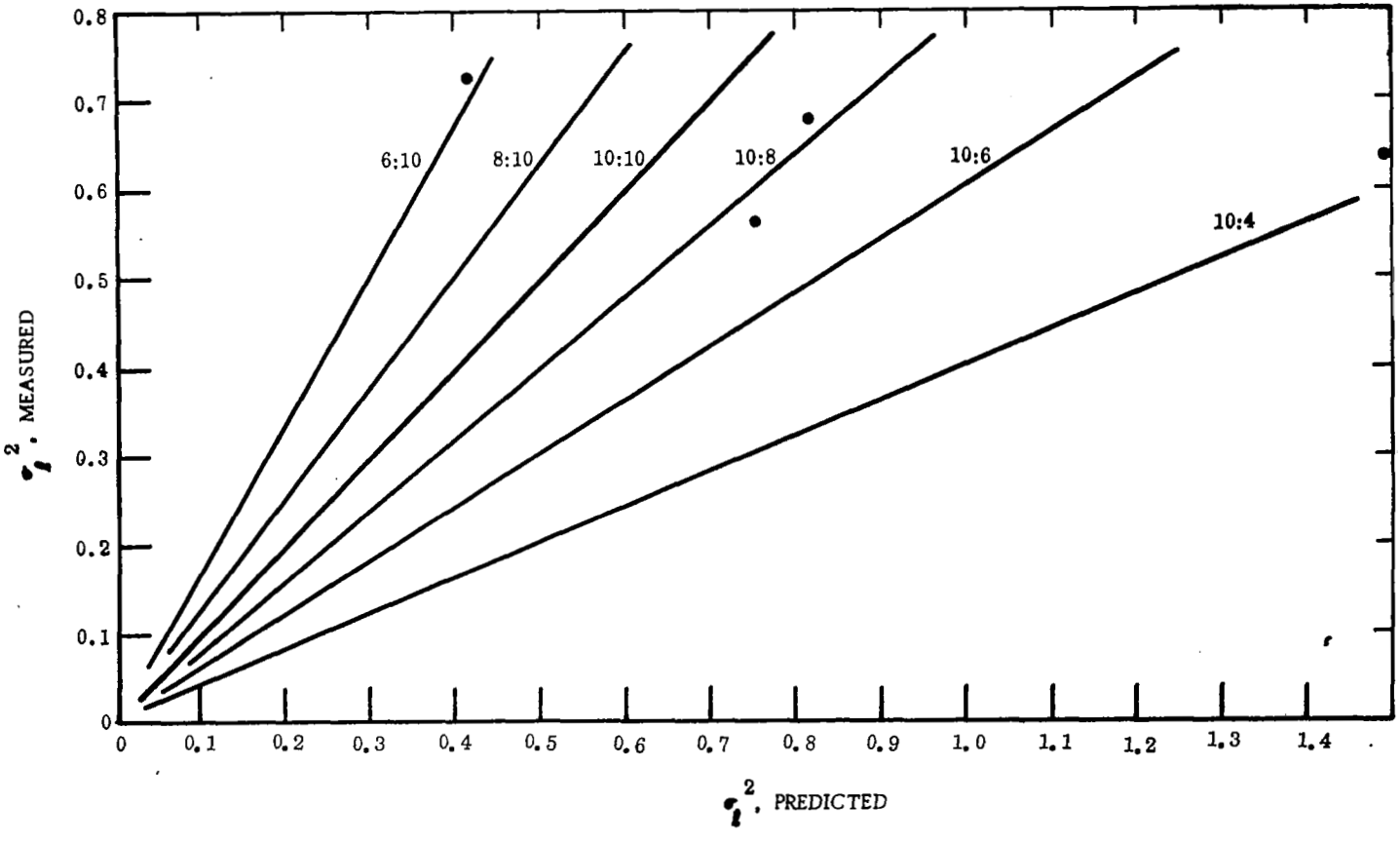

FIGURE 35. Measured vs. Predicted for 0.514 μ Measurements at 3.0 km. Data Runs No. 1308 - 1311 (7/13/68). Prediction based on 6.33 $\mu\, \sigma_\ell^2$ measured for 0.2 km.

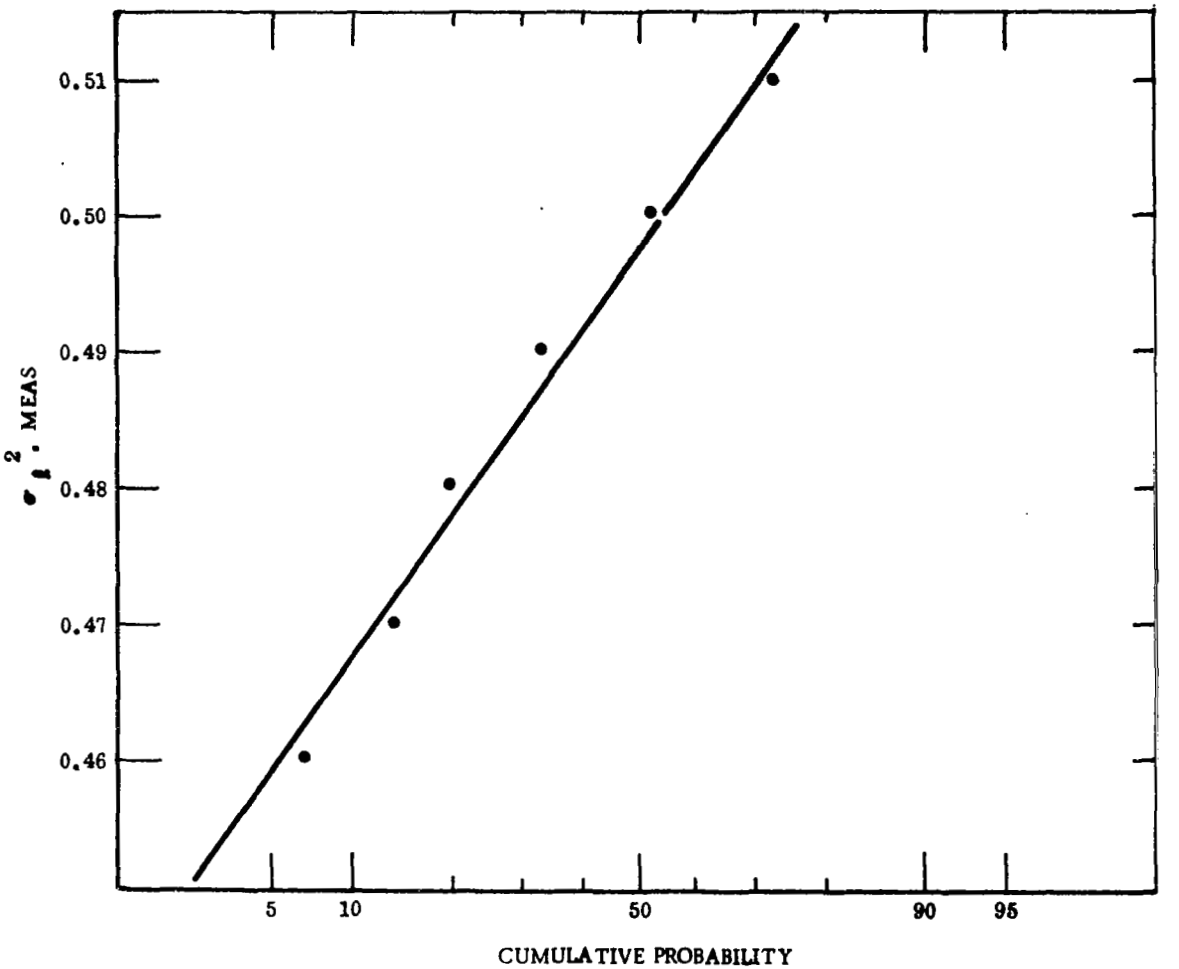

FIGURE 36. Probability Distribution of σ_ℓ^2, meas for 0.514 μ Measurements at 3.0 km. Data taken from Runs No. 406 - 505 (5/31/68).

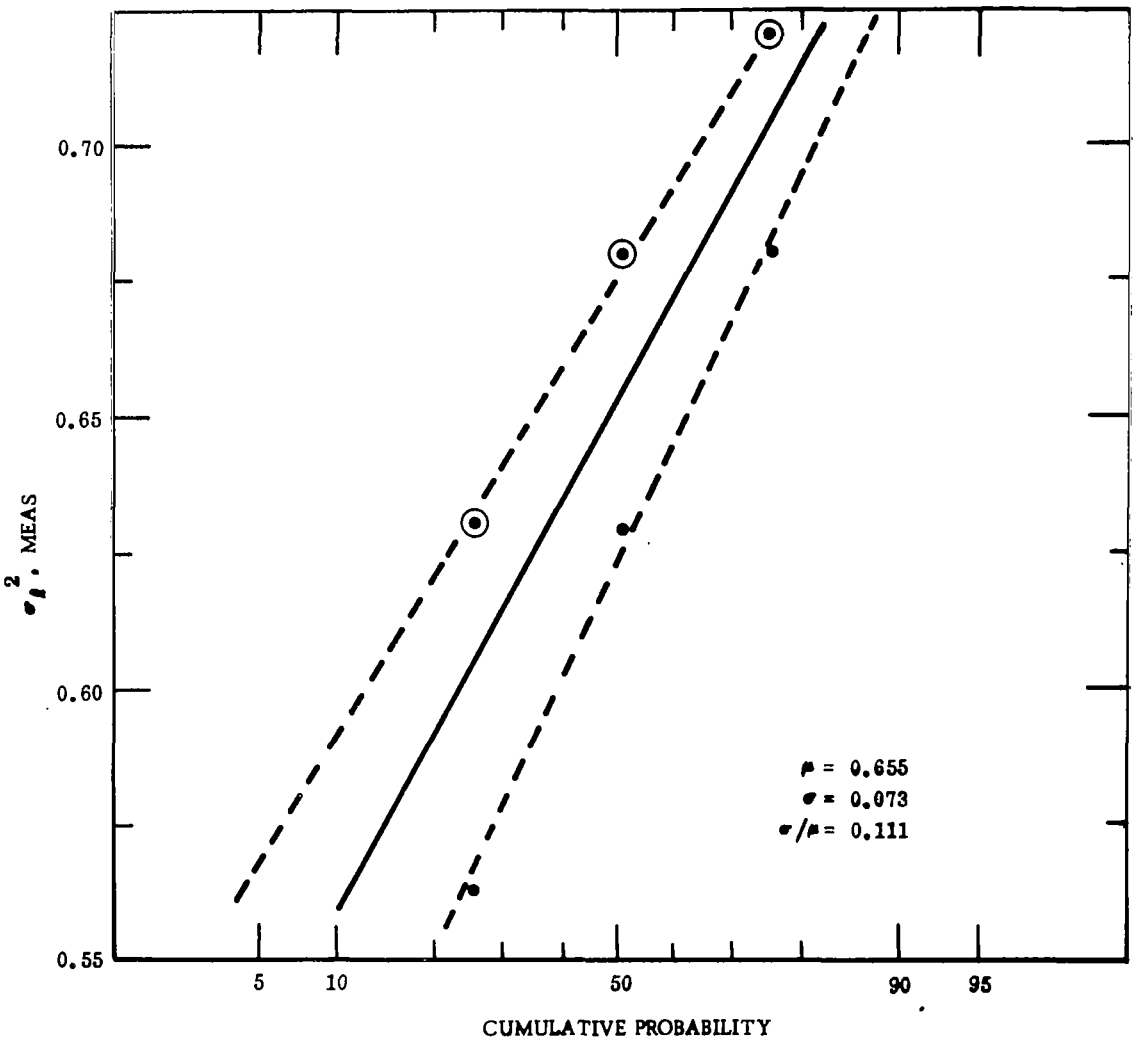

FIGURE 37. Probability Distribution of σ_ℓ^2, meas for 0.514 μ Measurements at 3.0 km. Data taken from Runs No. 1308 - 1311 (7/13/68).

certainly consistent with the domonstrated accuracy of our measurements. The spread of 11.1 percent for Data Set No. 1308 - 1311 is almost certainly a consequence of the very few data points involved and need not trouble us.

The only clear difference between the data taking conditions for the two data sets is that the optical strength of turbulence was apparently significantly stronger when Data Set No. 406 - 505 was taken than Data Set No. 1308 - 1311 was obtained. The predicted values of σ_ℓ^2 for the former set have a range from about 1.8 to 3.8, while the range for the latter data set is from 0.4 to 1.5. We believe that the difference in the strength of turbulence is the cause of the difference in measured results. In subsequent data sets, we shall be able to more fully explore this and shall develop the thesis that once saturation of scintillation applies, the larger the predicted value of σ_ℓ^2, smaller the measured value!

9. $\sigma_\ell^2(0.514, 5000)$ vs. $\sigma_\ell^2(0.633, 200)$

Further observations indicating saturation of scintillation were obtained during Data Runs No. 506 - 514, with the 0.514 μ laser source at a range of 5000 meters. Reference data collected with a 0.633 μ source at 200 meters was used to obtain predicted values of $\sigma_\ell^2(0.514, 5000)$ for comparison with the measured values. A scatter plot of the measured versus predicted values is shown in Figure 38. As can be seen, the measured values are relatively constant and virtually independent of the predicted values. A probability distribution for the measured values was obtained from the data and plotted in Figure 39. The probability distribution data was fitted to a straight line (i.e., to a Gaussian distribution). The mean value was 0.372, with an rms spread of 4.1 percent, entirely in keeping with the accuracy of our measurement procedure. It is interesting to note how small the spread is, in view of the fact that the predicted values show a spread of about 2:1. We also call attention to the smallness of the mean value relative to the data obtained for $\sigma_\ell^2(0.514, 1500)$ and $\sigma_\ell^2(0.514, 3000)$. This appears to be correlated with the greater magnitude of the predicted values of σ_ℓ^2 for this case than for the two earlier cases. We shall, subsequently, explore this more fully.

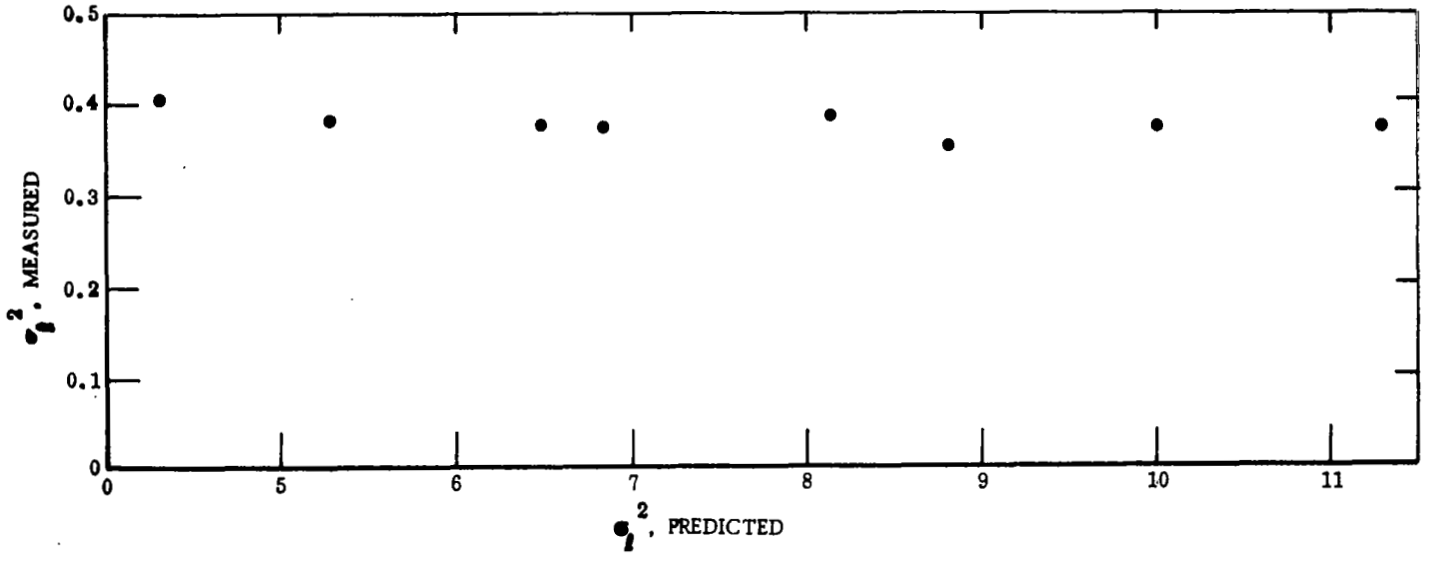

FIGURE 38. Measured vs. Predicted σ_ℓ^2 for 0.514 μ at 5.0 km. Data Runs No. 506 - 514 (5/31/68). Predictions based on 0.633 μ σ_ℓ^2 measured for 0.2 km.

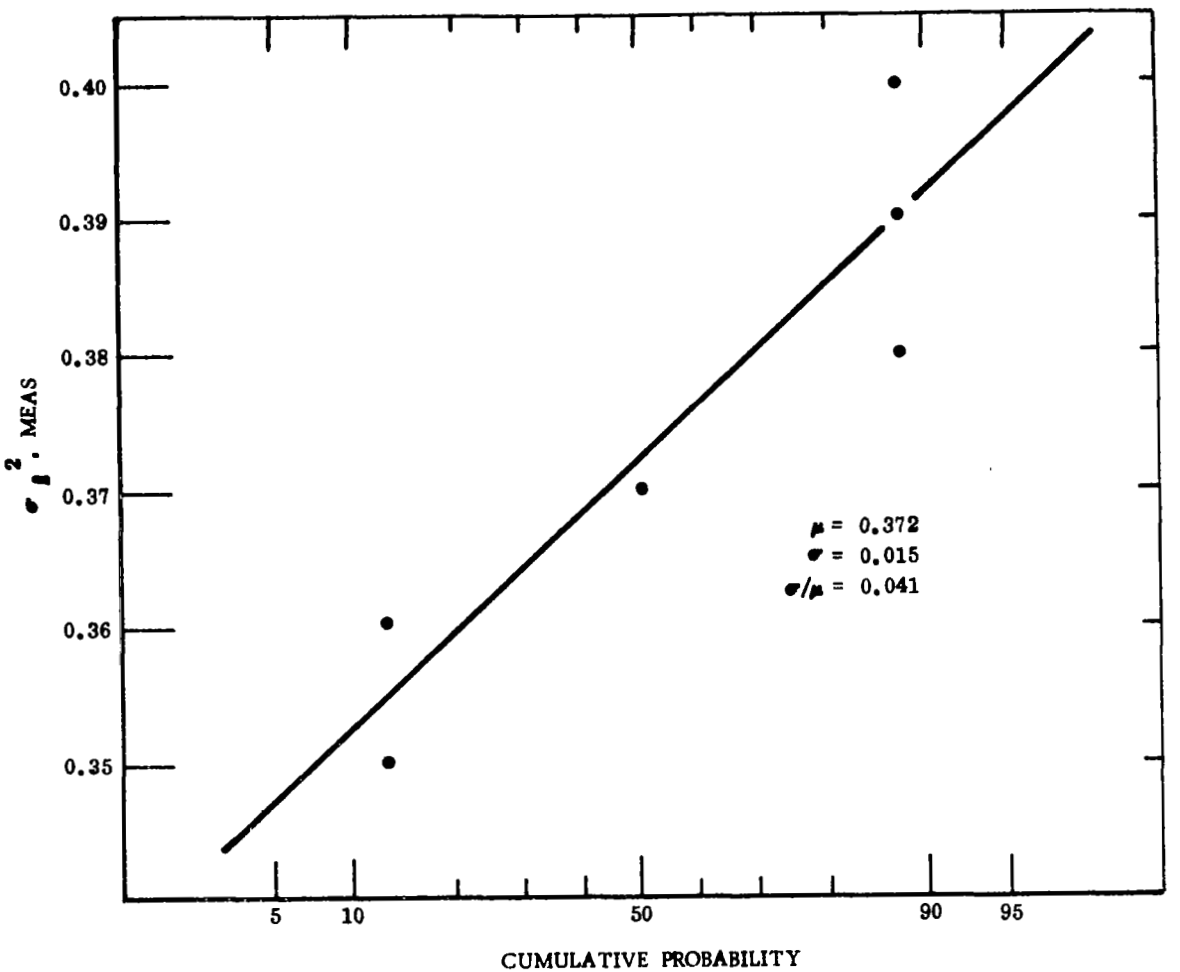

FIGURE 39. Probability Distribution of σ_ℓ^2 meas for 0.514 μ Measurement at 5.0 km. Data taken from Runs No. 506 - 514 (5/31/68).

10. $\sigma_\ell^2(1.15, 1500)$ vs. $\sigma_\ell^2(0.633, 200)$

During Data Runs No. 1201 - 1220, measurements were made of the log-amplitude variance of 1.15 μ radiation for a 1500 meter path length. These measurements of $\sigma_\ell^2(1.15, 1500)$ were compared with predictions based on 0.633 μ scintillation measurements over a 200 meter path. A scatter plot of measured versus predicted values for $\sigma_\ell^2(1.15, 1500)$ is shown in Figure 40. Examination of the scatter plot makes it clear that the measured value of σ_ℓ^2 was saturated, just as the measured values of σ_ℓ^2 for 0.514 μ radiation over this same 1500 meter path length. What is truly remarkable is the small values of σ_ℓ^2 involved. For 0.514 μ radiation, when the predicted values of σ_ℓ^2 were the same range as in Figure 40, i.e., mostly between 0.2 and 0.45, the measured values agreed quite well with the predicted values. Here, it is quite clear that there is no noticeable correlation between measured and predicted values. Apparently saturation of scintillation is not merely a matter of magnitude of the predicted value of σ_ℓ^2. It also has some separate dependence on path length and wavelength.* It is a matter for future theoretical studies to explore this subject.

In order to more precisely examine this set of data, the measured values of $\sigma_\ell^2(1.15, 1500)$ shown in Figure 40 were converted to a probability distribution. This distribution is shown in Figure 41. The mean value, corresponding to the saturation of scintillation for 1.15 μ radiation at 1500 meters, is seen to be 0.281 with a data spread of 5.4 percent. This is entirely compatible with our estimates of measurement accuracy - implying that little, if any, of the data spread represents fluctuations in atmospheric conditions changing the measured value.

11. Saturation of Scintillation

With the body of data we have just presented suggesting saturation of scintillation, it is worth taking a look at all of the data together. First, let us examine those data sets that imply saturation of scintillation. In Figure 42, we have plotted the results of all measurements taken over ranges of 1500 meters and greater. The data points

*There are, it must be noted, dimensional difficulties that make it hard to imagine what form the path length - wavelength dependence can take. To put it succintly, one-kilometer appears to be the distance at which the transition for unsaturated to saturated scintillation takes place. What is it that makes one-kilometer a "natural" unit of length for this subject? Later in this document we shall briefly explore the possibility that the "natural" unit of length is actually derived from the diameter of the laser.

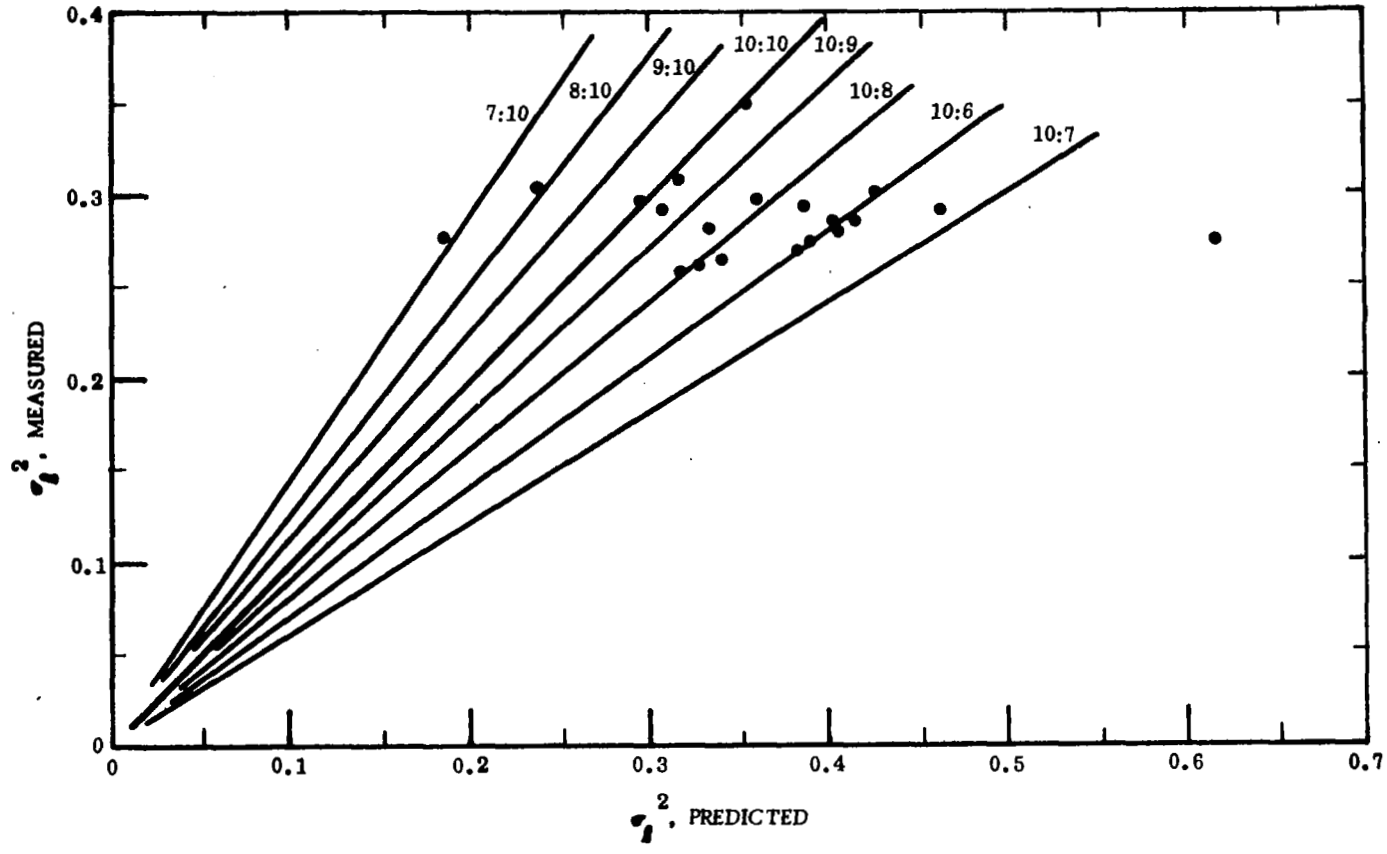

FIGURE 40. Measured vs. Predicted σ_ℓ^2 for 1.15 μ at 1.5 km. Data Runs No. 1201 - 1220 (7/11/68). Predictions based on 0.633 μ $\sigma_\ell{}^2$ measured for 0.2 km.

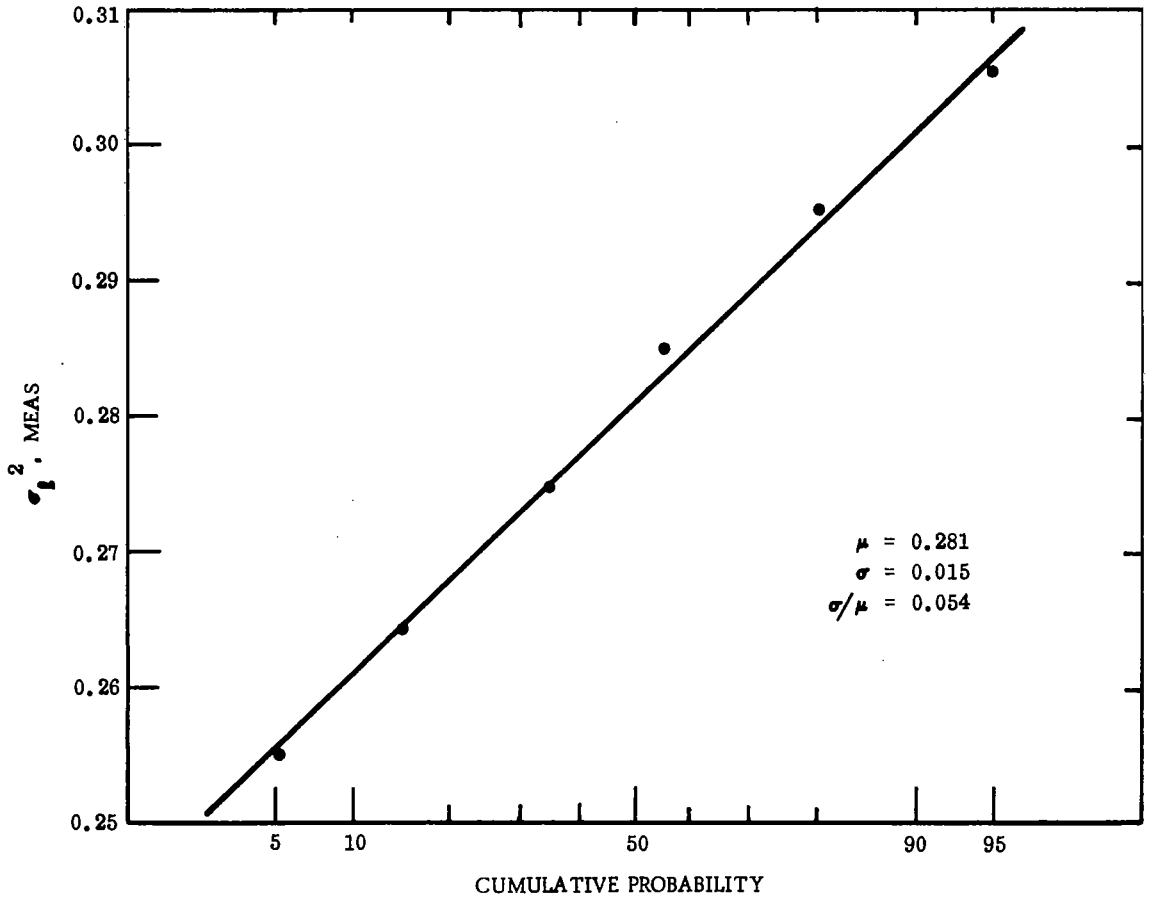

FIGURE 41. Probability Distribution of σ_ℓ^2, meas for 1.15 μ Measurements at 1.5 km. Data taken from Runs No. 1201 - 1220 (7/11/68).

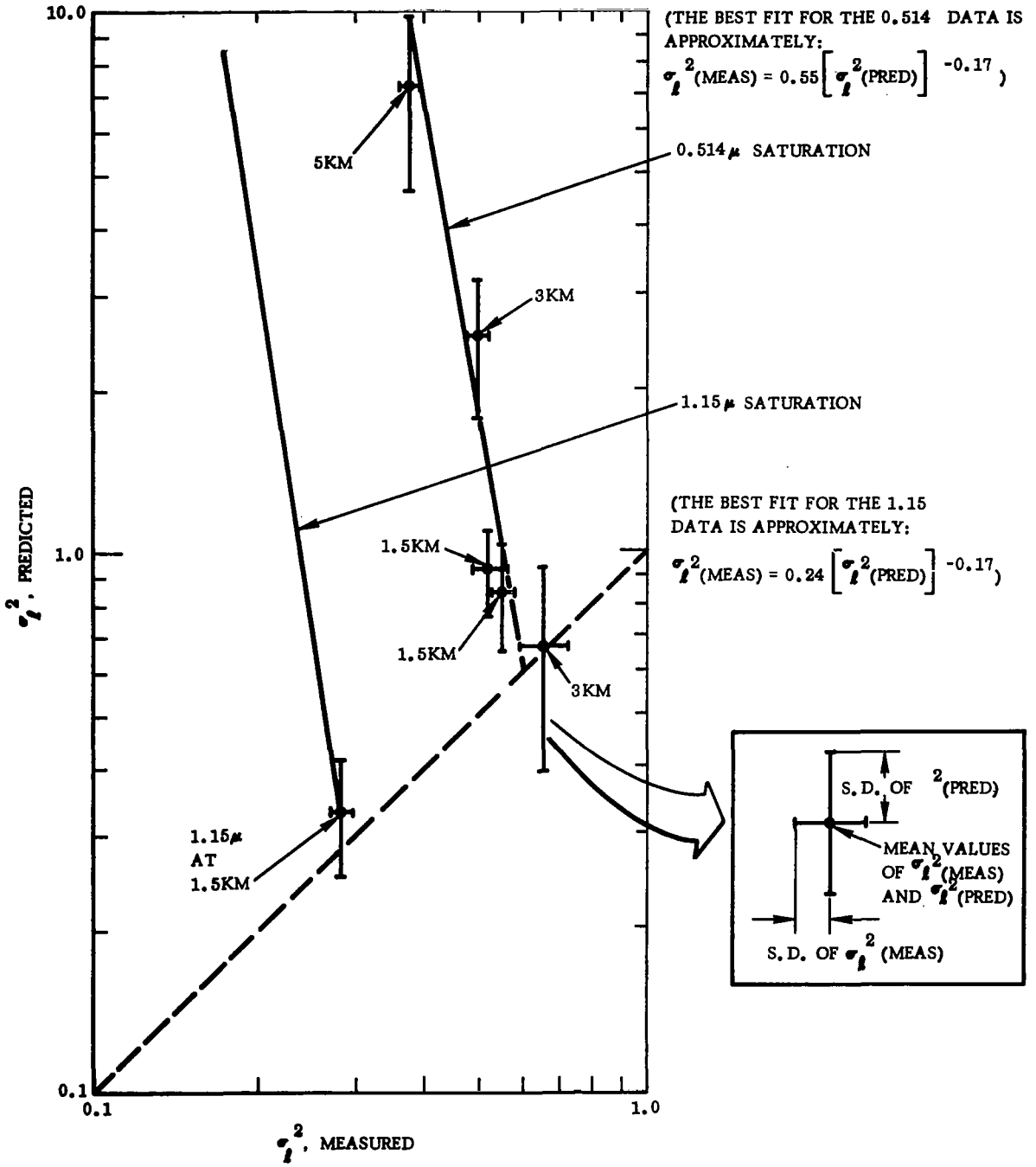

FIGURE 42. Measured vs. Predicted σ_ℓ^2 for Conditions of Scintillation Saturation at 0.514 μ and 1.15 μ. Data taken at ranges of 1.5, 3.0, and 5.0 km. Data Runs No. 406 - 505, 506 - 514, 1201 - 1220, 1301 - 1307 and 1308 - 1311. Predictions based on 0.633 μ σ_ℓ^2 measured for 0.2 km.

indicate the mean (with standard deviations indicated) for measured and predicted values of σ_ℓ^2. The dotted line shows the ideal relationship based on Rytov Approximation in the absence of saturation of scintillation. All of the data points except for the one at (σ_ℓ^2) pred = 0.33, (σ_ℓ^2) meas = 0.28, which is clearly marked as being for 1.15 μ radiation, apply to the 0.514 μ Argon laser propagation. The data shows a very clear trend of decreasing with increasing predicted value. On the log-log plot, we have fit a straight line to the 0.514 μ saturation data, shown by the heavy line labeled "0.514 μ-saturation." The equation for this line is

$$(\sigma_\ell^2)_{,\text{meas}} = 0.55\left[(\sigma_\ell^2)_{\text{pred}}\right]^{-0.17}, \text{ (for 0.514 } \mu\text{-saturation)}. \tag{11}$$

The single data point for the 1.15 μ radiation, indicates saturation at a much lower level. With the paucity of data on 1.15 μ scintilation saturation, it is difficult to draw firm conclusions. The line labeled "1.15 μ-saturation" was drawn through this single data point with the assumption that the 1.15 μ-saturation, though occurring at a lower value than 0.514 μ-saturation, shows the same dependence on predicted values of σ_ℓ^2, i.e., the -0.17 power dependence. This is clearly an extrapolation, which, while it might be true, must be recognized as only a, perhaps reasonable, conjecture at this time. The equation that goes with this fit is

$$(\sigma_\ell^2)_{\text{meas}} = 0.24\left[(\sigma_\ell^2)_{\text{pred}}\right]^{-0.17}, \text{ (for 1.15 } \mu\text{-saturation)}. \tag{12}$$

We have gathered up all of the values of σ_ℓ^2 measured and predicted, both in the saturation and unsaturated range 0.514 μ and 1.15 μ sources, with all predicted values based on the (0.633 μ, 200 meter) reference measurement and have plotted measured versus predicted values for $\sigma_\ell^2(0.514, R)$ in Figure 43 and plotted the measured versus predicted values for $\sigma_\ell^2(1.15, R)$ in Figure 44. In each case, we show both the ideal unsaturated scintillation curve based on the Rytov Approximation, and the saturation curve that we obtained by fitting the data in Figure 42 with the -0.17 power dependence on the predicted value of σ_ℓ^2.

To the extent that we can judge from the data, the two curves of saturation and of the unsaturated Rytov Theory adequately describe the data. The real theoretical problem will be to explain the origin of the saturation curve, its -0.17 power

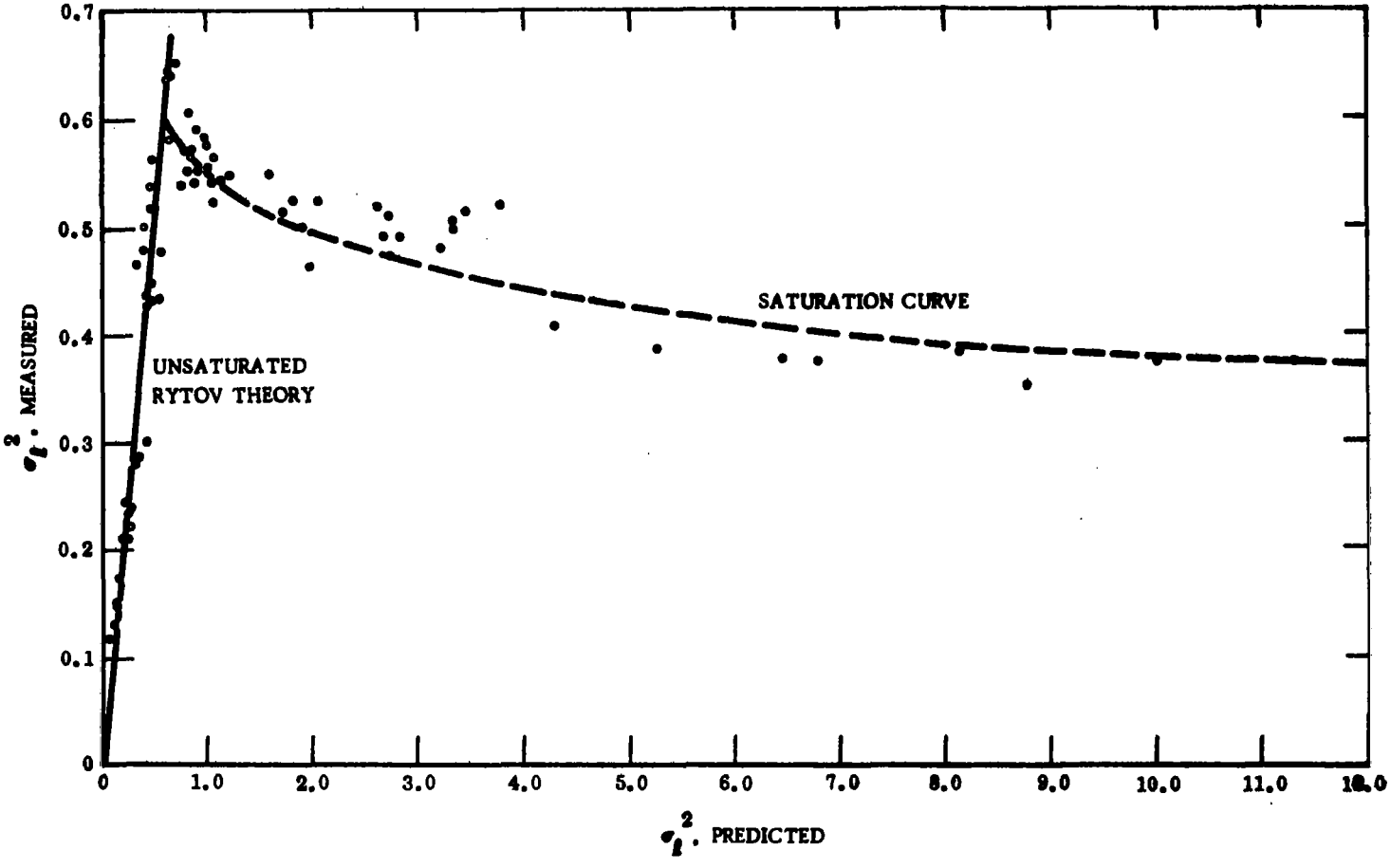

FIGURE 43. Measured vs. Predicted σ_ℓ^2 for 0.514 μ at 0.5, 1.0, 1.5, 3.0, and 5.0 km. Data Runs No. 101 - 115 (5/24/68), No. 308 - 405 (5/30/68), No. 406 - 514 (5/31/68), No. 903 - 1008 (7/3/68), and No. 1201 - 1220 (7/11/68). Predictions based on 0.633 μ σ_ℓ^2 measured for 0.2 km.

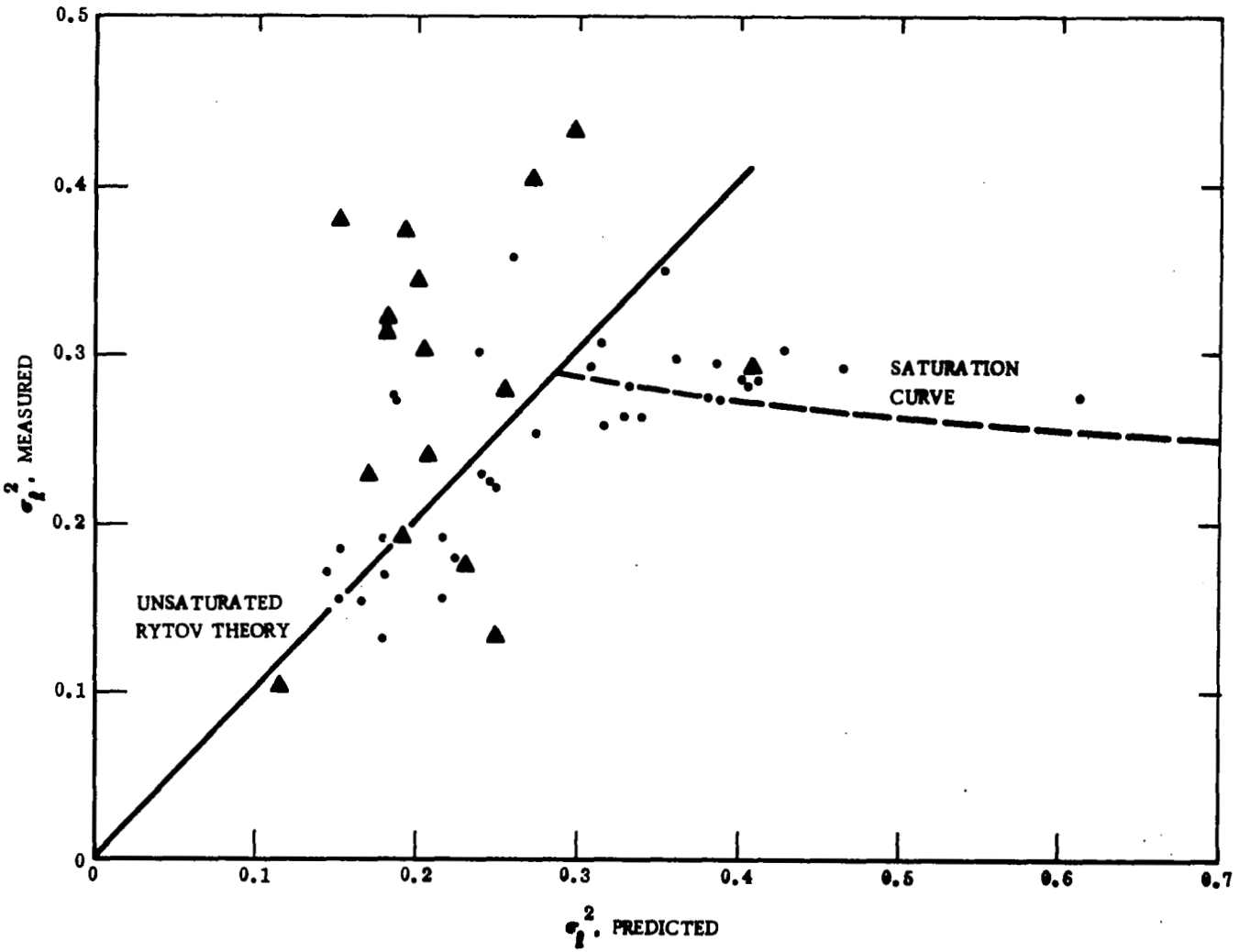

FIGURE 44. Measured vs. Predicted σ_ℓ^2 for 1.15 μ at 1.0 and 1.5 km. Data Runs No. 308 - 405 (5/30/68), No. 1101 - 1118 (7/10/68), and No. 1201 - 1220 (7/11/68). Predictions based on $0.633\mu\,\sigma_\ell^2$ measured for 0.2 km. (The points indicated by Δ are those data taken from Runs No. 1101 - 1118 which we suspect were affected by non-uniform turbulence conditions.)

dependence on the predicted value[∓] and its apparent path length - wavelength dependence. Until this is done it is unlikely that any progress on the whole host of related problems such as covariance of scintillation of two points, or the nature of wave front distortion for saturation scintillation, can be made theoretically.

12. Log-Normal Distribution

It is generally accepted that scintillation has a log-normal probability distribution, though recently there has been some question raised as to the possibility that the distribution is Rayleigh when the scintillation is saturated.[6] Though it was not originally expected, experimental evidence indicates that even when the collector aperture is large enough to produce an averaging of scintillation, the probability distribution is still log-normal.[7] The recent work of Mitchel[8] provides a theoretical explanation of some aspects of this.

To assess the accuracy of treating scintillation as having a log-normal distribution and particularly to evaluate the Rayleigh distribution hypothesis, we examine in detail a series of representative probability distributions obtained during the measurement program.

In Figure 45, we see the probability distribution for 0.633 μ radiation over the 200 meter path. The ordinate is a logarithmic scale in relative intensity and the abcissa has a scale of "standard deviations" corresponding to cumulative probabilities for a Gaussian distribution. As a consequence, on this and the next five figures, a straight line will correspond to a log-normal probability distribution. In examining Figure 45, it is interesting to note how well the data conforms to a log-normal distribution, with no significant deviations over a range of almost 7.5 standard deviations. This range, however, corresponds to an intensity range of just under one decade.

To study the range of accuracy of the log-normal distribution in terms of the number of decades of relative intensity over which it can be confirmed, we examine the data of Figures 46 and 47. Both measurements were made with a 0.514 μ radiation source at a 1000 meter range. The measurement times were very close to each other

---

[∓]Although the data fit was to a -0.17 power, it is equally reasonable to imagine that a more accurate determination would have found a -1/5 = -0.20 rather than the -1/6 = -0.17 power dependence.

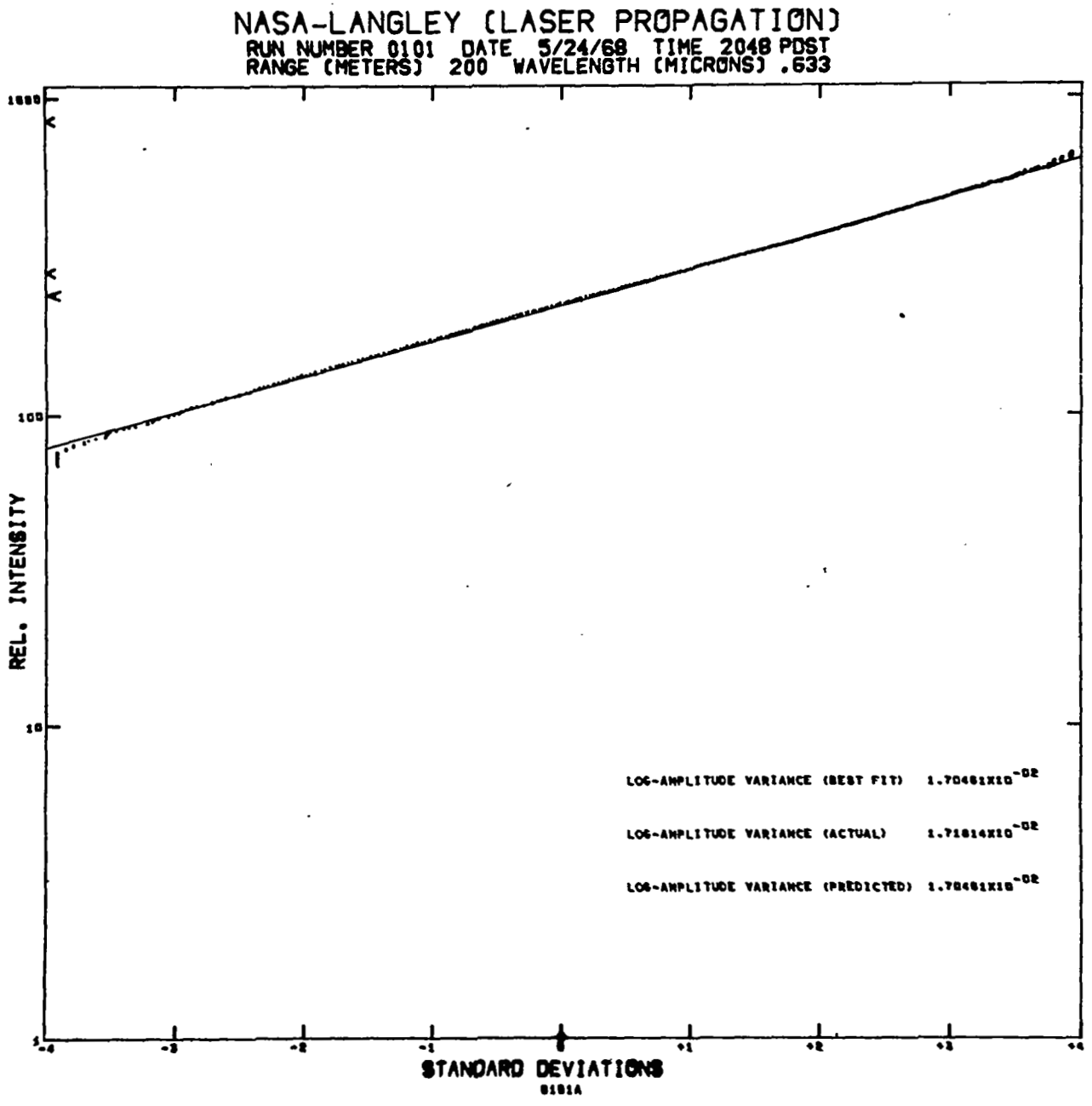

FIGURE 45. Probability Distribution of Scintillation for 0.633 μ "Point" Collector at 0.2 km Range - Run No. 101.

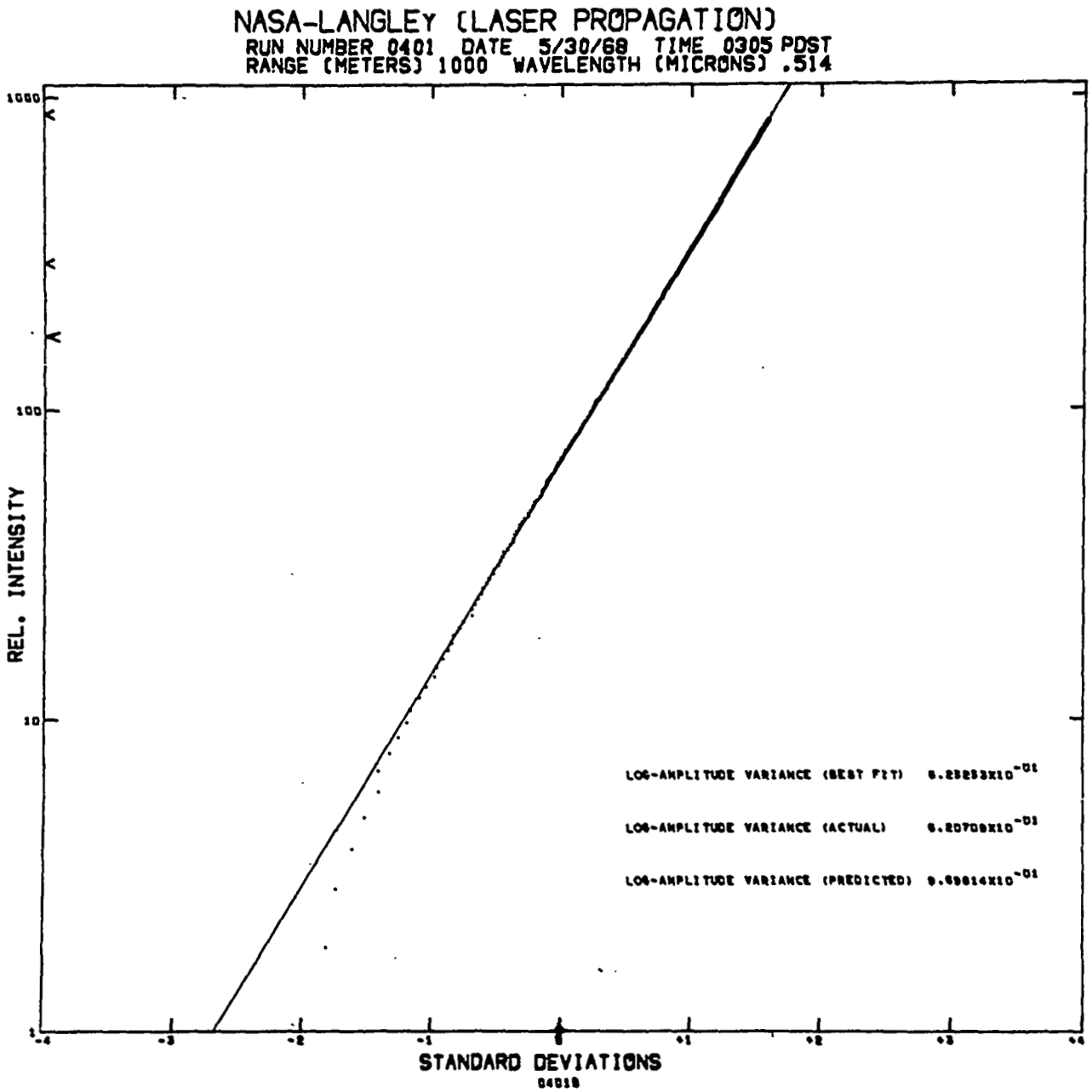

FIGURE 46. Probability Distribution of Scintillation for 0.514 μ "Point" Collector at 1.0 km Range - Run No. 401.

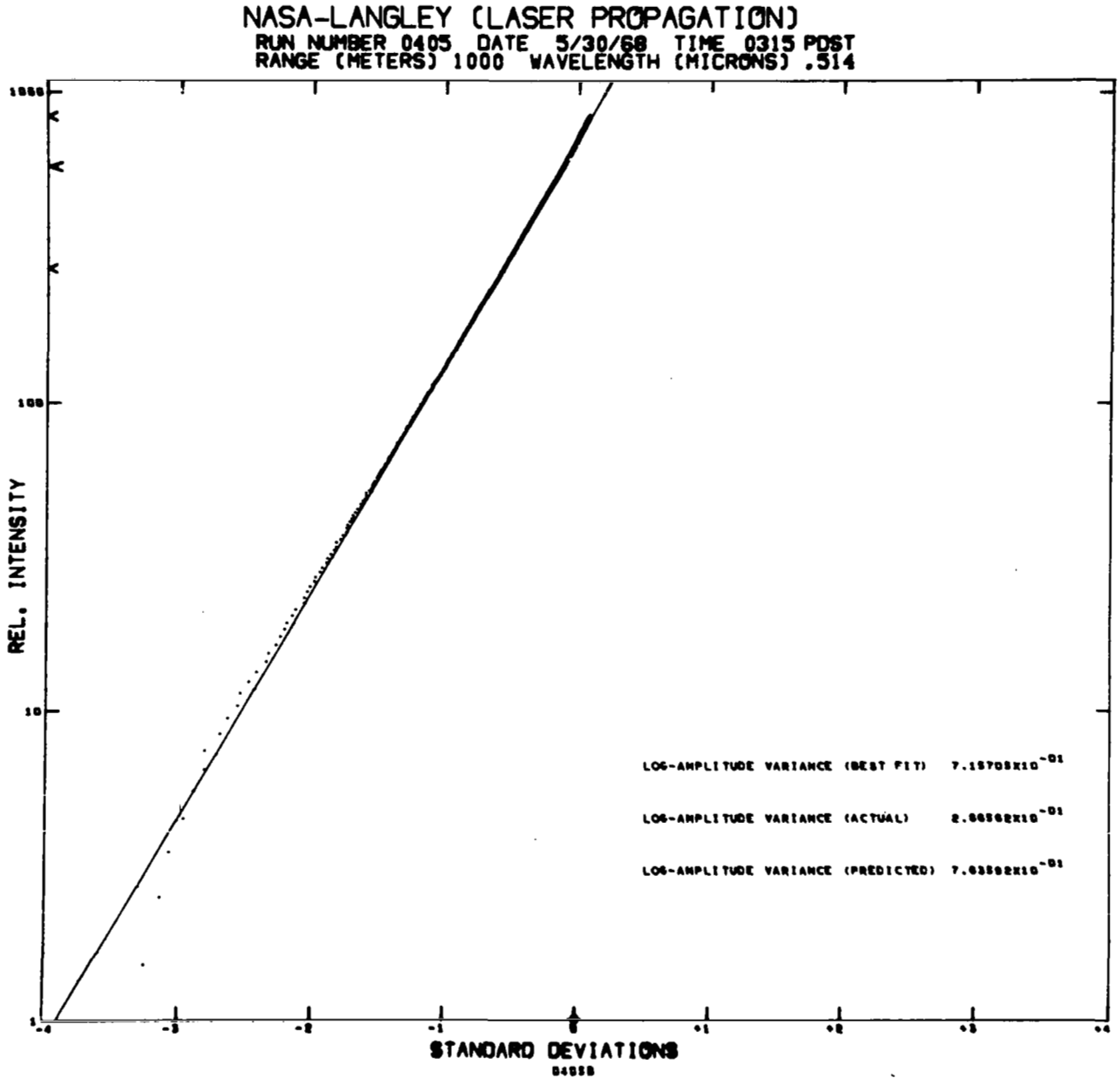

FIGURE 47. Probability Distribution of Scintillation for 0.514 μ "Point" Collector at 1.0 km Range - Run No. 405.

(0305 PDST and 0315 PDST) with approximately a factor of 10 attenuator placed over the collector for the data in Figure 46. This meant that the system noise would be comparable to the signal level closer to the 50 percent level, as can be seen by the fact that in Figure 46 the data points break away from the straight line (because of noise contamination of the data) at about -1.5 standard deviations, while in Figure 47 this occurs at about -3.0 standard deviations -- but it also means that saturation of the data channel (corresponding to the upper value abrupt end of the data points) occurs at about +1.75 standard deviation in Figure 46, while in Figure 47 it is at only +0.25 standard deviations. Recognizing that the relative intensities at the 50 percent level (zero standard deviations) can be equated between the two figures, we see that the composite distribution verifies the accuracy of the log-normal distribution at least over three decades, though in this case (unlike the data of Figure 45) it only corresponds to a range of 4.75 standard deviations.

The data in Figure 48 was taken with the 0.514 μ sources operating over a 3000 meter range and corresponds to saturation of scintillation. The accuracy with which the data fits the log-normal distribution, over about 4.0 standard deviations and about two decades of intensity, is fairly eloquent evidence that the probability distribution of saturated scintillation is log-normal rather than Rayleigh.

The data in Figures 49 and 50 explore the probability distribution for saturated scintillation when the collection aperture is not small and complement the data in reference 7. For Figure 49, the aperture diameter was 6 cm and for Figure 50 it was 10 cm. Both measurements were made with the 0.514 μ source operating over a 3000 meter range. The distributions are seen to be reasonably close to log-normal, though noticeable (and probably quite real) deviations of minor magnitude can be seen at the higher intensity values.

13. Aperture Averaging

During Data Runs No. 308 - 405 measurements of the scintillation of a 0.514 μ source over a 1000 meter range was made with both a point collector (very small diameter) and along side of it, a variable, finite size, diameter collector. Each of the collectors produced a log-normally distributed signal from which a log-amplitude variance $\sigma_{\ell,\text{aper}}^2$ or $\sigma_{\ell,\text{point}}^2$ was calculated. In Figure 51, we show the ratio $\sigma_{\ell,\text{aper}}^2/\sigma_{\ell,\text{point}}^2$ as a function of aperture diameter. The ratio, $(\sigma_{\ell,\text{aper}}^2/\sigma_{\ell,\text{point}}^2)$ may be

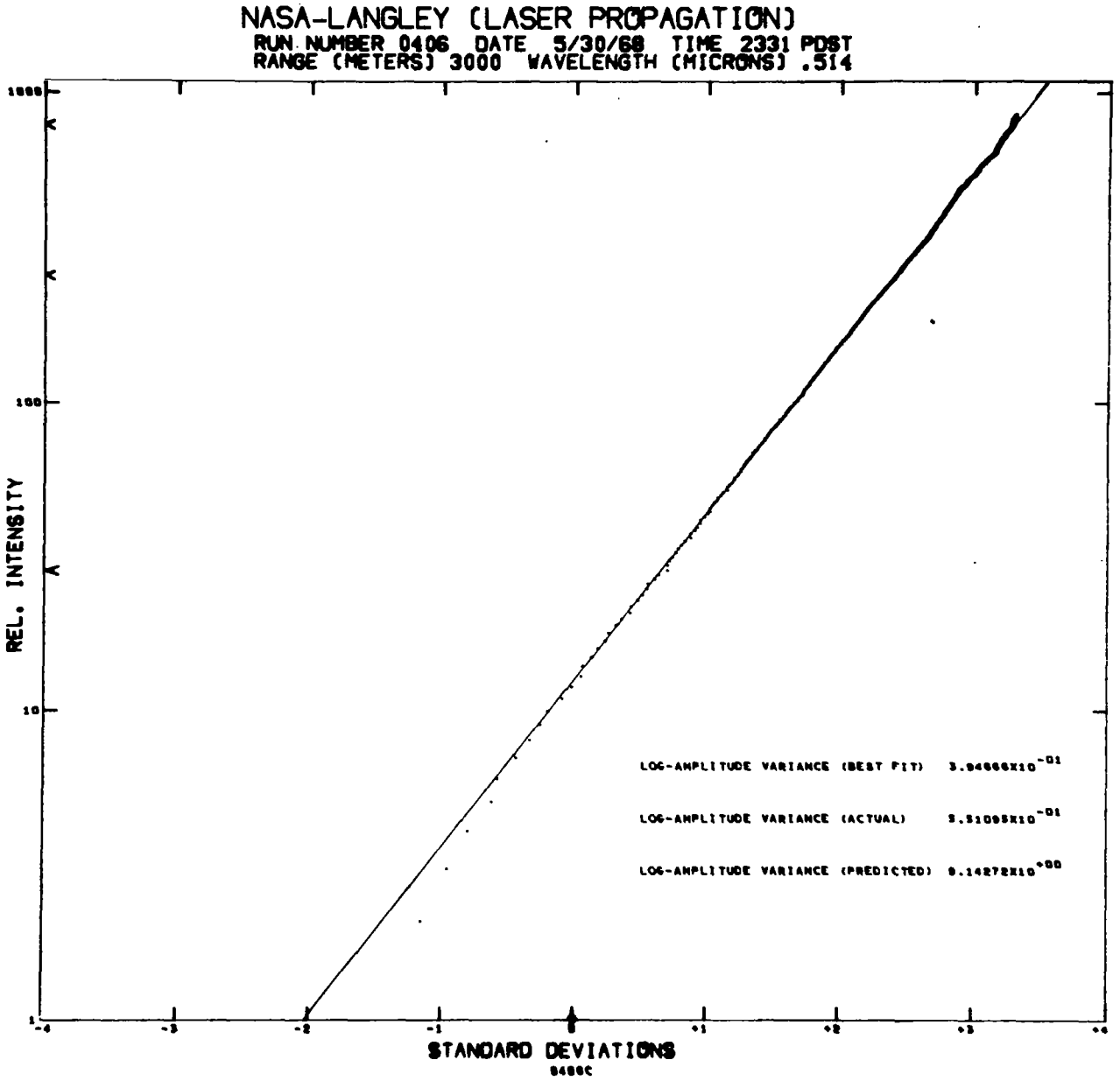

FIGURE 48. Probability Distribution of Scintillation for 0.514 μ "Point" Collector at 3.0 km Range - Run No. 406.

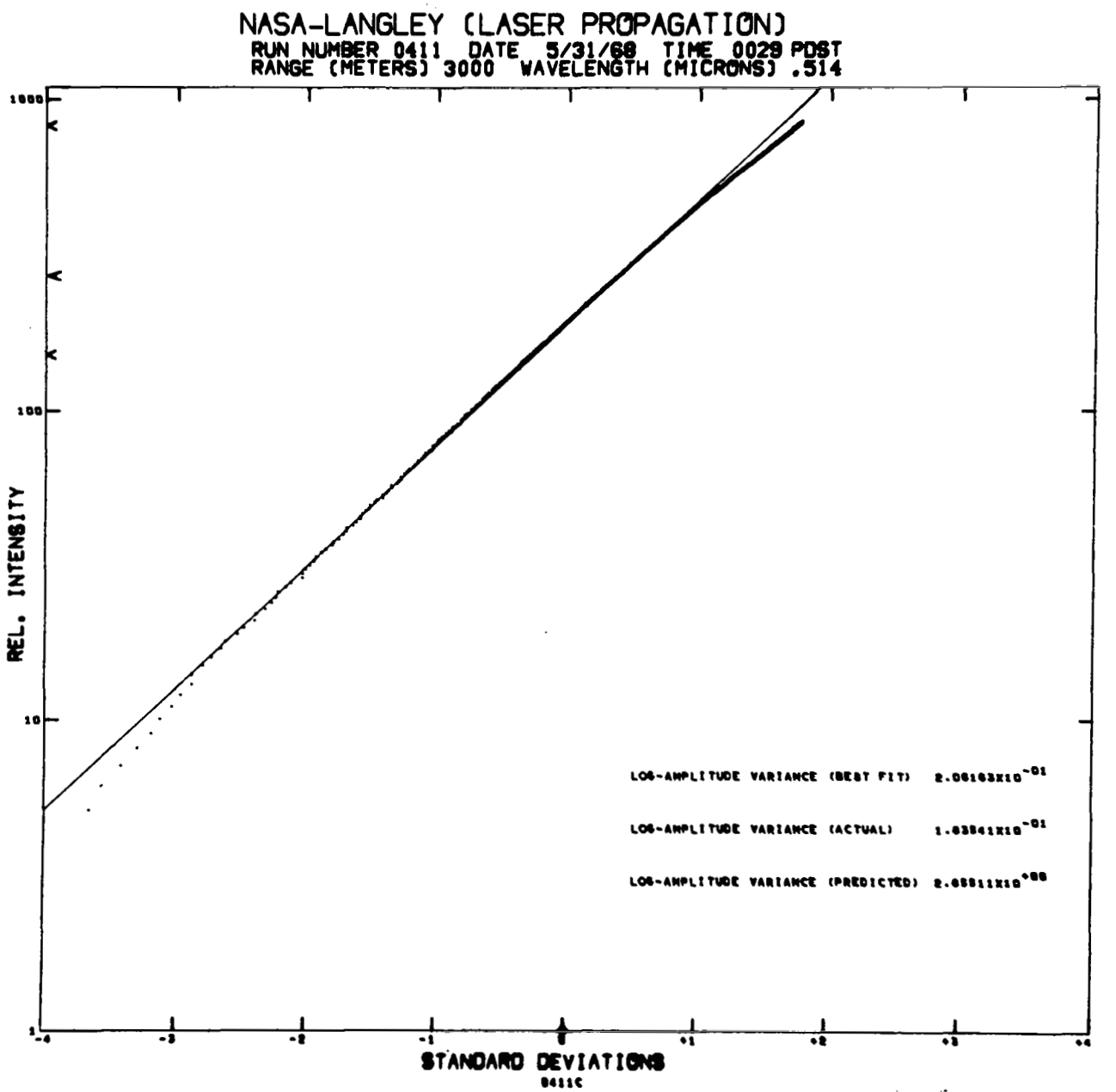

FIGURE 49. Probability Distribution of Scintillation for 0.514 μ 6-cm Aperture at 3.0 km Range - Run No. 411.

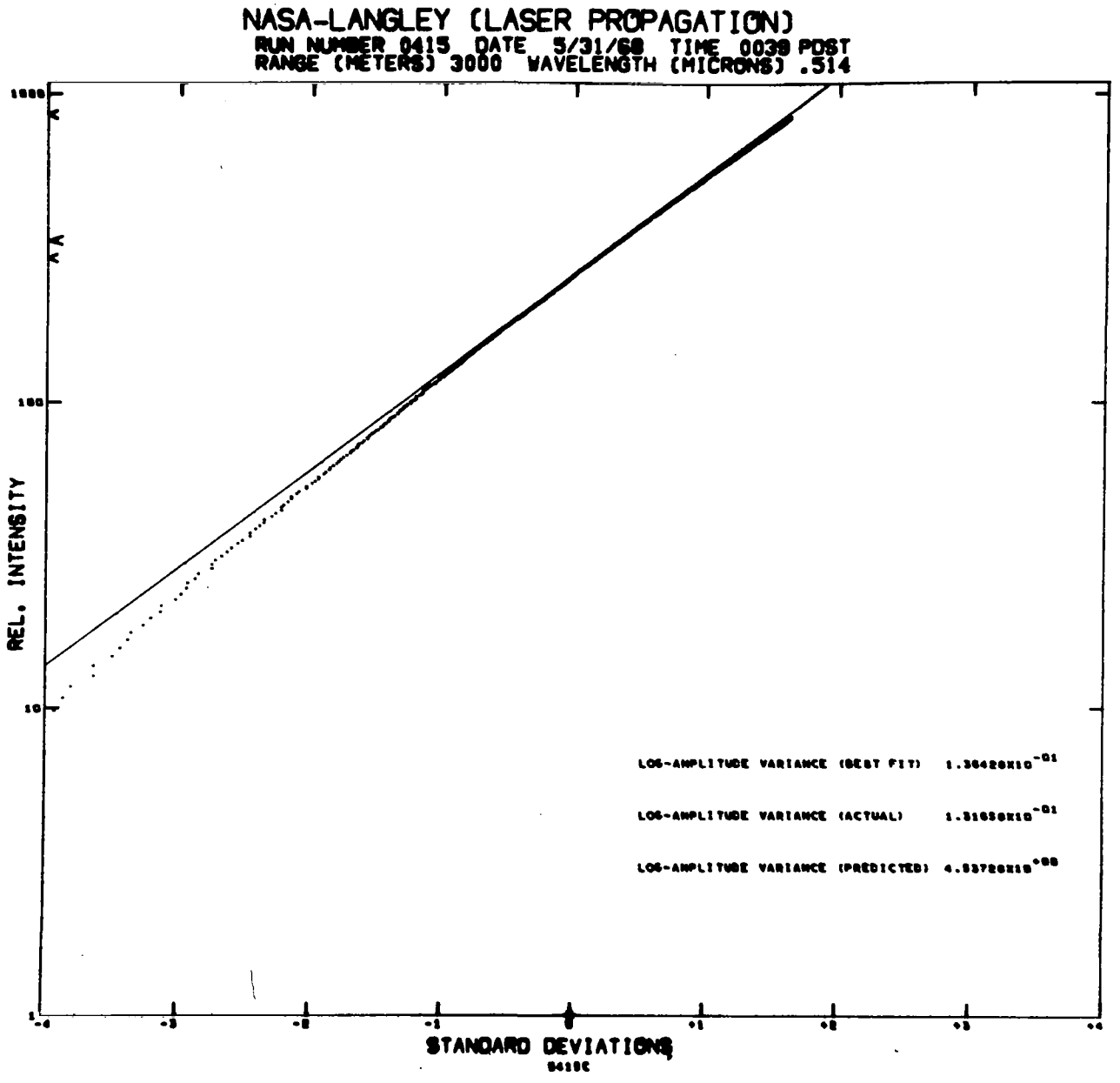

FIGURE 50. Probability Distribution of Scintillation for 0.514 μ 10-cm Aperture at 3.0 km Range - Run No. 415.

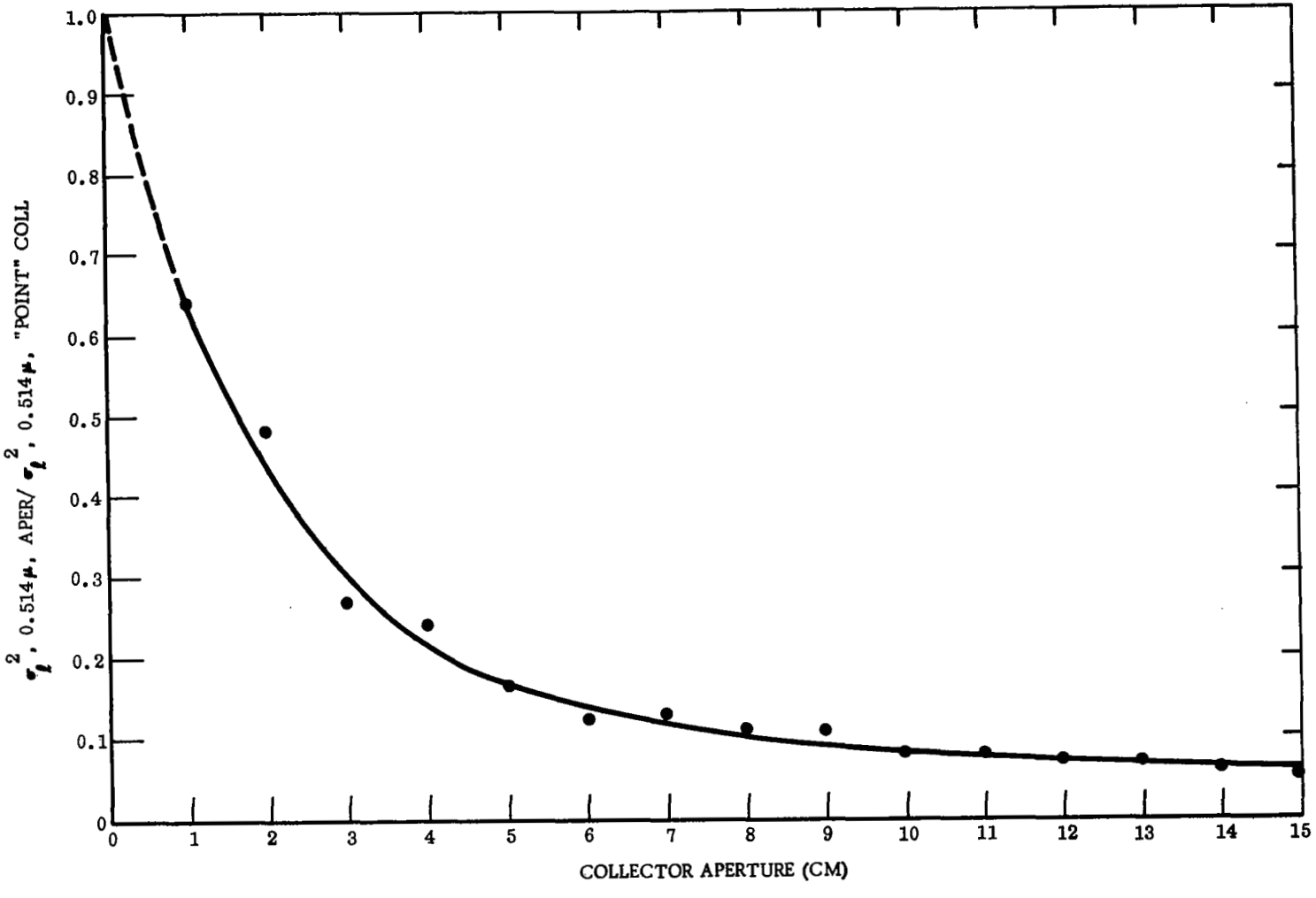

FIGURE 51. Ratio of Large Aperture σ_l^2 to "Point" Collector σ_l^2 vs. Large Aperture Diameter for 0.514 μ at 1.0 km. Data Runs No. 308 - 405 (5/30/68).

considered to be a measure of the aperture averaging factor and as such provides information on the log-amplitude covariance. The failure of the ratio to approach zero for large aperture diameters may be attributed to the use of a laser source rather than a point source, as discussed in reference 7. The rapid decrease of the ratio in the first several centimeters, as shown in Figure 51, is entirely compatible with the Fresnal diffraction length $\sqrt{\lambda Z} = 2.27 \times 10^{-2}$ meters.

In Figures 52 and 53, we show the same sort of data as in Figures 51, except that the data taking range was 3000 meters for Figure 52 and 5000 meters for Figure 53. In these two cases, the scintillation was saturated. The most remarkable difference, in contrast to the unsaturated scintillation data, is the very large residual value of the ratio $(\sigma_\ell^2, _{aper}/\sigma_\ell^2, _{point})$ for large aperture diameters. This is highlighted by Figure 54 which shows the curves for all three sets superimposed. This result seems to indicate that under saturated scintillation conditions, there is more of the same sort of effect that caused the laser beam to have a correlation at ranges larger than expected for a point source. This is a rather interesting point and is worth further development, at least as a conjecture.

The reason laser scintillation can show correlation over larger ranges than does point source scintillation is that the laser diameter, D, permits the definition of a second diffraction length $\lambda Z/D$, in addition to the Fresnel length, $\sqrt{\lambda Z}$, to act as a dimensional factor in any expression for the log-amplitude covariance function. In considering the occurrence of saturation of scintillation at different values of σ_ℓ^2 for different wavelengths, we are faced with the problem of finding enough length factors for at least a dimensional analysis of the problems. The three factors immediately available for consideration are λ, the wavelength; Z, the range; and C_N^2, the refractive-index structure constant. The magnitude of each of these is too radically different from the other two, (and C_N^2 has the dimensions of length to the minus two-thirds power rather than simply length) to permit meaningful comparison. Instead of comparing λ, Z, and C_N^2, it is more meaningful to compare ρ_o, the Fresnel diffraction length,

$$\rho_o = (\lambda Z)^{1/2} , \qquad (13)$$

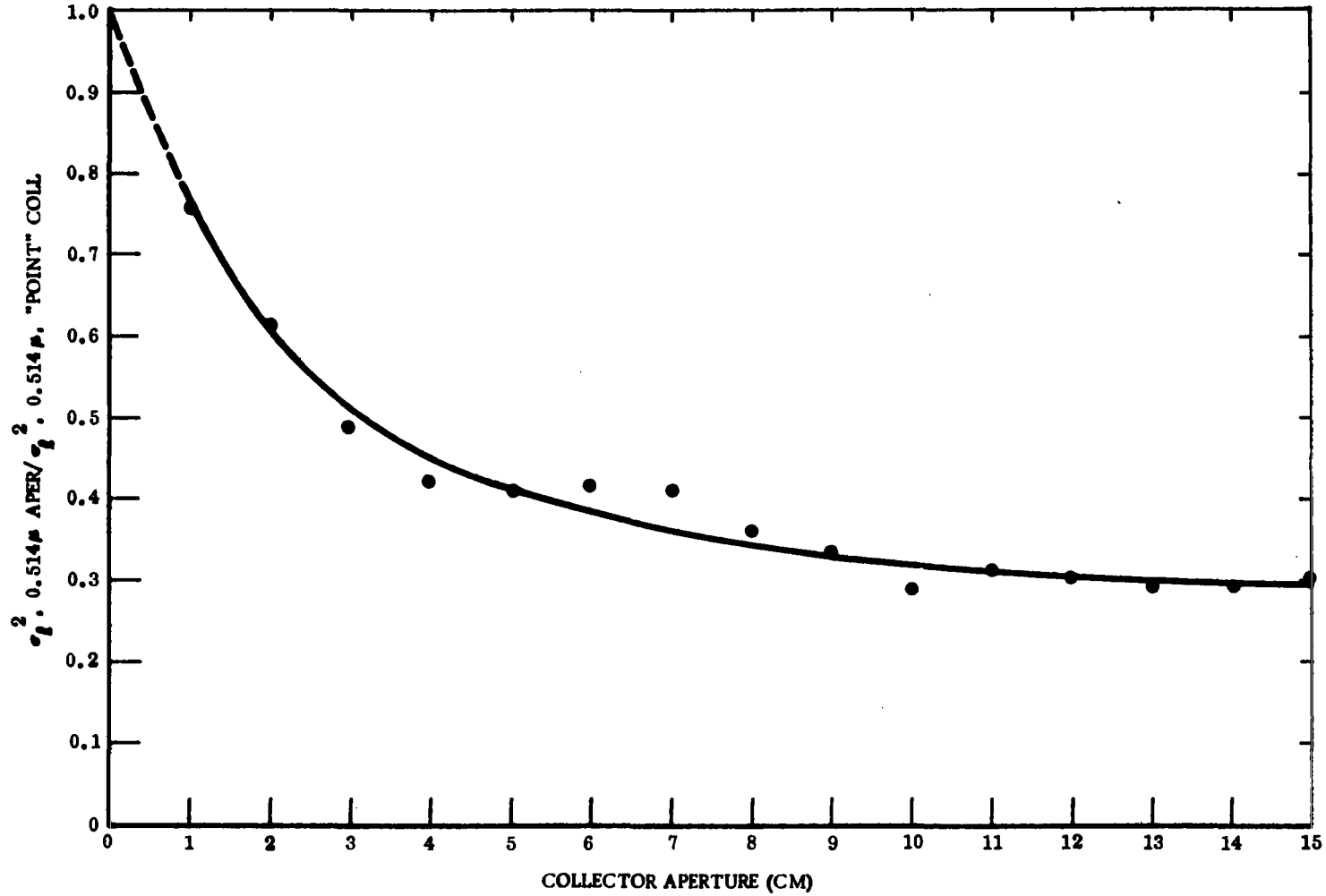

FIGURE 52. Ratio of Large Aperture σ_ℓ^2 to "Point" Collector σ_ℓ^2 vs. Large Aperture Diameter for 0.514 μ at 3.0 km. Data Runs No. 406 - 505 (5/31/68).

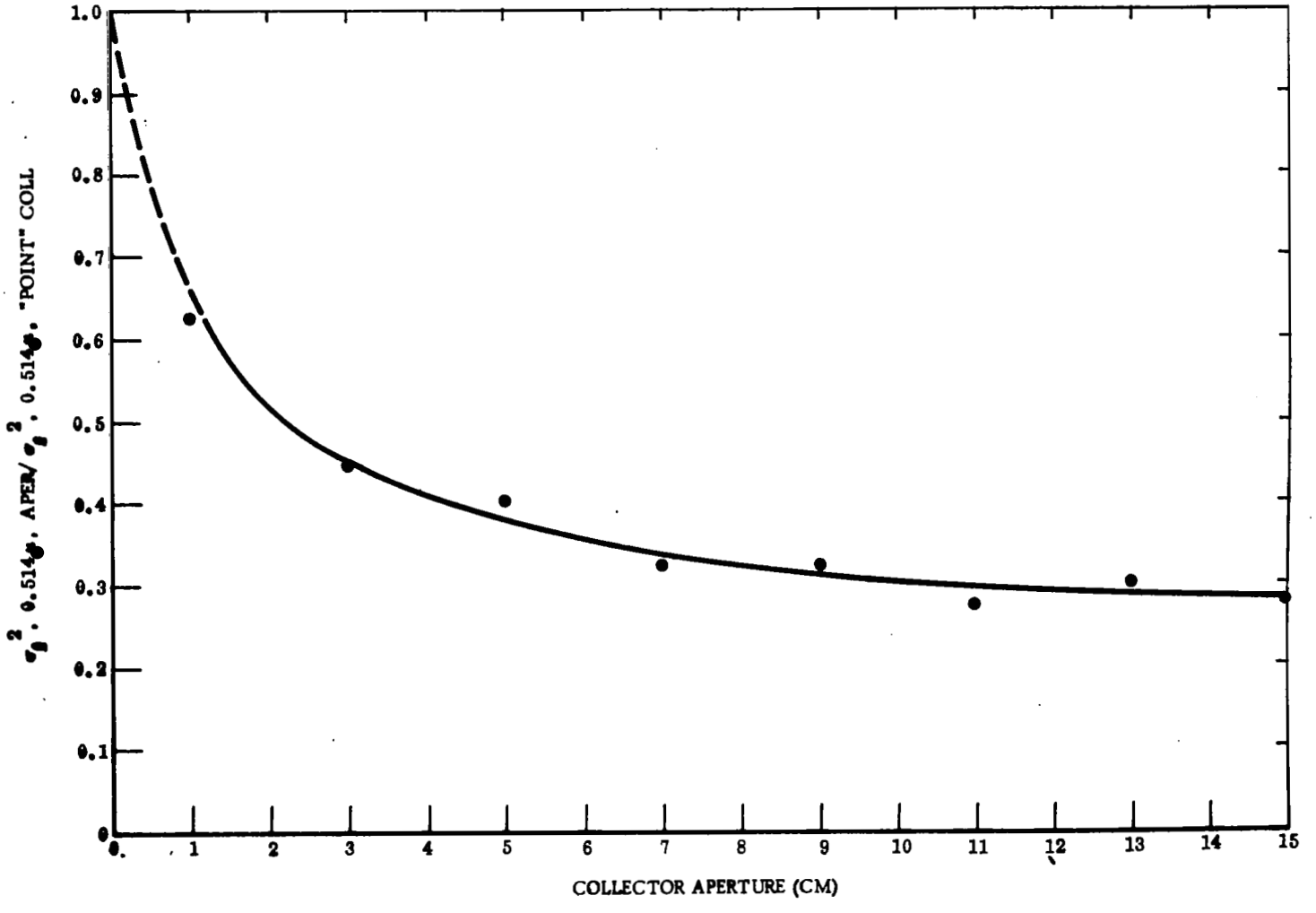

FIGURE 53. Ratio of Large Aperture σ_ℓ^2 to "Point" Collector σ_ℓ^2 vs. Large Aperture Diameter for 0.514 μ at 5.0 km. Data Runs No. 506 - 514 (5/31/68).

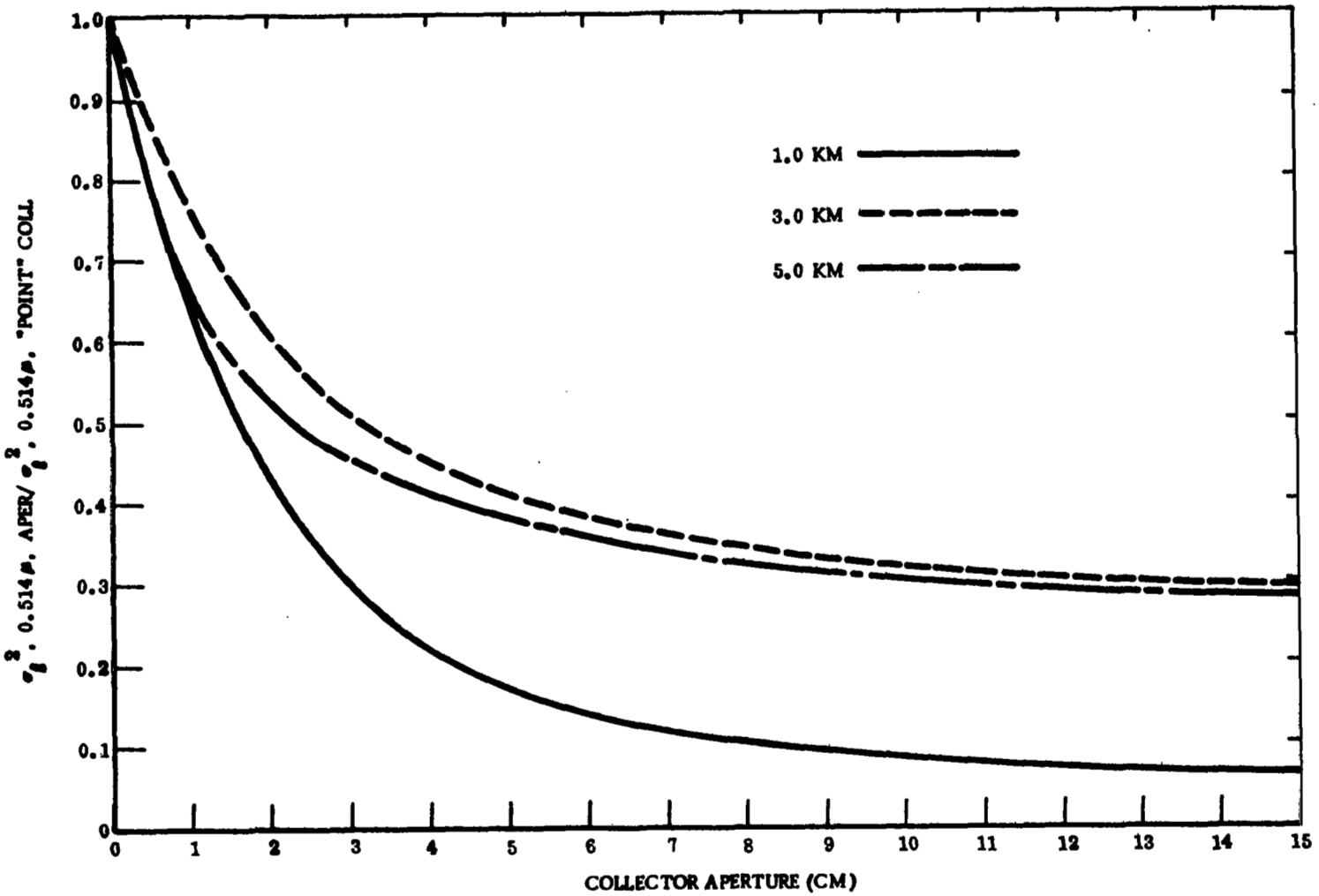

FIGURE 54. Ratio of Large Aperture σ_ℓ^2 to "Point" Collector σ_ℓ^2 vs. Large Aperture Diameter for 0.514 μ at 1.0, 3.0, and 5.0 km. Data Runs No. 308 - 405 (5/30/68), 406 - 505 (5/31/68), and 506 - 514 (5/31/68).

r_o, the wave front distortion coherence length,[9]

$$r_o = 0.19\lambda^{6/5} Z^{-3/5} (C_N^2)^{-3/5} \tag{14}$$

and any one of the original three, say λ or Z. We note that ρ_o and r_o are quite comparable in length so that their ratio could provide a quite meaningful handle on the problem of why different wavelengths saturate at different values of σ_ℓ^2 -- except that $(\rho_o/r_o)^{5/3}$ is directly proportional to the predicted value of σ_ℓ^2 and so the ratio ρ_o/r_o can not be used to explain why different values of σ_ℓ^2. Unfortunately, the third quantity, whether we take it as λ, Z, or even C_N^2 is not comparable to either ρ_o or r_o and so can not be used to provide a dimensional basis for explaining the facts observed. This is where, however, the laser diameter may prove to have great significance. Its dimension is of a size to be meaningfully compared with ρ_o or r_o (or some combination of the two), and so may provide a ratio that can be used to explain what value of σ_ℓ^2 various wavelengths will saturate at. We can only offer this as a conjecture which alleviates serious dimensional analysis difficulty and is suggested by the large-separation log-amplitude covariance behavior under saturatee conditions.

If the source diameter is a factor in determining the level at which σ_ℓ^2 saturates, then it may be that for a point source or an infinite plane wave, there is actually no saturation of scintillation. This last suggestion must be recognized as pure conjecture at this point, with really no evidence to back it up. In fact, in a certain sense, it is in conflict with the results of Appendix B. Nonetheless, it bares consideration in future thinking on this subject.

14. 10.6 μ Scintillation

During Data Runs No. 1101 - 1118, data on the scintillation of 10.6 μ radiation propagating over a 1000 meter path was obtained. Simultaneously, measurements were made with a 0.633 μ source over a 200 meter path and with a 1.15 μ source over the same 1000 meter path. It was possible to obtain predictions for σ_ℓ^2 (10.6, 1000) from both the σ_ℓ^2(0.633, 200) and σ_ℓ^2(1.15, 1000) measurements. Before presenting the comparison of measured and predicted values of σ_ℓ^2(10.6, 1000) let us first look at the 10.6 μ scintillation probability distribution. Figures 55 and 56 are two rather typical

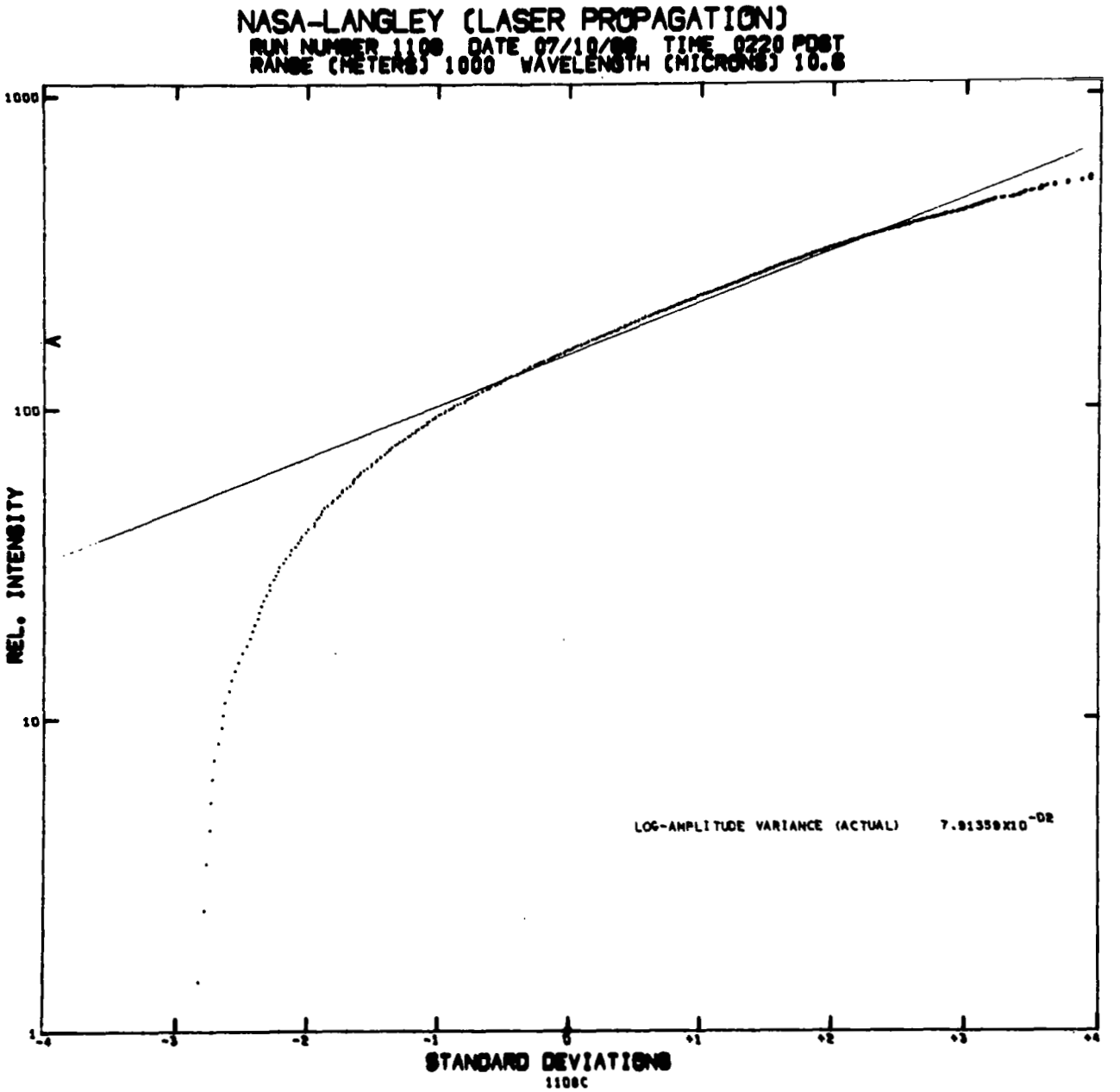

FIGURE 55. Probability Distribution of Scintillation for 10.6 μ "Point" Collector at 1.0 km Range - Run No. 1108.

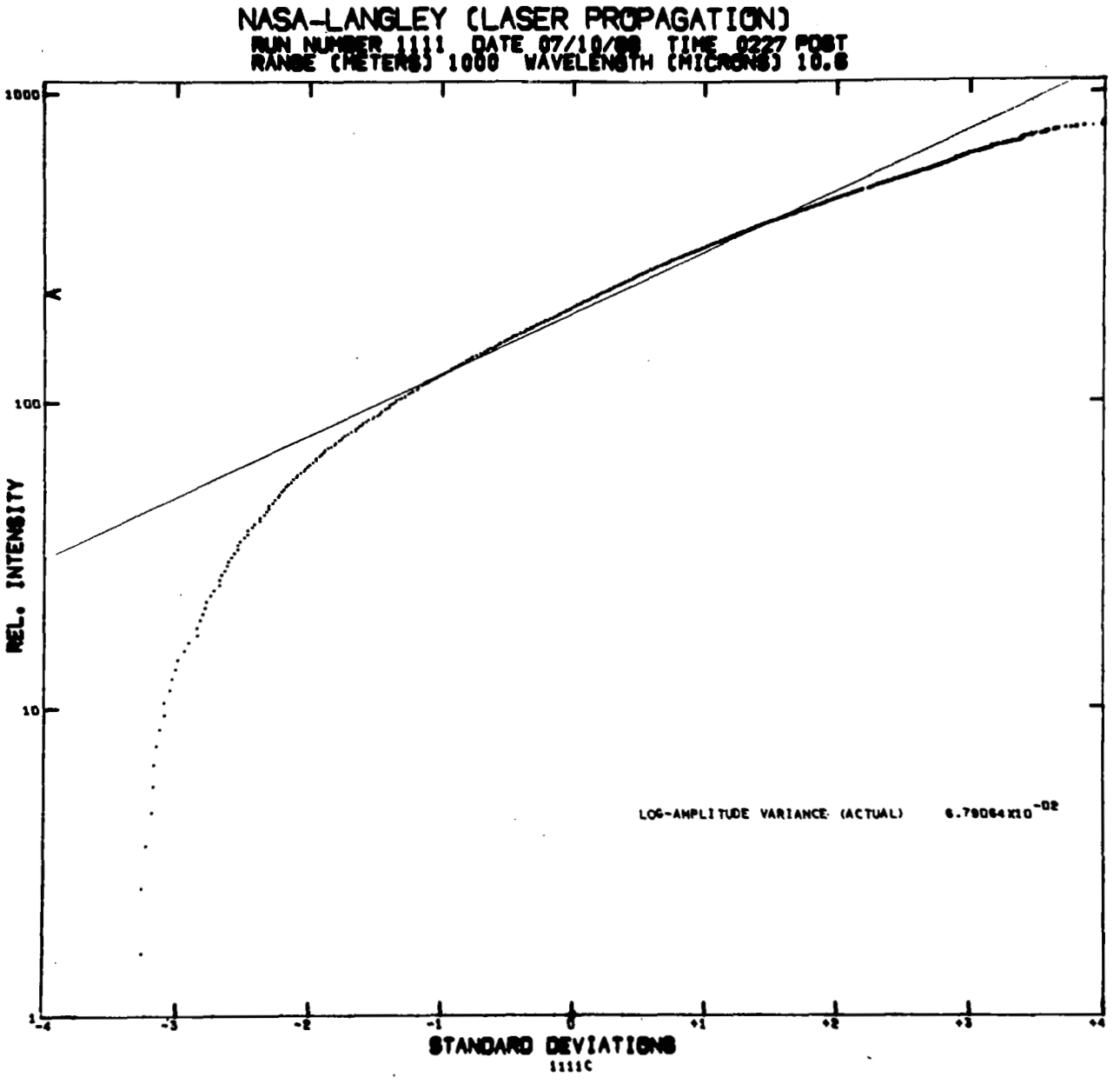

FIGURE 56. Probability Distribution of Scintillation for 10.6 μ "Point" Collector at 1.0 km Range - Run No. 1111.

examples of the probability distributions. Quite clearly, the distributions plotted do not conform well to the hypothesis that they are log-normal. This may be a genuine feature of 10.6 μ scintillation, though it is possible that it is an artifact of the measurement equipment. The roll-off at low intensities could be due to shot noise in the 10 μ Ge:Hg detector we used, and the slight-roll off at high intensities can be explained as due to a non-linearity of the detector at high signal levels. Unfortunately, we do not have the experimental evidence necessary to accept or reject this explanation. With the caveat that the 10.6 μ data may be of a questionable nature, we proceed with the data analysis for these measurements.

In each case, to obtain a measured value for $\sigma_\ell^2(10.6, 1000)$, a straight line fit to the data in middle of the probability range was made by eye, (with the quality of the fit fairly well represented by the straight lines drawn on Figures 55 and 56). The slope of the line was used to calculate $\sigma_\ell^2(10.6, 1000)$.

In Figure 57, we show in the form of a scatter plot a comparison between the measured values of $\sigma_\ell^2(10.6, 1000)$ and the values predicted from the measurement of $\sigma_\ell^2(0.633, 200)$. The agreement with theory is quite obviously poor. The data does not give any indication of saturation of scintillation. In Figure 58, we show the probability distribution of the ratio of measured to predicted values for this data. The distribution is Gaussian, but with a mean value of $\mu = 1.98$ and an exceptionally large rms spread of 58.5 percent. Quite obviously there is something seriously wrong here, either in the data, the data reduction, or the theory.

As further examination of this data, predicted values of $\sigma_\ell^2(10.6, 1000)$ were obtained from the measurements of $\sigma_\ell^2(1.15, 1000)$. The scatter plot for measured versus predicted values is shown in Figure 59. The corresponding probability distribution for the ratio of measured to predicted value is shown in Figure 60. Here the mean value is $\mu = 1.55$ (instead of the ideal value of unity), and the rms spread of the data is 18.7 percent. This is a very noticeable improvement compared to the situation depicted by Figure 58. We believe this is due, not to the change from predictions based on 0.633 μ scintillation to those based on 1.15 μ scintillation, but rather to the fact that in one case the prediction data was obtained from a 200 meter path while

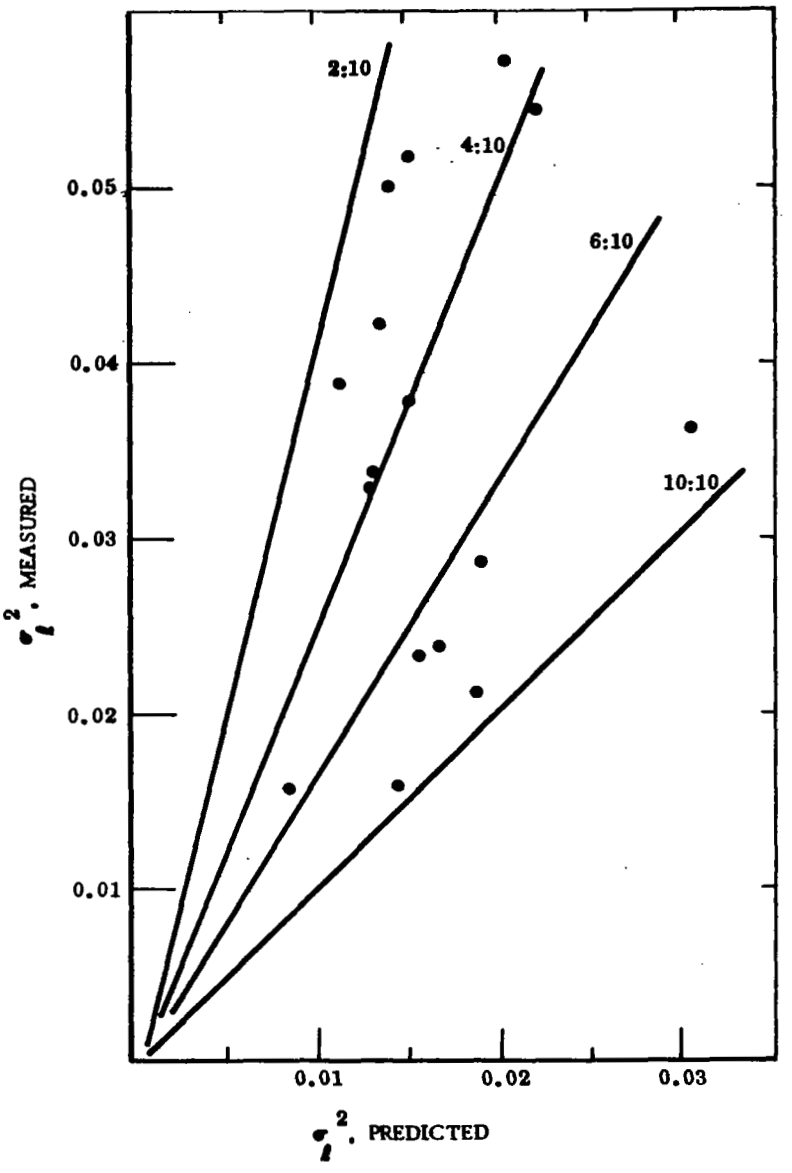

FIGURE 57. Measured vs. Predicted σ_ℓ^2 for 10.6 μ at 1.0 km. Data Runs No. 1101 - 1118 (7/10/68). Predictions based on 0.633 μ σ_ℓ^2 measured for 0.2 km.

CR-1733

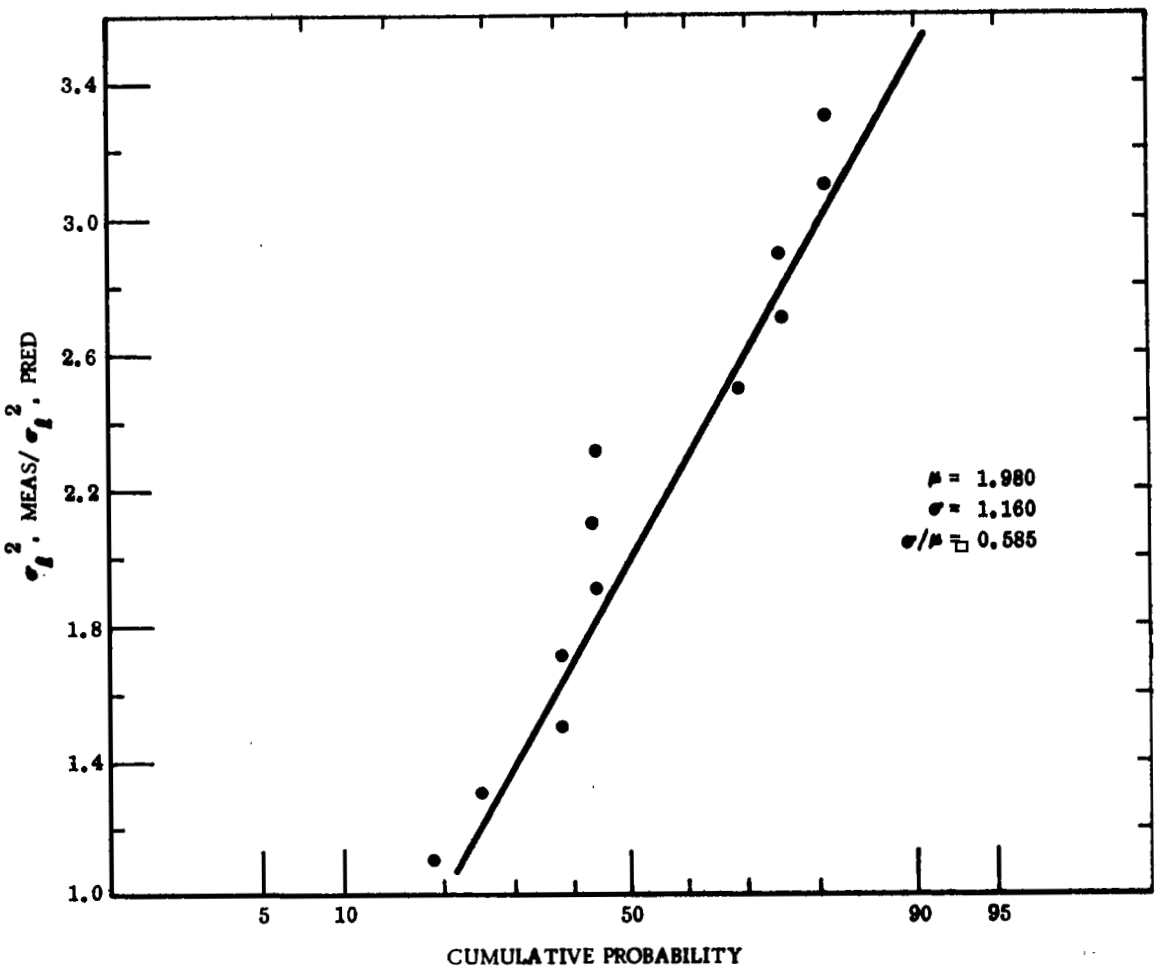

FIGURE 58. Probability Distribution of Ratio, σ_ℓ^2, meas/σ_ℓ^2, pred for 10.6 μ Measurements at 1.0 km. Predictions based on 0.633 μ measurements at 0.2 km. Data taken from Runs No. 1101 - 1118 (7/10/68).

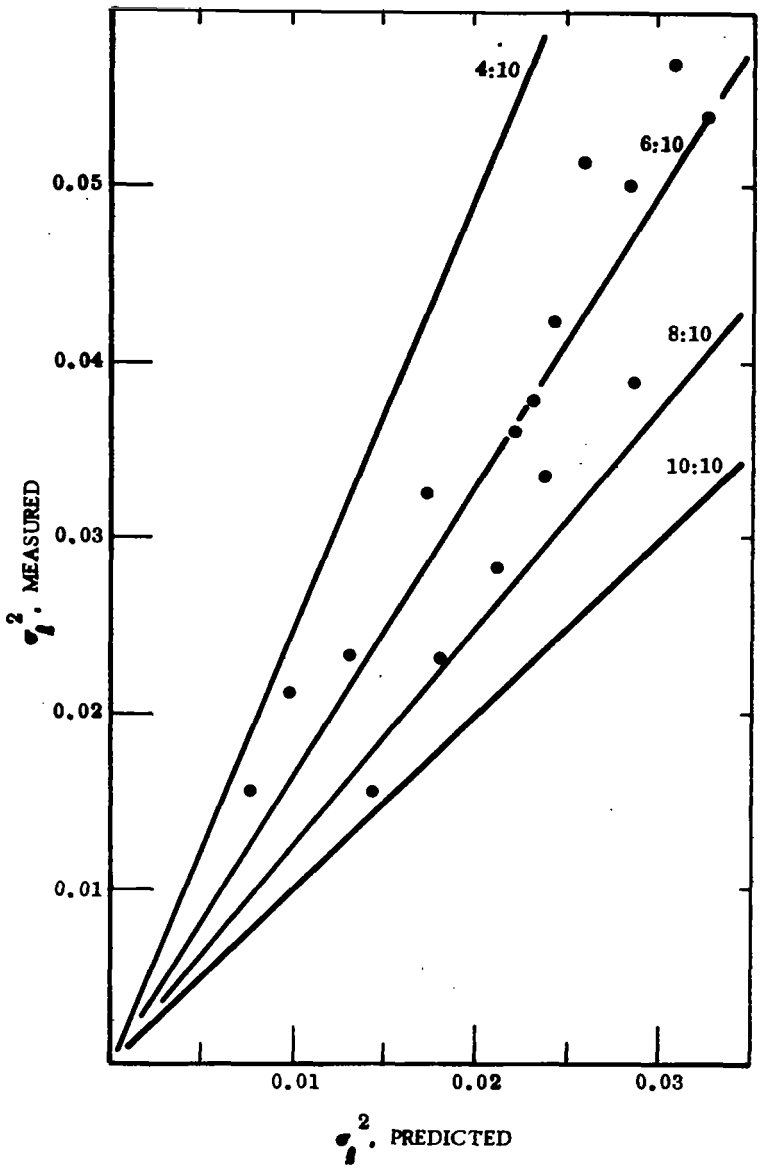

FIGURE 59. Measured vs. Predicted σ_ℓ^2 for 10.6 μ at 1.0 km. Data Runs No. 1101 - 1118 (7/10/68). Predictions based on 1.15 $\mu\sigma_\ell^2$ measured for 1.0 km.

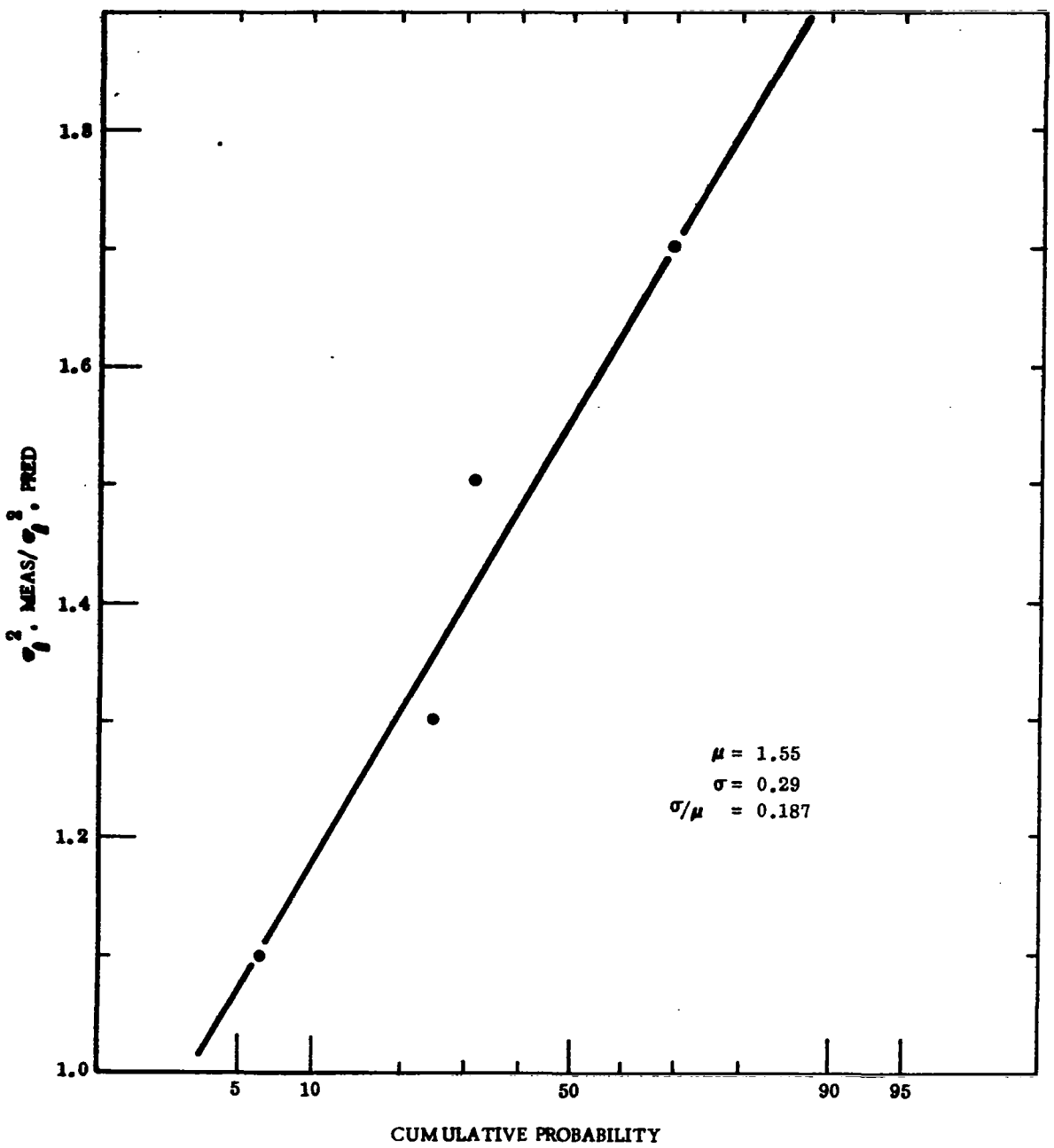

FIGURE 60. Probability Distribution of Ratio, σ_ℓ^2, pred for 10.6 μ Measurements at 1.0 km. Predictions based on 1.15 μ measurements at 1.0 km. Data taken from Runs No. 1101 - 1118 (7/10/68).

in the other case it was obtained from the same 1000 meter path used to obtain the measured 10.6 μ data. It is reasonable to conjecture that turbulence conditions were not normal during this measurement period and that this is the cause of all the anomalies in the data. In praticular, the conditions were not statistically uniform over the path -- hence, the difference between the quality obtained with the two different prediction path lengths. It is reasonable to believe that these same anomalous conditions in the turbulence were able to produce the unusual probability distributions we see in Figure 55 and 56. It is unfortunate, however, that the only time 10.6 μ scintillation data was taken the meteorological conditions appear to have been questionable.[§] As a consequence, we have no way of deciding whether the anomalies we saw were instrumentation effects, unusual turbulence conditions, or actually an unexpected feature of 10.6 μ propagation.

15. Anomalous Scintillation Data

Figure 61 shows the value of C_N^2 measured by the 0.633 μ source at 200 meters as a function of time of night. The data is obtained using the relationship

$$C_N^2 = 3.34 \times 10^{-2} \sigma_\ell^2(0.633, 200) \ . \qquad (15)$$

Values of C_N^2 obtained on each of the several day of field operation are superimposed on each other. Two things are reasonably apparent from this graph. First of all, for the path we are using, which was 1.75 meters above the lake bed, and during the middle of the night, a nominal value of C_N^2 is between 4×10^{-14} and 8×10^{-14} meter$^{-2/3}$. Second, we note that for most of the measurements periods C_N^2 held relatively constant, with only small changes over any period of time, except for the data obtained May 29, 1968. These data show very wide and rapid changes in the measured value of C_N^2. Such rapid changes indicate peculiar conditions and the absence of good averaging. In fact, the wind velocity during this measurement period was virtually zero, which would account for the poor averaging. The very low wind velocity is possibly a more serious factor than suggested by the matter of averaging. All of our

[§] If the data taken during this meteorologically questionable period is rejected, it is interesting to note that the comparison of measured and predicted values of σ_ℓ^2(1.15) will be very much improved, as the most serious deviations from combined theory (Rytov and Saturation) in the 1.15 μ data, are due to this measurement period.

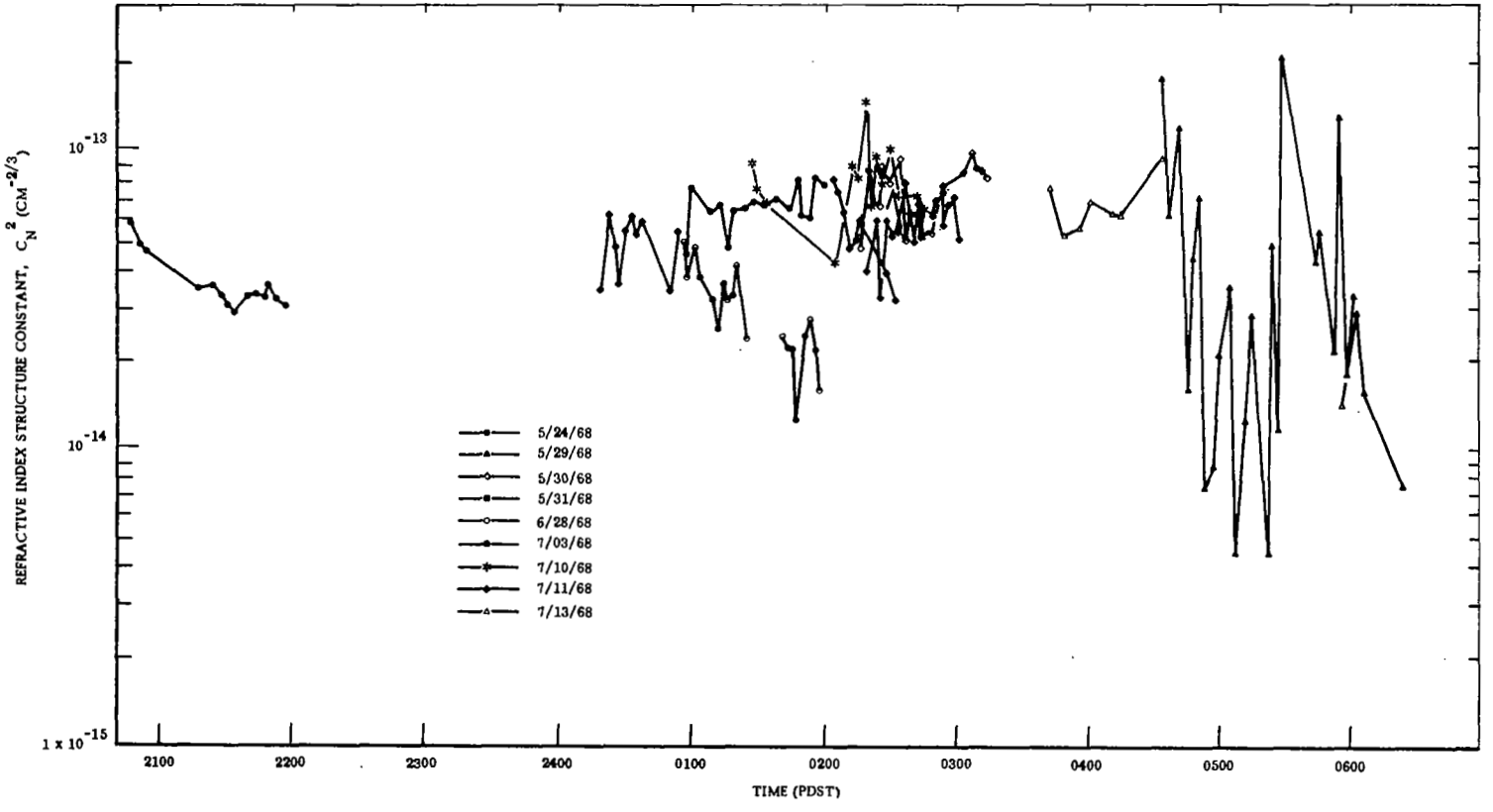

FIGURE 61. Temporal Variations of the Refractive Index Structure Constant, C_N^2. These data were collected with a 0.633 μ source over a path of 0.2 km. Data taken from Runs No. 101 through 1311.

understanding of optical propagation in the atmosphere starts from the Kolmogorov similarity theory of turbulence in the inertial subrange.[10] However, for the inertial subrange to exist, the Reynolds number of the flow (in this case the wind) must be very large. For the virtual dead calm of the May 29, 1968, data, the Reynolds number presumably was not large, the inertial subrange probably did not exist. Consequently, the entire concept of a quantity like C_N^2 (which measures the optical strength of turbulence in the inertial subrange) is irrelevent to the data. From this it follows that we have no applicable theory to even base predictions on. For this reason, together with consideration of the very peculiar scintillation probability distributions obtained during this period, it was decided to exclude all data collected during this period from any data reduction and analysis. For reference purposes, in Figures 62 to 67, we show some of the most and least anomalous of these probability distributions.*

*The probability distribution shown in Figure 63, though it does not fall with the scope of the theory we are investigating, is worthy of note because of its exceptionally large log-amplitude variance, which was in excess of unity.

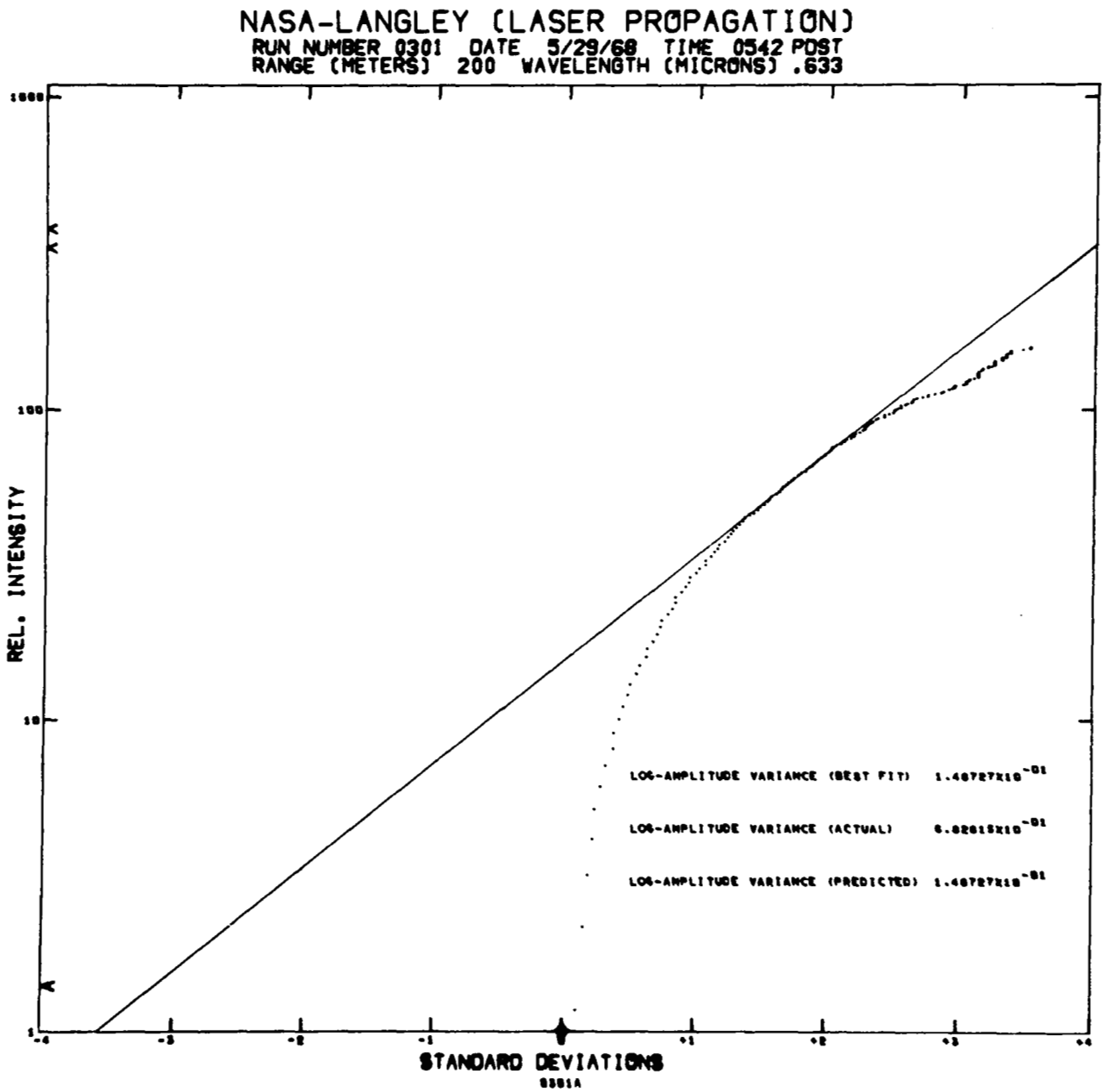

FIGURE 62. Probability Distribution of Scintillation for 0.633 μ "Point" Collector at 0.2 km Range - Run No. 301.

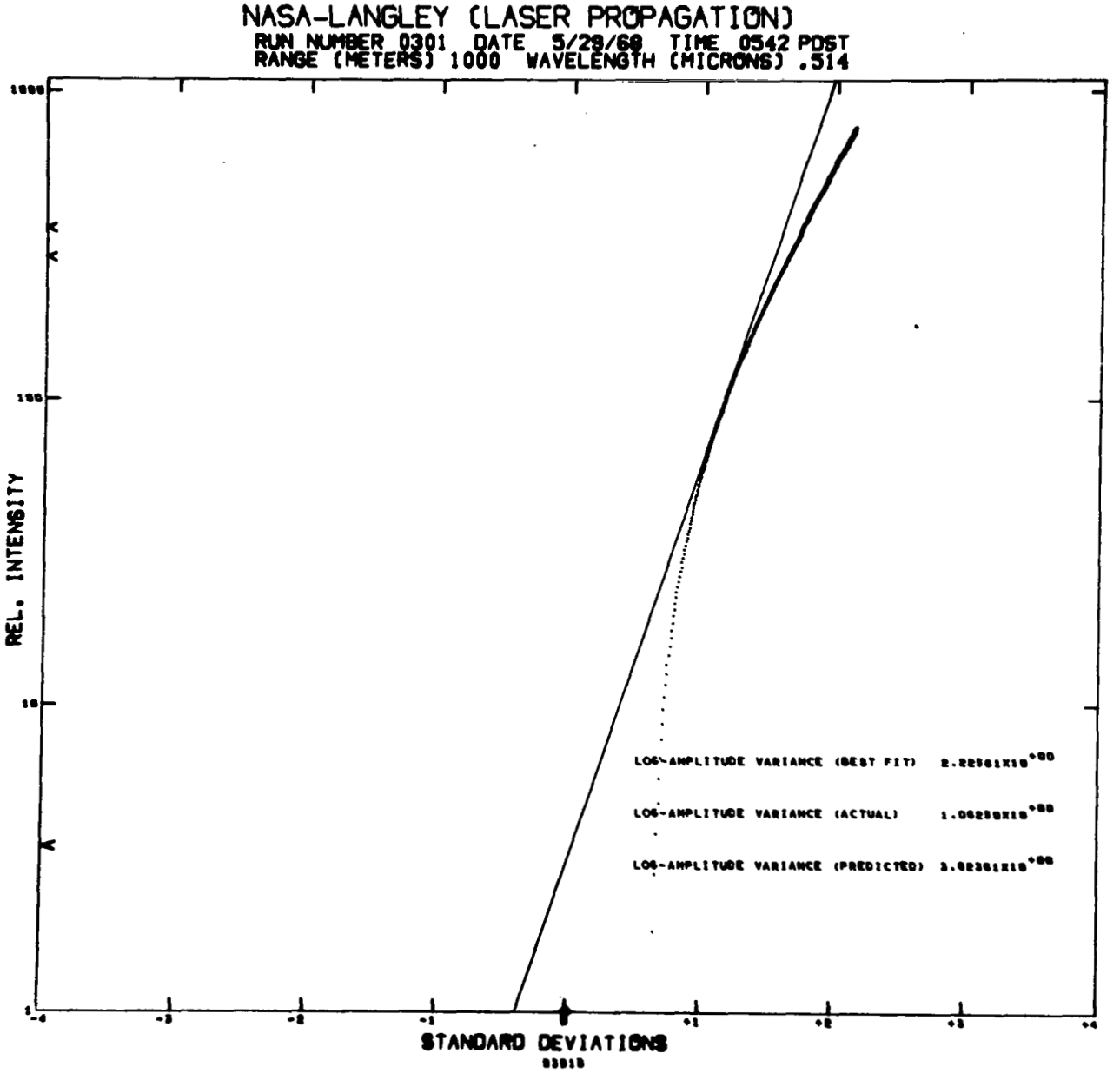

FIGURE 63. Probability Distribution of Scintillation for 0.514 μ "Point" Collector at 1.0 km Range - Run No. 301.

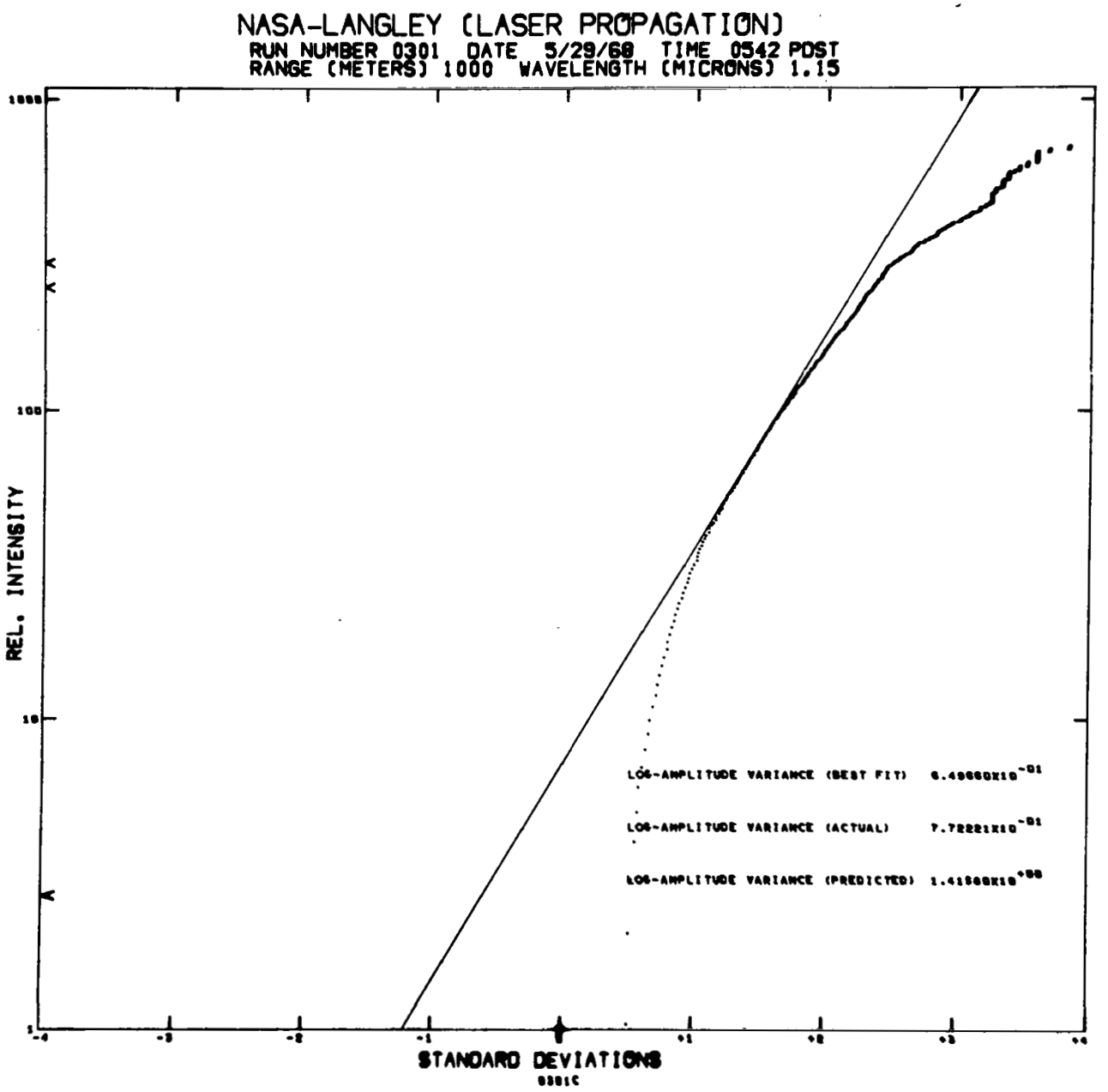

FIGURE 64. Probability Distribution of Scintillation for 1.15 μ "Point" Collector at 1.0 km Range - Run No. 301.

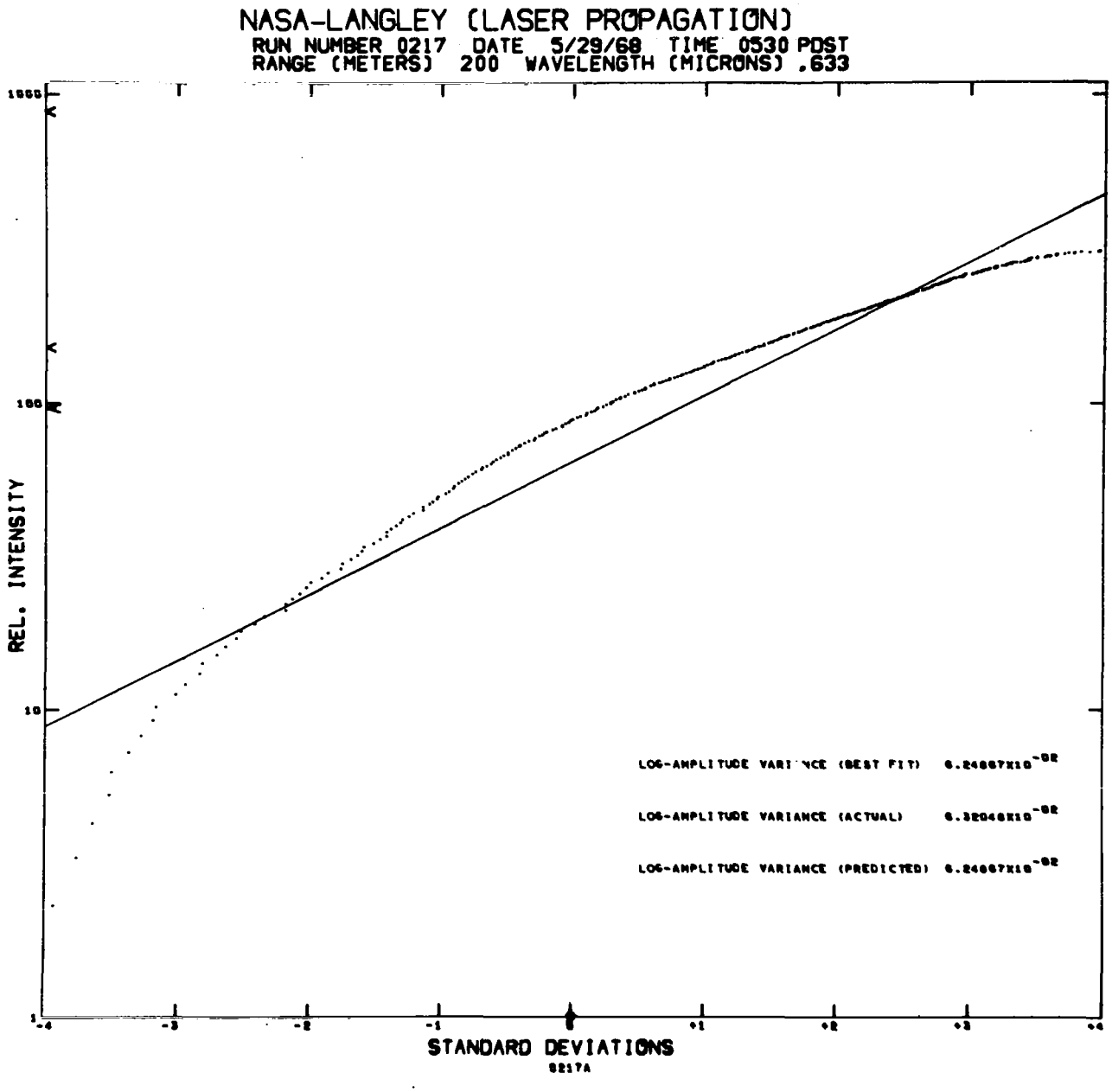

FIGURE 65. Probability Distribution of Scintillation for 0.633 μ "Point" Collector at 0.2 km Range - Run No. 217.

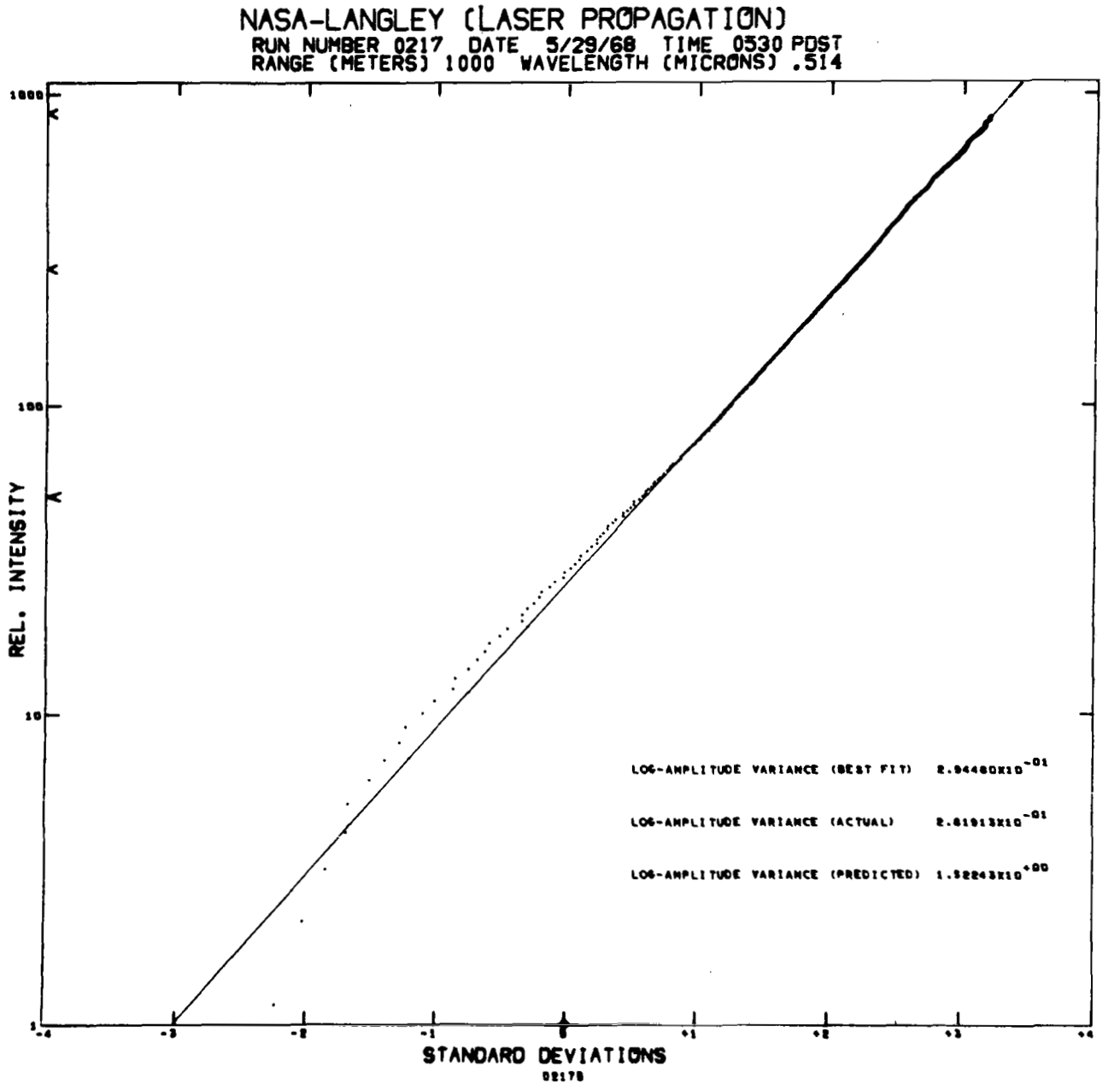

Figure 66. Probability Distribution of Scintillation for 0.514 u "Point" Collector at 1.0 km Range - Run #217.

FIGURE 66. Probability Distribution of Scintillation for 0.514 μ "Point" Collector at 1.0 km Range - Run No. 217.

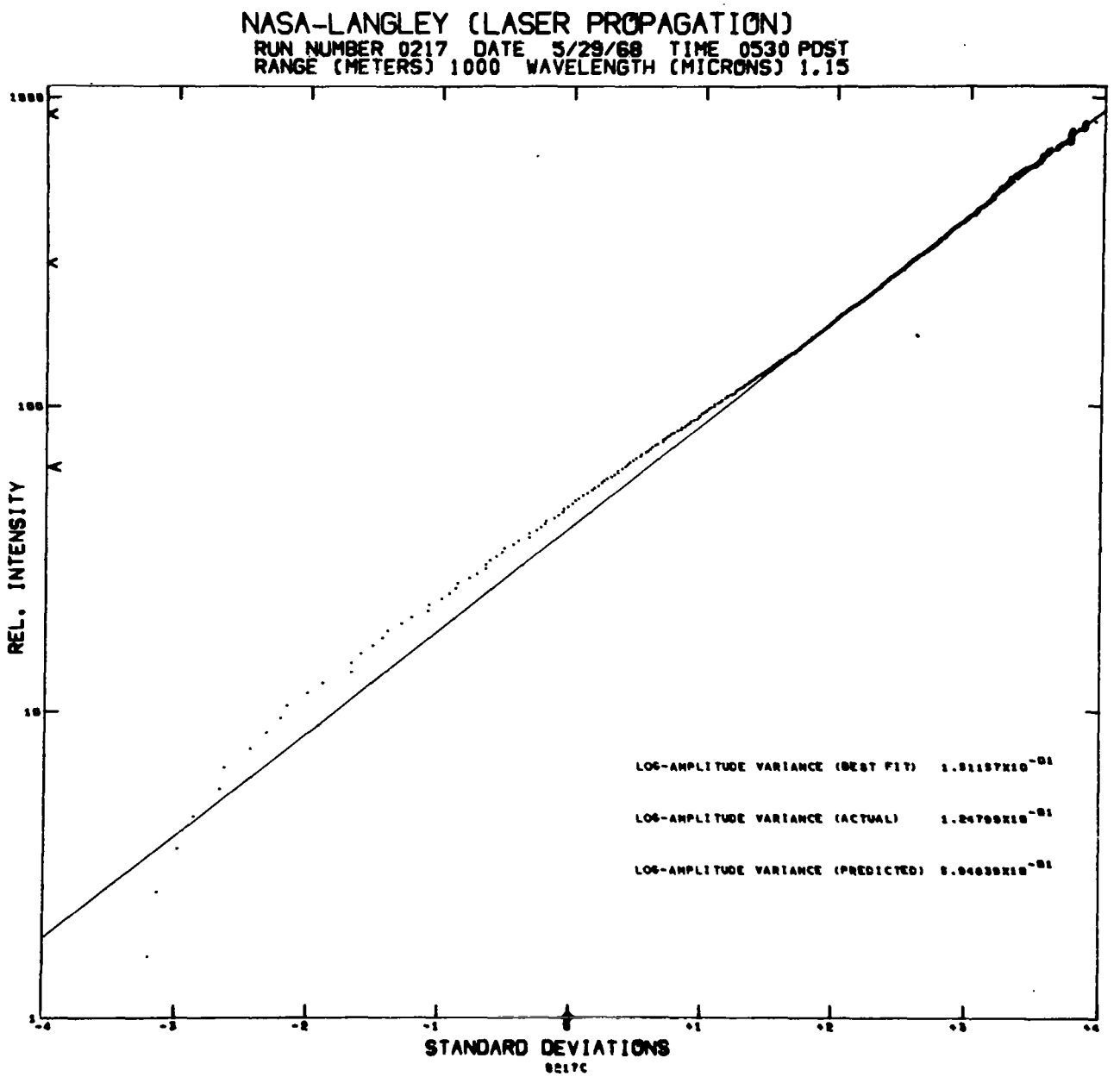

FIGURE 67. Probability Distribution of Scintillation for 1.15 μ "Point" Collector at 1.0 km Range - Run No. 217.

F. REFERENCES FOR SECTION IV

1. V.I. Tatarski, "Wave Propagation in a Turbulent Medium" (McGraw-Hill Book Co., New York, 1961) Chap. 9

2. D.L. Fried, J. Opt. Soc. Am. 57, 175 (1967)

3. D.L. Fried and J.R. Seidman, J. Opt. Soc. Am. 57, 181 (1967)

4. M.E. Gracheva and A.S. Gurbich, Radiofizika 8, 717 (1965)

5. P.H. Dietz and N.J. Wright, "Saturation of Scintillation in Near-Earth Optical Propagation" Memorandum Report No. 1941, U.S. Army Aberdeen Research and Development Center, Ballistic Research Laboratory, Aberdeen Proving Ground, Maryland.

6. D.A. deWolf, "Wave Propagation and Multiple Scattering in a Random Continum," Ph.D. Thesis, (de Technische Hoge School te Eindhoven, Eindhoven, Netherlands, Sept. 1968)

7. D.L. Fried, G.E. Mevers, and M.P. Keister, Jr., J. Opt. Soc. Am. 57 787 (1967)

8. R.L. Mitchel, J. Opt. Soc. Am. 58, 1267 (1968)

9. D.L. Fried, Proc. IEEE 55, 57 (1967)

10. A. Kolmogorov, in "Turbulence, Classic Papers on Statistical Theory," S.K. Friedlander and L. Topper, Eds. (Interscience Publishers, John Wiley and Sons, Inc., New York, (1961)

V. WAVEFRONT DISTORTION MEASUREMENTS

In addition to the scintillation measurements previously described, measurements of wavefront distortion were also made during this program. Since the basic data collection equipment and the data reduction techniques were different from those used in the scintillation measurements, we present the discussions of these activities in a separate section.

Ths basic premise on which these measurements were made is that if one observes a point source with a telescope through a turbulent atmosphere, the atmospheric-produced wavefront distortions will cause the image at the focal plane of the telescope to change size and position. Now if the light at the focal plane of the telescope is observed at the same time a knife edge is used to rapidly chop the focal spot, the signal from the photodetector, when referenced to a signal equivalent to the motion of the chopper, can be used to measure the average size of the focal spot. The theory of this instruments operation is presented in Appendix C. From this measurement, the average wavefront distortion produced by the atmosphere can be determined providing the quality of the telescope is known.[1] To make the wavefront distortion measurements, an instrument of this type was constructed (see Figure 68). The collector used was a 0.45 meter Cassegrain telescope, near diffraction limited for the full aperture. At the focal plane of the telescope was a 40 "tooth" chopper wheel driven by a synchronous motor through a belt drive. The chopper wheel was a glass plate on which 40 "pie-shaped" opaque sections had been placed using photographic techniques and was mounted in the interior of a precision bearing. An audio oscillator and power amplifier were used to provide 60 Hz signal to the synchronous motor for precise operating speed. The motor was operated at 1800 rpm which provided a 1200 Hz chopping rate of the focal spot. The laser signal detector was a photomultiplier assembly as used for the 0.514 micron scintillation measurements except that the collector lens assembly was removed and the signal bandwidth of its line driver was increased to 30 kHz. The reference source was a small 6 volt bulb powered by a battery used to illuminate a pin hole. A lens was used to focus an image of the pin hole on the chopper wheel. The reference signal detector was a small 6-stage photomultiplier coupled to a 30 kHz line driver. The chopper wheel-driver motor-detector assembly (shown in Figure 69) was mounted

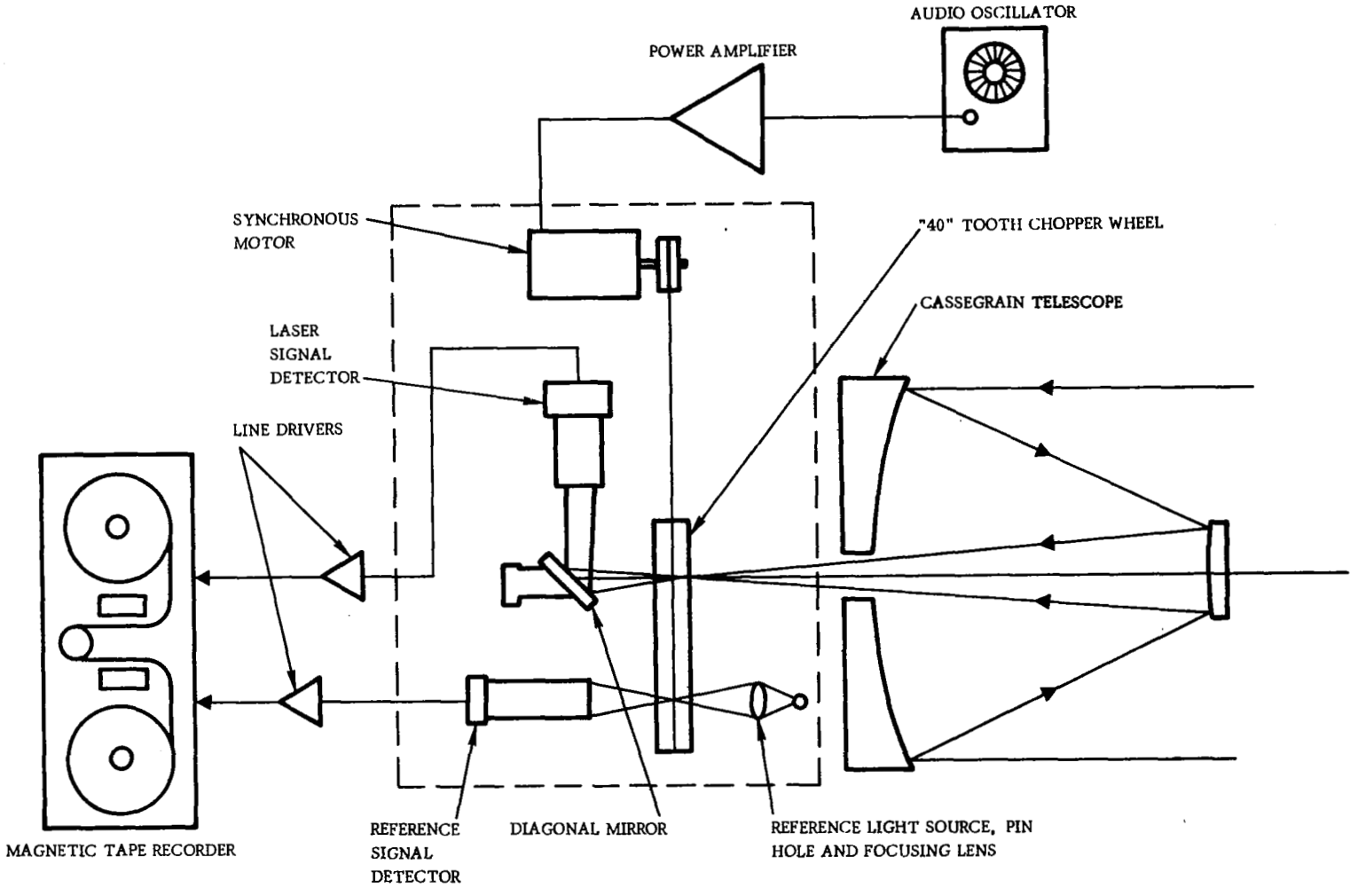

FIGURE 68. Wavefront Distortion Measurement Instrument

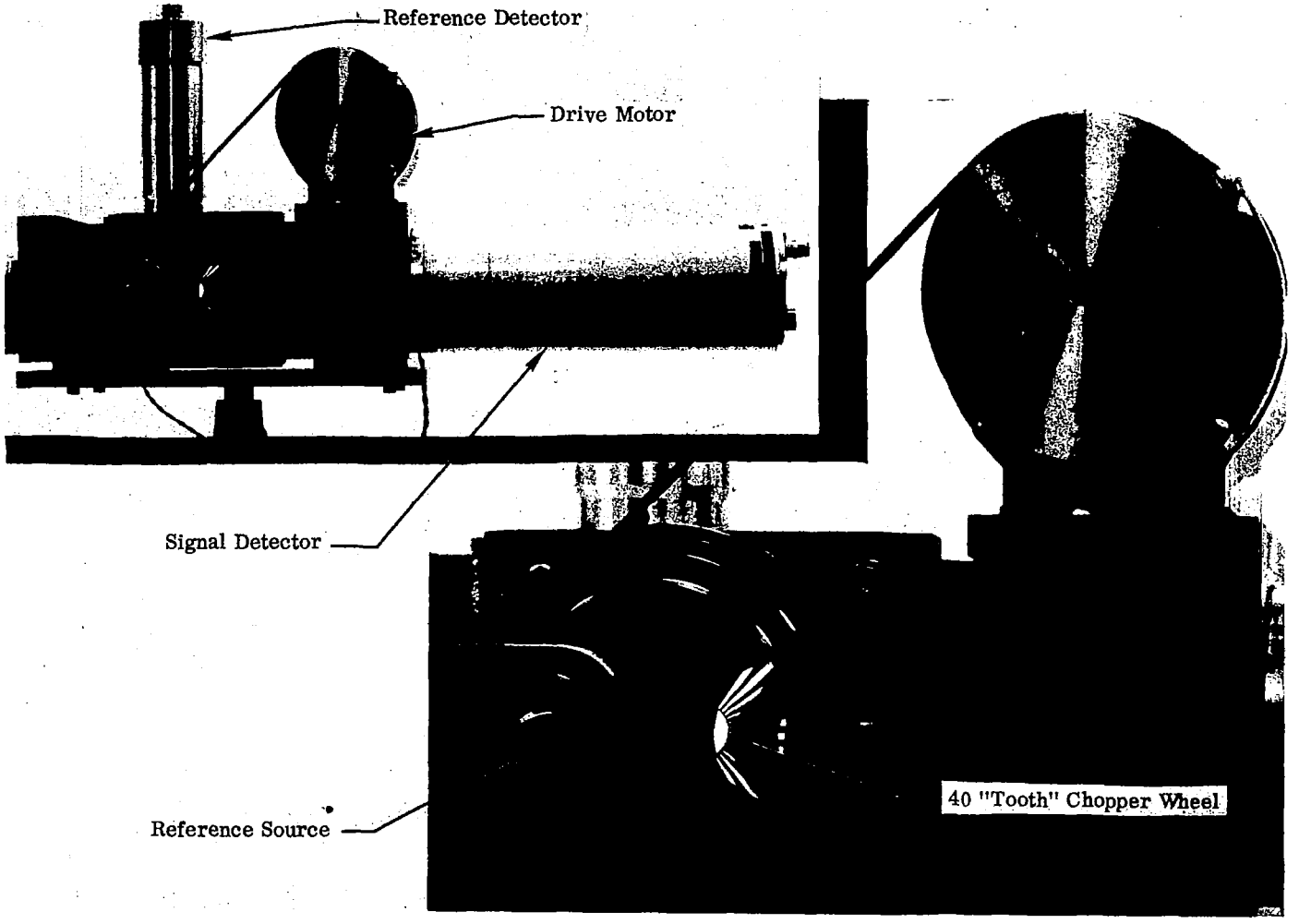

FIGURE 69. Chopper Wheel Assembly for Wavefront Distortion Measurements Instrument. This view shows the entrance aperture of the chopper wheel assembly which accepted light from the cassegrain telescope. On the back side of the assembly is a diagonal mirror that could be rotated, so that light passing through the chopper wheel could be directed into either the detector or observed for alignment purposes by means of a port at the top of the assembly.

on a large-heavy optical bench. The Cassegrain telescope was also mechanically attached to the optical bench. In this manner, it was possible to move the chopper wheel assembly either along the optic axis of the telescope for focusing or laterally to position the focal spot at the desired radius of the chopper wheel.

A. DATA COLLECTION

To make the wavefront distortion measurement in the field, the optical bench and telescope were mounted on the concrete received platform (described in a previous section) and the optic axis of the telescope carefully aligned to the laser source. The chopper wheel assembly was then mounted on the optical bench and adjusted laterally to locate the focal spot at the desired position on a radius of the chopper wheel. This position was selected in the following manner. With one of the opaque "pie-shaped" sectors set horizontally, the chopper wheel assembly was moved laterally until the visible focal spot was just hidden behind the opaque section. * To insure that the chopper wheel was previsely in the focal plane of the telescope, the output of the laser signal detector was fed into an audio spectrum analyzer and the chopper wheel assembly was adjusted along the optic axis of the telescope until the highest significant amplitude harmonic of the chopping rate could be obtained. A similar technique was used to precisely locate the focal plane of the reference source at the chopper wheel. When these adjustments were completed, four minutes of chopped signals from the laser source and reference source were recorded on magnetic tape for each of the measurements made. Just prior and just after wavefront distortion data was collected, scintillation data was collected with the 0.514 and 0.633 micron "point" collectors. Using the techniques that have been described, measurements of wavefront distortion were made at ranges of 1.5 and 3.0 km.

B. DATA REDUCTION

The wavefront distortion data was reduced using the equipment configuration shown in Figure 70. The chopped laser signal and reference signal were fed into a "lock-in" amplifier which produces a phase-detected voltage output with the phase set to maximize the average signal detected. The analog output signal of the lock-in amplifier was then fed into a 100 channel pulse-height analyzer. The pulse-height

*This measurement was made with safety goggles that attenuate the 0.514 micron line because of the intensity of the focal spot.

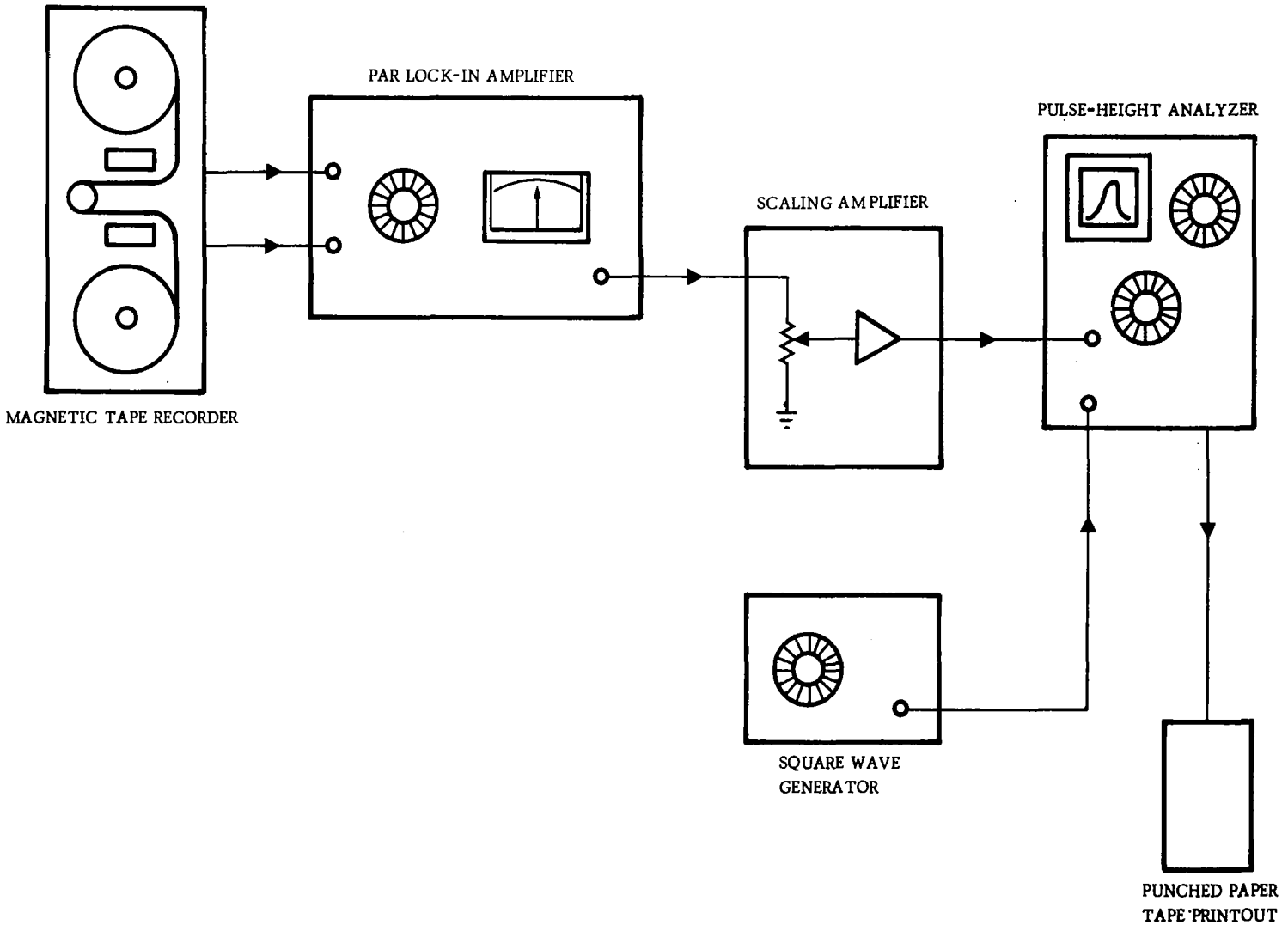

FIGURE 70. Data Reduction Equipment Block Diagram

analyzer generated the probability density of the analog signal from the lock-in amplifier which was then output in a digital format on punched paper tape. For each of the wavefront distortion measurements, the full 4 minutes of recorded chopped signals were fed into the lock-in amplifier 5 different times with the instrument set first to analyze the fundamental frequency and then each successive odd harmonic up to the 9th. During this part of the data analysis, we found that if signal gain of the lock-in amplifier was fixed when working with the fundamental frequency, then the signal out when operating on the 5th or higher harmonics was less than the output amplifier noise of the lock-in amplifier. Therefore, the signal gain was so adjusted each time such that if an ideal square wave input was used, the output of the lock-in amplifier would have been equal for all harmonics. This, in fact, provided the necessary compensation for the decreasing amplitude of square wave components, as developed in Appendix C. To complete the data processing, the output of the pulse-height analyzer was fed into a digital computer which was programmed to solve the following equations.

$$\bar{X}_s = \frac{1}{N_s} \sum_{i=1}^{100} C_{is} X_i \tag{16}$$

where

$\bar{X}_s$ is the average values of the output of the lock-in amplifier,

C_{is} is the number of counts in channel X_i of the pulse-height analyzer,

and

N_s is defined as

$$N_s = \sum_{i=1}^{100} C_{is} X_i \tag{17}$$

so that

C_{is}/N_s is the event probability in the increment defined by X_i.

These equations were solved for the fundamental through the 9th harmonic data for each of the wavefront distoration measurements made. The fact that 4 minutes of data was used to obtain the averages means that the effective integration time of the phase sensitive voltmeter was 4 minutes. Figure 71 is a plot of $\overline{X}_S$ for the different harmonics obtained from one of the wavefront distortion measurements and is typical of the results obtained. Since theory indicates that $\overline{X}_S$ as measured is of the form

$$\overline{X}_S = k \exp(\alpha f^{5/3}), \tag{18}$$

we have plotted $\overline{X}_S$ as a function of $f^{5/3}$ in Figure 71 so the results should be a straight line fit. The data does not appear to have a good fit, but this possibly is a result of noise influence in the output of the lock-in amplifier ($\overline{X}_S$ for the 5th harmonic is about twice the rms output noise of the lock-in amplifier). In addition to computing the relative average harmonic strength for each of the wavefront distortion measurements, the computer was also programmed to compute the probability distribution of the analog signal output of the lock-in amplifier. An example of the distributions of the different harmonics are shown in Figures 72 through 76. (These data are from the same measurement as those for Figure 71.) From these data on the relative average strength of the different harmonics, the quantity r_o and a value for C_N^2 were computed from the different wavefront distortion measurements according to the equation,

$$r_o = 3.44\,(3^{5/3}-1)\,\alpha^{5/3}/\ell n\, R, \tag{19}$$

where

$$\alpha = \lambda F f_o/\nu \tag{20}$$

f_o = the fundamental chopping frequency = 1200 Hz

F = the focal length of the telescope = 3.53 meters

λ = the optical wavelength = 5.145×10^{-7} meters

$\nu = 2\pi\Omega r$

Ω = 30 rev./sec.

r is the radial position of the focused spot on the chopper wheel,

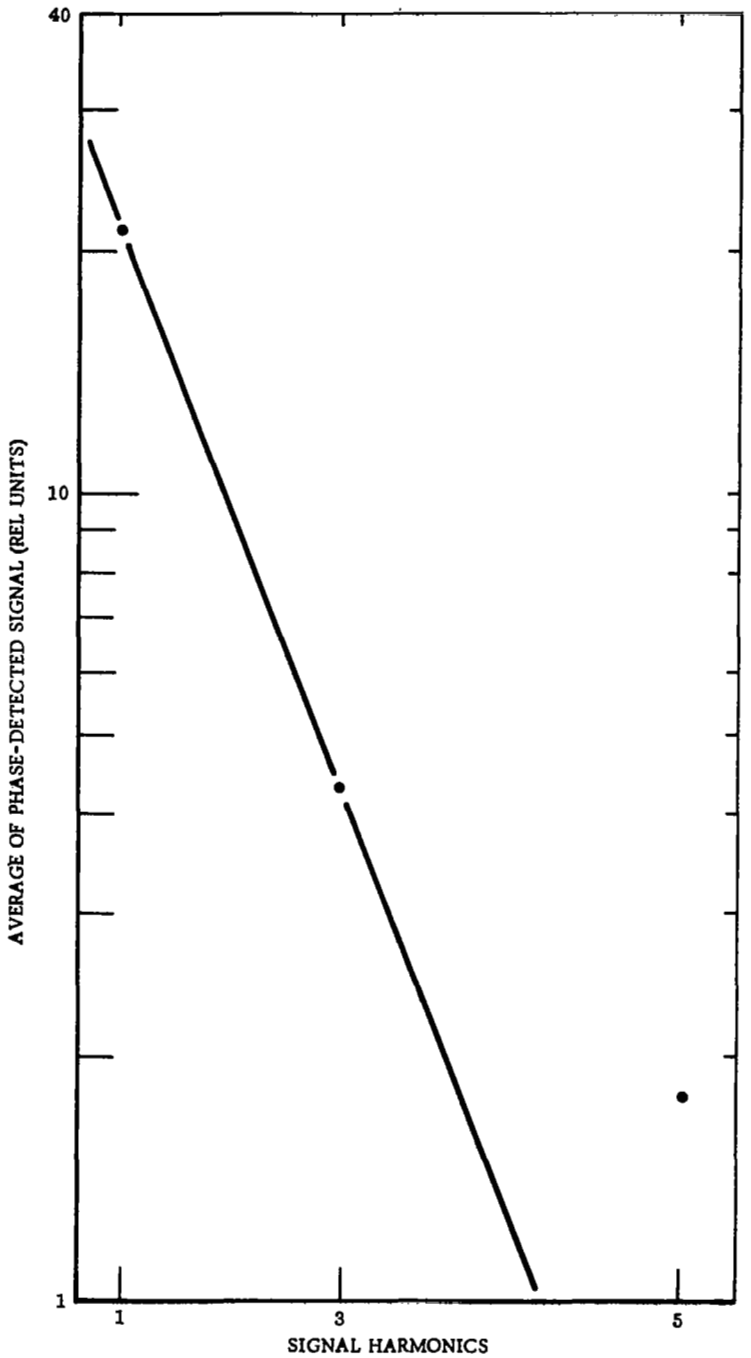

FIGURE 71. Average Value of Phase-Detected Signal vs. Signal Harmonics. A 5/3 power scale has been used for frequency. Data taken from wavefront distortion measurement made between runs #1303 and 1304 (7/13/68).

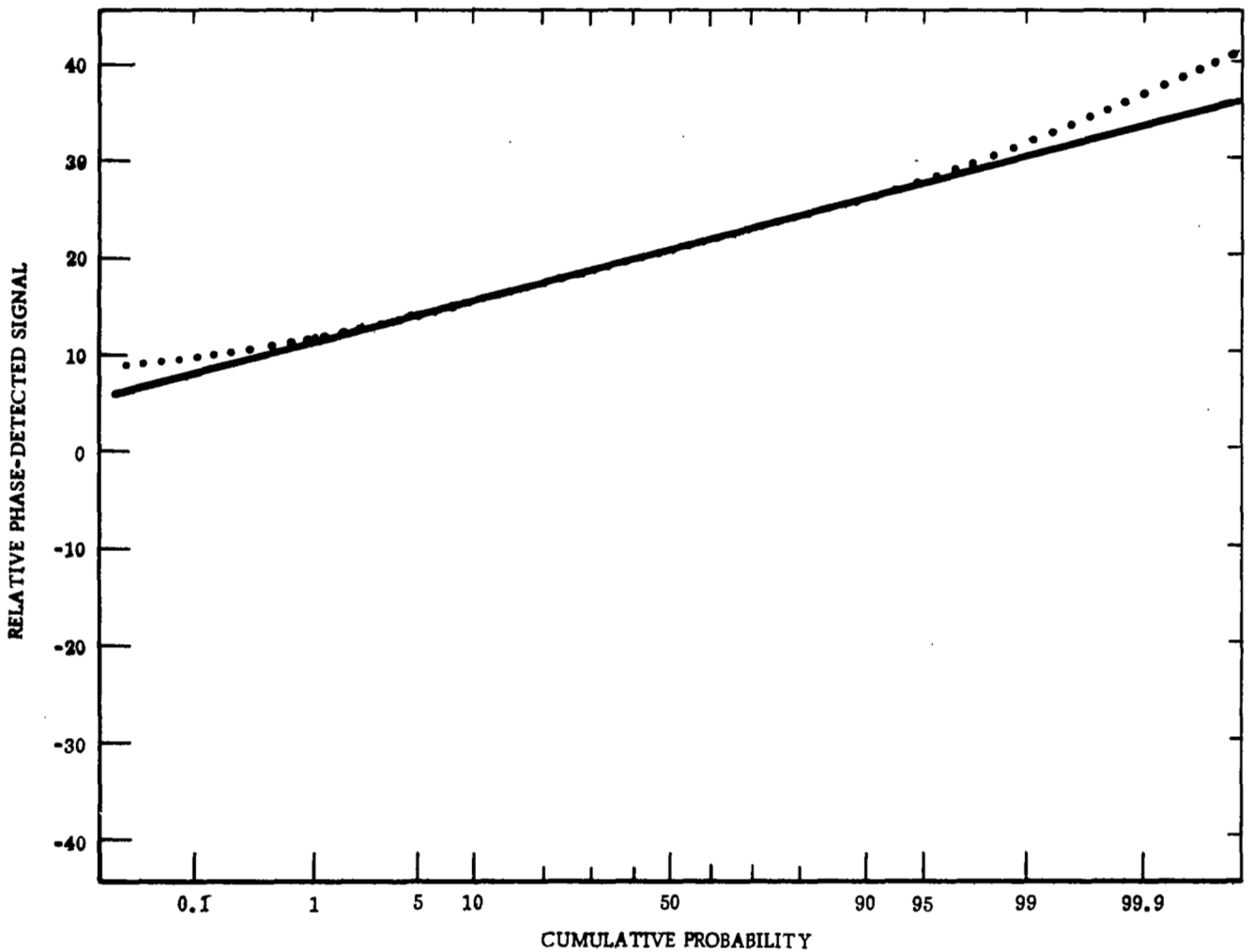

FIGURE 72. Probability Distribution of Phase=Detected Signal for Fundamental. Data taken from wavefront distortion measurement between Runs #1303 and #1304 (7/13/68).

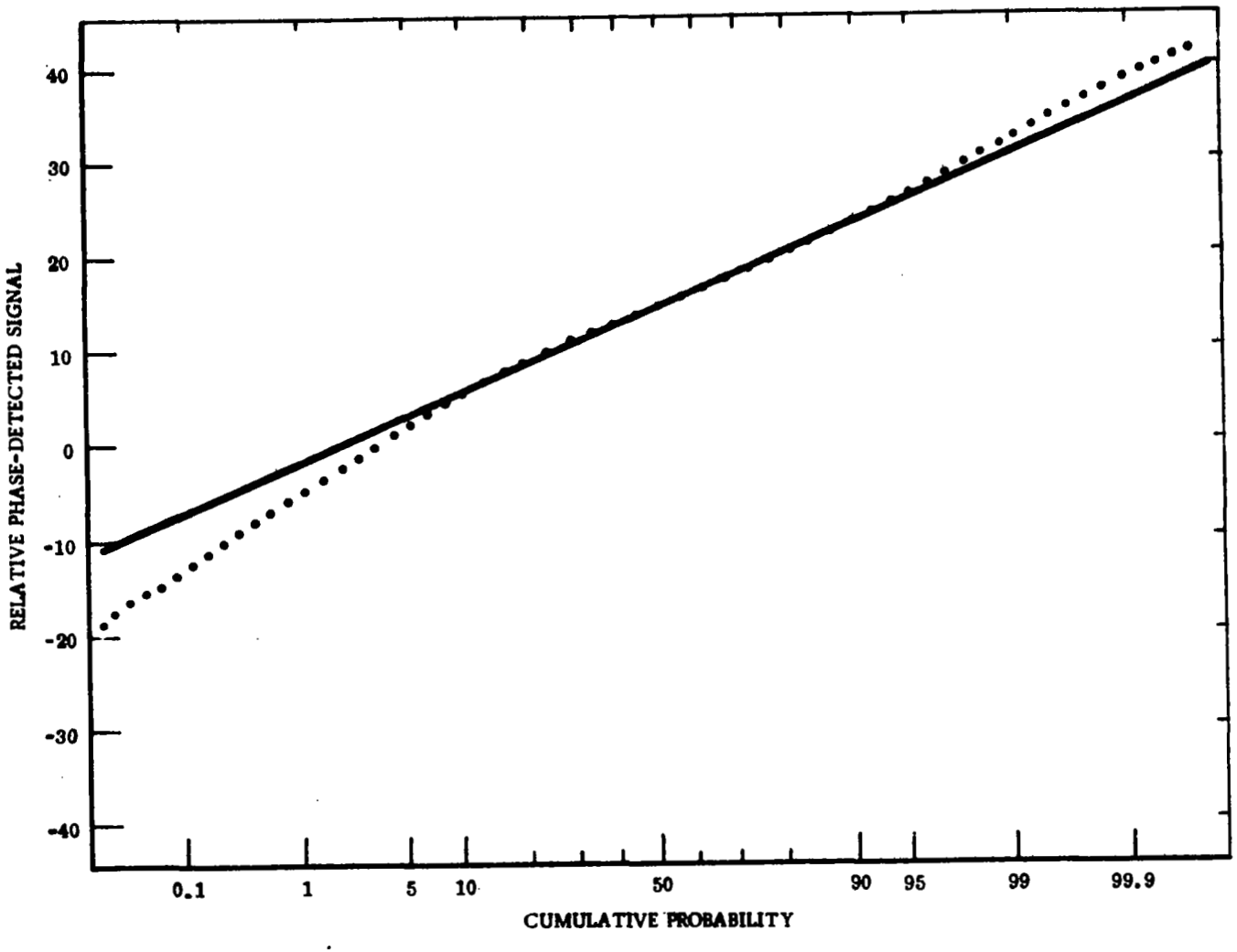

FIGURE 73. Probability Distribution of Phase-Detected Signal for 3rd Harmonic. Data taken from wavefront distortion measurement between Runs #1303 and #1304 (7/13/68).

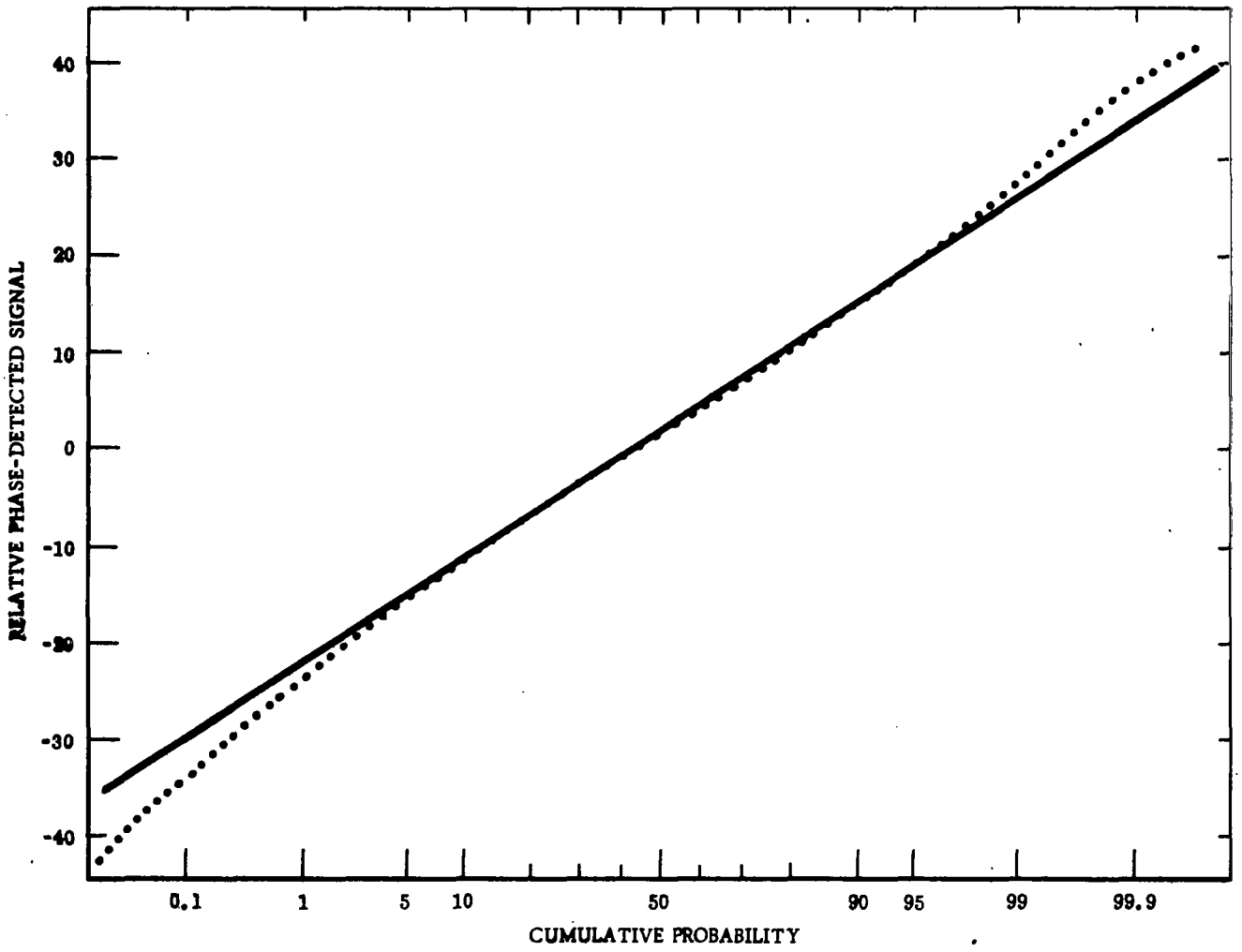

FIGURE 74. Probability Distribution of Phase-Detected Signal for 5th Harmonic. Data taken from wavefront distortion measurement between Runs #1303 and #1304 (7/13/68).

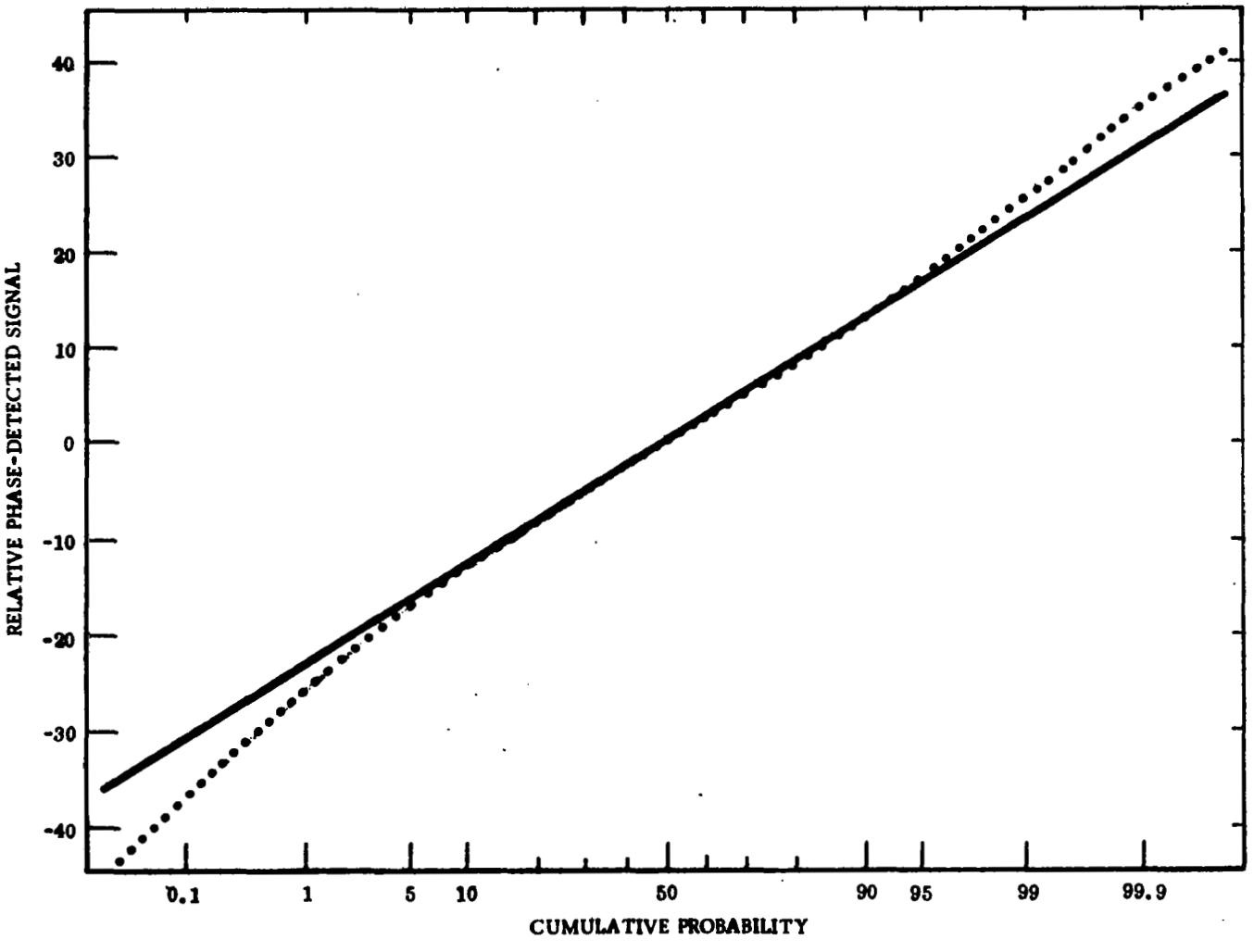

FIGURE 75. Probability Distribution of Phase-Detected Signal for 7th Harmonic. Data taken from wavefront distortion measurement between Runs #1303 and #1304 (7/13/68).

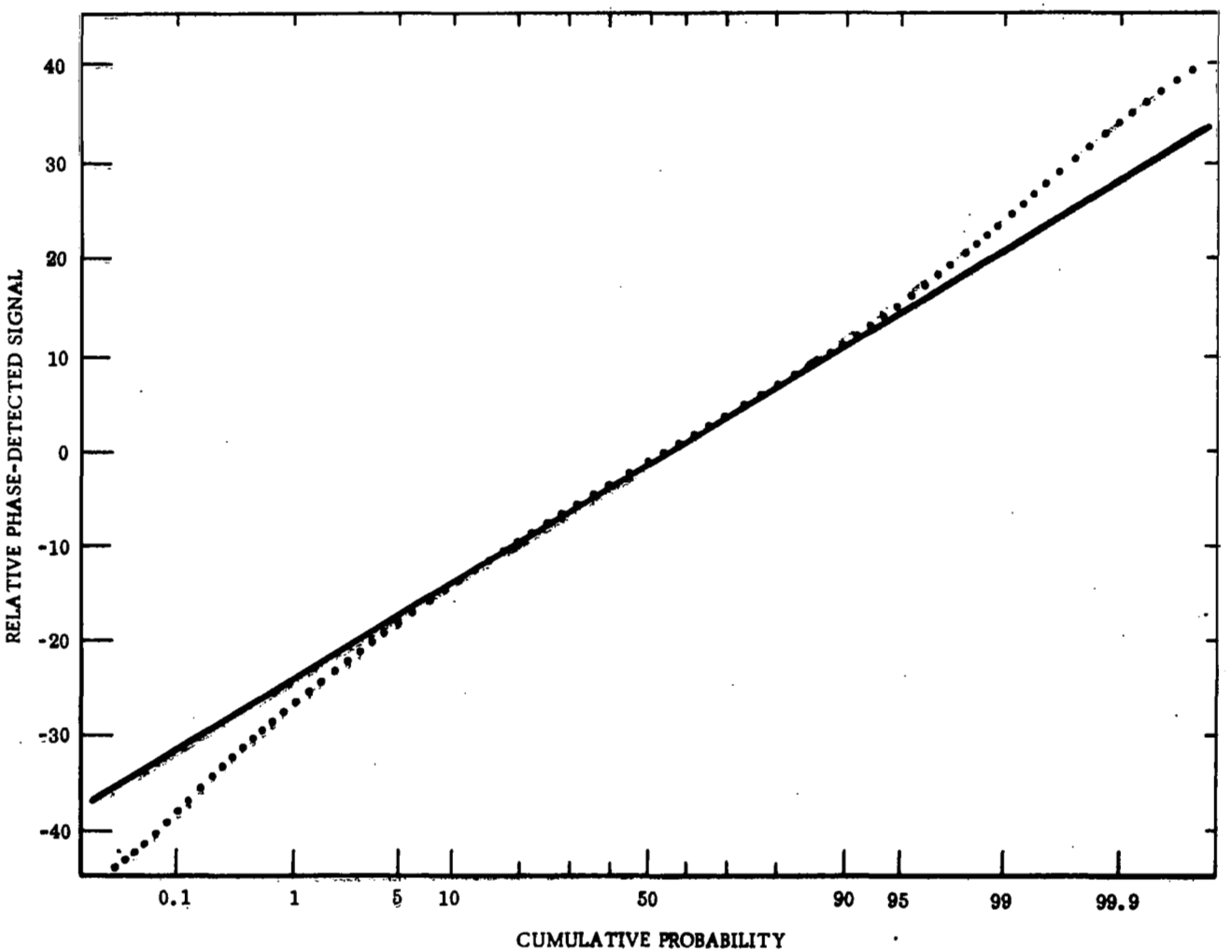

FIGURE 76. Probability Distribution of Phase-Detected Signal for 9th Harmonic. Data taken from wavefront distortion measurement between Runs #1303 and #1304 (7/13/68).

and

R is the ratio of the relative strength of the fundamental to 3rd harmonic of chopped signal.

From spherical wave theory, C_N^2 was computed from r_o as follows:

$$C_N^2 = (0.333/r_o)^{5/3} \times (\lambda^2/Z) \quad (21)$$

where

Z is transmission range in meters. These two equations are derived from Reference 1 and 2.

C. MEASUREMENT RESULTS

The results of these computations are shown in Table VII. The tabulation of data shown here is only for those measurements made at 1.5 km. On the 3.0 km data the average strength of the harmonic data beyond the fundamental was within the noise level of the output amplifier on the lock-in amplifier and, therefore, was not useable. This tabulation of data indicates a significant difference between the C_N^2 values computed from the wavefront distortion measurements and that obtained from the 0.633 micron "point" collector data. Since other experiments[3] have shown better agreement, we can only conclude that improvements in the data collection are necessary.

TABLE VII

WAVEFRONT DISTORTION DATA

RUN #	r (METERS)	R	COMPUTED r_o (METERS)	COMPUTED * C_N^2	MEASURED + C_N^2	AVERAGE SPOT SIZE COMPUTED FROM r_o (METERS)
1301	1.575-2	2.80	3.64-3	3.28-13	7.57-14	4.99-4
1302					5.03-14	
1303	1.575-2	3.72	3.14-3	4.19-13	5.46-14	5.78-4
1304					6.71-14	
1305	1.175-2	3.17	4.55-3	2.26-13	6.10-14	3.99-4
1306					5.99-14	
1307	1.175-2	3.79	4.18-3	2.61-13	9.42-14	4.34-4

* From wavefront distortion data

\+ From 0.633 μ scintillation

D. REFERENCE FOR SECTION V

1. D. L. Fried, J. Opt. Soc. Am. 56, 1372 (1966)
2. D. L. Fried, J. Opt. Soc. Am. 56, 1380 (1966)
3. C. E. Coulman, J. Opt. Soc. Am. 56, 1232 (1966)

VI. TEMPERATURE PROBE MEASUREMENTS

The inhomogeneities in the optical refractive index of the atmosphere arise when the imbalance between ground and air heating produces an air temperature gradient greater than the adiabatic lapse rate and, as a result, cause a mixing in the atmosphere of warmer and cooler parcels of air. The refractive index inhomogeneities are due to these random variations in air temperature, as warmer (cooler) air is less dense (more dense) and so has a lower (higher) refractive-index. Hence, it is possible to obtain a measure of the optical strength of turbulence by either a direct optical measurement (measure the refractive index structure constant, C_N^2) or a measurement of temperature fluctuations (measure the temperature structure constant, C_T^2). C_T^2 is simply relatable to C_N^2 if the mean air temperature and pressure are known. Since for measuring C_T^2 the equipment required is less difficult to handle (does not require a large volume of measurement space or very stable alignment, as with optical techniques) and reduction of the data easily performed, this would be a preferred method for obtaining a measure of the optical strength of turbulence if the results were useable on long path optical propagation.

Because of the relative simplicity of the temperature measurement technique several experimenters have used it to obtain a value of C_N^2 from which predictions of scintillation measurement results could be obtained. Their results have been characterized by a substantial spread in the data which would lead one to question the usefulness of this type measurement. Consequently, as part of this program a series of simultaneous optical and temperature measurements of C_N^2 were made for comparison.

A. DATA COLLECTION

To collect these data, the optical measurements were as described in previous sections ("point" collector scintillation measurements with 0.633 micron laser source transmitted over 0.2 km path). The temperature measurements were made with a high-speed temperature bridge that had been designed and developed by ESSA[1] and was set up and operated in the field for these tests by Mr. R. S. Lawrence and Mr. G. R. Ochs of that organization, for which favor we are greatly indebted. This instrument which uses platinum wire less than a micron in diameter and a millimeter long for

temperature detectors was located at a height equivalent to the optical beam elevation and about 3 meters in front of the optical detection equipment and about 0.5 meters to the side of the beam path. The two temperature detectors used in the instrument were spatially separated by 10 cm. Before starting the series of measurements a square wave calibration signal built into the ESSA instrument equivalent to a 1°C. temperature difference between detectors was recorded. Data collection was quite straightforward. The optical scintillation data was recorded as described in the section on scintillation (a 60 second plus a 30 second data collection period) and at the same time temperature fluctuation signals were also recorded.

B. DATA REDUCTION

The optical scintillation data was reduced as described in previous sections. The temperature data, however, was reduced using the configuration shown in Figure 70 of the previous section except that the "lock-in" amplifier was removed from the circuit. The 1°C. calibration signal that had been recorded was used to calibrate the output of the 100 channel pulse height analyzer, which provides a probability density of the recorded signal. Before continuing this discussion we should mention that from the spread in this calibrate signal we were able to ascertain the equivalent rms temperature fluctuation produced by amplifier noise in the ESSA instrument. This value was 0.04°C. which is in good agreement with measurement results reported by ESSA[1].

The output of the pulse height analyzer was then fed into a digital computer which had been programmed to solve the following equations:

$$D_T(r) = \left[\frac{\sum_{i=1}^{100} C_{is} (z_i)^2}{N_s} - \left[\frac{\sum_{i=1}^{100} C_{is} z_i}{N_s} \right]^2 \right] \times k^2, \qquad (22)$$

where

C_{is} is the number of counts in channel z_i of the pulse-height analyzer,

N_s is defined as

$$N_s = \sum_{i=1}^{100} C_{is}, \tag{23}$$

so that

C_{is}/N_s is the event probability in the increment defined by Z_i.

k is the calibration constant which equates pulse-height analyzer channel location to a given temperature difference of the detectors.

D_T (r) is the temperature structure function. The temperature structure constant C_T^2 is defined by

$$D_T(r) = C_T^2 \, r^2/_3. \tag{24}$$

Here, r is the spatial separation between temperature detectors (in meters). For the measurements made

$$r = 0.1,$$

so that

$$C_T^2 \, (^{o}m^{-2}/3) = D_T(r)\, 0.2158.$$

From Tatarski[2] the refractive index structure constant, C_N^2, can be computed from C_T^2 using the following equation:

$$C_N^2 \text{ (temp. probe)} = \left[\frac{4.76 \times 10^{-9} P^2}{T^4}\right] C_T^2 \qquad (25)$$

Where

P is the mean atmospheric pressure in millibars and T is the mean air temperature in °K.

For these measurements,

$$P = 936 \text{ mb}$$

and

$$T = 301.6 \text{ °K.}$$

Therefore,

$$C_N^2 \text{ (temp. probe)} = 5 \times 10^{-13} C_T^2.$$

C. MEASUREMENT RESULTS

Table VIII is a tabulation of the results of this series of measurements both from the optical and temperature data and Figure 77 is a plot of these results as a function of the time they were collected. Before discussion of these results let us briefly describe the apparent atmospheric conditions during the measurements. For the series of measurements between 0104 and 0126 PDST the wind speed was steady at about 3 to 3.6 m/sec. (anemometer located about 3 meters above the ground near the optical receiver). For the measurements between 0142 and 0159 PDST the wind slowly diminished from about 3 m/sec. at the start to less than 2 m/sec. At this point we stopped collecting data for fear that the low wind speed would not produce enough mixing of the air to insure existence of an inertial subrange in the turbulence spectrum, as assumed

TABLE VIII

HIGH-SPEED TEMPERATURE PROBE MEASUREMENTS

RUN #	$D_T(r)$ $(°C)^2$	C_T^2	C_N^2 (TEMP. PROBE)	C_N^2 (OPTICAL)
701	0.0500	0.232	11.60-14	4.82-14
702	0.0455	0.211	10.55-14	3.60-14
703	0.0462	0.214	10.70-14	3.32-14
704	0.0459	0.213	10.65-14	3.13-14
705	0.0284	0.132	6.60-14	2.40-14
706	0.0494	0.229	11.45-14	3.58-14
707	0.0476	0.221	11.05-14	3.11-14
708	0.0593	0.275	13.75-14	3.23-14
709	0.0330	0.153	7.65-14	4.16-14
710	0.0339	0.157	7.85-14	2.92-14
711	0.0359	0.166	8.30-14	2.28-14
801	0.0441	0.204	10.20-14	2.38-14
802	0.0381	0.177	8.85-14	2.15-14
803	0.0287	0.133	6.65-14	2.12-14
804	0.0293	0.136	6.80-14	1.23-14
805	0.0382	0.177	8.85-14	---
806	0.0199	0.092	4.60-14	2.42-14
807	0.0295	0.137	6.85-14	2.76-14
808	0.0171	0.079	3.95-14	2.18-14
809	0.0213	0.099	4.95-14	1.55-14

TABLE VIII - Concluded

RUN #	$D_T(r)$ $(°C)^2$	C_T^2	C_N^2 (TEMP. PROBE)	C_N^2 (OPTICAL)
810	0.0548	0.254	12.70-14	4.82-14
811	0.0587	0.272	13.60-14	8.65-14
812	0.0601	0.278	13.90-14	6.61-14
813	0.0463	0.215	10.75-14	6.64-14
814	0.0290	0.134	6.70-14	6.23-14
815	0.0388	0.180	9.00-14	8.71-14
816	0.0417	0.193	9.65-14	7.70-14
817	0.0410	0.190	9.50-14	7.83-14
818	0.0361	0.167	8.35-14	8.79-14
819	0.0432	0.200	10.00-14	9.38-14
820	0.0365	0.169	8.45-14	4.86-14
821	0.0307	0.142	7.10-14	7.56-14

in the Kolmogorov theory.[3] After waiting about twenty minutes the wind picked up again and varied between 3.6 and 4.5 m/sec. for the measurements made between 0219 and 0240 PDST.

From Figure 77 it appears that the C_N^2 (temp. probe) results indicate a greater strength of turbulence than do the C_N^2 (optical). Moreover, it appears that the time variations of these results are weakly correlated. To better illustrate these observations the ratio C_N^2 (temp. probe)/C_N^2 (optical) was taken for all the measurements made and the probability distribution of these ratios plotted in Figure 78. From these data we can see that on the average the temperature measurements indicated turbulence conditions about twice as strong as those obtained optically and that the correlation of time variations of the two measurements was weak. The rms of the variations of the

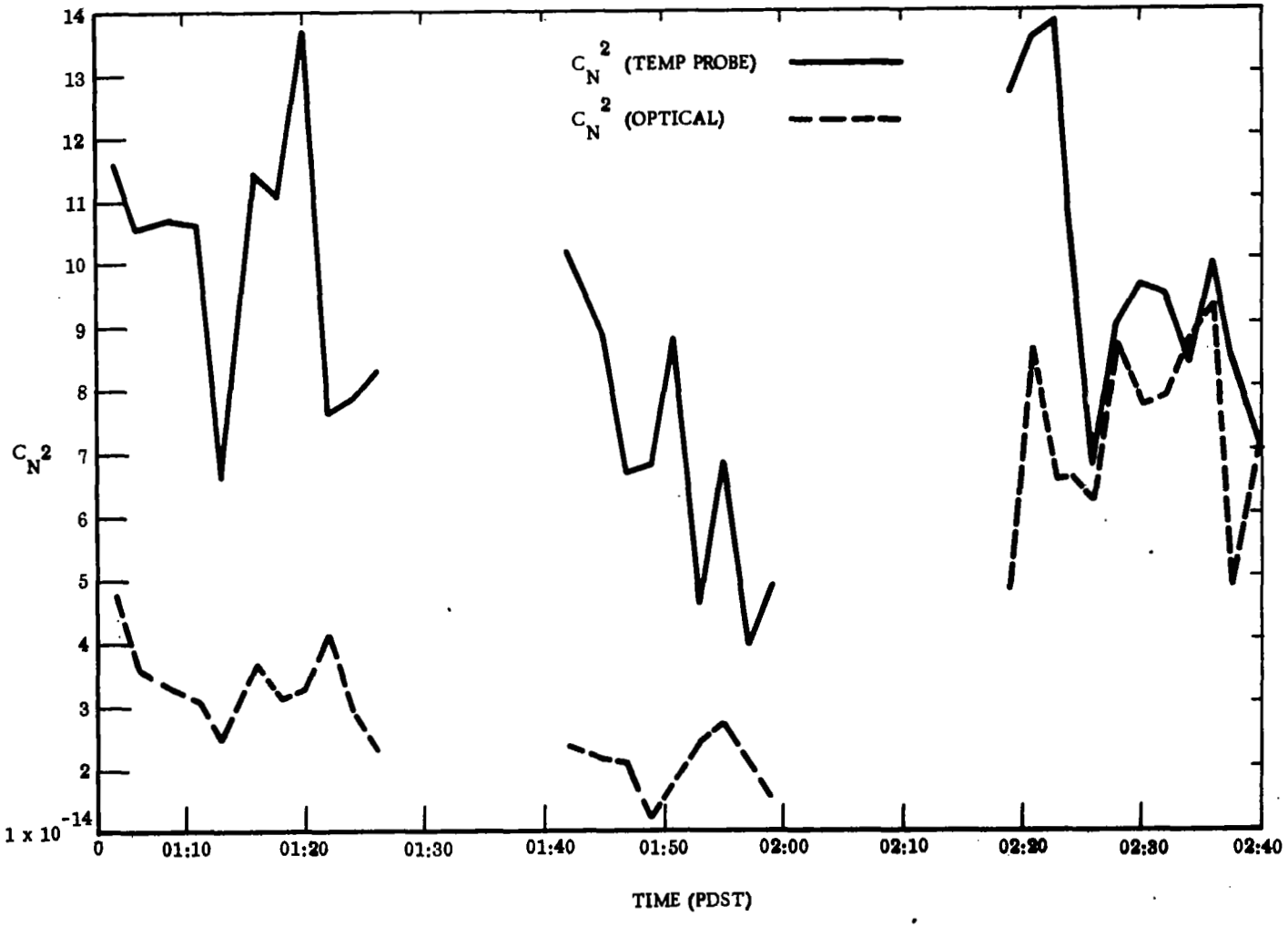

FIGURE 77. Temporal Variations of Refractive Index Structure Constant, C_N^2, as Measured Optically and with a High-Speed Temperature Probe. Data taken from data Runs #701 - #711 and #801 - #821, (6/28/68)

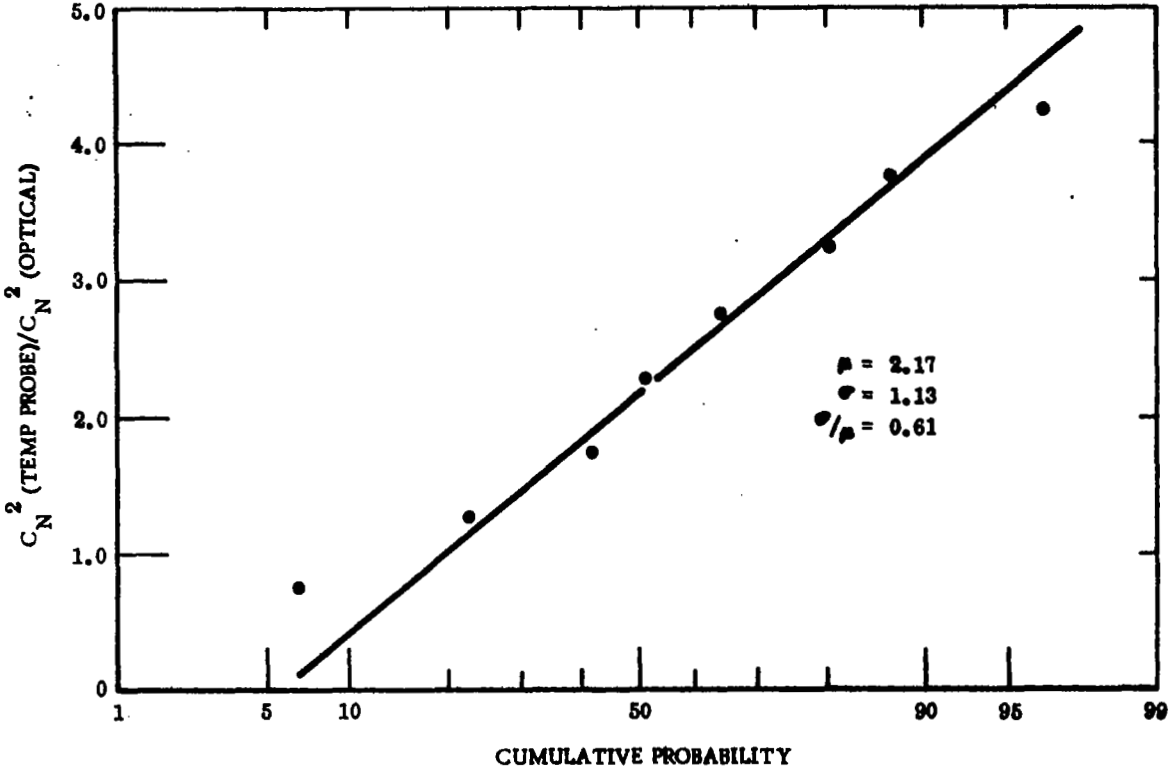

FIGURE 78. Probability Distribution of Ratio of C_N^2 (Temp. Probe) to C_N^2 (Optical). Data taken from Runs #701 - #821, (6/28/68).

ratio was about 60 percent of the mean. To see what was occurring during the different wind conditions, the probability distributions of the ratio of C_N^2 (temp. probe) to C_N^2 (optical for the three wind conditions were plotted and are shown in Figures 79 through 81. The only significant change was that the correlation seemed to improve for the steady wind, (Figure 81), and the spread of the ratio seemed to be least for the greater wind conditions, (Figure 79).

In addition to programming the computer to solve the equations given earlier in this section, it was also programmed to compute the probability distribution of the temperature fluctuations recorded. From these data the probability distribution of the temperature fluctuations were plotted. In Figures 82 through 86 are shown five of these plots which cover the range from the minimum to the maximum value of C_N^2 (temp. probe) recorded. The original purpose of this task was just for more complete data presentation, but we noticed in making the plots that if a straight line (exact Gaussion distribution) was best fitted to those data points about the mean, and C_N^2 (temp. probe) computed from this best fit Gaussian distribution, the results obtained were in better agreement with C_N^2 (optical). (This is indicative of apparently spuriously high probability wings in the probability distributions, as can be seen by reference to Figures 82 through 86.) Figure 87 shows a plot of the probability distributions of the ratio of C_N^2 (temp. probe) to C_N^2 (temp. probe - best fit) where the values of C_N^2 (temp. probe) were obtained from the original output and the values of C_N^2 (temp. probe - best fit) are computed from the best fit slopes such as those shown in Figures 82 through 86. As can be seen, the values of C_N^2 obtained from temperature data using standard data reduction techniques is consistantly (rms of the variations of the ratio is only 15 percent of the mean) about twice as great as those values of C_N^2 obtained using the best-fit technique. When these best fit data are used to obtain the probability distribution of the ratio of C_N^2 (temp. probe - best fit) to C_N^2 (optical), we obtain, as shown in Figure 88, a mean value for the ratio quite near unity, indicating good agreement for the temperature and optical measurements of the strength of turbulence.

From these comparisons presented of C_N^2 (temp. probe) (computed in the normal manner) to C_N^2 (optical) (which were clearly shown in the section on scintillation to be useable values), we must conclude that predictions of long-range optical system performance, based on temperature evaluations of the strength of turbulence, would be at

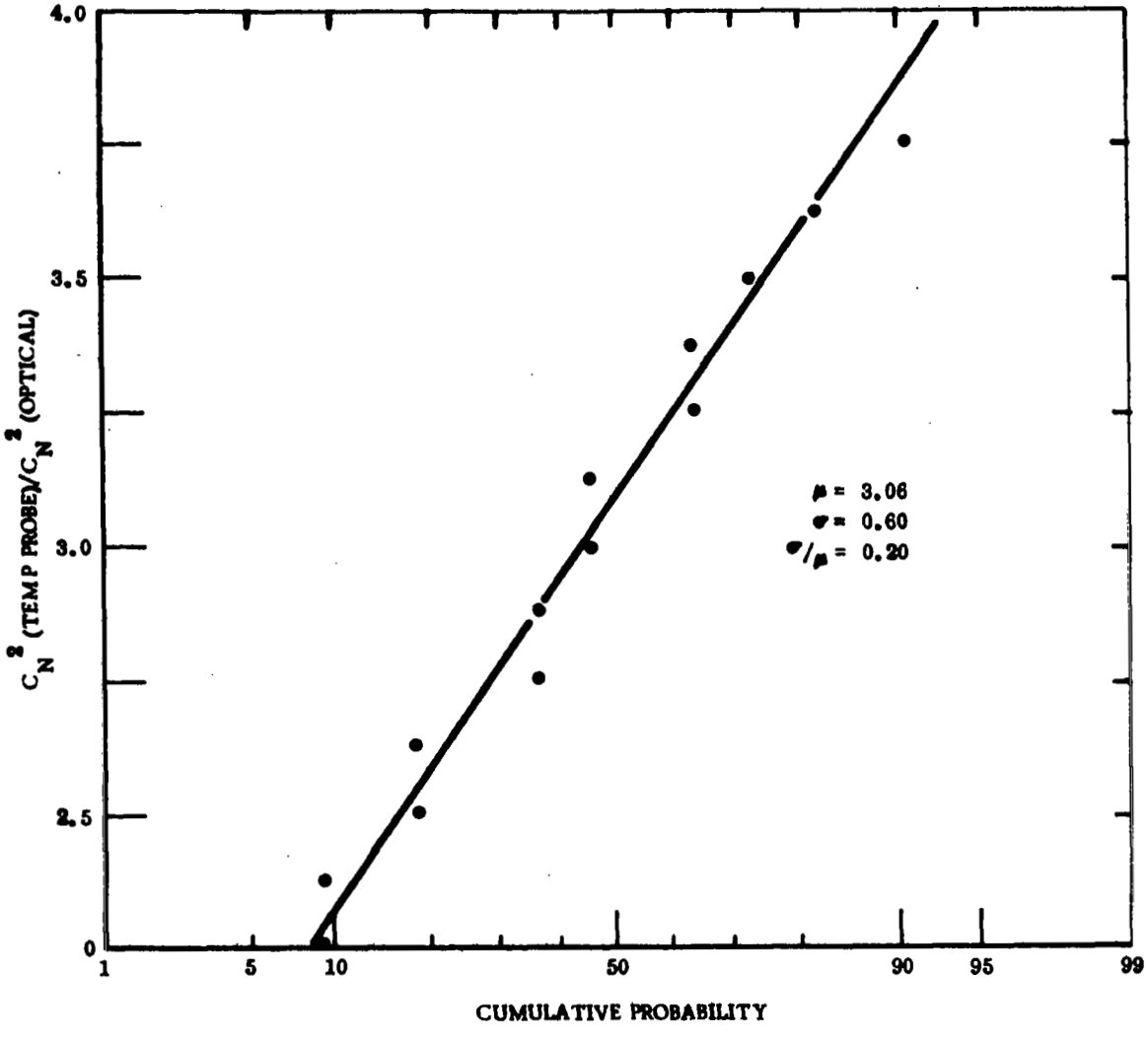

FIGURE 79. Probability Distribution of Ratio of C_N^2 (Temp Probe) to C_N^2 (Optical). Data taken from Runs #701 - #711, (6/28/68).

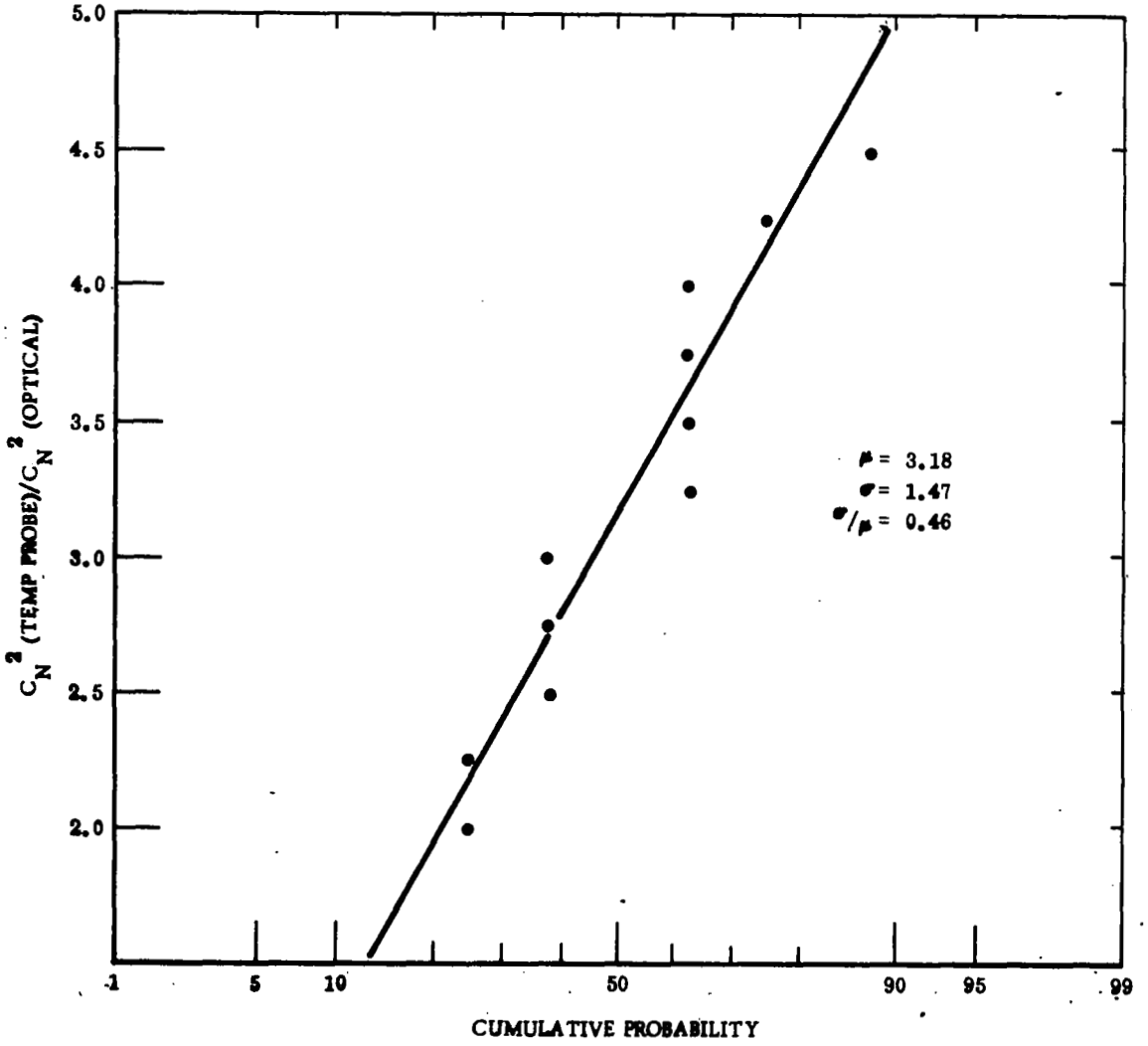

FIGURE 80. Probability Distribution of Ratio of C_N^2 (Temp Probe) to C_N^2 (Optical). Data taken from Runs #801 - #809, (6/28/68).

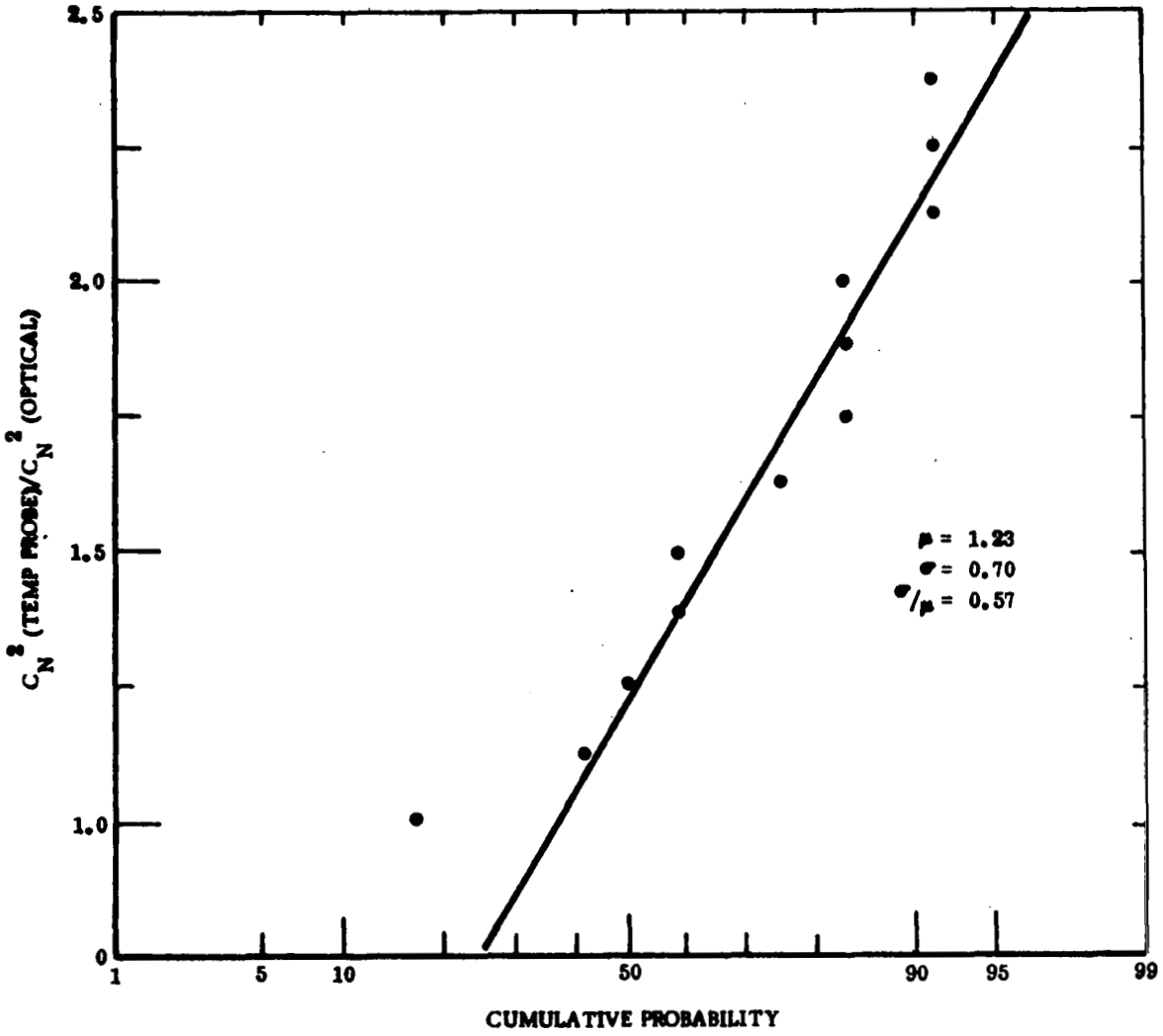

FIGURE 81. Probability Distribution of Ratio of C_N^2 (Temp Probe) to C_N^2 (Optical). Data taken from Runs #810 - #821, (6/28/68).

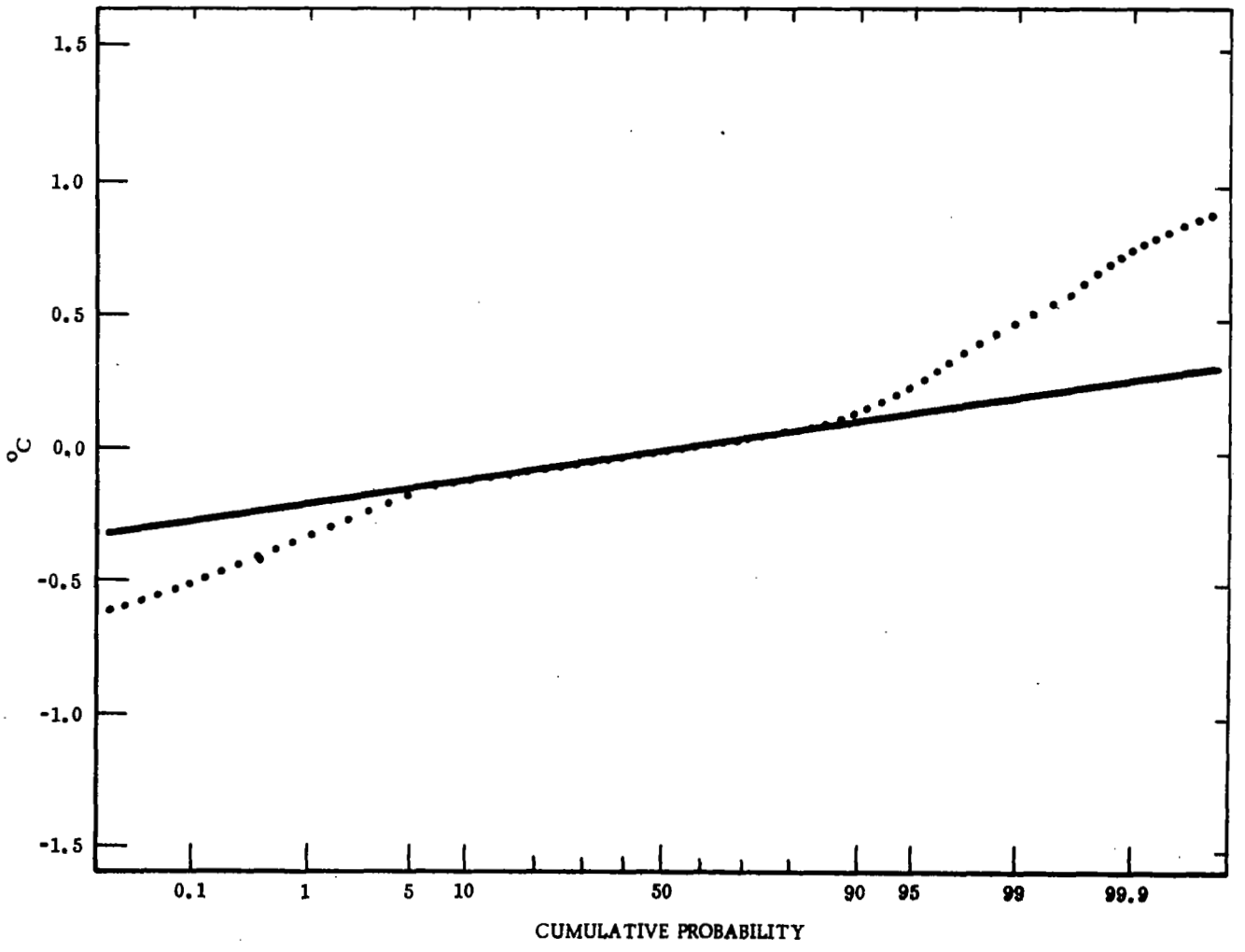

FIGURE 82. Probability Distribution of Temperature Fluctuations. Data taken from Run #808, (6/28/68).

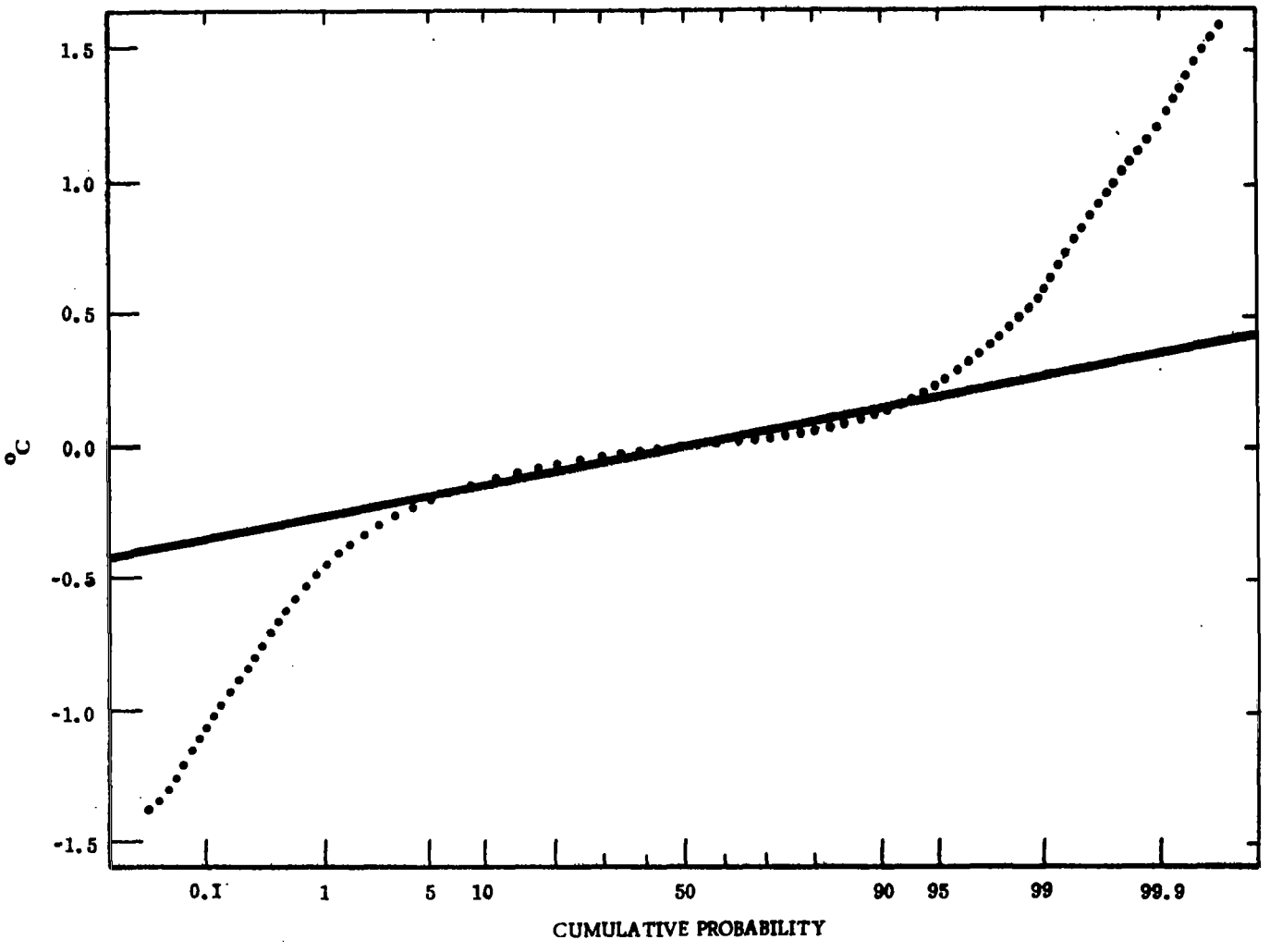

FIGURE 83. Probability Distribution of Temperature Fluctuations. Data taken from Run #705 (6/28/68).

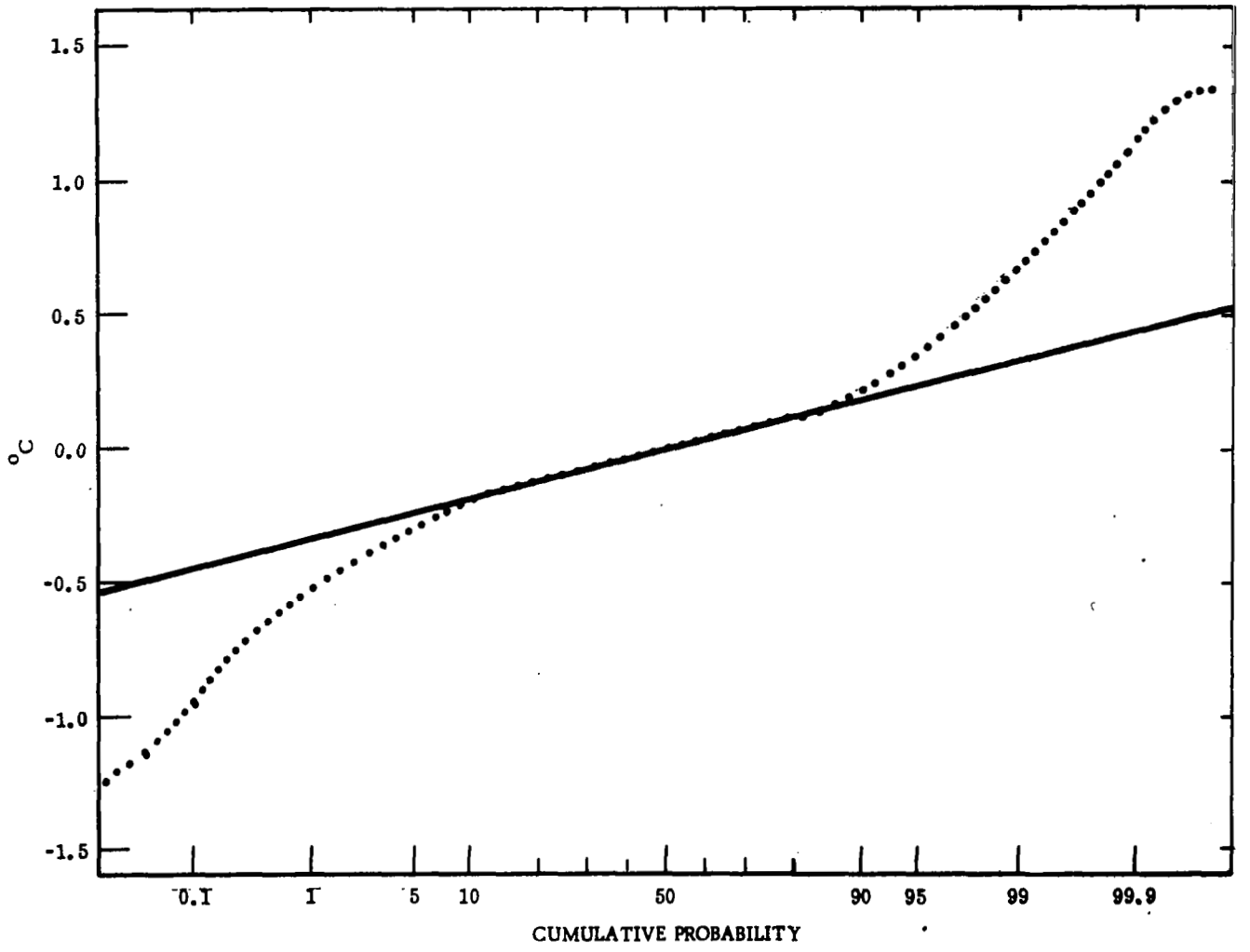

FIGURE 84. Probability Distribution of Temperature Fluctuations. Data taken from Run #816, (6/28/68).

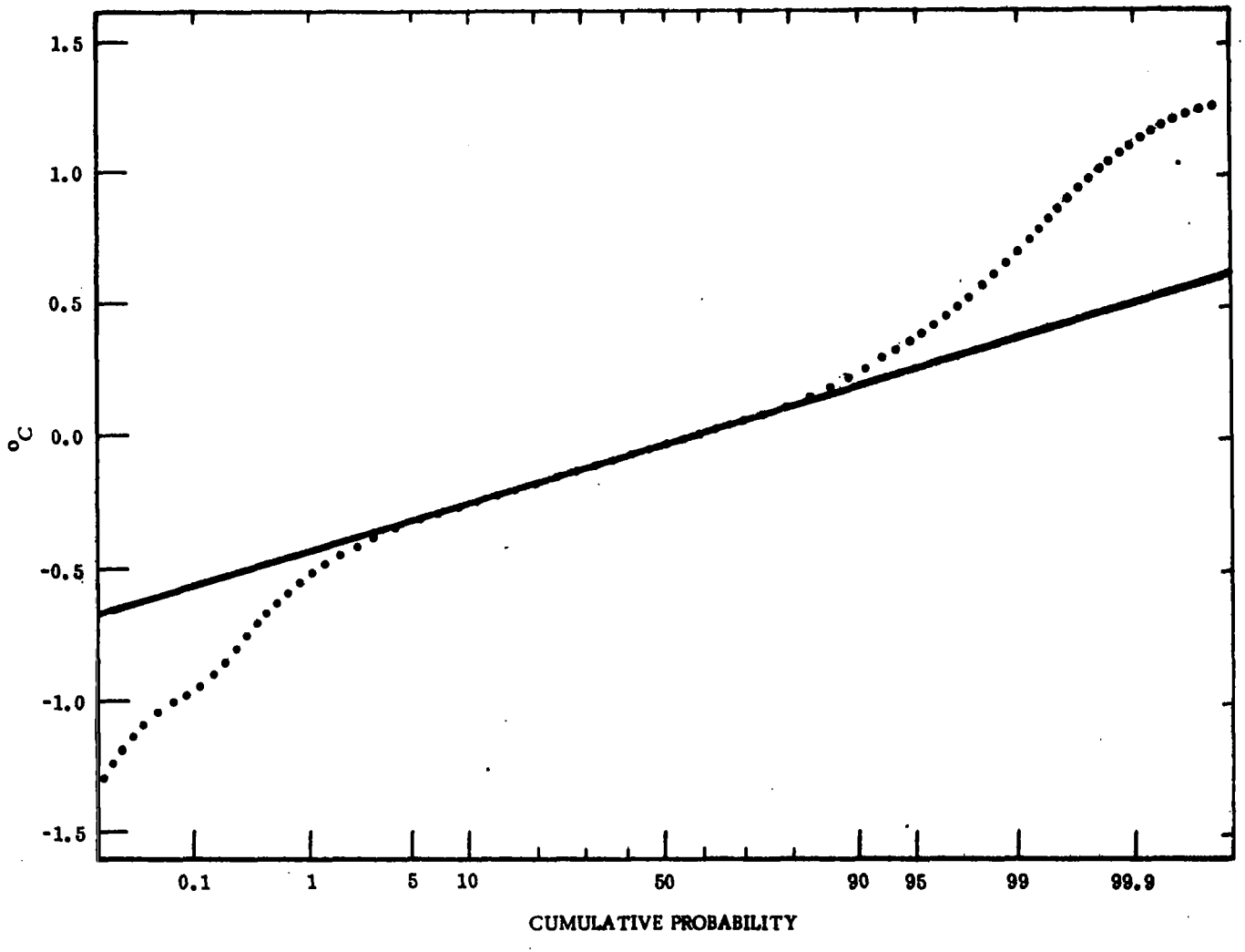

FIGURE 85. Probability Distribution of Temperature Fluctuations. Data taken from Run #701, (6/28/68).

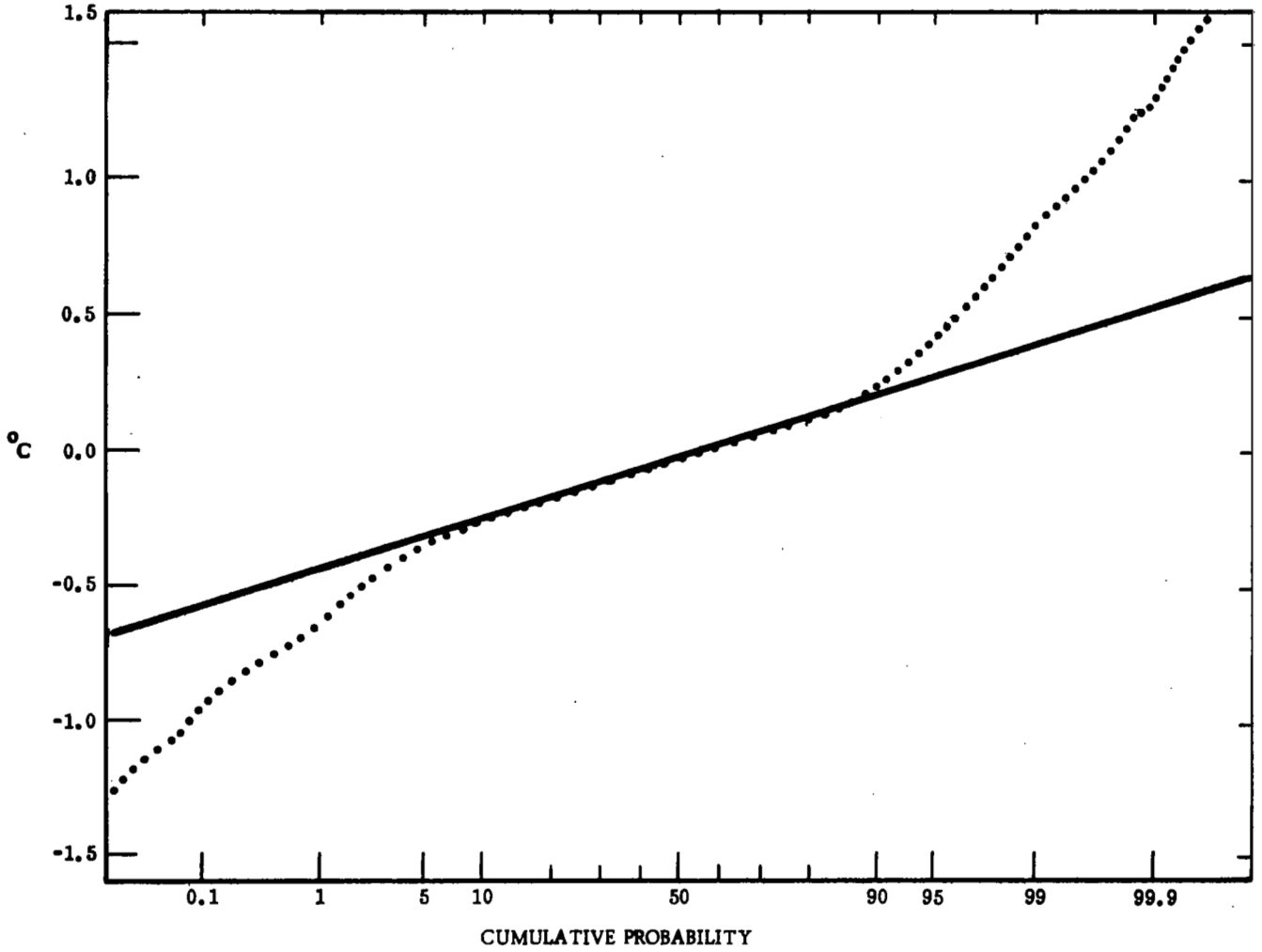

FIGURE 86. Probability Distribution of Temperature Fluctuations. Data taken from Run #812, (6/28/68).

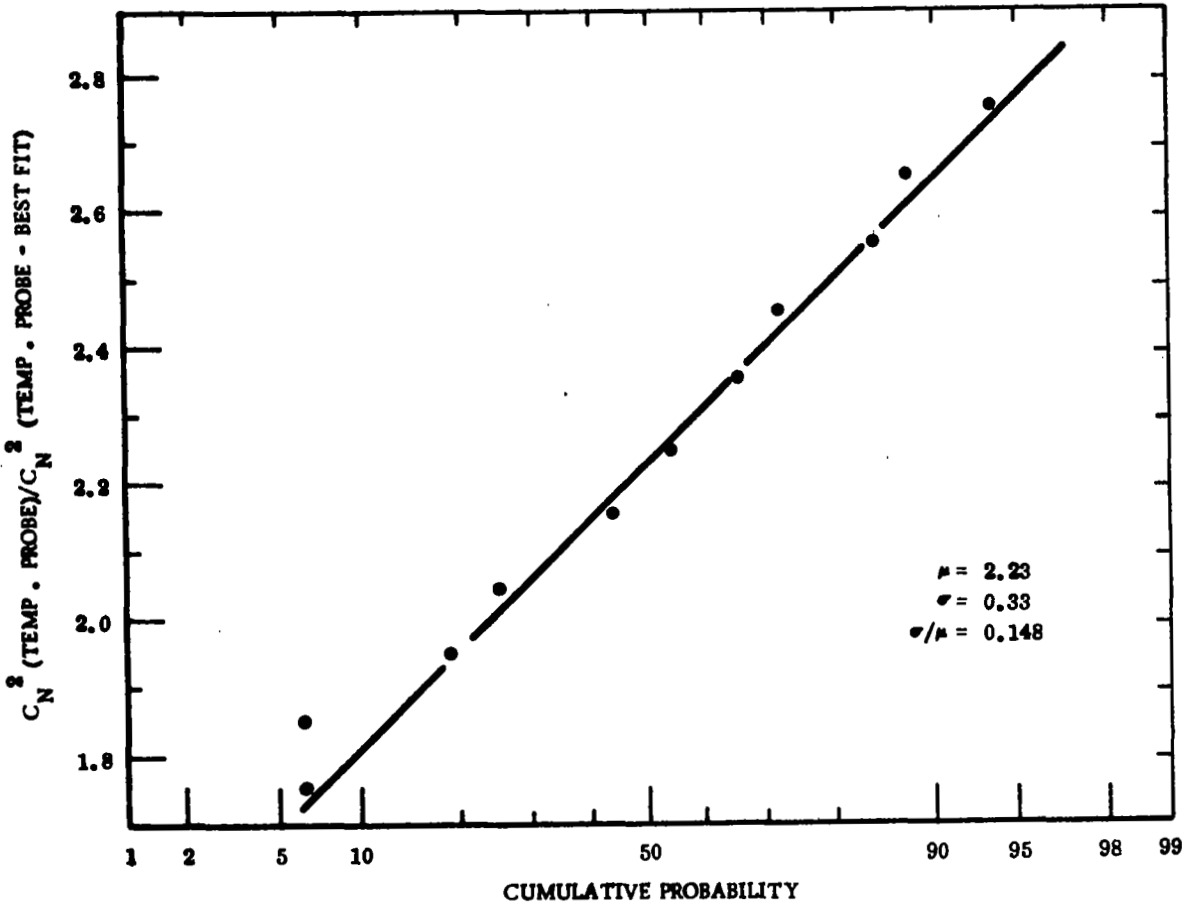

FIGURE 87. Probability Distribution of Ratio of C_N^2 (Temp Probe) to C_N^2 (Temp Probe - Best Fit). Data taken from Runs #808, #705, #816, #701 and #812, (6/28/68).

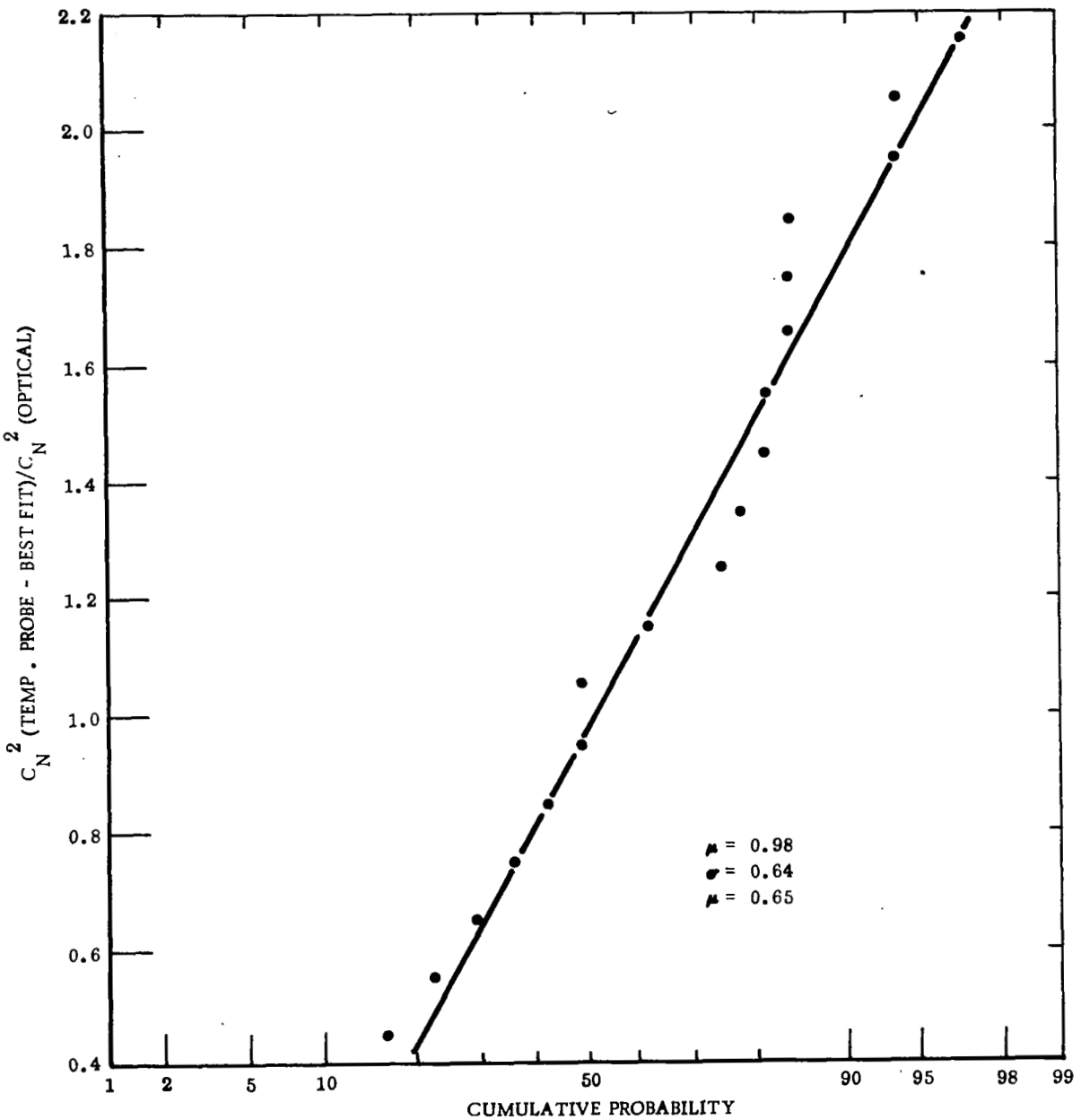

FIGURE 88. Probability Distribution of Ratio of C_N^2 (Temp Probe - Best Fit) to C_N^2 (Optical). Data taken from Runs #808, #705, #816, #701, and #812, (6/28/68).

least subject to question. It may, however, be possible, as we have shown, to obtain more useable values of strength of turbulence from temperature measurements with a modification to the normal method of data reduction. However, before such a technique can be used with confidence it will require considerable experimental verification. It is also, not inappropriate to ask to question "Why does it work?". The small amount of averaging associated with the temperature measurement, as compared to the optical measurements was considered as a possible cause of the discrepency. Since, all things considered equal, the optical measurement enjoyed 2000 times the averaging of the temperature measurement. However, it is difficult to define a mechanism acting through this factor that could produce the observed results. At present two conjectures appear as reasonable answers. First, there is the possibility that the temperature probes are subject to some type of spiking noise generation mechanism. Perhaps they are being struck by dust particles or buffeted by wind gusts that change the resistance at the point where the wire is mounted, thus giving rise to the apparently spurious, high probability wings of the distribution. The second possibility is that the spikes which produce the wings are due to sharp changes in the atmospheric temperature. These changes would be, characteristically, associated with turbulence in the spectral range outside the inertial subrange which does not effect the optical scintillation (because the irregularities are so large) and which are not properly included in the inertial subrange equation relating the temperature-structure function and the temperature structure constant.

D. REFERENCES FOR SECTION VI.

1. G. R. Ochs, "A Resistance Thermometer for Measurement of Rapid Air Temperature Fluctuations", ESSA Technical Report IER 47-ITSA, 1967.

2. V. I. Tatarski, "Wave Propagation in a Turbulent Medium", McGraw-Hill Book Company, New York, 1961, Equation 13.56, p. 225.

3. A Kolmogorov, in Turbulence, Classic Papers on Statistical Theory, S. K. Friedlander and L. Topper, Editors (Interscience Publishers, John Wiley and Sons, Inc., New York, 1961) p. 151.

VII. CONCLUSIONS AND RECOMMENDATIONS

A. CONCLUSIONS

Based on the experimental program we have performed and the data as presented in this report, there are four important conclusions that we can draw with relatively high certainty regarding the nature of optical propagation in the atmosphere. These concern (1) the validity of log-amplitude variance results obtained using the Rytov Approximation within a limited range of conditions; (2) the fact that magnitude of scintillation does not increase with increasing predicted values (as predicted by the Rytov Approximation), and in fact shows an unexpected dependence on wavelength and predicted value; (3) the fact that incoherent radiation scintillation shows the same dependence on wavelength, path length, and strength of turbulence as laser radiation, in the range of agreement with the Rytov Approximation; and (4) the fact that under most conditions, the probability distribution of scintillation is log-normal. The following expands upon these points.

(1) The Rytov Approximation predicts that the strength of scintillation, as measured by the log-amplitude variance, will be proportional to the seven-sixths power of the wave number, the eleven-sixths power of the path length, as well as to the refractive index structure constant. Moreover, these predictions are presented with claims of an unlimited range of abilities. We have found that the predictions* are very accurately obeyed whenever the predicted log-amplitude variance does not exceed some critical value. However, when the predicted log-amplitude variance exceeds this critical value, the Rytov Approximation is grossly incorrect.

(2) We have found that for those cases in which the Rytov Approximation prediction of the log-amplitude variance exceeds a critical value, the measured log-amplitude variance was never larger than the critical value. This has been reported previously in the Russian literature, and more recently in some unpublished American work. In these words, the phenomenon has

*In that range where the Rytov Approximation appears accurate we found that predictions made using spherical wave theory rather than present laser theory (both based on Rytov Approximation) provided a slightly better fit to our measurement data.

been referred to as saturation-scintillation, a nomenclature which we consider to adequately describe the results we have observed. Because of the way in whcih out data was taken, that is by actually measuring the probability distribution rather than one of the moments of the intensity scintillation, we can be certain that the saturation of scintillation that we observed was a true physical phenomen rather than an instrument effect. The observed saturation of scintillation demonstrated a value which decrease with increasing predicted values. The decrease was proportional to the predicted log-amplitude variance to the -0.17 power. The critical value for log-amplitude variance, i.e., the value beyond which saturation may be considered to have set in, was observed to be very strongly wavelength-dependent. This was an entirely unexpected dependence, the existence of which has fundamental implications derivable from dimensional consideration.

(3) Measurements were made with an 800 A-wide, filtered arc lamp source centered at about 5000 Å, along with measurements of the scintillation of an Argon laser, both propagating over nearly the same path. All measurements were taken in a range in which saturation was not expected. Both sources followed the Rytov Approximation well enough to confirm the theoretical predictions that a filtered incoherent source undergoes scintillation in very much the same manner as a laser source, at least in the range of validity of the Rytov Approximation.

(4) Measurements were made of the probability distribution of intensity scintillation. It was found that (with the exception of a limited number of cases in which the atmosphere could not be considered to have an inertial sub-range because of the very low wind velocity, estimated at almost zero mph), the probability distribution was always very close to log-normal. Equipment dynamic range limited the range over which the probability distribution could be measured. However, the range of data obtained very definitely confirmed the validity of the log-normal distribution. The measurement range over which consideration was attributable to confirmation of the log-normal distribution was obtained covers in one case a range of 8 standard deviations in probability, and in another case an intensity dynamic range of three decades. The results apply equally well for saturated

and unsaturated scintillation. The variety of different saturation log-amplitude variances observed precludes the possibility that the data could fit any distribution as lacking in degrees-of-freedom as the Rayleigh distribution.

In addition to these four major considerations, three more minor conclusions can be drawn from this work, concerning (5) the utilization of a temperature probe pair for measuring the refractive index structure constant; (6) the general utility of the scintillation measurements and data reduction process which was used in this work; and (7) the existence of anomalous turbulence conditions. We expand upon these points below.

(5) Measurements of the temperature structure constant, from which the refractive index structure constant can be derived, may be, but can not be confirmed to be, equivalent to optical scintillation measurements. It was found that using the standard method of reduction of the temperature probe data, based on calculation of the mean square temperature difference at the probes, the correlation between the temperature data and scintillation data was very poor.

Examining the probability distribution of the temperature data, it was observed that it followed a normal distribution for small and moderate temperature differences, but not for large temperature differences. Using the temperature difference variance obtained from the slope of the distribution in the small temperature difference range to calculate the temperature difference variance and from that the temperature structure constant, the temperature measurements were again compared with the scintillation measurements. It was found that these showed very good agreement between temperature and scintillation data. We conclude from this that with this modified procedure for data reduction, rather than the standard method, very good agreement can be obtained between temperature and scintillation measurements.

(6) The procedure for measurements log-amplitude variance which we utilized in all cases was based on obtaining the data to plot the probability distribution for scintillation, and then computing the log-amplitude variance from

the slope of a straight line fitted to the plotted distribution. In almost all cases, the apparent accuracy of the measurement, as determined in a number of ways, was very good, typical 5 to 10% approximate error. This is vastly superior to any of the measurement techniques utilized elsewhere.

(7) It was observed that under very low wind velocity, anomalous scintillation results were obtained. The distribution was definitely not log-normal. Under these conditions, we observed log-amplitude variances that were exceptionally high, much higher than saturation values. The measured log-amplitude variance showed no relation to any form of predicted value, neither the Rytov Approximation predictions nor saturation predictions. The probable cause of this situation is the fact that for near zero wind velocity, close to the ground the Reynolds number of the air flow is relatively low and an inertial sub-range is not generated, thus invalidating not only all theoretical work (based as it is on the existence of the Kolmogorov inertial sub-range), but also most all other experimental experience, generally obtained under conditions for which an inertial sub-range exists.

B. RECOMMENDATIONS

While this program has answered many questions, provided a surprising glimpse at other results, and given us a firm base for forming certain judgements, extrapolating, and planning future experimental work, it leaves many questions till untouched or only partially answered. These questions are of such a nature that they are fundamental to many future programs and should be answered before any of the more ambitious undertakings are intiated. All of these matters, which we consider to comprise five basic categories, are best planned for performance over the same horizontal ground path used in the present program, i.e., Emerson Lake.

The first of the recommended categories of additional experimental work involves further measurements at 10.6 microns. A concerted effort must be undertaken to obtain reliable measurements of the probability distribution of scintillation. We must establish whether or not the distribution observed in the current work was truly representative or spurious, due to instrument effects or anomalous turbulence conditions. The question of whether or not the log-amplitude variance conforms

accurately to the Rytov Approximation, at least for short ranges, must be answered (no matter what the probability distribution turns out to be.)

The second of the recommended categories of additional experimentation involves the saturation of scintillation. The basic 0.514 micron scintillation measurements need not be repeated; they were sufficiently conclusive. However, the 0.514 micron measurements should be re-run at, say, two kilometers with variable magnification transmitter optics to change the diameter of the transmitted beam to see if source size influences the level at which saturation of scintillation occurs. (In addition, the variable magnification transmitter when used at short ranges, $\leq$ 1km, will permit a more careful check of present theory concerned with finite laser sources by making it possible to obtain scintillation data over a wide range of Ω values.) The 1.15 micron scintillation measurements should be extended to larger ranges and thus obtain more data to confirm the wavelength dependence of the saturation of scintillation. The 10.6 micron measurements should also be pushed to larger ranges to provide additional data on this wavelength dependence -- assuming, of course, that the initial 10.6 micron work does not confirm the anomalous results obtained for the wavelength in the present work. (It is doubtful that enough laser power and detector sensitivity could be obtained at 3.39 microns to permit meaningful scintillation measurements at ranges large enough to give evidence of saturation of scintillation, but this should be re-examined.)

The third of the categories of recommended additional work involves obtaining wavefront distortion data both under conditions where scintillation obeys the Rytov Approximation, and for conditions in which scintillation is saturated. The existent "seeing monitor" should be sufficiently calibrated that we will be able to decide whether or not anomalous results we might get would be instrument effects or truly inherent in the physics of propagation -- which unfortunately was not possible in the current program. It should be sufficient to restrict these measurements to a 0.514 micron source.

The fourth category of recommended experiments concerns measurements of the covariance of scintillation under both saturated and unsaturated scintillation conditions. The measurements should be made at 0.514 microns utilizing a weak lens to spread the beam and make the source simulate a true point source.

The fifth category of recommended experiments involves work to resolve the question of how to measure the refractive-index structure constant utilizing temperature probes. The apparent result that proper measurements are obtained if the spread around the mean temperature-difference fluctuation is used to estimate the temperature-difference variance (rather than using the measured variance obtained from the full data), should be confirmed by more extensive tests.

It is our belief that these measurements are the most effective next step in expanding our general understanding of atmospheric optical effects, of laying the foundation for further theoretical work, and for developing the data base from which to plan the vertical propagation path investigations which are necessary for the planning of various ground-referenced space applications of optical technology, especially laser technology. This work could probably be most easily and effectively accomplished as a continuation of the work done under the present contract.

APPENDIX A

THE EFFECT OF INSTRUMENTATION DYNAMIC RANGE LIMITATIONS ON MEASURED VALUES FOR A LOG-NORMAL DISTRIBUTION -- AN ANALYTIC EXAMINATION

ABSTRACT

Because the moments of a log-normally distributed intensity are dominated by the infrequent very large spikes, a measurement system with limited dynamic range will have difficulty obtaining meaningful measurements. An analytic evaluation of the effect of the limited dynamic range shows that the dynamic range limitation will cause fixed log-amplitude variance to be measured (using intensity-moment measurement techniques), no matter how large the actual log-amplitude variance is. It is recommended that a probability distribution measurement technique be used to avoid this problem.

INTRODUCTION

Utilizing the so-called Rytov Approximation, it has been shown in theoretical analysis[1] that for propagation of an infinite plane wave over a statistically uniform path, that the log-amplitude variance, σ_ℓ^2 to be expected obeys the equation

$$\sigma_\ell^2 = 0.31\ k^{7/6}\ z^{11/6}\ C_N^2 \tag{1.1}$$

Here k is the wave-number of the radiation, z is the path length, and C_N^2, called the refractive-index structure constant, is a quantity which measures the optical strength of atmospheric turbulence. Similar equations have been derived for propagation of a spherical wave[2] and for a laser beam[3]. These results differ from Eq. (1.1) only in what is, in effect, the numerical constant on the right-hand side.

In recent years, a controversy has flourished[4,5,6,7] about the question of the accuracy of the Rytov Approximation. Until recently, and probably because most of the effort was theoretical rather than experimental, there had been little progress in resolving this question. With the recent appearance of some experimental examination of the matter[8,9,10], it now seems possible to resolve if not the full question of the accuracy of the Rytov Approximation*, at least the question of the accuracy of an equation such as Eq. (1.1). These experimental results appear to indicate that Eq. (1.1), or equivalent, is valid so long as the right-hand side does not predict too large a value -- but that for conditions that lead to the prediction of a value exceeding some upper limit, the measured value of log-amplitude variance remains near the upper limit rather than following the predictions. This surprising result, indicating a saturation of scintillation statistics, appears to clearly refute the results of Eq. (1.1), which is based on the Rytov Approximation.

The occurrence of this saturation raises the question of whether or not what we are seeing is actually an instrumentation effect, rather than a true physical phenomena. In particular, we are concerned that it may be the sensor, or sensor electronics, rather than the phenomena that is saturating. It is well known that the optical intensity scintillation induced by atmospheric turbulence is log-normally distributed[11,12] so that at a log-amplitude variance saturation level of $\sigma_\ell^2 = .6$, where the rms intensity fluctuation is in excess of 300%, intensity spikes of 3000%

of mean value are common, and spikes as high as 30,000% are not infrequent. It is quite reasonable to wonder whether or not the sensor equipment can accommodate such large fluctuations. This is an especially serious concern when one considers the importance of the infrequent but very large spikes in determining the intensity moments of the scintillation. For experimental work, such as that of references 8 and 9, which are based on measurement of intensity moments and infer the log-amplitude moments such as σ_χ^2 from this, the possibility that the equipment could not handle the large spikes and thereby produced the observed saturation results is a significant concern. In this paper, we examine the question of the relationship between the dynamic range of the sensor and the observed versus predicted log-amplitude variance for the measurement data handling configuration used in the work of reference 9. This data handling procedure is based on the measurement of the second moment of intensity, namely

$$\sigma_I^2 = \langle (I - \langle I \rangle)^2 \rangle / \langle I \rangle^2 , \tag{1.2}$$

and computes σ_χ^2 from the relationship

$$\sigma_I^2 = \exp (4 \sigma_\chi^2) - 1 \tag{1.3}$$

which is derived from a log-normal intensity distribution.[13]

While the data handling procedure used in reference 8 was somewhat different, based as it was on the measurement of $\langle | I - \langle \bar{I} \rangle | \rangle$, we may expect similar results to apply to it since it, too, measures a low order moment of the intensity and computes σ_χ^2 from the relation expected between these two moments for a log-normal intensity distribution.

In the next section, we go through the mathematical treatment necessary to simulate the effect of equipment saturation on the measurement of σ_χ^2 when the data handling is based on Eq.'s (1.2) and (1.3). In the final section, we discuss the implication of the results obtained.

Mathematical Analysis for a Saturating Sensor

A log-normal intensity distribution with log-amplitude variance σ_ℓ^2 obeys the probability distribution $P(I)\,dI$ for intensity, where

$$P(I)\,dI = \frac{\exp\{-[\frac{1}{2}/n(I) + \sigma_\ell^2]/2\sigma_\ell^2\}}{(2\pi\sigma_\ell^2)^{1/2}\,2I}\,dI \quad . \tag{2.1}$$

This distribution is normalized to a mean value of intensity of unity so that

$$\int_0^\infty P(I)\,dI = 1 \tag{2.2 a}$$

$$\int_0^\infty I\,P(I)\,dI \equiv \langle I \rangle = 1 \tag{2.2 b}$$

$$\int_0^\infty I^2\,P(I)\,dI \equiv \langle I^2 \rangle = \exp(4\sigma_\ell^2) \quad . \tag{2.2 c}$$

In agreement with Eq. (1.3), we see that

$$\sigma_I^2 = \langle (I - \langle I \rangle)^2 \rangle / \langle I \rangle^2$$

$$= \exp(4\sigma_\ell^2) - 1 \quad , \tag{2.3}$$

so that

$$\sigma_\ell^2 = \frac{1}{4}\,\ell n\,(1 + \sigma_I^2) \quad . \tag{2.4}$$

To carry out the calculation of the effect of equipment saturation, we have implemented a numerical integration over the probability distribution for the various moments of I, taking the integration over a limited range with the range limit corresponding to the various instrument saturation levels. In fact, for ease of computation, the range of integration was truncated at both the upper and lower ends, but the lower end truncation was at such a low value that its significance was always negligible. For a dynamic range of R_j (dB) the integration was taken over the range of values of I from $I_{lower} = I_o\ 10^{-(R_j/20)}$ to $I_{upper} = I_o\ 10^{(R_j/20)}$. The integration was performed using intervals uniformly spaced in a geometric

(rather than an arithmetic) sense. The size of the steps was adjusted for each value of σ_ℓ to have a ratio r_ℓ, where

$$r_\ell = \exp\left(\frac{\sigma_\ell^2}{20} + .01\right). \tag{2.5}$$

At the t^{th} step, I had the value

$$I_t = (r_\ell)^t \, I_o \,, \tag{2.6}$$

and the probability density had the value

$$P(I_t) = \frac{\exp\left[-t^2 \left(\frac{\sigma_\ell^2}{40} + .005\right)^2 / 2\sigma_\ell^2\right]}{I_t \left(8\pi\sigma_\ell^2\right)^{1/2}} \tag{2.7}$$

The step interval was ΔI_t, where

$$\Delta I_t = I_t - I_{t-1} = (1 - r_\ell^{-1}) \, I_t \,. \tag{2.8}$$

The truncated integrals for the zero, first, and second moments of I are then α_j, β_j, and γ_j, respectively, where

$$\alpha_j = \sum_{t=1}^{j} \left[P(I_t) \, \Delta I_t + P(I_{-t}) \, \Delta I_{-t}\right]$$

$$= (1 - r_\ell^{-1}) \sum_{t=1}^{j} \frac{\exp\left[-t^2 \left(\frac{\sigma_\ell^2}{40} + .005\right)^2 / 2\sigma_\ell^2\right]}{\left(2\pi\sigma_\ell^2\right)^{1/2}} \,, \tag{2.9 a}$$

$$\beta_j = \sum_{t=1}^{j} \left[I_t \, P(I_t) \, \Delta I_t + I_{-t} \, P(I_{-t}) \, \Delta I_{-t}\right]$$

$$= (1 - r_\ell^{-1}) \sum_{t=1}^{j} (I_t + I_{-t}) \, \frac{\exp\left[-t^2 \left(\frac{\sigma_\ell^2}{40} + .005\right)^2 / 2\sigma_\ell^2\right]}{\left(8\pi\sigma_\ell^2\right)^{1/2}} \,, \tag{2.9 b}$$

$$\gamma_j = \sum_{t=1}^{j} \left[I_t^2 \; P(I_t)\, \Delta I_t + I_{-t}^2 \; P(I_{-t})\, \Delta I_{-t} \right]$$

$$= (1 - r_\ell^{-1}) \sum_{t=1}^{j} (I_t^2 + I_{-t}^2) \; \frac{\exp\left[-t^2 \left(\frac{\sigma_\ell^2}{40} + .005 \right)^2 / 2\,\sigma_\ell^2 \right]}{(8\pi\,\sigma_\ell^2)^{1/2}} \qquad (2.9\,c)$$

The dynamic range in dB corresponding to truncation after the j^{th} step is

$$R_j = 20 \log_{10} (I_j/I_o)$$

$$= 20 \log_{10} (r_\ell)^j \; . \qquad (2.10)$$

With a sensor whose dynamic range was R_j, (assuming that the important aspect of the limited dynamic range is that it cuts off a very large spike, i.e., a very large value of I, which would otherwise dominate the computation of I^2, so that we may equally well consider the cut-off to reduce the spike to zero or to the dynamic range limit) the measured intensity variance will be

$$(\sigma_I^2)_{meas.} \approx \frac{\gamma_j - (\beta_j)^2}{(\beta_j)^2} \; . \qquad (2.11)$$

When we put this into Eq. (2.4), just as would be done in the experimental work of reference 9, we get

$$(\sigma_\ell^2)_{meas} \approx \frac{1}{4} \ell n \left[\gamma_j / (\beta_j)^2 \right] \qquad (2.12)$$

Utilizing Eq.'s (2.9 b), (2.9 c), and (2.12), we have calculated $(\sigma_\ell^2)_{meas}$ for various dynamic ranges, R, and true log-amplitude variances, σ_ℓ^2. The results of these calculations are shown in Fig. A-1. Each curve is labeled with the corresponding true value of log-amplitude variance, σ_ℓ^2, which is the value $(\sigma_\ell^2)_{meas}$ approaches as the dynamic range, R, approaches infinity.

Discussion of Results

The single most interesting feature of the results shown in Fig. A-1 is the fact that no matter how large σ_χ^2 is for some dynamic range, the measured result $(\sigma_\chi^2)_{meas}$ will be the same. For example, for a 50 dB dynamic range, the measured log-amplitude variance, $(\sigma_\chi^2)_{meas}$ will be about 0.57 (nepers)^2, no matter how large the true log-amplitude variance is. Thus, it is entirely possible that an experiment which attempted to measure log-amplitude variance by measuring the intensity variance might see a saturation of scintillation, due entirely to the limited dynamic range of the equipment -- even when the dynamic range, at first glance, appears entirely adequate.

The problem, of course, is that with a log-normal distribution, most of the variance is contained in a few very large spikes, so that σ_I^2 is dominated by the spikes outside the dynamic range of the equipment. This situation is equally true whether we measure $\langle I^2 - \langle I \rangle^2 \rangle / \langle I \rangle^2$, the case which was analyzed in this paper, or consider $\langle | I - \langle I \rangle | \rangle$ which was done in reference 8. The limited dynamic range makes the measurement of any of the moments of a log-normally distributed random variable a necessarily inaccurate process.

We recommend, as a result of the findings of this study, that measurements of log-amplitude variance not be based upon the measurement of intensity moments. This is because of the difficulty of being certain that observed saturation of scintillation is, indeed, a physical phenomena rather than an instrument effect.* Rather than measure any of the intensity moments, we believe the correct approach is to measure the accessible portion of the probability distribution and from this determine the log-amplitude variance. The method involves more sophisticated electronics and data processing, but has an almost unlimited dynamic range. With the use of this technique, there should be no question whether or not what was measured is a fact or an artifact.

* We wish to have it clearly understood that we are not suggesting that the saturation of scintillation reported in references 8 and 9 does not actually exist. Our own recent results indicate that it does exist. Rather, we wish to point out the difficulty of being certain that their results were not instrument effects, especially in view of the absence of relevant dynamic range information.

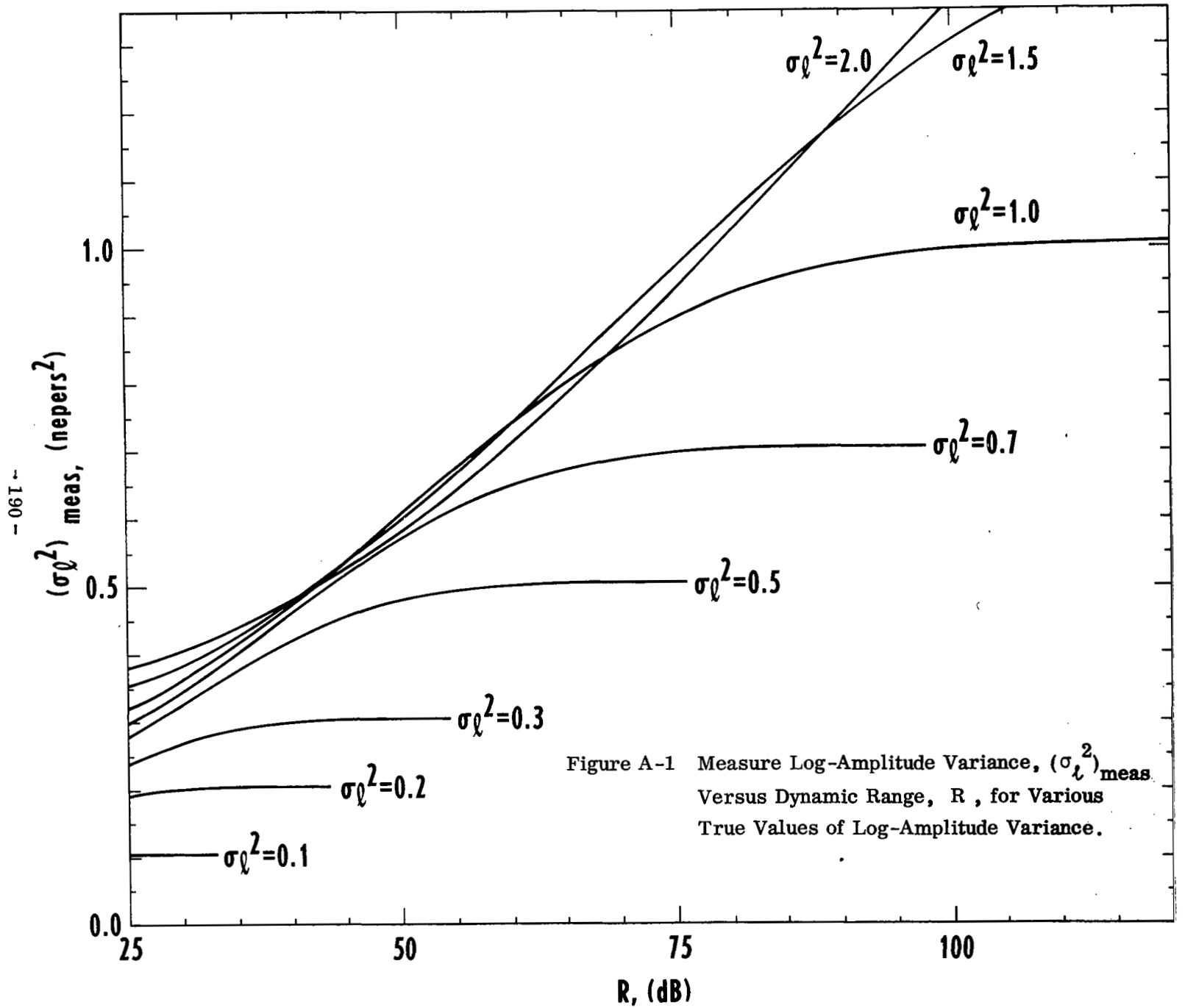

Figure A-1 Measure Log-Amplitude Variance, $(\sigma_\ell^2)_{meas}$ Versus Dynamic Range, R , for Various True Values of Log-Amplitude Variance.

References

1. V. I. Tatarski, "Wave Propagation in a Turbulent Medium" (McGraw-Hill Book Co., New York, 1961), Chapt. 7.
2. Ibid, Chapt. 9
3. D. L. Fried and J. R. Seidman, J. Opt. Soc. Am. 57 , 181 (1967)
4. R. E. Hufnagel and N. R. Stanley, J. Opt.Soc. Am. 54, 52 (1964)
5. D. A. deWolf, J. Opt. Soc. Am. 56 , 812 (1966)
6. W. P. Brown, J. Opt. Soc. Am. 56 , 1045 (1966)
7. D. L. Fried, J. Opt. Soc. Am. 57, 268 (1967)
8. M. E. Gracheva and A. S. Gurvich, Izv.-Radiofizika 8, 717 (1965)
9. P. H. Dietz and N. J. Wright, "Saturation of Scintillation Magnitude in Near-Earth Optical Propagation", Memorandum Report No. 1941, Oct. 1968, U. S. Army Aberdeen Research and Development Center, Ballistic Research Laboratory, Aberdeen Proving Grounds, Maryland.
10. Experimental results on the current contract.
11. Op cit , ref. 1, Fig. 25
12. D. L. Fried, G. E. Mevers, and M. P. Keister, Jr., Jr. Opt. Soc. Am. 57, 787 (1967)
13. D. L. Fried, J. Opt. Soc. Am. 57, 169 (1967)

APPENDIX B

AN EXAMINATION OF THE RYTOV APPROXIMATION

ABSTRACT

A new method of evaluating the accuracy of the Rytov Approximation is presented based on utilization of a formal but exact solution to the propagation equation. By dropping a term in the formal solution, an exact correspondence with the ordinary Rytov Approximation is established. Comparison of the magnitude of the dropped and retained terms permits a clearly meaningful evaluation of the range of validity of the Rytov Approximation. It is found that the approximation is self-consistent, so long as the predicted log-amplitude variance is of the order of magnitude of unity, or less.

INTRODUCTION

The Rytov Approximation, originally applied by Obukhov[1] to the problem of optical propagation in a random medium, has been used extensively since then by workers such as Tatarski[2], Chernov[3], Schmeltzer[4,5], Fried[5,6], Cloud[6], Ho[7], and others. It is probably the most versatile technique that has been applied to the study of optical propagation in the turbulent atmosphere. In fact, almost all of the quantitative theoretical results that we have concerning the statistics of optical propagation in a turbulent medium have been derived using the Rytov approximation. A number of workers have raised questions concerning the accuracy of the Rytov Approximation, e.g. Hufnagel and Stanley[8], Brown[9], and Yura[10]. Generally speaking, these workers have not addressed themselves to an evaluation of the Rytov Approximation per se, but rather to an analysis of some feature of the problem which the author in question considered equivalent or more significant. Whether or not any of these alternative investigations is actually equivalent to an evaluation of the Rytov Approximation is open to some question.

While arguments against the Rytov Approximation have claimed that it was either entirely invalid, or of no greater accuracy than first order wave-function perturbation theory, i.e., it is valid only so long as small perturbations of the optical wave function are predicted[11], the conventional arguments justifying the Rytov Approximation have given no hint that the accuracy of the approximation was bounded in any way. This has led to a belief that the results of the approximation were valid entirely independently of what the magnitude of the results were. In fact, recent experimental results[12,13,14,15] have indicated that the theoretical results obtained with the Rytov Approximation are neither as good as the optimistic estimates nor as bad as the pessimistic predictions. The Rytov Approximation appears to give good accuracy when it predicts small and even moderately large atmospheric-optical effects, but apparently fails when it predicts very large atmospheric optical effects. Experimental results in agreement with theoretical predictions have been obtained even when the results involved a 300% rms intensity scintillation, a quantity clearly outside the accuracy bounds assigned to first order perturbation theory. On the other hand, when the predicted results were much larger than that, the experimental results failed to follow the prediction and instead manifested an apparent saturation, i.e., an apparent upper (saturation) limit on the magnitude of the observed effect. Obviously then, the results of the Rytov Approximation are nowhere near as good as has been claimed by some, nor as bad as has been predicted by others.

Because those analyses that were intended to show that the Rytov Approximation was no better than first-order perturbation theory did not actually address themselves to the proof normally given for the approximation, it seems desirable that a careful examination founded within the context of the normally given arguments should be developed to study the Rytov Approximation and why it appears to be limited. Such an analysis is the subject of this paper. Hopefully, this will lay the foundation for a future effort to extend the range of validity of our approximate solutions to the problem of optical propagation in a randomly inhomogeneous medium.

Statistical Aspects of the Rytov Approximation

The normal approach to the Rytov Approximation starts with the time-independent scalar-wave equation

$$\nabla^2 u(\vec{r}) + [1 + \mu(\vec{r})]\, k^2 u(\vec{r}) = 0 \tag{1}$$

where $u(\vec{r})$ is the wave-function sought, k is the wave-number associated with the temporal oscillations in the boundary conditions, and $\mu(\vec{r})$ is a weak random variation of the refractive-index about its nominal mean value of unity. Then, by utilizing $u_o(\vec{r})$, which is the wave-function compatible with the boundary conditions that would exist if $\mu(\vec{r}) \equiv 0$, it is customary to introduce the complex-phase perturbation $\psi(\vec{r})$, which is defined by Eq. (2),

$$u(\vec{r}) = u_o(\vec{r}) \exp[\psi(\vec{r})], \tag{2}$$

and recast Eq. (1) into the form

$$\nabla^2 \psi(\vec{r}) + 2 \frac{\vec{\nabla} u_o(\vec{r})}{u_o(\vec{r})} \cdot \vec{\nabla} \psi(\vec{r}) + 2 k^2 \mu(\vec{r}) + k^2 \mu^2(\vec{r}) - \vec{\nabla} \psi(\vec{r}) \cdot \vec{\nabla} \psi(\vec{r}) = 0 \tag{3}$$

in which the function to be solved for is now $\psi(\vec{r})$ instead of $u(\vec{r})$. In this formulation, the $k^2\mu^2(\vec{r})$ term is normally dropped with the argument that since μ is very small, the $k^2\mu^2$ term can be dropped since it is much smaller than the $2k^2\mu(\vec{r})$ term which is retained. There is little question that this is generally a valid approximation, but for heuristic purposes, we shall retain the $k^2\mu^2$ term for awhile.

The essence of the Rytov Approximation, as it is normally presented, is the argument that the $\vec{\nabla}\psi \cdot \vec{\nabla}\psi$ term can also be dropped from Eq. (3) since it too is very much smaller than $2k^2\mu$. To see that this is the case, it is only necessary to note that $\vec{\nabla}\psi$ has the

dimensions of one-over-length, and that the length in question is that length in which the wave-function's phase is changed one radian (or its log-amplitude one neper) by the random medium. This length corresponds, with a reasonable degree of accuracy, to the diameter, D, of an optical system whose diffraction limit is equal to the atmospheric limit on angular resolution. Thus the Rytov Approximation is customarilly justified on the basis of the inequality

$$2\,k^2\,\mu >> (1/D)^2 \tag{4}$$

which can be rewritten in the form

$$2\,(2\pi)^2\,\mu >> (\lambda/D)^2. \tag{5}$$

When the atmospheric limit on angular resolution is as poor as one-milliradian, so that $\lambda/D = 10^{-3}$, the inequality of Eq. (5) is amply satisfied even when μ is as small as 10^{-6}. Since refractive index variations in the atmosphere are generally at least an order of magnitude larger than 10^{-6}, and since seeing conditions are generally significantly better than one-milliradian, the conventional conditions for justification of the Rytov Approximation may be considered well satisfied.

We shall now show, however, that the conditions justifying the Rytov Approximation are not properly embodied in Eq. (4) or Eq. (5), and that a quite different formulation is required which will take account of the statistical aspects of the problem. To demonstrate this, we write the full formal solution to Eq. (3), treating $2\,k^2\,\mu$, $k^2\mu^2$, and $\vec{\nabla}\psi\,.\,\vec{\nabla}$ all on a par. The solution has the form

$$\psi(\vec{r}) = \frac{1}{4\pi\,\imath} \int d\vec{r}\; \frac{\exp(\imath k|\vec{r}-\vec{r}'|)}{|\vec{r}-\vec{r}'|} \quad \frac{u_o(\vec{r}')}{u_o(\vec{r})} \left[2\,k^2\mu(\vec{r}') - \vec{\nabla}\psi(\vec{r}')\,.\,\vec{\nabla}\psi(\vec{r}') \right]. \tag{6}$$

We will now examine the Rytov Approximation from the point of view of dropping each of the terms in this integral. First, simply as a brief exercise to emphasize the statistical aspect of the problem, to highlight the fact that we are not asking merely for the statistical aspect of some approximate solution to a differential equation, but for an approximation of some statistical aspect of the exact solution to a differential equation, let us consider the calculation of the mean value of $\psi(\vec{r})$, i.e., $\langle\psi(\vec{r})\rangle$.

Starting with Eq. (6) and utilizing the fact that the operations of integration and summation both commute with the operation of taking an ensemble average, we see that $\langle \psi(\vec{r}) \rangle$ can be expressed as an integral which has in its integrand the factor $[2k^2 \langle \mu(\vec{r}) \rangle + k^2 \langle \mu^2(\vec{r}') \rangle - \langle \vec{\nabla} \psi(\vec{r}') \cdot \vec{\nabla} \psi(\vec{r}') \rangle]$. If the normal approximations had been made prior to obtaining the solution in Eq. (6) from Eq. (3), then the integrand would contain only $[2k^2 \langle \mu(\vec{r}') \rangle]$. Since, however, μ is the variation of the refractive-index about its mean value, then $\langle \mu(\vec{r}') \rangle \equiv 0$ and the conventional approximations would have resulted in the dropping of the non-vanishing terms, namely $k^2 \langle \mu^2(\vec{r}') \rangle$ and $\langle \vec{\nabla} \psi(\vec{r}') \cdot \vec{\nabla} \psi(\vec{r}') \rangle$ in favor of a term which vanished. Clearly no valid arguments can justify such an approximation. The conclusion that we must draw is that before the dropping of any term can be justified, we must examine, not the magnitude of the term as it appears in the differential equation, or the random magnitudes it may assume, but rather the contribution of the term to the statistical quantity being evaluated.

The consideration of the calculation of $\langle \psi(\vec{r}) \rangle$ is a somewhat misleading example since it so clearly gives no role to the $2k^2 \mu(\vec{r}')$ term, which is normally considered to be the only significant term of the three in question in Eq. (3). The calculation of the second moments associated with $\psi(\vec{r})$ are more directly of interest and more relevant to the discussion, as they each involve a non-vanishing contribution arising from the $2k^2 \mu(\vec{r})$ term in Eq. (3). In this case, the justification of the Rytov Approximation hinges on the much more complicated matter of estimating and comparing the contribution due to the terms normally retained and those normally dropped. In calculating a second moment of ψ, starting from Eq. (6), we obtain a product of two integrals over $\vec{r}'$- and $\vec{r}''$-space, which we convert into a double integral over $\vec{R}$- and $\vec{\rho}$-space, where $\vec{R} = \frac{1}{2}(\vec{r}' + \vec{r}'')$ and $\vec{\rho} = (\vec{r}' - \vec{r}'')$. The integrand now contains various statistical quantities, such as $\langle \mu(\vec{R} + \frac{1}{2}\vec{\rho}) \mu(\vec{R} - \frac{1}{2}\vec{\rho}) \rangle$, all of which clearly depend on $\vec{\rho}$. In justifying the Rytov Approximation, we must ask not only how large the statistical terms in the integrand are, but also over what volume in $\vec{\rho}$-space are they significant. It is this matter of estimating the volume over which there is a contribution which is principally a statistical matter that has been overlooked in all previous work on this problem. To see this aspect of the problem more clearly, let us examine a particular problem in detail. Before doing this, however, we wish to clean up one minor matter concerning the $k^2\mu^2$ term which will simplify our future notation.

The term $\vec{\nabla}\psi \cdot \vec{\nabla}\psi$ can be rewritten as

$$\vec{\nabla}\psi \cdot \vec{\nabla}\psi \equiv \left(\frac{\partial}{\partial x}\psi\right)^2 + \left(\frac{\partial}{\partial y}\psi\right)^2 + \left(\frac{\partial}{\partial z}\psi\right)^2 . \tag{7}$$

We will let the z-axis correspond to the nominal direction of propagation of the wave. By the very simple matter of ray-tracing over a distance less than a millimeter, it can be shown (and should be apparent from inspection) that the $k^2\mu^2$ term in Eq. (6) almost exactly cancels the $\left(\frac{\partial}{\partial z}\psi\right)^2$ part of the $\vec{\nabla}\psi \cdot \vec{\nabla}\psi$ term in Eq. (6). (As a matter of fact, the $k^2\mu^2$ term and the $\left(\frac{\partial}{\partial z}\psi\right)^2$ term are both negligibly small in all calculations of interest. We have introduced the matter of their almost exact cancellation more to obtain a simplification of the formulation than as part of the approximation study.) If we introduce the notation $\vec{\nabla}_T$ to denote the gradient transverse to the z-axis, i.e., containing only the x- and y-derivatives, so that

$$\vec{\nabla}_T\psi \cdot \vec{\nabla}_T\psi = \left(\frac{\partial}{\partial x}\psi\right)^2 + \left(\frac{\partial}{\partial y}\psi\right)^2 , \tag{8}$$

then we can rewrite Eq. (6) as

$$\psi(\vec{r}) = \frac{1}{4\pi i}\int d\vec{r}' \frac{\exp(ik|\vec{r}-\vec{r}'|)}{|\vec{r}-\vec{r}'|}\frac{u_o(\vec{r}')}{u_o(\vec{r})}\left[2k^2\mu(\vec{r}') - \vec{\nabla}_T\psi(\vec{r}')\cdot\vec{\nabla}_T\psi(\vec{r}')\right] . \tag{6'}$$

Now with Eq. (6'), we are ready to proceed with a more realistic and detailed comparison of the terms dropped and the terms retained in the Rytov Approximation, as appropriate in a statistical calculation.

Second Moment Calculation

The calculation of a second moment of ψ, such as the log-amplitude variance $C_\chi(0)$, which is formally defined by the equation

$$C_\chi(0) = \langle [\mathrm{Re}[\psi(\vec{r}) - \langle\psi(\vec{r})\rangle]]^2\rangle \tag{9}$$

involves a $\vec{\rho}$-integration with the integrand having the statistical factor $\langle\mu(\vec{R}+\frac{1}{2}\vec{\rho})\,\mu(\vec{R}-\frac{1}{2}\vec{\rho})\rangle$ as the normally retained term in the Rytov Approximation.

From Eq. (6') we see that the term normally dropped in the Rytov Approximation involves a $\vec{\rho}$-integration having as the statistical factor $\langle \{ \mathrm{Re} [\vec{\nabla}_T \psi (\vec{R} + \frac{1}{2}\vec{\rho}) \cdot \vec{\nabla}_T \psi (\vec{R} + \frac{1}{2}\vec{\rho}) - \langle \vec{\nabla}_T \psi (\vec{R} + \frac{1}{2}\vec{\rho}) \cdot \vec{\nabla}_T \psi (\vec{R} + \frac{1}{2}\vec{\rho}) \rangle] \} \{ \mathrm{Re} [\vec{\nabla}_T \psi (\vec{R} - \frac{1}{2}\vec{\rho}) \cdot \vec{\nabla}_T \psi (\vec{R} - \frac{1}{2}\vec{\rho}) - \langle \vec{\nabla}_T \psi (\vec{R} - \frac{1}{2}\vec{\rho}) \cdot \vec{\nabla}_T \psi (\vec{R} - \frac{1}{2}\vec{\rho}) \rangle] \} \rangle$[16]. We shall denote these terms as I_R for the term retained in the Rytov Approximation and factor it into $(2k^2)^2 \cdot V_R \cdot S_R$, where V_R is the relevant volume in $\vec{\rho}$-space for the retained term and S_R is the magnitude of the statistical quantity in the $\vec{\rho}$ integrand of the retained term, and the source of the $(2k^2)^2$ term is apparent from examination of Eq. (6'),

$$I_R = (2k^2)^2 \; V_R \cdot S_R \,, \tag{10a}$$

and shall denote the term dropped by I_D with factors V_D and S_D relating to the volume in $\vec{\rho}$-space and magnitude of the statistical factor in the dropped term, so that

$$I_D = V_D \cdot S_D \tag{10b}$$

Our problem is to estimate I_R and I_D and establish the conditions under which $I_R > I_D$, since this is the requirement for the Rytov Approximation to give valid results.

To simplify our notation, we shall consider propagation over a statistically homogeneous path of length L and shall restrict our attention to the point at which $\vec{R}$ has a z-component equal to αL, where α is a constant between zero and one. We shall assume that the boundary conditions correspond to a point source, as the example most nearly representative of the cases of actual interest.

The evaluation of V_R and S_R are greatly simplified by possession of the large body of knowledge that has developed in calculation of quantities like $C_\ell(0)$ within the domain of the Rytov Approximation. This knowledge tells us that at the point of interest in $\vec{R}$-space, the $\vec{\rho}$-integral is dominated by the contribution due to the harmonic components of spatial frequencies associated with the wavelength ρ_o. Here

$$\rho_o = (4L/k)^{1/2} \; \alpha^{1/2} \; (1 - \alpha)^{1/2} \tag{11}$$

is the Fresnel diffraction length associated with the distance between the point $\vec{R}$ and the two ends of the propagation path.[17] The quantity S_R is the portion of the refractive-index covariance associated with the separation ρ_o and may be estimated as one-half the refractive-index structure function, i.e.

$$S_R = \frac{1}{2} \mathcal{D}_n(\rho_o) , \tag{12}$$

where $\mathcal{D}_n(\rho)$, the refractive-index structure function is formally defined as

$$\mathcal{D}_n(\rho) = \langle [\mu(\vec{r} + \tfrac{1}{2}\vec{\rho}) - \mu(\vec{r} - \tfrac{1}{2}\vec{\rho})]^2 \rangle \tag{13a}$$

and in the Kolmogorov inertial subrange has the value[18]

$$\mathcal{D}_n(\rho) = C_N^2 \rho^{2/3} . \tag{13b}$$

Here C_N^2 is a quantity, called the refractive-index structure constant which measures the optical strength of random refractive index variations in a turbulent medium. This means that S_R takes the value

$$S_R = \frac{1}{2} C_N^2 \rho_o^{2/3} . \tag{12'}$$

Since the refractive-index structure function is isotropic in three dimensions, then it follows that V_R is of the order of magnitude of a sphere of radius ρ_o, i.e.,

$$V_R = \frac{4}{3} \pi \rho_o^3 . \tag{14}$$

Combining Eq.'s (12') and (14) in Eq. (10a), we see that

$$I_R = \frac{8}{3} \pi k^4 C_N^2 \rho_o^{11/3} \tag{15}$$

Now making use of Eq. (11), we obtain the result that

$$I_R = \frac{8}{3} \pi (2)^{11/3} \alpha^{11/6} (1 - \alpha)^{11/6} k^{13/6} L^{11/6} C_N^2 \tag{16}$$

This is the term which we shall compare with I_D to assess the predictable range of validity of the Rytov Approximation. We carry out the estimation of I_D in the next section.

Estimation of the Term Dropped in the Rytov Approximation

To evaluate I_D we start by noting that the term corresponding to S_D, namely $\langle \{ \mathrm{Re} [\vec{\nabla}_T \psi (\vec{R} + \frac{1}{2}\vec{\rho}) \cdot \vec{\nabla}_T \psi (\vec{R} + \frac{1}{2}\vec{\rho}) - \langle \vec{\nabla}_T \psi (\vec{R} + \frac{1}{2}\vec{\rho}) \cdot \vec{\nabla}_T \psi (\vec{R} + \frac{1}{2}\vec{\rho}) \rangle]] \{ \mathrm{Re} [\vec{\nabla}_T \psi (\vec{R} - \frac{1}{2}\vec{\rho}) \cdot \vec{\nabla}_T \psi (\vec{R} - \frac{1}{2}\vec{\rho}) - \langle \vec{\nabla}_T \psi (\vec{R} - \frac{1}{2}\vec{\rho}) \cdot \vec{\nabla}_T \psi (\vec{R} - \frac{1}{2}\vec{\rho}) \rangle]] \rangle$ bears a very strong resemblance to the fourth cross moment between the transverse derivatives of ψ at $\vec{R} + \frac{1}{2}\vec{\rho}$ and $\vec{R} - \frac{1}{2}\vec{\rho}$. It is fairly well established that ψ obeys a Gaussian distribution [19] and a fortiari the derivates of ψ. The standard Gaussian relationship between the fourth and second moments is that the former is equal to three times the square of the latter. The factor of three applies when the fourth moment involves four identical terms (i.e., random variables), so that three equal value pairings of sets of two-and-two are possible. In this case, the terms are not quite identical nor are all possible pairings possible -- in fact, only one well specified pairing is involved. For this case, we may approximate our fourth moment by the square of the second moment. The second moment of interest is associated with the derivative of ψ at $\vec{R} + \frac{1}{2}\vec{\rho}$ and at $\vec{R} - \frac{1}{2}\vec{\rho}$. (Note that the second moment with both values taken at $\vec{R} + \frac{1}{2}\vec{\rho}$, or both at $\vec{R} - \frac{1}{2}\vec{\rho}$, is made irrelevant to the problem by virtue of the subtraction of $\langle \vec{\nabla}_T \psi \cdot \vec{\nabla}_T \psi \rangle$ in each of the two factors of S_D.)

To evaluate the second moment of the derivatives of some function, we need only recall it is equal to minus the second derivative of the covariance of the function. I.e., if $C_{\nabla_T \psi}(\rho)$ is the second moment (covariance) of the transverse derivative of ψ, and $C_\psi(\rho)$ is the covariance of ψ, then

$$C_{\nabla_T \psi}(\rho) = -\nabla_T^2 \, C_\psi(\rho) . \tag{17}$$

Since the structure function, $\mathcal{D}_\psi(\rho)$, is twice the variance, $C_\psi(0)$, minus the covariance, $C_\psi(\rho)$, i.e.,

$$\mathcal{D}_\psi(\rho) = 2[C_\psi(0) - C_\psi(\rho)] , \tag{18}$$

it follows that

$$C_{\nabla_T \psi}(\rho) = \frac{1}{2} \nabla_T^2 \, \mathcal{D}_\psi(\rho) . \tag{19}$$

For the purposes of this study, we may consider $\mathcal{D}_\psi(\rho)$ to be given by the expression

$$\mathcal{D}_\psi(\rho) = \frac{3}{8} (2.91) k^2 C_N^2 \, L\alpha \, \rho^{5/3} \tag{20}$$

which applies for a point source and has been derived (at least in its infinite plane wave source form) by several methods besides the use of the Rytov Approximation[8,20,21]. Substituting Eq. (20) into (19) and recalling that as developed at the start of this section,

$$S_D = [C_{\nabla_T \psi}(\rho)]^2 \ , \tag{21}$$

we see that

$$S_D = [\ \frac{5}{24}\ (2.91)\ k^2\ C_N^{\ 2}\ L\alpha\ \rho^{-1/3}\ ]^2 \tag{22}$$

For the moment we leave unanswered the question of what is the appropriate value of ρ to substitute in Eq. (22). Instead we proceed with an estimation of the value of V_D to go with any value of ρ .

To estimate the correlation volume, V_D , we distinguish between the transverse dimensions which can be approximated by a circle of radius ρ , and the length along the z-axis which is a much more complicated matter. Correlation between wavefront distortion of scale ρ measured at z and at $z + \xi$ will only be meaningful if both z and $z + \xi$ are less than L , i.e., are in the allowed range of the $\vec{\rho}$-integration, and if ξ does not exceed the near field distance for ρ , i.e., if

$$\xi \leq k\rho^2/2\pi \ , \tag{23}$$

for if the distance ξ is any larger, diffraction will have smeared out the correlation that existed between the wavefront distortion at two points a transverse distance ρ apart at z . Thus V_D is either equal to $\pi\rho^2$ times $L(1-\alpha)$, when the range of integration limits V_D , or equal to $\pi\rho^2$ times $k\rho^2/2\pi$ when diffraction limits V_D . We argue that the dominant contribution to I_D occurs when the value of ρ is such as to make these two forms of V_D equal, namely: $[\,2\pi L(1-\alpha)/k\,]^{1/2}$. Obviously, for values of ρ less than this, S_D . V_D is reduced in value. For larger values of ρ , which would make the product increase in value, we argue that propagator-type terms arising from the exponential and u_o functions in Eq. (6') will suppress the contribution. We advance this argument on the basis of a physical insight which requires that diffraction effects be possible if interference effects which cause strong intensity variations are to occur. Without such a restriction, we would find that we seemed to be obtaining a contribution to intensity variations due to the correlation of wavefront distortions at two points far enough apart, say several meters,

which could not possibly interfere in the distance of the propagation path, say one kilometer.

With the value of ρ necessary to make the two forms of V_D equal, i.e.,

$$\rho = [2\pi L(1-\alpha)/k]^{1/2} \quad (24)$$

taken as the dominant value in determining I_D, we find that

$$V_D = \pi \rho^2 L(1-\alpha) \quad (25)$$

and that

$$I_D = \frac{25}{576}(2.91)^2 \pi (2\pi)^{2/3} \alpha^2 (1-\alpha)^{5/3} k^{10/3} (C_N^2)^2 L^{11/3} \quad (26)$$

We are now in a position to compare I_R and I_D and determine the conditions under which the Rytov Approximation may be considered accurate.

Comparison of Terms and Conclusions

The condition for the Rytov Approximation to be accurate is that I_R be greater than I_D, i.e., that the contribution of the term retained exceed the contribution of the term dropped. Because of the approximate nature of the estimating procedures we have used, too much attention should not be paid to the numerical constants. We will retain them but be much more interested in the dimensional aspects of the comparison. The ratio I_R/I_D, obtained from Eq.'s (16) and (26) has the value

$$\frac{I_R}{I_D} = \frac{2^{12} \times 3}{5^2}(2.91)^{-2} \pi^{-2/3} \left(\frac{1-\alpha}{\alpha}\right)^{1/6} k^{-7/6} L^{-11/6} (C_N^2)^{-1} \quad (27)$$

Noting that for a point source, the Rytov Approximation predicts that the log-amplitude variance, $C_\ell(0)$, will have the form

$$C_\ell(0) = 0.124 k^{7/6} L^{11/6} C_N^2 \quad (28)$$

so that the ratio I_R/I_D in Eq. (27) can be rewritten in the form

$$\frac{I_R}{I_D} = 3.35/C_\ell(0) \, . \tag{29}$$

The conclusion that we draw from this result is that so long as the log-amplitude variance, $C_\ell(0)$, predicted by the Rytov Approximation is not too large, the terms dropped in making the Rytov Approximation are apparently negligible. When, however, the predicted value is of order unit or larger, then it is apparently an unjustified approximation to drop those terms as they can contribute significantly to the result. The precise calculation of exactly how much they contribute is, unfortunately, still a matter for future study.

Footnotes

1. A. M. Obukhov, Izv. Akad. Nauk. SSSR, Ser. Geofiz., 2 , 155 (1953).

2. V. I. Tatarski, Wave Propagation in a Turbulent Medium , (McGraw-Hill Book Co., New York, 1961).

3. L. A. Chernov, Wave Propagation in a Random Medium, (McGraw-Hill Book Co., New York, 1960).

4. R. A. Schmeltzer, Quart. Appl. Math. 24, 339 (1967).

5. D. L. Fried and R. A. Schmeltzer, IEEE 1965 International Antenna and Propagation Symposium Program and Digest, p.123.

6. D. L. Fried and J. D. Cloud, "Optical Propagation in the Atmosphere: Theoretical Evaluation and Experimental Determination of the Phase Structure Function", presented at and reported in the proceedings of the Conference on Atmospheric Limitations to Optical Propagation, at the U. S. National Bureau of Standards, CRPL, 18-19 March 1965.

7. T. L. Ho, "Log-Amplitude Fluctuations of a Laser Beam in a Turbulent Atmosphere", submitted for publication to J. Opt. Soc. Am.

8. R. E. Hufnagel and N. R. Stanley, J. Opt. Soc. Am. 54, 52 (1964).

9. W. P. Brown, J. Opt. Soc. Am. 56, 1045 (1966).

10. H. T. Yura, "Electromagnetic Field and Intensity Fluctuations in a Weakly Inhomogeneous Medium", RM-5697-PR, July 1968.

11. The significance of claiming that the calculations were no better than first order perturbation theory can only be properly comprehended when it is realized that the intensity scintillation associated with optical propagation through the atmosphere is log-normally distributed, so that even when the rms intensity fluctuations are as small as 30%, there are frequent intensity spikes of more than twice normal intensity, and these spikes contribute significantly to the rms value of the scintillation. If the Rytov Approximation were no better than first order perturbation theory, it probably could not be relied on even when it predicted rms intensity scintillations as low as 30%, corresponding to a log-amplitude variance, $C_\chi(0)$, equal to 0.02 -- indeed a small value yet apparently outside the range of first order perturbation theory.

12. M. E. Gracheva and A. S. Gurvich, Izv. -Radiofizika 8, 717 (1965).

13. M. E. Gracheva, Izv.-Radiofizika 10, 775 (1967).

14. P. H. Dietz and N. J. Wright, "Saturation of Scintillation Magnitude in Near-Earth Optical Propagation", Memorandum Report No. 1941, Oct. 1968, U. S. Army Aberdeen Research and Development Center, Ballistic Research Laboratory, Aberdeen Proving Grounds, Maryland.

15. Results on the current contract.

Footnotes (Continued)

16. There are two other terms not contained in the rather lengthy expression given in the text, which we have not bothered to include in the discussion. The first is a cross term between the $2k^2\mu$ and the $\vec{\nabla}_T \psi \cdot \vec{\nabla}_T \psi$ factors which we have ignored as it is odd in its lowest order in the random variables and at least in that lowest order should vanish. The second is a pair of terms similar to the one in the text, except that one of the real operators, i.e. Re , is replaced by the imaginary operator, Im . We argue that these terms vanish by virtue of symmetry considerations.

17. For an infinite plane wave source, instead of a spherical wave (or laser) source, the factor $\alpha^{1/2}$ would be missing in Eq. (11).

18. A. Kolmogorov, in Turbulence, Classic Papers on Statistical Theory, edited by S. K. Friedlander and L. Topper (Interscience Publishers, Inc., New York, 1961) p.151.

19. C. L. Wyman, "Angular Fluctuations of a Laser Beam Propagated Through the Atmosphere", Masters Thesis, University of Alabama, 1968. p.14 and Fig. 8.

20. M. J. Beran, J. Opt. Soc. Am. 56, 1475 (1966).

21. D. L. Fried, J. Opt. Soc. Am. 58, 961 (1968).

APPENDIX C

"EXPLANATION AND ANALYSIS OF A SEEING METER FOR MEASUREMENT OF THE ATMOSPHERE ON FINITE EXPOSURE IMAGES"

ABSTRACT

The problem of defining and measuring the MTF achievable through the atmosphere for a finite exposure image is explained and a formal definition developed. An instrument to carry out such measurements, representing a variant of the device used by Coulman, and originally developed by Ransay and Kobler, is described and its explanation set forth heuristically. The operation of the instrument is subjected to a full formal analysis demonstrating that it does, indeed, measure the finite exposure MTF, providing its operation conforms to certain requirements set forth in the analysis.

INTRODUCTION

The concept of modulation transfer function (MTF) has proven particularly powerful in assessing the imaging quality of an optical system, both in the specification and the evaluation stage. While the concept is most commonly applied to the more tangible portions of an optical system, namely the lenses, the film, and the platform, it can also be applied to the intervening medium between the object and the optics, i.e., the atmosphere.[1,2,3,4] In this latter case, it not only permits discussion of the quality of an image formed, working through the atmosphere, but by measuring the quality of the image and working the data reduction in the reverse direction, it makes possible the measurement of certain of the statistics for optical propagation through the atmosphere. Because of an exposure-time dependence in the MTF, obtained through the atmosphere, it is not possible to directly apply the type of MTF-measurement equipment commercially available for the measurement of atmospheric effects. It is the purpose of this paper to describe and analyze an optical system that permits direct measurements of the MTF achieved through the atmosphere.

In the next section, we shall discuss in detail the concept of MTF and its exposure time dependence. In subsequent sections, we shall describe the measurement apparatus, which is closely related to that used by Coulman[5,6] and originally described by Ramsey and Kobler[7], as well as try to present in heuristic terms the principles of operation of the device, and will then present a detailed analytic treatment of the device's performance. Finally, we shall discuss the details concerning proper operation, as derived from the analysis.

MTF and Time Exposure MTF

The concept of MTF is often presented in terms of the ratio of contrast achieved by an optical system imaging a sinusoidal illumination pattern of a particular spatial frequency, relative to the contrast of the illumination pattern. Since the ratio varies with the spatial frequency, the MTF is a function of spatial frequency. This frequency may be measured in cycles per unit length in the image plane, in cycles per radian field-of-view -- a particularly useful form when the object is effectively at infinity and emphasis is on angular resolution, as it is in discussing atmospheric effects, or in cycles per unit length in the object plane -- a useful form when emphasis is placed on achievement of ground truth. Since

these frequencies are easily converted from one form to the other by knowledge of the effective focal length of the optics and the optics-to-object distance, we shall discuss spatial frequency measured in the image plane, but consider this entirely equivalent to using any of the other forms.

The concept of MTF as described above is entirely equivalent to the electrical engineering concept of transfer function as applied to a circuit, and as in that concept, is restricted to linear time invariant slowly varying devices -- although in the case of optics, we are interested in devices which are position invariant (or slowly varying with position), since it is focal plane position rather than time that acts as the principal independent variable in imagery. In electrical engineering, although the transfer function is definable in terms of the ability of the circuit to pass a signal of some frequency, it is often more convenient and on a fundamental basis is formally equivalent to work with the transfer function definition stated as the Fourier-exponential transform of the circuit's response to a unit impulse input. In optics, the same sort of definition is equally applicable. The modulation transfer function is very conveniently defined as the Fourier-exponential transform of the image of a unit strength point source. This is the same as stating that the MTF is the transform of the point spread function. We shall work with the MTF defined this way. Thus the modulation transfer function, $\mathfrak{I}(\vec{f})$ for a spatial frequency $\vec{f}$ is definable as

$$\mathfrak{I}(\vec{f}) = \int d\vec{r}\ \exp(-\imath 2\pi \vec{f} \cdot \vec{r})\ I(\vec{r}), \tag{2.1}$$

where $\vec{r}$ is a position vector in the focal plane and $I(\vec{r})$ is the spread image formed from a point object. The $\vec{r}$-integration is over the infinite plane. Note that $\vec{f}$ is a vector since spatial frequency has a direction as well as a magnitude. Often the MTF is isotropic and depends only on the magnitude of $\vec{f}$, denoted by f. Although $\mathfrak{I}(\vec{f})$ can be complex, if $I(\vec{r}) = I(-\vec{r})$, then the Fourier exponential transform reduces to a Fourier cosine transform and $\mathfrak{I}(\vec{f})$ is restricted to real values. The occurrence of complex values of the MTF implies a significant asymmetry between right and left, or up and down in the point spread function. (Thus the occurrence of coma will yield a complex MTF, while astigmatism will not.)

In the above discussion on imagery, we have considered the situation as time invariant and as a consequence, the time dimension does not appear in Eq. (2.1). In dealing with imaging through the turbulent atmosphere, the point spread function

is continuously changing and $I(\vec{r})$ is more properly represented as a function of time, $I(\vec{r},t)$.* (We shall later use $I(x,y,t)$ to denote the same quantity, x and y denoting the coordinates of the position vector $\vec{r}$.) It would be easy enough to generalize Eq. (2.1) to the form

$$\mathfrak{I}(\vec{f},t) = \int d\vec{r}\ \exp(-i\,2\pi\,\vec{f}\,.\,\vec{r})\, I(\vec{r},t) \qquad (2.1')$$

This would correspond to a single sample short exposure MTF, and just as the atmospheric turbulence and $I(\vec{r},t)$ are random variables, $\mathfrak{I}(\vec{f},t)$ would also be a random variable. It is possible by taking the average of $\mathfrak{I}(\vec{f},t)$ or of its magnitude to proceed to either the long or short exposure MTF[2]. This approach, avoiding the middle ground of treating finite length exposures, leaves us without a basis for judging whether an exposure is short and when it is very short, and thus providing a basis for developing a measurement procedure, and therefore is not the formulation we shall use. Rather, we shall use a formulation with a much clearer physical interpretation which clearly brings out the relevance of the exposure time, and which allows us to deal with the treatment of finite length exposures.

---

* To properly understand the kind of complexity that the time dependence can introduce into the measurement, let us consider a very simple example of an optical system which forms an ideal point image (zero spread) except that the location of the point image fluctuates randomly with time. If we consider an ensemble of zero length exposures, all the images are of zero width and have the same uniform power spectrum. However, the transform of the image, in distinction to the power spectrum, is random to the extent that at any frequency, while the sum of the squares of the sine and cosine amplitudes are fixed, the relative magnitude and signs of the two amplitudes are random. For a non-zero duration exposure, the image is no longer a point but appears somewhat smeared. How smeared (or spread) the image is depends on the duration of the exposure. As a consequence of the width of the image, the power spectrum is no longer uniform, but rather decreases with increasing spatial frequency. The fall off in power spectrum can be thought of as due to the fact that the image transform is the average of the instantaneous image transforms that go with the multitude of zero duration exposures that make up our finite length exposure. Averaging of the random amplitudes, with their possible sign reversals between samples, does not preserve the energy in the power spectrum. It is the difficulty of properly treating this time averaging, considering that the time dimension has to serve both to define the duration of the exposure and to provide the ensemble of data for statistical averaging, that makes the matter of treating the finite duration exposure a non-trivial problem.

We define an exposure of duration Δt in terms of the exposure function $W(t;\Delta t)$. The exposure function is defined as a pulse of half width Δt centered at $t = 0$, with unity peak height. The exposure function is smoothly varying and corresponds to the integration process of film or a vidicon in forming an image. Δt (or more properly, $2\Delta t$) is the exposure time. In place of the instantaneous point spread function $I(\vec{r}, t)$, we shall use $\mathcal{I}(\vec{r}; \Delta t)$, the exposure total point spread function, where

$$\mathcal{I}(\vec{r}; \Delta t) = \int_{-\infty}^{+\infty} dt\ W(t; \Delta t)\ I(\vec{r}, t) \tag{2.2}$$

It is obvious that $\mathcal{I}$ is the spread function image corresponding to the instantaneous spread function I formed by time exposure during the period Δt defined by the function W. From Eq. (2.2), we can develop the finite exposure MTF, $\mathfrak{I}(\vec{f}; \Delta t)$ in analogy to Eq. (2.1) as

$$\mathfrak{I}(\vec{f}; \Delta t) = \int d\vec{r}\ \exp(-2\pi i \vec{f} \cdot \vec{r})\ \mathcal{I}(\vec{r}; \Delta t), \tag{2.3}$$

which we can reduce to the form

$$\mathfrak{I}(\vec{f}; \Delta t) = \int_{-\infty}^{+\infty} dt \int d\vec{r}\ \exp(-2\pi i \vec{f} \cdot \vec{r})\ I(\vec{r}, t)\ W(t; \Delta t) \tag{2.4}$$

Expressed in (x,y) components with (f_x, f_y) denoting the components of $\vec{f}$ we have

$$\mathfrak{I}(f_x, f_y; \Delta t) = \int_{-\infty}^{+\infty} dt \int_{-\infty}^{+\infty} dx \int_{-\infty}^{+\infty} dy\ \exp[-2\pi i (xf_x + yf_y)] \times I(x,y;t)\ W(t; \Delta t) \tag{2.4'}$$

Eq. (2.4') is the form which we shall consider as definitive of the finite exposure, duration Δt, modulation transfer function.

The stochastic aspects of the problem, which consider the fact that $I(x,y;t)$ is a random variable and so $\mathfrak{I}(f_x, f_y; \Delta t)$ also is, may be computed by taking the ensemble average of $\mathfrak{I}$ or of some non-linear functions of $\mathfrak{I}$, such as $|\mathfrak{I}|$, $\mathfrak{I}^2$, etc.

The problem of the mathematical treatment of the ensemble average of a non-linear function of the r.h.s. of Eq. (2.4') is part of a program of theoretical studies which need not concern us here. Our interest is in developing a mechanism which will produce random sample values of $\mathfrak{I}(f_x,f_y;\Delta t)$, from which the various statistical averages can be determined by means of analog computer circuitry and averaging. Although the problem ultimately is statistical, we can consider the objective of the device we are studying to be the measurement of sample values of $\mathfrak{I}(f_x,f_y;\Delta t)$. The statistical computations based on $\mathfrak{I}$ can be implemented in so straightforward a manner that we need not be concerned with them. In the next section, we shall describe a device which can measure $\mathfrak{I}$, and will attempt to explain in heuristic terms just why the device works. In the section following that, we shall present the analysis of the device.

MTF Measurement Apparatus

In measuring MTF, there are at least two approaches. The first, and commercially most popular approach, is to cause the image of a point source to be formed and place in the image plane a spatially varying transmittance mask with a sinusoidal pattern. The total transmitted light is the integral of the product of the sinusoid and the point spread function, which is equivalent to the MTF for the spatial frequency of the mask, at least if the spread function is temporally invariant. It is difficult, however, to decide how to apply this technique to evaluation of the MTF for a finite exposure time, temporally varying point spread function. Instead we shall consider a second approach. This approach is based on scanning the point spread function's image with a narrow slit or a knife edge and measuring the total transmitted light as the edge passes across the image. The MTF can be derived by Fourier transforming the measurement data treated as a function of position. If the edge moves very slowly, the measurements can be digitized and the data processed in a digital computer. If the edge moves rapidly, since the edge position is a function of time, the measurements appear to be a function of time and it is convenient to process the signal by conventional electronic filtering techniques, achieving the Fourier transform in a very easily implemented analog fashion.* The device we shall consider is developed along these latter lines.

* It should be noted that the ordinary narrow band filter or power spectrum analyzer is unsuited for this process, as they can not distinguish between the in-phase and quadrature components, i.e., between the real and imaginary parts of the MTF. To achieve this distinction, filtering will have to be accomplished by a phase sensitive voltmeter or its equivalent, using as a reference some signal derived from the mechanical position of the edge.

The apparent problem with this approach is how to achieve measurements corresponding to a finite exposure time. If the edge crosses the point spread function's image in less time than the time in which the image can change significantly, then the temporal variations will be due entirely to the scanning and the filtered signal will, indeed, represent an MTF, but only that of a short exposure (effectively a zero-time) image. If the edge scans very slowly, the image being scanned will appear to be a very long exposure image (assuming irrelevant rapid fluctuations of the signal due to scintillation are suppressed by filtering) and the analog processed signal would also correspond to an MTF, but only that of a long exposure (effectively an infinite-time) image. The former suffers from the problems of knowing how fast an edge scan is fast enough, and from a potential lack of signal-to-noise ratio due to the very short data collection time. The latter suffers from the problems of knowing how slow is slow enough, from consideration of the fact that a slow enough scan may take many minutes, and from the difficulty of performing meaningful spectral analysis of such a slowly varying signal. The immediately obvious compromise of using an intermediate speed scan to obtain the data is entirely unacceptable, as the data will be hopelessly contaminated by the temporal fluctuations of the instantaneous point spread function's image, varying with the random fluctuations of the atmosphere. These fluctuations will be in the same spectral range as the temporal variations caused by the moving edge, which latter contain the information we desire.

To get around this problem, we shall use a repetitive scan, with high speed scanning. The electrical signal will be processed by filtering at the high frequency corresponding to the scan velocity, but will be processed using narrow band techniques. The narrow bandwidth, by forcing the combination of the signals obtained from a series of the scans, results in effect in the processing of an exposure integrated signal. The effective duration of the exposure is approximately the inverse of the bandwidth. By varying the bandwidth, or resolution of the electric signal spectrum analysis, the effective exposure time for the MTF can be controlled. Measurements can be made at all electronic frequencies corresponding to odd multiples of the scan repetition frequency. Each electronic frequency can be related to an MTF spatial frequency by dividing by the scan velocity.

Proof of the above statements will be provided in the detailed analysis of the next section. Before proceeding to that, however, we will describe the general

features of a realization of this type of device.

The optical portion of the MTF measurement equipment consists of a motor-driven, rapidly rotating reticle positioned in the plane of the image for which the MTF is to be determined. It is oriented so that the velocity vector on the reticle at the image spot corresponds to the direction of the spatial frequency vector for which the MTF is to be determined. The reticle pattern consists of a large number of alternately transmitting and opaque, equal width spokes. A photodetector in back of the reticle collects all of the image light that passes through the reticle. This provides the basic electric signal from which the MTF is determined. In a separate region of the reticle, a locally-generated point source of light is imaged on the reticle and then photodetected. This provides a square-wave standard signal, which in a sense encodes the position of the reticle and permits the MTF to be determined. The electronics which actually determine the MTF consist of a pair of phase-sensitive voltmeters such as those made by Princeton Applied Research The voltmeters are tuned to detect at some odd harmonic of the reticle chopping frequency and use the square-wave standard signal as the reference for the phase demodulation. The phase shift in the two meters is adjusted so that one unit is sensitive to the cosine of the frequency, and the other to the sine of the frequency. The voltmeters process the electric signal derived from the image whose MTF is to be determined. The exposure time for which the MTF is being measured is set by the integration time to which the voltmeter is set. The output of the two voltmeters are electrical voltages corresponding to the real and imaginary parts of the MTF. The statistics of the MTF can then be determined by an analog computer circuit processing and averaging the voltmeter outputs.

Formal Analysis

In this section, we shall carry out a formal analysis of the operation of the device described in the previous section. We start with the intensity pattern $I(x,y,t)$ which is the intensity distribution of the image formed by the optical system at the instant of time t. x and y are coordinates in the image plane. We assume that there is some small radius R such that

$$I(x,y,t) \approx 0 \quad \text{if} \quad x^2 + y^2 > R^2 . \tag{4.1}$$

For a moment, let us restrict our attention to any one reticle transmission blade, also located in the image plane. Without loss of generality, we may assume

that the y-axis is parallel to the edges of the blade. We shall let a denote the blade width and v the velocity of the reticle motion in the vicinity of the image spot.* Then the irradiance passing through this particular blade may be written as

$$\iota(t) = \int_{-\infty}^{+\infty} dy \int_{-\frac{a}{2}+vt}^{\frac{a}{2}+vt} dx \; I(x,y,t) \; . \tag{4.2}$$

The total signal $S(t)$ generated by an unending sequence of reticle transmission blades passing the image spot is

$$S(t) = \sum_{j=-\infty}^{+\infty} \iota\,(t + j\,\frac{2a}{v}) \; . \tag{4.3}$$

It is this signal that is put into the phase-sensitive voltmeters to be decomposed into its Fourier sine and cosine components. For mathematical simplicity, rather than deal separately with the sine and with the cosine transforms, we shall treat the exponential transform, the real part of which is the cosine transform, and the imaginary part of which is the sine transform. Thus we consider $\mathcal{S}'(\Omega)$

$$\mathcal{S}'(\Omega) = \int_{-\infty}^{+\infty} dt \;\; \exp(-\iota\Omega t) \;\; S(t) \; , \tag{4.4}$$

where Ω is a temporal frequency in radians per unit time. The finite spectral resolution of the phase-sensitive voltmeter may be denoted by the function $\mathfrak{w}(\Omega - \Omega_o ; \Delta\Omega_o)$ which correspon to a pulse in Ω-space of width $\Delta\Omega_o$ centered at Ω_o .

We note that the Fourier transform of $\mathfrak{w}(\Omega; \Delta\Omega_o)$, namely

$$W(t; \tau_o) = \int_{-\infty}^{+\infty} d\Omega \; \mathfrak{w}(\Omega;\Delta\Omega_o) \; \exp(-\iota\Omega t) \; , \tag{4.5}$$

* Actually, of course, the reticle is rotating so it has different velocities everywhere. However, there is a well defined velocity in the vicinity of the image spot -- providing we do not cause the center of the reticle to be located close to the image spot. The distance from the center to the spot should be some large multiple of R to insure this.

is a pulse of width τ_o where

$$\tau_o \approx 1/\Delta\Omega_o \tag{4.6}$$

and corresponds to the time averaging duration of the phase-sensitive voltmeter.

The actual output of the voltmeter will not be $S'(\Omega)$ but rather

$$S(\Omega_o;\Delta\Omega_o) = \int_{-\infty}^{+\infty} d\Omega \; \mathfrak{w}(\Omega - \Omega_o;\Delta\Omega_o)\; S'(\Omega)\,. \tag{4.7}$$

By combining the above equations, we get

$$S(\Omega_o;\Delta\Omega_o) = \int_{-\infty}^{+\infty} d\Omega \int_{-\infty}^{+\infty} dt \; \mathfrak{w}(\Omega - \Omega_o;\Delta\Omega_o)\; S(t)\; \exp(-\imath\Omega t)$$

$$= \int_{-\infty}^{+\infty} dt \; S(t)\; W(t;\tau_o)\; \exp(-\imath\Omega_o t)$$

$$= \sum_{j=-\infty}^{+\infty} \int_{-\infty}^{+\infty} dt \; \imath\left(t + j\frac{2a}{v}\right)\; W(t;\tau_o)\; \exp(-\imath\Omega_o t)$$

$$= \sum_{j=-\infty}^{+\infty} \int_{-\infty}^{+\infty} dt \int_{-\infty}^{+\infty} dy \int_{-\frac{a}{2}+vt+aj}^{\frac{a}{2}+vt+2aj} dx \; I(x,y,t)\; W(t;\tau_o)\,(-\imath\Omega_o t). \tag{4.8}$$

We note that because of the finite extent of $I(x,y,t)$, only for values of t satisfying the inequality

$$-j\,\frac{2a}{v} - \frac{R}{v} < t < -j\frac{2a}{v} + \frac{R}{v}$$

will the integrand of Eq. (4.8) be non-zero. With properly designed equipment, the time $2R/v$ will be so short that during that time $I(x,y,t)$ can not change significantly. As a consequence, we may replace $I(x,y,t)$ in Eq. (4.8) by

$I(x,y,-j\frac{2a}{v})$, and at the same time replace $W(t;\tau_o)$ by $W(-j\frac{2a}{v};\tau_o)$. Thus we get

$$S(\Omega_o;\Delta\Omega_o) = \sum_{j=-\infty}^{+\infty} \int_{-\infty}^{+\infty} dt \int_{-\infty}^{+\infty} dy \int_{-\frac{a}{2}+vt+2aj}^{\frac{a}{2}+vt+2aj} dx \; I(x,y,-j\frac{2a}{v}) \; W(-j\frac{2a}{v};\tau_o)$$

$$\times \exp(-\imath\Omega_o t). \tag{4.9}$$

This replacement of t by $-j\frac{2a}{v}$ is crucial to the entire analysis. It is made possible because the reticle blades cross the image spot as rapidly as they do, i.e., more rapidly than the shape of the image spot can change. This makes it possible to keep the time dependent variation of $I(x,y,t)$ separate from the time dependent reticle produced dissection of the spot. (Note that the t dependence in $\exp(-\imath\Omega_o t)$ is not replaced by $-j\frac{2a}{v}$ since we shall consider values of Ω_o large enough that $\Omega_o t$ will change when t changes by the image-crossing time of $2R/v$.)

We now make the change of variable, within the summation that

$$\mu_j = vt + 2a_j \tag{4.10 a}$$

$$x_j = x + \mu_j \tag{4.10 b}$$

so that

$$S(\Omega_o;\Delta\Omega_o) = \sum_{j=-\infty}^{+\infty} \frac{1}{v} \int_{-\infty}^{+\infty} d\mu_j \int_{-\infty}^{+\infty} dy \int_{-a/2}^{+a/2} dx_j \; I(x_j+\mu_j, y, -j\frac{2a}{v})$$

$$\times W(-j\frac{2a}{v};\tau_o) \exp[\imath\Omega_o(j\frac{2a}{v} - \frac{\mu_j}{v})]. \tag{4.11}$$

Within the summation, we can drop the subscripts from x_j and μ_j , as these variables are bound by their integrations and not by the summation. We now bring all the factors in the integrand that do not depend on the variables of integration outside the integrals and interchange the orders of μ- and x-integrations.

$$S(\Omega_o; \Delta\Omega_o) = \sum_{j=-\infty}^{+\infty} \frac{1}{v} \exp\left(j\frac{2a}{v}\, \iota\, \Omega_o\right) W\left(-j\frac{2a}{v}; \tau_o\right)$$

$$\times \int_{-a/2}^{a/2} dx \int_{-\infty}^{+\infty} dy \int_{-\infty}^{+\infty} d\mu\; I(x+\mu, y, -j\frac{2a}{v}) \exp\left(-\iota\Omega_o \frac{\mu}{v}\right). \quad (4.12)$$

Within the x-integration, we replace μ by

$$\nu = \mu + x \,, \quad (4.13)$$

so that

$$S(\Omega_o; \Delta\Omega_o) = \sum_{j=-\infty}^{+\infty} \frac{1}{v} \exp\left(j\frac{2a}{v}\, \iota\, \Omega_o\right) W\left(-j\frac{2a}{v}; \tau_o\right) \int_{-a/2}^{a/2} dx \exp\left(\iota\, \Omega_o\, x/v\right)$$

$$\times \int_{-\infty}^{+\infty} dy \int_{-\infty}^{+\infty} d\nu\; I(\nu, y, -j\frac{2a}{v}) \exp\left(-\iota\Omega_o \frac{\nu}{v}\right). \quad (4.14)$$

At this point, we call attention to the fact that the x-integration is disjointed from the y- and ν-integrations and can, therefore, be performed separately —

$$\int_{-a/2}^{a/2} dx \exp\left(\iota\, \Omega_o\, x/v\right) = \frac{2v}{\Omega_o} \sin\left(\frac{\Omega_o\, a}{2v}\right). \quad (4.15)$$

When we substitute Eq. (4.15) into Eq. (4.14), make appropriate manipulations, and interchange the order of summation and integration, we get

$$S(\Omega_o; \Delta\Omega_o) = \frac{a}{v} \frac{\sin\left(a\,\Omega_o/2v\right)}{\left(a\,\Omega_o/2v\right)} \int_{-\infty}^{+\infty} dy \int_{-\infty}^{+\infty} d\nu$$

$$\times \sum_{j=-\infty}^{+\infty} W\left(-j\frac{2a}{v}; \tau_o\right) I(\nu, y, -j\frac{2a}{v}) \exp\left(-\iota\,\Omega_o\,\nu/v\right). \quad (4.16)$$

To revert to a more familiar form, we shall replace the symbol ν by x . The summation over j may be replaced by an integration over j , thus

$$\sum_{j=-\infty}^{+\infty} f\left(-j\frac{2a}{v}\right) = \int_{-\infty}^{+\infty} dj \; f\left(-j\frac{2a}{v}\right) , \tag{4.17 a}$$

or replacing j by

$$t = -j\frac{2a}{v} \tag{4.17 b}$$

so that

$$\int_{-\infty}^{+\infty} dj \; f\left(-j\frac{2a}{v}\right) = \frac{v}{2a} \int_{-\infty}^{+\infty} dt \; f(t) . \tag{4.17 c}$$

(where the minus sign in $-2a/v$ has been absorbed in interchanging upper and lower limits of integration). Now we can rewrite Eq. (4.16) as

$$\mathcal{S}(\Omega_o ; \Delta\Omega_o) = \frac{1}{2} \frac{\sin(a\,\Omega_o/2v}{(a\,\Omega_o/2v)} \int_{-\infty}^{+\infty} dt \int_{-\infty}^{+\infty} dy \int_{-\infty}^{+\infty} dx \; \exp\left[-\pi i \left(x\frac{\Omega_o}{2\pi v}\right)\right]$$

$$\times \; I(x, y, t) \; W(t; \tau_o) . \tag{4.18}$$

With the exception of the factor $\frac{1}{2} \frac{\sin(a\,\Omega_o/2v)}{(a\,\Omega_o/2v)}$, the right-hand side of Eq. (4.18) is identical to the right-hand side of Eq. (2.4'), thus proving that $\mathcal{S}(\Omega_o ; \Delta\Omega_o)$, the sine and cosine responses out of the phase-sensitive voltmeters, does indeed measure the time exposure MTF. The integration time, τ_o , of the phase-sensitive voltmeter corresponds to Δt , the exposure time for the MTF. The frequency, $\Omega_o/2\pi$ that the voltmeter is operating at corresponds to the spatial frequency, $\vec{f} = (f_x , f_y)$ of the MTF according to the relationships

$$f_x = \Omega_o/2\pi v \tag{4.19 a}$$

$$f_y = 0$$

In normal operation, perhaps the simplest way to take account of the factor $\frac{\sin (a \Omega_o/2v}{(a \Omega_o/2v)}$ is to note that this is the amplitude of the components of a square-wave, so that if the square-wave reference signal generated by the reticle chopper is put into both the signal and the reference side of the phase-sensitive voltmeter, and the gain of the meter is adjusted to produce unity output for the sine condition of phase shift, then the factor in question is automatically compensated for.

References

1. R. E. Hufnagel and N. R. Stanley, J. Opt. Soc. Am. 54, 52 (1964).
2. D. L. Fried, J. Opt. Soc. Am. 56, 1372 (1966).
3. E. Djurle and A. Bäck, J. Opt. Soc. Am. 51, 1029 (1961).
4. E. A. Trabka, J. Opt. Soc. Am. 56, 128 (1966).
5. C. E. Coulman, J. Opt. Soc. Am. 55, 806 (1965).
6. C. E. Coulman, J. Opt. Soc. Am. 56, 1232 (1966).
7. J. V. Ramsay and H. Kobler, Observatory 82, 107 (1962).

NASA-Langley, 1971 – 13
Coml., Newport News, Va.